Universität Stuttgart
Institut für Statik und Dynamik
der Luft- und Raumfahrtkonstruktionen

Theory and model implementation of gaseous transport and reaction processes in porous media applied to methane oxidation in landfill cover layers

Andrea Thom

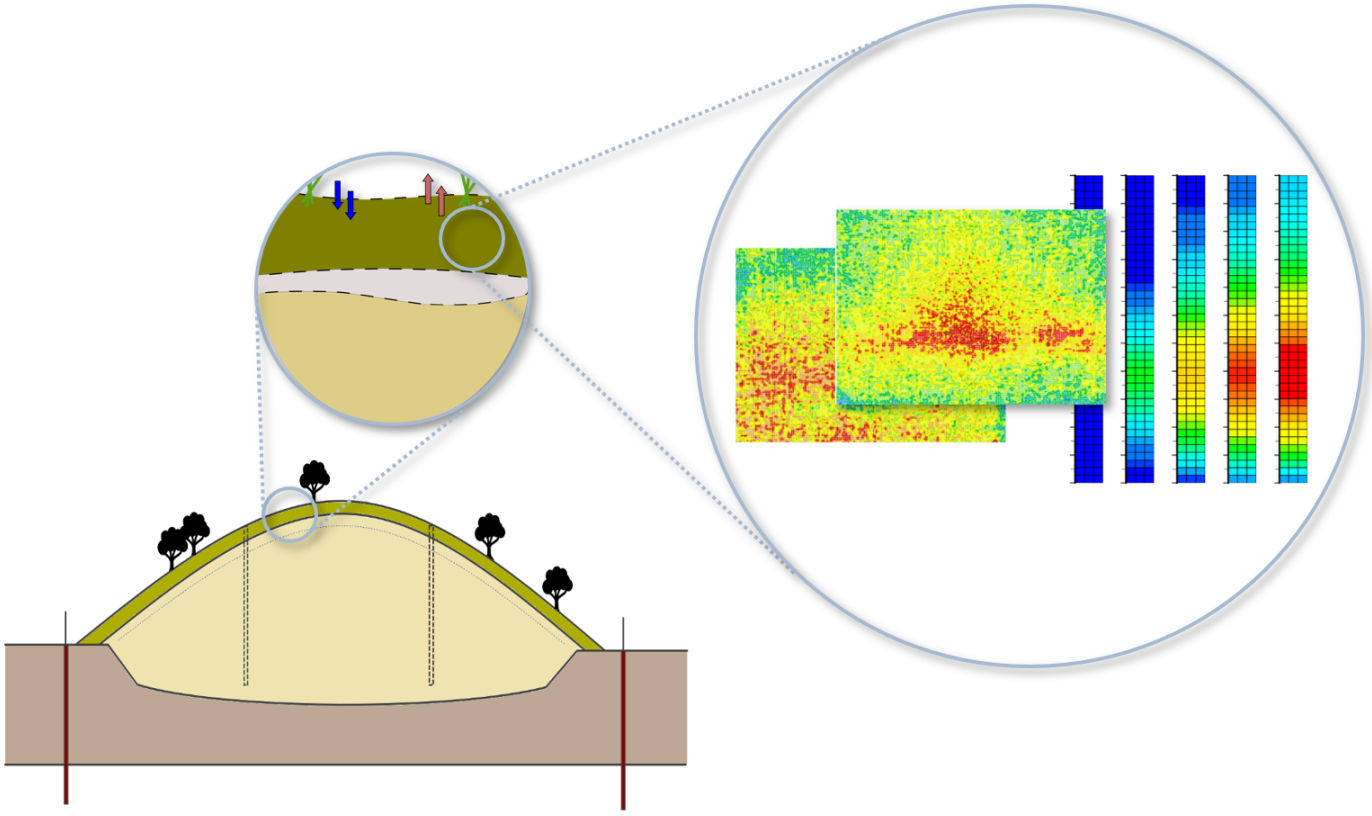

Bericht Nr. 2 (2022)

Theory and model implementation of gaseous transport and reaction processes in porous media applied to methane oxidation in landfill cover layers

A thesis accepted by the Faculty of Aerospace Engineering and Geodesy of the University of Stuttgart in fulfillment of the requirements for the degree of Doctor of Engineering Sciences (Dr.-Ing.)

by
Dipl.-Ing. Andrea Thom
born in Duisburg

Main referee:	Prof. Dr.-Ing. Tim Ricken
Co-referee:	Prof. Dr.-Ing. Dr. h.c. Wolfgang Ehlers
	Prof. Dr.-Ing. Renatus Widmann
Day of defense:	May 31, 2022

Institute of Structural Mechanics and
Dynamics in Aerospace Engineering
University of Stuttgart
2022

Publikationsreihe des
Instituts für Statik und Dynamik
der Luft- und Raumfahrtkonstruktionen (ISD)
Universität Stuttgart (D 93)

Bericht Nr. 2

Herausgeber: Univ.-Prof. Dr.-Ing. Tim Ricken

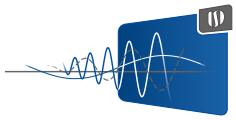

Berichte können bezogen werden über:

Institut für Statik und Dynamik
der Luft- und Raumfahrtkonstruktionen (ISD)
Universität Stuttgart
Pfaffenwaldring 27
70569 Stuttgart

Tel.: 0711 - 685 63612
Fax.: 0711 - 685 63706
E-Mail: office@isd.uni-stuttgart.de
URL: www.isd.uni-stuttgart.de

ISBN 978-3-942807-09-8

Life is like riding a bicycle. To keep your balance, you must keep moving.

– Albert Einstein

Preface

This dissertation was written during my time as a research assistant at the Chair of Structural Mechanics/Statics at the Technical University of Dortmund and at the Institute of Structural Mechanics and Dynamics in Aerospace Engineering at the University of Stuttgart.

My special thanks go to my supervisor, Professor Tim Ricken, who gave me the opportunity to do my doctorate, and has always accompanied, supported and encouraged me on my scientific path, both professionally and personally. I am grateful for his scientific guidance, and the numerous experiences I was able to gain during my doctoral phase in my daily work, and also at workshops and conferences together with him and the entire team.
Furthermore, I would like to express my sincere thanks to Professor Wolfgang Ehlers for taking over the first co-chair in my dissertation procedure. The opportunity for professional consultation was a great support in the run-up to the defense of my dissertation thesis, and I benefit from his comprehensive expertise. Many thanks also to Professor Renatus Widmann for taking on the second co-chair and providing broad expertise regarding the aspects of environmental modeling and waste management of my thesis.
A big thank you also to all my current and former colleagues for the great working atmosphere, the helpfulness, the extracurricular activities and their backing in any situation. I will always have very fond memories of my doctoral time.

Finally, I would like to thank my dear family for their all-round support in all phases of my life. Special thanks go to my mother, who always accompanied me unconditionally on my way and supported me in every decision I made, just in the spirit of our dear dad. Last but not least the best thanks to my husband Benni for motivating me again and again, for keeping my back free and enduring my moods, and for providing the necessary balance together with our beloved daughter Juni.

Stuttgart, November 2022 Andrea Thom

Contents

Nomenclature

Conventions

In addition to the following list of symbols, all symbols and abbreviations are explained in detail in the course of the text when they are used for the first time. The used tensor calculus notation is used following de Boer [35] and Holzapfel [65].

Scalar, vector, and tensor notation

quantity	example	description
scalar	ρ, t, H	small and capital characters with or without indices
vector	$\mathbf{b}$	small characters upright, bold type with or without indices
tensor	$\mathbf{F_S}$	capital characters upright, bold type with or without indices

General sub-/superscripts, operators

symbol	example	description
$(\cdot)$		place holder for arbitrary quantities
$\boldsymbol{\alpha}$	$\varphi^{\boldsymbol{\alpha}}$	index for macroscopic main phase/constituent
β	φ^{β}	index for miscible component/solute
$\alpha\beta$	$\varphi^{\alpha\beta}$	dual index for affiliation of component β to main phase $\boldsymbol{\alpha}$ - solute φ^{β} is solved in $\varphi^{\boldsymbol{\alpha}}$
γ	φ^{γ}	index for miscible gas component
$\mathrm{G}\gamma$	$\varphi^{\mathrm{G}\gamma}$	dual index for gas component φ^{γ} solved in gas mixture $\varphi^{\mathbf{G}}$

symbol	example	description
$(\cdot)_{\boldsymbol{\alpha}}$	$\mathbf{C}_{\boldsymbol{\alpha}}$	kinematic quantity of constituent $\varphi^{\boldsymbol{\alpha}}$
$(\cdot)_{\beta}$	$\mathbf{D}_{\beta}$	kinematic quantity of component φ^{β}
$(\cdot)^{\boldsymbol{\alpha}}$	$\mathbf{T}^{\boldsymbol{\alpha}}$	non-kinematic quantity of constituent $\varphi^{\boldsymbol{\alpha}}$
$(\cdot)^{\beta}$	$\mathbf{T}^{\beta}$	non-kinematic quantity of component φ^{β}
$(\cdot)_0$	G_0	initial value at t=0
$(\cdot)^{\boldsymbol{\alpha}}_{0\boldsymbol{\alpha}}$	$\mathrm{K}^{\mathbf{S}}_{0\mathbf{S}}$	initial value at t=0 with respect to reference configuration of $\varphi^{\boldsymbol{\alpha}}$
$(\cdot)_m$	$\mathrm{c}^{\alpha\beta}_m$	quantity in molar units
$(\cdot)^h$	$\mathbf{u}^h_{\mathbf{S}}$	spatially discretized quantity for finite element implementation
$(\cdot)^I$	$\mathbf{X}^I_{\mathbf{S}}$	discrete nodal value in finite element implementation
$(\cdot)^i$, $(\cdot)^{i+1}$		NEWTON iterations
$(\cdot)_n$, $(\cdot)_{n+1}$		NEWMARK iterations
$\mathrm{d}(\cdot)$		differential operator
$\partial(\cdot)$		partial derivative operator
$\delta(\cdot)$		test function of primary unkowns
$\dot{(\cdot)}$	$\dot{\rho}$	total time derivative
$(\cdot)'_{\boldsymbol{\alpha}}$	$(\mathrm{n}^{\mathbf{S}})'_{\mathbf{S}}$	material time derivative with respect to motion of $\varphi^{\boldsymbol{\alpha}}$
$(\cdot)'_{\beta}$	$(\mathrm{c}^{\alpha\beta}_m)'_{\beta}$	material time derivative with respect to motion φ^{β}
$\mathrm{Grad}_{\boldsymbol{\alpha}}(\cdot)$		partial derivative of $(\cdot)$ with respect to reference position $\mathbf{X}_{\boldsymbol{\alpha}}$
$\mathrm{grad}(\cdot)$		partial derivative of $(\cdot)$ with respect to actual position $\mathbf{x}$
$\hat{(\cdot)}$	$\hat{\rho}^{\boldsymbol{\alpha}}$, $\hat{\mathrm{c}}^{\mathrm{G}\gamma}_m$	production term

Symbols

Greek symbols

symbol	unit	description
$\alpha_{\nabla\theta}$	[W/(mK)]	heat conduction coefficient of body φ
$\alpha_{\mathbf{S}}$	[1/K]	thermal expansion coefficient of solid phase

symbol	unit	description
$\boldsymbol{\alpha}$		index for macroscopic main phase ($\mathbf{S}/\mathbf{L}/\mathbf{G}$)
β		general index for miscible solute
$\alpha\beta$		general dual index for solute φ^{β} solved in $\varphi^{\boldsymbol{\alpha}}$
γ		index for gaseous component (M,O,C,N)
Gγ		dual index for gaseous component solved in $\varphi^{\mathbf{G}}$
γ	[1/K]	coefficient of expansion
ε, $\varepsilon^{\boldsymbol{\alpha}}$, ε^{β}	[J/kg]	mass-specific internal energy of $\varphi/\varphi^{\boldsymbol{\alpha}}/\varphi^{\beta}$
$\hat{\varepsilon}^{\boldsymbol{\alpha}}$, $\hat{\varepsilon}^{\beta}$	[J/(m^{3}s)]	volume-specific direct energy production for $\varphi^{\boldsymbol{\alpha}}/\varphi^{\beta}$
η, $\eta^{\boldsymbol{\alpha}}$, η^{β}	[J/(kgK)]	mass-specific entropy of $\varphi/\varphi^{\boldsymbol{\alpha}}/\varphi^{\beta}$
$\eta^{\alpha\beta}$	[J/(m^{3}K)]	volume-specific entropy of $\varphi^{\alpha\beta}$
$\eta^{\boldsymbol{\alpha}\mathrm{R}}$	[Ns/m^2]	true dynamic viscosity of mixture $\varphi^{\boldsymbol{\alpha}}$
$\hat{\zeta}^{\boldsymbol{\alpha}}$, $\hat{\zeta}^{\beta}$	[J/(m^{3}Ks)]	volume-specific direct entropy production of $\varphi^{\boldsymbol{\alpha}}/\varphi^{\beta}$
$\hat{\eta}$, $\hat{\eta}^{\boldsymbol{\alpha}}$, $\hat{\eta}^{\beta}$	[J/(m^{3}Ks)]	volume-specific entropy production of $\varphi/\varphi^{\boldsymbol{\alpha}}/\varphi^{\beta}$
θ, $\theta^{\boldsymbol{\alpha}}$, θ^{β}	[K]	temperature of $\varphi/\varphi^{\boldsymbol{\alpha}}/\varphi^{\beta}$
κ	[1/Pa]	coefficient of compressibility
λ	[N/m^2]	Lagrange multiplier
$\lambda^{\mathbf{S}}$, $\mu^{\mathbf{S}}$	[N/m^2]	1^{st} and 2^{nd} Lamé constant
μ, μ_i	[J/mol]	overall molar chemical potential and of substance i
μ^{β}	[J/kg]	mass-specific chemical potential of φ^{β}
μ_m^{β}	[J/mol]	molar-specific chemical potential of φ^{β}
$\mu^{\alpha\beta}$	[J/m^3]	vol-specific chemical potential of $\varphi^{\alpha\beta}$
ξ, $\boldsymbol{\xi}$, $\xi^{\boldsymbol{\alpha}}$, $\boldsymbol{\xi}^{\boldsymbol{\alpha}}$, ξ^{β},$\boldsymbol{\xi}^{\beta}$		supply of arbitrary field quantity of $\varphi/\varphi^{\boldsymbol{\alpha}}/\varphi^{\beta}$ in volume
ρ	[kg/m^3]	density of overall aggregate
ρ^{β}, $\rho^{\alpha\beta}$	[kg/m^3]	partial/ true mass concentration of component φ^{β}
$\rho^{\boldsymbol{\alpha}}$, $\rho^{\boldsymbol{\alpha}\mathrm{R}}$	[kg/m^3]	partial/true density of constituent $\varphi^{\boldsymbol{\alpha}}$
$\hat{\rho}^{\mathrm{SB}}$	[$\cdot$/s]	growth rate of bacteria
$\hat{\rho}_{\mathrm{GM}}^{\mathrm{GM}}$,$\hat{\rho}_{\mathrm{GO}}^{\mathrm{GM}}$,$\hat{\rho}_{\theta}^{\mathrm{GM}}$	[-]	rate limiting functions of max. methane oxidation rate
$\hat{\rho}^{\boldsymbol{\alpha}}$, $\hat{\rho}^{\beta}$, $\hat{\rho}^{\boldsymbol{\alpha}\mathrm{R}}$	[kg/(m^{3}s)]	partial mass production term of $\varphi^{\boldsymbol{\alpha}}/\varphi^{\beta}$ and true mass supply
τ	[-]	tortuosity factor

symbol	unit	description
Υ,$\Upsilon^{\boldsymbol{\alpha}}$,$\Upsilon^{\beta}$	$[\cdot/\mathrm{m}^3]$	scalar-valued, volume-specific arbitrary field quantity of φ,$\varphi^{\boldsymbol{\alpha}}$,$\varphi^{\beta}$
$\boldsymbol{\Upsilon}$,$\boldsymbol{\Upsilon}^{\boldsymbol{\alpha}}$,$\boldsymbol{\Upsilon}^{\beta}$	$[\cdot/\mathrm{m}^3]$	vector-/tensor-valued, volume-specific arbitrary field quantity of φ,$\varphi^{\boldsymbol{\alpha}}$,$\varphi^{\beta}$
$\hat{\Upsilon}$,$\hat{\Upsilon}^{\boldsymbol{\alpha}}$,$\hat{\Upsilon}^{\beta}$	$[\cdot/\mathrm{m}^3]$	scalar-valued, volume-specific production of arbitrary field quantity of φ,$\varphi^{\boldsymbol{\alpha}}$,$\varphi^{\beta}$
$\hat{\boldsymbol{\Upsilon}}$,$\hat{\boldsymbol{\Upsilon}}^{\boldsymbol{\alpha}}$,$\hat{\boldsymbol{\Upsilon}}^{\beta}$	$[\cdot/\mathrm{m}^3]$	vector-/tensor-valued, volume-specific production of arbitrary field quantity of $\varphi/\varphi^{\boldsymbol{\alpha}}/\varphi^{\beta}$
φ,$\varphi^{\boldsymbol{\alpha}}$,$\varphi^{\beta}$		overall mixture body/constituent/component
$\varphi^{\alpha\beta}$		component φ^{β} solved in mixture $\varphi^{\boldsymbol{\alpha}}$
$\boldsymbol{\phi}$,$\boldsymbol{\phi}^{\boldsymbol{\alpha}}$,$\boldsymbol{\phi}^{\beta}$		scalar-valued, density efflux of $\varphi/\varphi^{\boldsymbol{\alpha}}/\varphi^{\beta}$ of field quantity
$\boldsymbol{\Phi}$,$\boldsymbol{\Phi}^{\boldsymbol{\alpha}}$,$\boldsymbol{\Phi}^{\beta}$		vector-/tensor-valued, density efflux of $\varphi/\varphi^{\boldsymbol{\alpha}}/\varphi^{\beta}$ of field quantity
$\boldsymbol{\phi}_{\eta}$,$\boldsymbol{\phi}_{\eta}^{\boldsymbol{\alpha}}$,$\boldsymbol{\phi}_{\eta}^{\beta}$	$[\mathrm{J}/(\mathrm{m}^2\mathrm{Ks})]$	entropy efflux of $\varphi/\varphi^{\boldsymbol{\alpha}}/\varphi^{\beta}$
χ, $\chi_{\boldsymbol{\alpha}}$, χ_{β}		motion function of $\varphi/\varphi^{\boldsymbol{\alpha}}/\varphi^{\beta}$
$\psi^{\boldsymbol{\alpha}}$, ψ^{β}	$[\mathrm{J/kg}]$	mass-specific Helmholtz free energy for $\varphi^{\boldsymbol{\alpha}}/\varphi^{\beta}$
$\psi^{\alpha\beta}$	$[\mathrm{J}/\mathrm{m}^3]$	volume-specific Helmholtz free energy for $\varphi^{\alpha\beta}$
$\Psi^{\mathbf{S}}$	$[\mathrm{J}/\mathrm{m}^3]$	volume-specific strain energy Helmholtz function of $\varphi^{\mathbf{S}}$
$\Psi^{\boldsymbol{\alpha}}$	$[\mathrm{J}/\mathrm{m}^3]$	volume-specific Helmholtz free energy of $\varphi^{\boldsymbol{\alpha}}$
$\omega^{\alpha\beta}$	[-]	mass fraction of component φ^{β} solved in $\varphi^{\boldsymbol{\alpha}}$
Ω, $\partial\Omega$		spatial domain and its surface
Ω_e, $\partial\Omega_e$		finite element domain and its surface

Latin symbols

symbol	unit	description
A_i		general chemical component, e.g. H_2, O_2
$\mathbf{A}_{\boldsymbol{\alpha}}$	[-]	Almansi strain tensor of constituent $\varphi^{\boldsymbol{\alpha}}$
$\mathbf{b}$	$[\mathrm{m}/\mathrm{s}^2]$	body force vector of φ

symbol	unit	description
$\mathrm{B}_{0\boldsymbol{\alpha}}$, $\partial\mathrm{B}_{0\boldsymbol{\alpha}}$		geometric domain in referential configuration and its surface
$\mathbf{B}_{\boldsymbol{\alpha}}$	[-]	left CAUCHY-GREEN deformation tensor of $\varphi^{\boldsymbol{\alpha}}$
$\bar{\mathrm{c}}^{\mathrm{SB}}$	[-]	amount of methanotrophic bacteria
$\mathrm{c_p}$, $\mathrm{c_V}$	[J/(kg K)]	specific heat capacity for isobaric/isochoric condition
$\mathrm{c}_{\mathrm{V}}^{\boldsymbol{\alpha}}$, $\mathrm{c}_{\mathrm{V}}^{\beta}$	[J/(kg K)]	isochoric specific heat capacity of $\varphi^{\boldsymbol{\alpha}}/\varphi^{\beta}$
c_m	[mol/m^3]	molar concentration of overall aggregate
$\mathrm{c}_m^{\alpha\beta}$	[mol/m^3]	true molar concentration of component $\varphi^{\alpha\beta}$
$\hat{c}_m^{\alpha\beta}$	[mol/(m^{3}s)]	true molar production of component $\varphi^{\alpha\beta}$
$\mathrm{c}_m^{\boldsymbol{\alpha}}$, $\mathrm{c}_m^{\boldsymbol{\alpha}\mathrm{R}}$	[mol/m^3]	partial/true molar concentration of constituent $\varphi^{\boldsymbol{\alpha}}$
$\mathbf{d}_{\boldsymbol{\alpha}}$, ${}_m\mathbf{d}_{\boldsymbol{\alpha}}$	[m/s]	mass/molar diffusion velocity of mixture $\varphi^{\boldsymbol{\alpha}}$ to φ
$\mathbf{d}_{\beta\boldsymbol{\alpha}}$, ${}_m\mathbf{d}_{\beta\boldsymbol{\alpha}}$	[m/s]	mass/molar diffusion velocity of $\varphi^{\alpha\beta}$ to solution $\varphi^{\boldsymbol{\alpha}}$
$\mathbf{C}_{\boldsymbol{\alpha}}$	[-]	right CAUCHY-GREEN deformation tensor of $\varphi^{\boldsymbol{\alpha}}$
$D_{\beta\iota}$, ${}_mD_{\beta\iota}$	[m^2/s]	mass/molar binary diffusion coefficient FICK's law
$D_{\alpha\beta}$, ${}_mD_{\alpha\beta}$	[m^2/s]	mass/molar mixture diffusion coefficient BLANC's law
$D_{\beta\nu}$, ${}_mD_{\beta\nu}$	[m^2/s]	multi-component mass/molar diffusion coefficient
$\mathbf{D}$		damping matrix
$\mathbf{D}_{\boldsymbol{\alpha}}$, $\mathbf{D}_{\beta}$	[1/s]	symmetric part of spatial velocity gradient of $\varphi^{\boldsymbol{\alpha}}/\varphi^{\beta}$
$\hat{\mathrm{e}}^{\boldsymbol{\alpha}}$, $\hat{\mathrm{e}}^{\beta}$	[J/(m^{3}s)]	vol.-specific total energy supply of $\varphi^{\boldsymbol{\alpha}}/\varphi^{\beta}$
$\mathbf{E}_{\boldsymbol{\alpha}}$	[-]	GREEN-LAGRANGE strain tensor of constituent $\varphi^{\boldsymbol{\alpha}}$
F	[J]	free HELMHOLTZ energy
$\mathbf{F}_{\boldsymbol{\alpha}}$	[-]	material deformation gradient of constituent $\varphi^{\boldsymbol{\alpha}}$
$\mathbf{g}$		vector collecting weak formulations
G	[J]	free enthalpy/GIBBS energy
h, $h^{\boldsymbol{\alpha}}$, h^{β}	[J/kg]	mass-specific enthalpy of $\varphi/\varphi^{\boldsymbol{\alpha}}/\varphi^{\beta}$
$\mathbf{h}$	[kg/(ms)]	angular momentum of φ
$\hat{\mathbf{h}}^{\boldsymbol{\alpha}}$, $\hat{\mathbf{h}}^{\beta}$	[N/m^2]	vol.-specific total angular momentum production for $\varphi^{\boldsymbol{\alpha}}/\varphi^{\beta}$
H	[J]	total enthalpy
$\mathbf{I}$	[-]	identity tensor
$\mathbf{j}_{tot}^{\beta}$, $\mathbf{j}_{tot}^{\alpha\beta}$	[kg/(m^{2}s)]	partial/true total mass flux of component $\varphi^{\alpha\beta}$
$\mathbf{j}_{diff}^{\beta}$, $\mathbf{j}_{diff}^{\alpha\beta}$	[kg/(m^{2}s)]	partial/true diffusive mass flux of component $\varphi^{\alpha\beta}$
$\mathbf{j}_{adv}^{\beta}$, $\mathbf{j}_{adv}^{\alpha\beta}$	[kg/(m^{2}s)]	partial/true advective mass flux of component $\varphi^{\alpha\beta}$

symbol	unit	description
${}_m\mathbf{j}^{\beta}_{tot}$, ${}_m\mathbf{j}^{\alpha\beta}_{tot}$	[mol/(m^{2}s)]	partial/true total molar flux of component $\varphi^{\alpha\beta}$
${}_m\mathbf{j}^{\beta}_{diff}$, ${}_m\mathbf{j}^{\alpha\beta}_{diff}$	[mol/(m^{2}s)]	partial/true diffusive molar flux of component $\varphi^{\alpha\beta}$
${}_m\mathbf{j}^{\beta}_{adv}$, ${}_m\mathbf{j}^{\alpha\beta}_{adv}$	[mol/(m^{2}s)]	partial/true advective molar flux of component $\varphi^{\alpha\beta}$
$\mathrm{J}_{\boldsymbol{\alpha}}$	[-]	JACOBI determinant of constituent $\varphi^{\boldsymbol{\alpha}}$
$\mathrm{k}^{\mathbf{S}}$	[N/m^2]	bulk modulus of solid
$\mathrm{k}^{\boldsymbol{\beta}}_0$	[m^4/Ns]	proportionality coefficient of filter velocity of $\varphi^{\mathbf{L}}/\varphi^{\mathbf{G}}$
$\mathrm{k}^{\boldsymbol{\beta}}_D$	[m^4/Ns]	DARCY coefficient for $\varphi^{\mathbf{L}}/\varphi^{\mathbf{G}}$
$\mathrm{k}^{\boldsymbol{\beta}}$	[m/s]	permeability coefficient of $\varphi^{\mathbf{L}}/\varphi^{\mathbf{G}}$
$\mathrm{K}^{\mathbf{S}}$	[m^2]	intrinsic permeability of $\varphi^{\mathbf{S}}$
$\mathbf{k}$	[N]	external forces acting in the volume of φ
K	[J]	kinetic energy
K_{GM}, K_{GO}	[-]	half saturation constants methane and oxygen
$\mathbf{K}$, $\mathbf{K}^*$		tangential/effective stiffness matrix
$\mathbf{K}_{\boldsymbol{\alpha}}$, $\overset{\mathrm{R}}{\mathbf{K}}_{\boldsymbol{\alpha}}$	[-]	material/spatial KARNI-REINER strain tensor of $\varphi^{\boldsymbol{\alpha}}$
$\mathbf{l}$	[kg/(m^{2}s)]	linear momentum of φ
$\mathbf{L}_{\boldsymbol{\alpha}}$, $\mathbf{L}_{\beta}$	[1/s]	spatial velocity gradient of $\varphi^{\boldsymbol{\alpha}}/\varphi^{\beta}$
m	[kg]	mass
$\hat{\mathbf{m}}^{\boldsymbol{\alpha}}$, $\hat{\mathbf{m}}^{\beta}$	[N/m^2]	volume-specific direct angular momentum production for $\varphi^{\boldsymbol{\alpha}}/\varphi^{\beta}$
M, $\mathrm{M}^{\boldsymbol{\alpha}}$, M^{β}	[kg]	total mass/partial mass/ mass of component φ^{β}
M_m	[kg/mol]	molar mass constant of overall aggregate
$\mathrm{M}^{\boldsymbol{\alpha}}_m$	[kg/mol]	mixture molar mass of constituent $\varphi^{\boldsymbol{\alpha}}$
M^{β}_m	[kg/mol]	molar mass of component φ^{β}
n_i		number of particles of substance i
$\mathrm{n}^{\boldsymbol{\alpha}}$	[-]	volume fraction of solid/liquid/gas phase
$\mathrm{n}^{\mathbf{F}}$	[-]	volume fraction of fluid phase $\mathrm{n}^{\mathbf{L}} + \mathrm{n}^{\mathbf{G}}$
$\mathbf{n}$	[-]	outward orientated surface normal vector
$\mathbf{n}^{\beta}$, $\mathbf{n}^{\alpha\beta}$	[kg/(m^{2}s)]	partial/true total mass flux of component φ^{β}
$\mathbf{n}^{\boldsymbol{\alpha}\mathrm{R}}$	[kg/(m^{2}s)]	true total mass flux of constituent $\varphi^{\boldsymbol{\alpha}}$
${}_m\mathbf{n}^{\beta}$, ${}_m\mathbf{n}^{\alpha\beta}$	[mol/(m^{2}s)]	partial/true total molar flux of component φ^{β}
${}_m\mathbf{n}^{\boldsymbol{\alpha}\mathrm{R}}$	[mol/(m^{2}s)]	true total molar flux of constituent $\varphi^{\boldsymbol{\alpha}}$
p, p^i	[N/m^2]	general pressure/partial pressure of substance i
$\mathrm{p}^{\alpha\beta}$, $\mathrm{p}^{\boldsymbol{\alpha}\mathrm{R}}$	[N/m^2]	partial pressure of $\varphi^{\alpha\beta}$/ true mixture pressure of $\varphi^{\boldsymbol{\alpha}}$

symbol	unit	description
$\hat{\mathbf{p}}^{\boldsymbol{\alpha}}$, $\hat{\mathbf{p}}^{\beta}$	[N/m^3]	volume-specific direct momentum supply of $\varphi^{\boldsymbol{\alpha}}/\varphi^{\beta}$
$\hat{\mathbf{p}}_{\mathrm{E}}^{\boldsymbol{\alpha}}$, $\hat{\mathbf{p}}_{\mathrm{E}}^{\beta}$	[N/m^3]	volume-specific extra direct momentum supply of $\varphi^{\boldsymbol{\alpha}}/\varphi^{\beta}$
$\mathbf{P}$, $\mathbf{P}^{\boldsymbol{\alpha}}$	[N/m^2]	1^{st} PIOLA-KIRCHHOFF stress tensor of $\varphi/\varphi^{\boldsymbol{\alpha}}$
$\mathbf{q}$, $\mathbf{q}^{\boldsymbol{\alpha}}$, $\mathbf{q}^{\beta}$	[J/(m^{2}s)]	heat influx vector of $\varphi/\varphi^{\boldsymbol{\alpha}}/\varphi^{\beta}$
Q	[J]	total heat
r, $\mathrm{r}^{\boldsymbol{\alpha}}$, r^{β}	[J/(kg s)]	mass-specific external energy source (radiation) of $\varphi/\varphi^{\boldsymbol{\alpha}}/\varphi^{\beta}$
R, R^{β}	[J/(kg K)]	specific gas constant of mixture/component φ^{β}
R_m	[J/(molK)]	molar/universal gas constant
$\mathbf{R}_{\boldsymbol{\alpha}}$	[-]	proper orthogonal rotation tensor of constituent $\varphi^{\boldsymbol{\alpha}}$
$\mathrm{s}^{\mathbf{L}}$, $\mathrm{s}^{\mathbf{G}}$	[-]	saturation of liquid/gas phase
$\hat{\mathbf{s}}^{\boldsymbol{\alpha}}$, $\hat{\mathbf{s}}^{\beta}$	[N/m^3]	volume-specific total momentum supply of $\varphi^{\boldsymbol{\alpha}}/\varphi^{\beta}$ (interaction forces)
$\mathbf{S}$, $\mathbf{S}^{\boldsymbol{\alpha}}$	[N/m^2]	2^{nd} PIOLA-KIRCHHOFF stress tensor of $\varphi/\varphi^{\boldsymbol{\alpha}}$
t	[s]	time
$\mathbf{t}$, $\mathbf{t}^{\boldsymbol{\alpha}}$	[N/m^2]	traction vector of body φ/ of constituent $\varphi^{\boldsymbol{\alpha}}$
T	[K]	absolute temperature
$\mathbf{T}$, $\mathbf{T}^{\boldsymbol{\alpha}}$, $\mathbf{T}^{\beta}$	[N/m^2]	Cauchy stress tensor of $\varphi/\varphi^{\boldsymbol{\alpha}}/\varphi^{\beta}$
$\mathbf{T}_{\mathrm{E}}^{\mathbf{S}}$	[N/m^2]	extra Cauchy stress tensor of solid matrix
$\mathbf{u}$, $\dot{\mathbf{u}}$, $\ddot{\mathbf{u}}$		vector of field unknowns/their velocity/acceleration
$\mathbf{u}_{\mathbf{S}}$	[m]	solid displacement vector
U	[J]	total internal energy
$\mathbf{U}_{\boldsymbol{\alpha}}$	[-]	material right stretch tensor of constituent $\varphi^{\boldsymbol{\alpha}}$
v_i		stoichiometric coefficient
$V_{\max}$	[mol/(kgs)]	maximum oxidation rate per unit soil
V	[m^3]	volume
V_m	[m^3/mol]	molar volume
V, $\mathrm{V}^{\boldsymbol{\alpha}}$	[m^3]	total volume of φ/partial volume of constituent $\varphi^{\boldsymbol{\alpha}}$
$\mathbf{V}_{\boldsymbol{\alpha}}$	[-]	spatial left stretch tensor of constituent $\varphi^{\boldsymbol{\alpha}}$
$\mathbf{w}_{\boldsymbol{\alpha}\mathbf{S}}$, ${}_m\mathbf{w}_{\boldsymbol{\alpha}\mathbf{S}}$	[m/s]	mass/molar seepage velocity
$\mathbf{w}_{\beta\mathbf{S}}$	[m/s]	difference velocity
W	[J]	mechanical work

symbol	unit	description
$\mathbf{W}_{\boldsymbol{\alpha}}$	[1/s]	skew-symmetric part of spatial velocity gradient of constituent $\varphi^{\boldsymbol{\alpha}}$
x_i, $x_m^{\alpha\beta}$	[-]	mole fraction of substance i/ of component $\varphi^{\alpha\beta}$
$\mathbf{X}_{\boldsymbol{\alpha}}$, $\mathbf{x}$	[m]	position vector for reference/actual configuration
$\dot{\mathbf{x}}$, ${}_m\dot{\mathbf{x}}$	[m/s]	mean mass/molar barycentric velocity vector of body φ
$\mathbf{x}'_{\boldsymbol{\alpha}}$, ${}_m\mathbf{x}'_{\boldsymbol{\alpha}}$	[m/s]	mean mass/molar velocity vector of constituent $\varphi^{\boldsymbol{\alpha}}$
$\mathbf{x}'_\beta$	[m/s]	independent velocity vector of component φ^β
$\mathbf{x}''_{\boldsymbol{\alpha}}$, $\mathbf{x}''_\beta$	[m/s^2]	acceleration vector of $\varphi^{\boldsymbol{\alpha}}/\varphi^\beta$

Acronyms

ADM advection-diffusion model
AR5 Fifth Assessment Report

DFG German Research Foundation
DGM dusty-gas model

EPS extrapolymeric substance
eTPM extended Theory of Porous Media

FE finite element
FEA finite element analysis
FEAP finite element analysis program
FEM finite element method
FSI fluid structure interaction

GHG global greenhouse gases
GWP global warming potential

IBVP initial boundary value problem
IPCC Intergovernmental Panel on Climate Change

MSW municipal solid waste

PDE partial differential equation
ppb parts per billion
ppm parts per million

TPM Theory of Porous Media

UDE University of Duisburg-Essen

Kurzfassung

Die vorliegende Arbeit wurde im Rahmen des von der Deutschen Forschungsgemeinschaft (DFG) geförderten interdisziplinären Forschungsprojekts zur Modellierung und Simulation der Funktionsweise der bakteriellen Methanoxidation in Abdeckschichten auf Siedlungsabfalldeponien erstellt. Durch die bakterielle Zersetzung des organischen Anteils des deponierten Siedlungsabfalls werden über mehrere Dekaden hinweg die klimaschädlichen Gase Methan (CH_4) und Kohlendioxid (CO_2) produziert, und eine Behandlung dieser Emissionen ist auch nach Deponieschließung behördlich vorgeschrieben.

Methan gehört zu den stärksten Treibern des Treibhauseffekts und wirkt auf einen 20-Jahres Zeitraum gesehen ca. 85-mal stärker als Kohlendioxid. Die passiv stattfindende Umwandlung von Methan zu Kohlendioxid durch die natürlich vorkommende bakterielle Methanoxidation in belüfteten Böden ist eine sowohl ökologische als auch wirtschaftliche Möglichkeit, um die verbleibenden Emissionen in der Nachsorgephase der Deponie zu behandeln. Durch Messungen müssen die verbleibenden Emissionen qualitativ und quantitativ nachgewiesen werden. Eine numerische Simulation kann diesen Nachweis unterstützen.

Um die Funktionsfähigkeit einer Methanoxidationsschicht erfassen und letztendlich nachweisen zu können, wurden im Rahmen des Projektes einerseits experimentelle Untersuchungen im Labor zur Messung der Gasflüsse unter verschiedenen Einflussparametern als auch zur chemischen Analyse durchgeführt. Zum Anderen wurde von der Autorin dieser Arbeit ein mathematisches Modell basierend auf der kontinuumsmechanischen Theorie poröser Medien (TPM) für numerische Simulation der Methanoxidation in Böden erstellt. Dieses wurde anhand der kleinskaligen Experimente aus dem Labor mit variierenden Anfangs- und Randbedingungen verifiziert und validiert. Das daraus resultierende numerische Berechnungskonzept soll es ermöglichen, Gasflüsse durch bestehende Abdeckschichten unter den gegebenen Bedingungen zu bilanzieren und weiterhin Abdeckschichten auf Deponien so zu planen, dass die Funktionsfähigkeit der Methanoxidation auch unter ungünstigen äußeren Umwelteinflüssen

flüssen wie sehr trockenen oder nassen Jahreszeiten und lebensfeindlichen Böden für die methanoxidierenden Bakterien gewährleistet werden kann.

Abgeleitet aus dem angestrebten Projektziel sowie der Aktualität klimarelevanter Themen wurde ein allgemeines theoretisches Konzept für die numerische Simulation von mehrphasigen und mehrkomponentigen natürlichen Systemen im Kontext der Umweltwissenschaften aufgestellt. Die jeweils unterschiedlichen makroskopischen Phasen natürlicher Systeme - fest, flüssig und gasförmig - setzen sich in der Regel aus mehreren Mischungskomponenten zusammen, die durch biologische und/oder chemische Prozesse miteinander reagieren, und durch physikalische Transportprozesse räumlich und zeitlich umverteilt werden können. Dazu wurde die klassische Theorie poröser Medien um Mischungsbeschreibungen der makroskopischen Phasen erweitert (eTPM). Der Schwerpunkt in der vorliegenden Arbeit liegt dabei auf reaktiven kompressiblen Gasgemischen, welche als ideale Gase modelliert werden und eine Festkörpermatrix durchströmen. Die Festkörpermatrix stellt im Fall der Methanoxidation einen Bodenkörper dar, so dass gegenseitige Wechselwirkungen nicht nur zwischen den Gaskomponenten, sondern auch zwischen Boden und Gasgemisch auftreten können. Weitere Anwendungen des theoretischen Modells wären z.B. numerische Simulationen der auftauenden Permafrostböden oder der biologischen Abluftreinigung in Biofilteranlagen. Darüber hinaus ermöglicht das Mehrkomponentenkonzept die Beschreibung von Produktion oder Reduktion einzelner Kozentrationen durch chemische Reaktionen, angetrieben durch biologische Aktivitä. Auch die Stofftransportmechanismen der Diffusion und Advektion lassen sich anhand der erweiterten Theorie poröser Medien (eTPM) thermodynamisch konsistent modellieren. Mit Modifikationen kann dieses Berechnungskonzept auch auf inkompressible Festkörper-Flüssigkeit-Mischungen angewandt werden.

Als theoretische Grundlage des Modells dient die fundierte Theorie poröser Medien, eine kontinuumsmechanische Beschreibung für Mehrphasensysteme. Diese Beschreibung hat sich als sehr gut geeignet erwiesen, um ein Modell für multiphysikalische Probleme aus der Bodenmechanik und den Umweltwissenschaften zu erstellen. Die ganzheitliche Modellbeschreibung in dieser Arbeit vereint zudem weitere Teilbereiche der theoretischen Herleitungen. Zu diesen Teilbereichen gehören die Grundlagen der Thermodynamik, die in Verbindung mit der Kontinuumsmechanik sowie den Gleichungen für den Stoffaustausch in Fluidgemischen zu einer thermodynamisch konsistenten Materialbeschreibung gesetzt werden. Die Materialtheorie und die ihr

zugrundeliegenden Axiome für die Materialmodellierung bieten eine solide Grundlage für die Aufstellung von konstitutiven Gleichungen, ohne dabei physikalische und thermodynamische Gesetze zu verletzen, und somit zu einer mathematischen Beschreibung des phänomenologischen thermo-biochemo-mechanischen Verhaltens eines Festkörpers und der gekoppelten dissipativen Mechanismen führt.

Die konsistenten Modell- und Materialgleichungen bilden das Gleichungssystem, welches zur numerische Berechnung in die Finite-Elemente-Methode umgesetzt wird. Dazu wird das System nichtlinearer, gekoppelter partieller Differentialgleichungen mit der variationellen Galerkin-Methode in seine schwache Form transformiert, und das resultierende Gleichungssystem mit der Newton-Raphson-Methode kombiniert mit dem impliziten Zeitintegrationsschema des Newmark-β-Verfahrens gelöst.

Durch die Kombination verschiedener mathematischer und theoretischer Teilbereiche wird ein umfassendes, stabiles rechnerisches Konzept für die Untersuchung und Simulation umweltmechanischer Probleme aufgestellt und verifiziert, und durch die Anwendung auf die bakterielle Methanoxidation in Böden validiert.

Abstract

The present work was initiated and realized within the framework of the interdisciplinary research project on the modeling and simulation of the bacterial methane oxidation in landfill cover layers, which was funded by the German Research Foundation (DFG). Landfill sites produce methane (CH_4) and carbon dioxide (CO_2) in nearly equal shares by the bacterial degradation of the organic fraction of the deposited municipal solid waste over several decades. Therefore, an aftercare treatment of the gas emissions still occurring after landfill closure is required by authorities.

Methane is one of the strongest drivers of the greenhouse effect and is approximately 85 times more potent than carbon dioxide over a 20-year period. Passive conversion of methane to carbon dioxide by naturally occurring bacterial methane oxidation in aerated soils is both an environmental and economic option to address residual emissions in the post-closure phase of landfilling. Measurements must be used to provide qualitative and quantitative evidence of the remaining emissions by authorities. Numerical simulation can support this verification.

In order to monitor and prove the functionality of a methane oxidation layer in the framework of the project, experimental investigations were carried out on the one hand in the laboratory to measure the gas fluxes under various influencing parameters as well as for chemical analysis. On the other hand, a mathematical model based on the continuum mechanical Theory of Porous Media (TPM) was developed by the author of this thesis for numerical simulation of methane oxidation in soils. This was verified and validated using the small-scale experiments from the laboratory with varying initial and boundary conditions. The resulting numerical calculation concept makes it possible to balance gas fluxes through existing cover layers under the given conditions and furthermore to design cover layers on landfills in such a way that the functionality of methane oxidation can be guaranteed even under unfavorable external environmental conditions such as very dry or wet seasons and hostile soils for the methane-oxidizing bacteria.

Derived from the intended project goal as well as the topicality of climate-relevant

issues, a general theoretical concept for the numerical simulation of multi-phase and multi-component natural systems in the context of environmental sciences was established. The respective different macroscopic phases of natural systems - solid, liquid and gaseous - are usually composed of several mixture components, which can react with each other due to biological and/or chemical processes, and can be redistributed spatially and temporally by physical transport processes. For this purpose, the classical Theory of Porous Media was extended to include mixture descriptions of the macroscopic phases (eTPM). The focus in the present work is on reactive compressible gas mixtures, which are modeled as ideal gases and pass through a solid matrix. In the case of methane oxidation, the solid matrix represents a soil body, so that mutual interactions can occur not only between the gas components, but also between soil and gas mixture. Further applications of the theoretical model would be, for example, numerical simulations of thawing permafrost soils or biological exhaust air treatment in biofilter plants. In addition, the multi-component concept allows the description of production or reduction of individual concentrations by chemical reactions driven by biological activity. The mass transport mechanisms of diffusion and advection can also be modeled in a thermodynamically consistent manner using the extended Theory of Porous Media. With modifications, this computational concept can also be applied to incompressible solid-liquid mixtures.

The overarching theoretical basis used for the model is the well-founded Theory of Porous Media, a continuum-mechanical theory for multiphasic systems. This description has proven to be well suited for the establishment of a model for multi-physical problems from soil mechanics and environmental sciences. However, the holistic model description in this thesis combines further subsets of theoretical derivations. These subsections include the fundamentals of thermodynamics, which is set in connection with continuum mechanics as well as the equations for mass transfer in fluid mixtures in order to obtain a thermodynamically consistent material description. The material theory and its underlying axioms for material modeling provide a solid basis for setting up constitutive equations without violating physical and thermodynamical laws, ending up in a mathematical description of the phenomenological thermo-biochemo-mechanical behavior of a solid body and the coupled dissipative mechanisms.

Together, the consistent model and material equations form the basis for implementation into the applied numerical calculation with the finite element method. For

this purpose, the derived set of non-linear coupled partial differential equations is transformed into their weak forms using the variational GALERKIN method, and the resulting equation system is solved using the NEWTON-RAPHSON method with an implicit time integration scheme of the NEWMARK-β procedure.

The combination of different mathematical and theoretical disciplines leads to a comprehensive, stable computational concept for investigations and simulations of environmental mechanical problems, which is verified and validated by the application to bacterial methane oxidation in soils.

1. Introduction

Physical systems to which the laws of thermodynamics apply, and which can be interpreted as deformable bodies, can be modeled and simulated with the help of the continuum mechanical theory, which contains solid mechanics, fluid mechanics, as well as the theory of gases. As a fundamental assumption, the microscopic material structure is overlooked and the subject of investigation is supposed to be a continuum. During the transfer of the material body to the mathematical space, the body is homogenized by replacing the matter distributed on atoms by an idealized continuum, in which at each point of the continuum body physical properties such as velocity, density and temperature are given.

The Theory of Porous Media (TPM) provides a derivation to formulate a continuum mechanical model of a porous medium consisting of immiscible macroscopic constituents. The theory traces back to the school of Bowen [18, 19] and de Boer and Ehlers [36], de Boer [33, 34], and Ehlers [45]. It is basically understood as the Theory of Mixtures, which assumes a complete mixing of all substances in a control space, see e.g. Truesdell and Toupin [105], Truesdell [103] and Bowen [21, 22], but additionally combined with the concept of volume fractions, which provides micro-structural information of the medium under investigation. With the help of the volume fractions, that are a measure of the local portion of the individual constituents of the overall medium, further independent fields can be incorporated as local averages of the corresponding quantities of the underlying micro-structure.

Moreover, the TPM approach, in combination with the material theory, offers a thermodynamic consistent investigation of the mechanical behavior of a porous medium, which in general is composed of the following constituents, also called phases: a solid skeleton, which encloses pores filled with a fluid, whereas the fluid can either be liquid or gaseous (saturated), or both (partially saturated). Furthermore, the

fluid phase itself can be a chemical mixture consisting of different components. The liquid phase for example might be a solution, which is made of substances dissolved in a solvent, e.g. salt in water or nutrients transported in blood. Gas mixtures like atmospheric air consist of various single gases and can constitute the gas phase. In case of a macroscopic fluid phase, which itself is composed of miscible components, the extended Theory of Porous Media (eTPM), cf. Ricken et al. [90],[88, 91] and Ricken, Thom et al. [89] is utilized, which offers a more precise description of the mutual interaction between the miscible solutes as well as the interplay of the solutes and their solvents, all set in relation to the deformable solid body.

Phenomena and processes related to fluid mixtures, regardless of whether they are liquid or gaseous, are mass transport processes like diffusion and advection, chemical changes through production or reduction during chemical reactions leading to a pressure and/or density increase or decrease, which in turn can again initiate a mass transport process. Chemical reactions are always induced by the input of any kind of energy, e.g. light, kinetic, electrical or thermal energy, but also can be driven by biological activity.

Thus, in order not to violate physical or thermodynamical laws for the constitutive material equations, the fundamentals of thermodynamics need to be considered, which are e.g. given in Callen [24]. An approach used also as basis for the thermochemistry of reacting mixtures of elastic materials is given by Bowen [20]. The computational investigation of thermodynamic issues requires the definition of representative systems, that are appropriate to solve the physical problem at hand. More specificly, system boundaries need to be defined, which separate the system from its surrounding or an adjacent system. The boundaries can be given by the surface of a solid body or for open systems, like fluids, by an imagined fixed frame. Open boundaries allow material and energy exchange and thus, define an artificial control space to look at, whereas a closed system is impermeable to material flow, but still open for energy flux. However, a closed boundary is movable and furthermore allows shrinking or expansion of the system, whereas the control boundary of an open system is stationary. An isolated system is closed for both, material and energy exchange. Special cases can also be defined, e.g. thermally or mechanically isolated systems. In the case of a multi-phase description as given in the Theory of Porous Media, the solid component serves as the fixed but deformable frame for the flowing fluid. Moreover, the overall aggregate

under investigation is interpreted as closed system, whereas the included phases are applied as open system allowing mass exchange.

Therefrom, thermodynamic processes can be understood as a mutual influence of systems and environment. The influence is ensued by the mechanical, thermal or material-bound transfer of energy, which causes a change of state of the system, e.g. in pressure and temperature. Mechanical energy transfer e.g. is characterized by a force acting on the system boundary, so that energy in form of mechanical work passes over the system boundary. Thermal energy is transferred, when the investigated system and environment have different temperatures, so that energy in form of heat is transferred across the boundary. Energy transfer bound to material flow can cross via various types of energy the system boundary, e.g. kinetic energy due to its flow velocity.

Physically accurate material models that can represent not only the purely mechanical but also thermal and energetic material behavior or chemical reactions and mass transport provide a comprehensive approach for the simulation of environmental mechanical problems. These can be of various nature, but nowadays climate-related topics and different aspects of climate models have high priority, to which computer-aided simulations can make their contribution. Motivated by a still relevant topic, an application of the model equations to a simulation of bacterial methane oxidation in landfill cover layers was executed. Even after closure, landfill sites emit methane over several decades, so that it is of social and economic interest to estimate the behavior of the bacterial methane oxidation in aged landfill covers due to an adequate long-term treatment of these gas emissions, see Schulte et al. [93]. The oxidation taking place in the cap layer offers a naturally occuring passive treatment, since methane oxidizing bacteria are ubiquitous in soils. However, the oxidation capacity is subject to several influences such as the design of the topsoil cover like thickness, its soil parameters like intrinsic permeability, moisture or pH value, and also the methane load by the degradation of organic waste. Not only these intrinsic parameters have an influence, but also varying atmospheric conditions like wind and changing barometric pressure induce advective gas flow within the disposal sites. A comprehensive overview of the microbial methane oxidation processes and technologies for the mitigation of landfill gas emissions can e.g. be found in Scheutz et al. [92]. Moreover, a detailed introduction including the state of the art regarding methane oxidation models from the experimental and modeling perspective is given in Chapter 7.

The model equations derived in the course of this work are solved using a finite element analysis (FEA). The finite element (FE) method offers a numerical procedure for the calculation of an approximative solution of a set of partial differential equation (PDE)s, and is mainly used in the field of solid mechanics. There is a great wealth of available literature dealing with the basics of finite element method (FEM), see e.g. Zienkiewitz and Taylor [112] and Zienkiewitz and R. L. Taylor [111] and Bathe [10] to name a few relevant works. However, customized research FE codes offer the possibility to extend the set of PDEs describing e.g. a thermo-elastic solid material by further balance equations yielding a monolithic coupled simulation of fluid structure interaction (FSI). For this work, the academic research code finite element analysis program (FEAP) developed by Taylor [98] at the University of California, Berkeley, has been used.

To provide the equations required for model implementation, the fundamentals of thermodynamics are first discussed in Chapter 2. This includes an introduction to the thermodynamic state and variables of a material system, the thermodynamic energy potentials and their differentials denoted by fundamental equations. Moreover, a closer look is taken on the description of the chemical potential and the ideal gas law. This chapter is followed by the presentation of the extended Theory of Porous Media in Chapter 3. The eTPM section includes the general descriptions for the immiscible main phases and the concept of volume fractions as well as the miscible components and their definitions in mass and molar units. The kinematics for a multi-phase and multi-component medium is presented by a comprehensive continuum mechanical description including general derivations for mass and molar fluxes. Moreover, the material independent balance equations based on the master balance principle introduced e.g. by Holzapfel [65] are given for the overall continuum, the main phases and the mixture components. Chapter 4 gives an overview of fluid mass transport in porous media. Chapter 5 subsequently provides the specific model equations for a solid - gas mixture continuum based on the previous chapters. To close the model concept, this chapter also provides the constitutive material theory, including the axioms to be considered for material modeling. This leads to a thermodynamically consistent approach for the specific problem at hand. The governing model equations need to be prepared for the implementation to the FE research code. Thus, Chapter 6 presents the transformation of the equations to their weak formulations by a standard Galerkin procedure, and furthermore the

discretization for the FE implementation. Moreover, the implicit solution procedure for the non-linear PDEs via a combined Newton-Raphson and Newmark-method is presented.

Chapter 7 shows the application of the derived model concept to methane oxidation in landfill cover layers, including the motivation to the topic and the state of the art regarding methane oxidation models. The application also serves as verification and validation of the derived model equations. For this purpose, experimental data, which were provided in the course of the interdisciplinary project on the monitoring and modeling of methane oxidation in landfill cover layers, funded by the German Research Foundation (DFG), were additionally used. The detailed introduction to the aims and procedures of the project is given in Section 7.3. Moreover, the documentation of the model validation based on the lab-scale experiments performed by the project partners follows in Sections 7.3.1 and 7.3.2.

More aspects of mass transport regarding advective processes were not able to be validated by experiments from laboratory. For that, the general functionality of the model and the verification of the mass transport processes of diffusion and advection were investigated by different simulations in form of academic examples and documented in Section 7.4. Closing the thesis, a summary and outlook on further work is discussed in Chapter 8. Supplementary mathematical calculation rules as well as derivations of various differential equations are given in appendices A and B. Appendix C provides supplementary information on the discretization of the system of equations as well as the linearization for the Newton-Raphson method, and Appendix D provides further evaluations of the simulation examples of Chapter 7.

2. Principles of thermodynamics

In the following the principles of thermodynamics are introduced for the overall body as single phase material, where a 0-dimensional notation is used as is common in classical thermodynamics. However, all principles are transferable to the multi-phase description presented in Chapter 5, considering the preliminary assumptions for the system boundaries given in Chapter 1. Additionally, the coupling of thermodynamics to classical continuum mechanics is described in Section 2.3.1.

2.1. Thermodynamic state and its variables

The thermodynamic state of a system is characterized by its measurable, macroscopic state variables, which are independent on the one hand of the shape of the system and on the other hand independent of the path to reach this state. That is, they resume their initial values when the initial state is recovered after going through a process of change. The thermodynamic state is most easily described in a closed system for the condition of equilibrium, which is reached, when all mechanical, thermal and/or chemical processes come to a standstill and the corresponding differences in pressure, temperature and density have spatially and temporally balanced each other.
For an open system the equivalent is described by the steady state, where the state variables may differ spatially but are temporarily steady. Moreover, the steady state is reached, when a temporarily constant influx of material and energy equals the outflow rate of these.

In that context, different state variables can be classified: Intensive, extensive as well as thermodynamic potentials, which belong to the extensive state variables, since they are functions of other extensive variables.

Intensive quantities are independent of the amount of substance and do not change their value, when the system is e.g. halved. Examples are temperature T and pressure p, but also specific quantities[1] like density ρ or molar concentration c. **Extensive quantities** however are proportional to the amount of substance, so that they increase or decrease with the same factor when the system is scaled. Examples are the volume V, the molar amount n, the total internal energy U and entropy S. Extensive variables can be changed to intensive ones by referring them to unit of mass, volume or molar amount. Following that, all specific quantities are intensive variables. **Thermodynamic potentials** are scalar quantities which fully represent the thermodynamic state of a system. Thus, the internal energy U is one, and definitions for other potentials can be derived on the basis of U, what is briefly shown in the next sections.

Finally, a distinction between thermal (pressure, temperature, density and volume) and caloric (internal energy, enthalpy, entropy) state variables can be made, which is characterized by the fact that the thermal variables can be measured and the caloric variables have to be calculated from the thermal ones.

2.2. Thermodynamic potentials

By adding or removing energy in form of mechanical work W and/or heat Q, a thermodynamic system is able to change its state. A multi-component system additionally can change the energy state due to its alternating composition provoked by chemical reactions. The **internal energy** U defines that amount of energy the system contains for a given condition, which changes to gain from one state to another. The differential change is given by the **first law of thermodynamics** for a closed system with

$$\mathrm{d}U = \delta Q + \delta W \; + \sum_i \mu_i \mathrm{d}n_i \,. \tag{2.1}$$

Therein, the chemical potential μ_i of component i in the system is introduced in connection with the number of particles n_i of substance i. The known relations (valid

[1] A physical quantity which is normalized to an extensive quantity like mass or volume.

for slow, reversible processes) for heat and mechanical work given with

$$\delta Q = T\mathrm{d}S \quad \text{and} \quad \delta W = -p\,\mathrm{d}V\,. \tag{2.2}$$

are invoked, so that the standard differential form of the internal energy (also denoted as *fundamental equation*) is obtained with

$$\mathrm{d}U = T\mathrm{d}S - p\mathrm{d}V + \sum_i \mu_i \mathrm{d}n_i\,. \tag{2.3}$$

Besides the total internal energy of the system, further quantities defining energy are introduced. The **enthalpy** H may be used for an open system to balance the energy amount additionally carried by a mass flux, which yields an extra amount of work over the system boundary by 'pushing' the mass in front of it. It is defined as the sum of internal energy and the product of pressure and volume with

$$H = U + pV. \tag{2.4}$$

The state variable **entropy** S is furthermore introduced to derive other thermodynamic potentials. The entropy is an energetic variable, that gives information about the convertibility and reversibility of a thermodynamic process. Revealing the derivation of Clausius [27] in the context of classical thermodynamics, it is given as the ratio of the reversible transferred heat and absolute temperature

$$\mathrm{d}S = \delta Q/T\,. \tag{2.5}$$

Nevertheless, the term *entropy* always comes along with the **second law of thermodynamics** which illustrates, that in a closed system the entropy never decreases. More specific, a closed system will enter, among all attainable states, that state as equilibrium which has the highest entropy at the given internal energy, which is known as maximum principle of entropy. Hence,

$$\mathrm{d}S \geq 0. \tag{2.6}$$

This fits the colloquially known definition as *measure of disorder*, which means, that particles in a system strive for the highest value of disorder, that is the state of highest

possible mixing.

Considering the outlined energetic behavior, the definition for the **free energy** F, also known as HELMHOLTZ free energy, is introduced to account for the fact, that a system will always adjust to the state of minimum internal energy and maximum disorder. Thus, the free energy is defined with

$$F = U - TS\,. \tag{2.7}$$

Together with the previously presented energy formulations, the **free enthalpy** G, also known as GIBBS energy, is introduced with

$$G = H - TS \tag{2.8}$$

or by using (2.4)

$$G = U + pV - TS\,. \tag{2.9}$$

By means of the GIBB's energy, which is a quantity describing the chemical composition of the system (more on this later), statements can be made about the behavior of the system, such as the direction of spontaneous processes or as a criterion for equilibrium. That is, a spontaneous process, which is about to achieve equilibrium, is connected with an increasing total entropy of the system and its surrounding (see aforementioned keyword *measure of disorder*). Hence, a closed system at constant temperature and constant pressure strives to that state as equilibrium, at which the free enthalpy has the lowest possible value. If a system is not in equilibrium, it will enter spontaneously states of lower GIBB's energy until equilibrium is reached.

Summarizing, the thermodynamic potentials can be applied to the following physical meanings:

- Internal energy U gives the capacity to do work (mechanical and non-mechanical like chemical) and to release heat
- Enthalpy H denotes the capacity for chemical work plus the capacity to release heat
- HELMHOLTZ free energy F describes the capacity to do mechanical work plus non-mechanical work

- GIBBS free energy G is the capacity to do non-mechanical work

From these meanings (which actually apply in specific conditions, e.g. constant pressure, temperature, etc.), one can say that ΔU is the energy added to the system, ΔF is the total work applied, ΔG is the non-mechanical work, and ΔH is the sum of non-mechanical work applied to the system and the heat given to it.

2.3. Fundamental equations

The differential forms of the energy potentials, e.g. (2.1) for the internal energy, constitute the fundamental equations in thermodynamics. By means of the fundamental relations all thermodynamic information about the system can be derived if the partial derivatives of the potential are taken with respect to its natural variables. Natural variables are those quantities, which are held constant in order to minimize the corresponding energy[2].

The natural variables of the internal energy are entropy, volume and amount of substance $U = U(S, V, \{n_i\})$, and the total differential is obtained by partial differentiation with respect to these with

$$\mathrm{d}U = \frac{\partial U}{\partial S}\,\mathrm{d}S + \frac{\partial U}{\partial V}\,\mathrm{d}V + \sum_i \frac{\partial U}{\partial n_i}\,\mathrm{d}n_i\,. \tag{2.10}$$

Comparing the partial differential formulation (2.10) to (2.3), the relations for temperature, pressure and chemical potential are revealed with

$$T = \left(\frac{\partial U}{\partial S}\right)_{V,\{n_i\}}, \quad p = -\left(\frac{\partial U}{\partial V}\right)_{S,\{n_i\}}, \quad \mu_i = \left(\frac{\partial U}{\partial n_i}\right)_{S,V,n_{j\neq i}}. \tag{2.11}$$

These partial derivatives specify the intensive parameters of the thermodynamic state. Moreover, by exchanging the variables using the LEGENDRE transformation[3], one obtains the fundamental relations of the other potential energies given in Section 2.2. Conjugate thermodynamic variables in fluid mechanics are temperature T and entropy

[2] Priniciple of minimum energy, cf. Callen [24]

[3] A LEGENDRE transform is a linear change in variables in which one or more products of conjugate variables are subtracted from the internal energy to define a new thermodynamic potential, cf. Alberty [7].

S for the thermal part, pressure p and volume V describing mechanical changes, and chemical potential μ and particle number n regarding the state of substance. Which one is used depends e.g. on the experimental point of view, since S and V are often inconvenient variables rather than T and p. Considering the energetically conjugate variables, the fundamental relations read after LEGENDRE transformation

$$\begin{aligned} \mathrm{d}U &= T\mathrm{d}S - p\mathrm{d}V + \sum_i \mu_i \mathrm{d}n_i \\ \mathrm{d}F &= -S\mathrm{d}T - p\mathrm{d}V + \sum_i \mu_i \mathrm{d}n_i \\ \mathrm{d}H &= T\mathrm{d}S + V\mathrm{d}p + \sum_i \mu_i \mathrm{d}n_i \\ \mathrm{d}G &= -S\mathrm{d}T + V\mathrm{d}p + \sum_i \mu_i \mathrm{d}n_i \,. \end{aligned} \tag{2.12}$$

Therein, the HELMHOLTZ energy F is the partial LEGENDRE transform of U replacing the entropy by the temperature, the enthalpy H is the transform which replaces the volume by the pressure as independent variable, and for the derivation of the GIBB's free energy, simultaneously the entropy is replaced by the temperature and the volume by the pressure.

With the differential fundamental relations (2.12), the following correlations for temperature, pressure, volume, entropy and chemical potential are found:

$$\begin{aligned} T &= \left(\frac{\partial U}{\partial S}\right)_{V,\{n_i\}} = \left(\frac{\partial H}{\partial S}\right)_{p,\{n_i\}} \\ -p &= \left(\frac{\partial U}{\partial V}\right)_{S,\{n_i\}} = \left(\frac{\partial F}{\partial V}\right)_{T,\{n_i\}} \\ V &= \left(\frac{\partial H}{\partial p}\right)_{S,\{n_i\}} = \left(\frac{\partial G}{\partial p}\right)_{T,\{n_i\}} \\ -S &= \left(\frac{\partial G}{\partial T}\right)_{p,\{n_i\}} = \left(\frac{\partial F}{\partial T}\right)_{V,\{n_i\}} \\ \mu_j &= \left(\frac{\partial (\bullet)}{\partial n_i}\right)_{(X,Y,\{n_{i\neq j}\})} \,. \end{aligned} \tag{2.13}$$

In $(2.13)_5$, $(\bullet)$ is representative for one of the thermodynamic potentials $\{U, F, H, G\}$,

where the corresponding natural variables, general speaking of (X, Y) besides $\{n_{j\neq i}\}$, of the chosen potential are held constant. It becomes clear, that the chemical potential of substance j, μ_j, can be derived of any of the energy potentials with constant related natural variables.

2.3.1. Reference to continuum mechanics

Referring to the thermodynamically consistent material modeling within the framework of the Theory of Porous Media presented in Chapter 5, a closer look is given to the LEGENDRE transformation of internal energy to HELMHOLTZ free energy in the context of fluid and solid mechanics.[4] Whilst the thermal pair of conjugate variables remains

Table 2.1.: Energetically conjugated variables.

	thermal	mechanical
fluid mechanics	$T \leftrightarrow S$	$p \leftrightarrow V$
solid mechanics	$\theta \leftrightarrow \eta$	$\frac{1}{\rho_0}\mathbf{S} \leftrightarrow \mathbf{E}$

equal for fluid and solid mechanics with temperature T/θ, respectively and entropy S/η, the latter mass-specific, a distinction is made for the mechanical conjugate variables, where the equivalent to pressure-volume of fluid mechanics is the stress-strain relation in solid mechanics, see Table 2.1. Therein, $\mathbf{S}$ denotes the second PIOLA-KIRCHHOFF stress tensor, see Section 3.4 for a more detailed description, and ρ_0 denotes the reference density.

In solid mechanics the mass-specific internal energy ε is given as a function of strain $\mathbf{E}$ and specific entropy η with $\varepsilon = \varepsilon(\mathbf{E}, \eta)$, so that the change rate of the internal energy reads

$$\dot{\varepsilon} = \frac{\partial \varepsilon}{\partial \mathbf{E}} \cdot \dot{\mathbf{E}} + \frac{\partial \varepsilon}{\partial \eta}\,\dot{\eta} = \frac{1}{\rho_0}\mathbf{S} \cdot \mathrm{d}\mathbf{E} + \theta\,\mathrm{d}\eta\,, \tag{2.14}$$

with the relations

$$\frac{\partial \varepsilon}{\partial \mathbf{E}} = \frac{1}{\rho_0}\mathbf{S} \quad \text{and} \quad \frac{\partial \varepsilon}{\partial \eta} = \theta\,. \tag{2.15}$$

[4] The derivations of this section base on Ehlers [44].

see also $(2.13)_1$. For a variable change from η to θ, the right hand side is rewritten and combined to

$$\begin{aligned} \dot{\varepsilon} &= \frac{1}{\rho_0}\mathbf{S}\cdot\dot{\mathbf{E}} + \underbrace{\theta\dot{\eta}}_{(\theta\eta)^{\cdot}} - \dot{\theta}\eta \\ \rightarrow \underbrace{(\varepsilon - \theta\eta)^{\cdot}}_{\psi} &= \frac{1}{\rho_0}\mathbf{S}\cdot\dot{\mathbf{E}} - \eta\dot{\theta}\,, \end{aligned} \tag{2.16}$$

where the mass-specific HELMHOLTZ free energy ψ is introduced according to (2.7). Thus, the rate of change of $\psi = \psi(\mathbf{E}, \theta)$ reads

$$\dot{\psi} = \frac{\partial\psi}{\partial\mathbf{E}}\cdot\dot{\mathbf{E}} + \frac{\partial\psi}{\partial\theta}\,\dot{\theta} = \frac{1}{\rho_0}\mathbf{S}\cdot\dot{\mathbf{E}} - \eta\dot{\theta} \tag{2.17}$$

Concluding from (2.14) and (2.17), stresses can either be derived from the internal or the HELMHOLTZ free energy with

$$\mathbf{S} = \rho_0\frac{\partial\varepsilon}{\partial\mathbf{E}} = \rho_0\frac{\partial\psi}{\partial\mathbf{E}} \tag{2.18}$$

and the thermal variables are derived via

$$\theta = \frac{\partial\varepsilon}{\partial\eta} \quad \text{and} \quad \eta = -\frac{\partial\psi}{\partial\theta} \tag{2.19}$$

Likewise, the derivative of the absolute potential of the internal energy U used e.g. in gas theory is computed by

$$\dot{U} = \frac{\partial U}{\partial V}\,\dot{V} + \frac{\partial U}{\partial S}\,\dot{S}\,, \tag{2.20}$$

where

$$\frac{\partial U}{\partial V} = -p \quad \text{and} \quad \frac{\partial U}{\partial S} = T \tag{2.21}$$

is invoked, cf. (2.13). Comparing (2.14) to (2.20) reveals, that a volume change of a gas or generally a density change of a fluid corresponds to the strain of a solid and induces stresses.

A comprehensive description of the LEGENDRE transforms in the context of continuum mechanics is e.g. given in Haupt [60].

2.4. Euler equation and alternative energy formulations

For a direct formulation of the internal energy, (2.3) needs to be integrated. The internal energy U and its natural variables entropy, volume, amount of substance, are extensive quantities and thus, change proportional with system scaling by factor α like

$$U(\alpha S\,, \alpha V\,, \alpha\{n_i\}) = \alpha\, U(S,\, V,\, \{n_i\})\,. \tag{2.22}$$

Thus, EULER's homogeneous function theorem, see e.g. Callen [24], can be applied so that finally

$$U = TS - pV + \sum_i \mu_i\, n_i \tag{2.23}$$

is obtained. Eq. (2.23) is known as the EULER equation of the internal energy. Moreover, (2.23) can also be derived by integration for constant values of the intensive quantities.

Considering the EULER equation (2.23) and implementing it into (2.9) yields the direct formulation for the GIBBS energy, which is defined as that part of (2.23) describing the composition of the system with

$$G = \sum_i \mu_i\, n_i\,. \tag{2.24}$$

Finally, bringing together and substituting the direct formulation of the internal energy into the other potentials yield alternative expressions for the HELMHOLTZ free energy as well as the enthalpy with

$$F = -pV + \sum_i \mu_i\, n_i \quad \text{and} \quad H = TS + \sum_i \mu_i\, n_i\,. \tag{2.25}$$

2.5. Gibbs energy, chemical potential and reactions

Revealing the fundamental relation for G, $(2.12)_4$, the chemical potential μ_i describes that part of G, that alters the amount of G when the number of particles of substance i changes by $\mathrm{d}n_i$ (for constant temperature and pressure). With that, the chemical potential μ is defined as the molar-specific GIBB's energy for a one-component system,

and the partial molar-specific GIBBS's energy μ_i for a multi-component system, respectively, with

$$\frac{G}{n} = \mu = \sum_i \mu_i \, x_i \,, \tag{2.26}$$

wherein the mole fraction $x_i = n_i/n$ is introduced. Differences in the amount of chemical potentials of one substance i in e.g. different states of aggregation or in separated reference volumes are always compensated. Hence, the chemical potential characterizes the possibilities of a substance to react with other components, for phase transition and also for redistribution in space (diffusion).

Furthermore, reaction equations of chemical reactions follow generally

$$\sum_i v_i A_i \rightleftharpoons 0 \,, \tag{2.27}$$

where v_i denote the stoichiometric coefficients, which represent the mole numbers of the chemical components A_i of the considered reaction equation[5]. Thus, the change of the GIBB's potential $(2.12)_4$ induced by a change of the mole numbers $\mathrm{d}n_i$ has to be proportional to the stoichiometric coefficients. For that, the proportionality factor $\mathrm{d}\bar{n}_i$ is introduced with

$$\frac{\mathrm{d}n_1}{v_1} = \frac{\mathrm{d}n_2}{v_2} = ... := \mathrm{d}\bar{n}_i \quad \rightarrow \quad \mathrm{d}n_i = v_i \, \mathrm{d}\bar{n}_i \,. \tag{2.28}$$

By implementing (2.28) into $(2.12)_4$, the equilibrium condition for a chemical reaction at constant temperature and pressure is obtained as

$$\mathrm{d}G = \mathrm{d}\bar{n}_i \sum_i v_i \, \mu_i = 0 \,, \tag{2.29}$$

and moreover

$$\sum_i v_i \, \mu_i = 0 \,. \tag{2.30}$$

For the case that more energy is released than needed for activation during a chemical reaction, the process is called exothermic[6]. The products of an exothermic reaction end up with a lower enthalpy than the initial substances. Considering the enthalpy

[5] Using the example of oxyhydrogen gas reaction to water with $2H_2 + O_2 \rightleftharpoons 2H_2O$, the v_i are in proportion (-2 : -1 : 2), and the chemical components A_i are H_2, O_2, H_2O

[6] The lower the activation energy, the faster proceeds the exothermic reaction

as the *potential for heat flux* at constant pressure, see last paragraph of Section 2.2, the change in enthalpy during chemical reactions is equal to the heat flux from the surroundings to the system. With (2.24), $(2.25)_2$ and $(2.13)_4$, the enthalpy can be expressed as

$$H = G - T \left(\frac{\partial G}{\partial T} \right)_{p,n_i} . \tag{2.31}$$

A virtual chemical reaction $\mathrm{d}\bar{n}_i$ at constant pressure leads to changes of both H and G with

$$\mathrm{d}H = \left(\frac{\mathrm{d}H}{\mathrm{d}\bar{n}_i} \right) \mathrm{d}\bar{n}_i = \left(\frac{\mathrm{d}G}{\mathrm{d}\bar{n}_i} \right) \mathrm{d}\bar{n}_i - T \, \frac{\partial}{\partial T} \left(\frac{\mathrm{d}G}{\mathrm{d}\bar{n}_i} \right)_{p,n_i} \mathrm{d}\bar{n}_i \tag{2.32}$$

The change of the GIBB's potential is given invoking (2.29)

$$\frac{\mathrm{d}G}{\mathrm{d}\bar{n}_i} = \sum_i v_i \, \mu_i \, , \tag{2.33}$$

which vanishes for equilibrium, whereas the temperature derivative given in the second part of (2.32) remains. Thus, in the vicinity of equilibrium the change in enthalpy becomes

$$\frac{\mathrm{d}H}{\mathrm{d}\bar{n}_i} = -T \, \frac{\partial}{\partial T} \left(\sum_i v_i \mu_i \right)_{p,n_i} , \tag{2.34}$$

which is denoted as *heat of reaction*, which is positive for *endothermic* reactions and negative for *exothermic* reactions. The derivations made in this section are based on Callen [24].

2.6. Ideal gas

The physical model of the **ideal gas** is based on the idea that the cohesion forces as well as the volume of the gas molecules are negligible. This is said to be fulfilled for low pressure and high temperature conditions so that the gas density tends to zero. Figuratively speaking, a diluted real gas contains less molecules in a reference volume, leading to a greater distance between them. Additionally, a rising temperature increases the molecular motion so that the influence of the forces between the molecules decreases. Thus, the behavior of a real gas approaches that one of an ideal gas, which is an adequate approximation for many gases under standard conditions.

2.6.1. Thermal equation of state

The state variables describing the thermodynamic system, namely pressure, temperature, volume and amount of substance, are related for a closed system through the implicit form

$$f(p, V, T, n) = 0\,, \tag{2.35}$$

where each variable itself can be explicitly specified as a function of the remaining ones:

$$p = p(T, V, n)\,, \quad T = T(p, V, n)\,, \quad V = V(T, p, n)\,. \tag{2.36}$$

Considering the volume V, the total differential reads

$$\mathrm{d}V = \left(\frac{\partial V}{\partial T}\right)_{p,n} \mathrm{d}T + \left(\frac{\partial V}{\partial p}\right)_{T,n} \mathrm{d}p + \left(\frac{\partial V}{\partial n}\right)_{T,p} \mathrm{d}n\,, \tag{2.37}$$

where the following coefficients for the partial differentials are introduced with

$$\gamma = \frac{1}{V}\left(\frac{\partial V}{\partial T}\right)_{p,n}\,, \quad \kappa = -\frac{1}{V}\left(\frac{\partial V}{\partial p}\right)_{T,n}\,, \quad V_m = \left(\frac{\partial V}{\partial n}\right)_{T,p}\,. \tag{2.38}$$

Therein, γ denotes the coefficient of expansion, κ the compressibility factor, and V_m the molar volume. By implementing these factors into (2.37), the thermal equation of state is obtained as

$$\mathrm{d}V = (\gamma\, V)\,\mathrm{d}T - (\kappa\, V)\,\mathrm{d}p + V_m\,\mathrm{d}n\,. \tag{2.39}$$

For the case of an ideal gas, the coefficients for expansion and compressibility become

$$\gamma = \frac{1}{T} \quad \text{and} \quad \kappa = \frac{1}{p}\,, \tag{2.40}$$

so that (2.39) simplifies to

$$\mathrm{d}V = \left(\frac{V}{T}\right)\mathrm{d}T - \left(\frac{V}{p}\right)\mathrm{d}p + \left(\frac{V}{n}\right)\mathrm{d}n\,. \tag{2.41}$$

By building a definite integral of (2.41) the well-known **ideal gas law** can be

formulated with

$$p\,V = m\,\mathrm{R}\,T \quad \Leftrightarrow \quad p\,V = n\,\mathrm{R}_m\,T \tag{2.42}$$

where both formulations (mass and molar) are equivalent. Therein, R denotes the specific gas constant, which is derived by dividing the universal (or molar) gas constant R_m ($8,314\,\mathrm{J/(mol\,K)}$) through the molar mass M_m of the individual gas:

$$\mathrm{R} = \frac{\mathrm{R}_m}{\mathrm{M}_m}\,. \tag{2.43}$$

The mole amount n of the gas is defined by dividing its mass m by the molar mass constant M_{mol} with

$$n = \frac{m}{\mathrm{M}_m} \tag{2.44}$$

Eq. (2.42) is given for a one-component gas, but can be equally applied to gas mixtures. For that, Dalton's law of partial pressure is considered, which gives the relation of the partial pressure p_i of component i in the system to the total mixture pressure p with

$$p = \sum_i n_i\,\frac{R\,T}{V} = \sum_i p^i\,, \tag{2.45}$$

in connection to the *ideal gas law*. Moreover, rewriting (2.45) by relating the partial pressure to the total pressure and furthermore implementing (2.42) gives the correlation to the mole fraction x_i via

$$\frac{p^i}{p} = \frac{n_i}{\sum_i n_i} = x_i\,. \tag{2.46}$$

2.6.2. Caloric equation of state

In analogy to (2.36), also the thermodynamic potentials can be calculated as a function of the state variables. The functional relationship for the internal energy and enthalpy read

$$U = U(V,T,n) \quad \text{and} \quad H = H(p,T,n)\,, \tag{2.47}$$

from which the total differentials are derived with

$$\mathrm{d}U = \left(\frac{\partial U}{\partial T}\right)_{V,n}\mathrm{d}T + \left(\frac{\partial U}{\partial V}\right)_{T,n}\mathrm{d}V + \left(\frac{\partial U}{\partial n}\right)_{T,V}\mathrm{d}n\,, \tag{2.48}$$

and

$$\mathrm{d}H = \left(\frac{\partial H}{\partial T}\right)_{p,n} \mathrm{d}T + \left(\frac{\partial H}{\partial p}\right)_{T,n} \mathrm{d}V + \left(\frac{\partial H}{\partial n}\right)_{T,p} \mathrm{d}n\,. \tag{2.49}$$

Assuming a constant molar amount with $\mathrm{d}n = 0$ and moreover ideal gas conditions (the internal energy is independent of pressure and volume), the differentials $\mathrm{d}U$ and $\mathrm{d}H$ only depend on the temperature, so that the caloric equations of state read in their mass-specific forms[7] for internal specific energy $\varepsilon = U/m$ and the specific enthalpy $h = H/m$

$$\mathrm{d}\varepsilon = \mathrm{c_v}\,\mathrm{d}T \quad \text{and} \quad \mathrm{d}h = \mathrm{c_p}\,\mathrm{d}T\,. \tag{2.50}$$

Therein, the specific heat capacities $\mathrm{c_v}$ and $\mathrm{c_p}$ are introduced for the partial differentials with

$$\mathrm{c_v} = \left(\frac{\partial \varepsilon}{\partial T}\right)_v \quad \text{and} \quad \mathrm{c_p} = \left(\frac{\partial h}{\partial T}\right)_p\,, \tag{2.51}$$

which represent proportionality factors to temperature change for isochoric and isobaric conditions, respectively.

2.6.3. Mixture of ideal gases and chemical potential

The chemical potential can also be expressed with the approach for the ideal gas (2.42). For that, a constant temperature in a pure ideal gas is assumed initially, so that the differential of the Gibb's free energy $(2.12)_4$ becomes

$$\mathrm{d}G = V\,\mathrm{d}p\,. \tag{2.52}$$

For a change of pressure from p_0 to p, the variation of the free enthalpy then reads

$$\Delta G = G - G_0 = \int_{G_0}^{G} \mathrm{d}G = \int_{p_0}^{p} V\,\mathrm{d}p\,. \tag{2.53}$$

Inserting (2.42) and integrating yields the Gibb's free energy of a gas with respect to the state of reference (p_0, G_0):

$$G - G_0 = n\,\mathrm{R}_m\,T \ln(\frac{p}{p_0})\,, \tag{2.54}$$

[7] The mass-specific formulation is used to gain an intensive and thus a scale-independent equation.

cf. Huyghe and Bovendeerd [67]. With the relation for the chemical potential $\mu = G/n$, see (2.26), the formulation for the chemical potential of the gas is obtained with

$$\mu = \mu_0 + \mathrm{R}_m\, T \ln(\frac{p}{p_0})\,. \tag{2.55}$$

For a mixture of ideal gases it can be shown, e.g. [67], that the chemical potential of gas i in the mixture can be set up with the mole fraction via

$$\mu^i = \mu_0^i + \mathrm{R}_m\, T \ln x_i\,, \tag{2.56}$$

where use has been made of the reference partial pressure $\mathrm{p}^i = x_i\, p_0$, cf. also (2.46).

3. Extended Theory of Porous Media

3.1. Concept of volume fractions for immiscible constituents

In general, a porous body φ can consist of $\boldsymbol{\kappa}$ immiscible constituents $\varphi^{\boldsymbol{\alpha}}$ with

$$\varphi = \bigcup_{\boldsymbol{\alpha}} \varphi^{\boldsymbol{\alpha}} \,, \tag{3.1}$$

whereas, for example, the pores within a solid skeleton ($\mathbf{S}$) are filled with a fluid ($\mathbf{F}$), which may be a single liquid ($\mathbf{L}$) or a single gas ($\mathbf{G}$) or both:

$$\begin{aligned} \varphi &= \varphi^{\mathbf{S}} \cup \varphi^{\mathbf{F}} \\ &= \varphi^{\mathbf{S}} \cup \varphi^{\mathbf{L}} \cup \varphi^{\mathbf{G}} \,. \end{aligned} \tag{3.2}$$

The concept of volume fractions as a fundamental basis for the TPM proceeds from the assumption of a statistical distribution of the constituents over a control domain, so that the exact location of the individual constituents has not to be taken into consideration. The solid mass occupying the control space, as well as the mass of the liquid and/or gas are homogeneously 'smeared' over the space of the representative volume element (RVE)[1], with the result, that all $\boldsymbol{\kappa}$ substitutes $\varphi^{\boldsymbol{\alpha}}$ occupy the total volume of space dv simultaneously, cf. Fig. 3.1. The fluid contained in the pores can leave or enter the control space, which is set up by the solid matrix, which is, thus, considered as closed system.

All real geometrical and physical properties of the phases, such as stress, deformation or density are given after homogenization as averaged macroscopic quantities. To

[1]The control space must be large enough to allow statistical modeling.

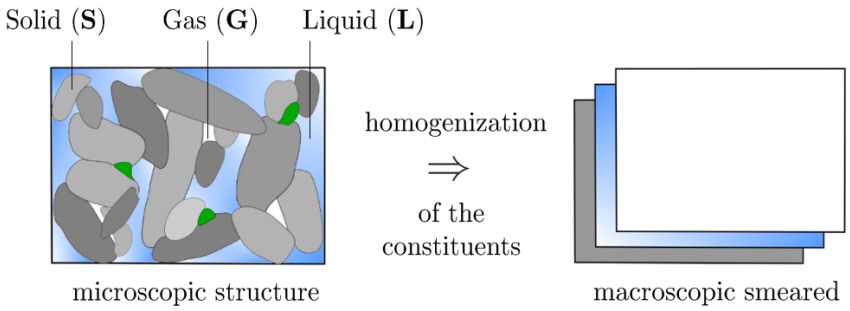

Figure 3.1.: Homogenization of the macroscopic constituents φ^{α}

consider the local composition of the porous medium, the measure of volume fractions $n^{\alpha} = n^{\alpha}(\mathbf{x}, t)$ is introduced, where $\mathbf{x}$ denotes the position vector of the material particle X_{α} in the actual configuration at time t. The volume fraction is defined as the local ratio of the partial volume element dv^{α} of constituent φ^{α} with respect to the bulk volume element dv of the overall body with

$$n^{\alpha} = \frac{dv^{\alpha}}{dv} . \tag{3.3}$$

Summing up the κ volume fractions leads to the constraint in form of the saturation condition

$$\sum_{\alpha} n^{\alpha} = 1 , \tag{3.4}$$

which claims, that the whole medium is 'filled' by the constituents with no vacant space. For a triphasic model additionally the saturation is defined, which relates the volume of the liquid and gas phase to their combined pore space:

$$s^{L} = \frac{n^{L}}{n^{F}} \quad \text{and} \quad s^{G} = \frac{n^{G}}{n^{F}} \quad \text{with} \quad n^{F} = 1 - n^{S} = n^{L} + n^{G} . \tag{3.5}$$

Moreover, the constraint

$$s^{L} + s^{G} = 1 \tag{3.6}$$

is valid for the saturation, too. The partial volume V^{α} of constituent φ^{α} in the control space B_S is given with (3.3) as

$$V^{\alpha} = \int_{B_S} n^{\alpha} dv , \tag{3.7}$$

so that the total volume V can be derived by summing up the partial volumes with

$$\mathrm{V} = \int_{\mathrm{B_S}} \mathrm{dv} = \sum_{\boldsymbol{\alpha}} \mathrm{V}^{\boldsymbol{\alpha}} = \int_{\mathrm{B_S}} \sum_{\boldsymbol{\alpha}} \mathrm{dv}^{\boldsymbol{\alpha}} = \int_{\mathrm{B_S}} \sum_{\boldsymbol{\alpha}} \mathrm{n}^{\boldsymbol{\alpha}} \mathrm{dv}\,. \tag{3.8}$$

The true (or realistic) density $\rho^{\boldsymbol{\alpha}\mathrm{R}} = \rho^{\boldsymbol{\alpha}\mathrm{R}}(\mathbf{x}, \mathrm{t})$ of a material $\varphi^{\boldsymbol{\alpha}}$ is defined as

$$\rho^{\boldsymbol{\alpha}\mathrm{R}} = \frac{\mathrm{dm}^{\boldsymbol{\alpha}}}{\mathrm{dv}^{\boldsymbol{\alpha}}}\,, \tag{3.9}$$

referring the partial mass element $\mathrm{dm}^{\boldsymbol{\alpha}}$ to its partial volume element $\mathrm{dv}^{\boldsymbol{\alpha}}$. Relating the partial mass instead to the bulk volume element dv defines the partial density $\rho^{\boldsymbol{\alpha}}$ of constituent $\varphi^{\boldsymbol{\alpha}}$ with

$$\rho^{\boldsymbol{\alpha}} = \frac{\mathrm{dm}^{\boldsymbol{\alpha}}}{\mathrm{dv}}\,. \tag{3.10}$$

The partial and true densities, (3.10) and (3.9), are connected through the concept of volume fraction (3.3) as follows:

$$\rho^{\boldsymbol{\alpha}} = \mathrm{n}^{\boldsymbol{\alpha}} \rho^{\boldsymbol{\alpha}\mathrm{R}}\,. \tag{3.11}$$

By means of (3.11) it becomes clear, that the partial density $\rho^{\boldsymbol{\alpha}}$ of an inherently incompressible material ($\rho^{\boldsymbol{\alpha}\mathrm{R}} = const.$) can change due to varying local volume fractions. This turns out to be a benefit of the TPM, such that local volume deformations within a model domain can be considered.

In analogy to (3.7) and (3.8), relations for the partial mass $\mathrm{M}^{\boldsymbol{\alpha}}$ and for the total mass M in the actual placement $(\mathbf{x}, \mathrm{t})$ of control space $\mathrm{B_S}$ can be formulated with

$$\mathrm{M}^{\boldsymbol{\alpha}} = \int_{\mathrm{B_S}} \rho^{\boldsymbol{\alpha}}\, \mathrm{dv} = \int_{\mathrm{B_S}} \rho^{\boldsymbol{\alpha}\mathrm{R}}\, \mathrm{dv}^{\boldsymbol{\alpha}} \tag{3.12}$$

and

$$\mathrm{M} = \int_{\mathrm{B_S}} \rho\, \mathrm{dv} = \sum_{\boldsymbol{\alpha}} \mathrm{M}^{\boldsymbol{\alpha}} = \int_{\mathrm{B_S}} \sum_{\boldsymbol{\alpha}} \rho^{\boldsymbol{\alpha}} \mathrm{dv} = \int_{\mathrm{B_S}} \sum_{\boldsymbol{\alpha}} \mathrm{n}^{\boldsymbol{\alpha}} \rho^{\boldsymbol{\alpha}\mathrm{R}}\, \mathrm{dv}\,. \tag{3.13}$$

Finally, summing up the partial densities yields the bulk density of the overall mixture body:

$$\rho = \sum_{\boldsymbol{\alpha}} \rho^{\boldsymbol{\alpha}}\,. \tag{3.14}$$

3.2. Miscible components

As previously described, each macroscopic, immiscible fluid phase $\varphi^{\boldsymbol{\alpha}}$ can be composed of several miscible components φ^{β}, which together form the liquid or gaseous solution. In the framework of the eTPM, the macroscopic phases are described by extending (3.1) and (3.2), respectivley, to

$$\varphi = \bigcup_{\boldsymbol{\alpha}} \varphi^{\boldsymbol{\alpha}} \quad \text{with} \quad \varphi^{\boldsymbol{\alpha}} = \bigcup_{\beta} \varphi^{\alpha\beta} \,. \tag{3.15}$$

As each component φ^{β} in general can occur in each of the macroscopic phases $\varphi^{\boldsymbol{\alpha}}$, the prefixed '$\alpha$' in $\varphi^{\alpha\beta}$ indicates, to which main phase ($\widehat{=}$ solution) $\varphi^{\boldsymbol{\alpha}}$ it belongs. For the description of the components portions within the solution either mass or molar concentration definitions can be used, depending on the problem to investigate.

3.2.1. Molar concentrations

When dealing with chemical reactions or gaseous mixtures, usually the measure of molar concentrations $\mathrm{c}_m^{\alpha\beta}$ are preferred, viz,

$$\mathrm{c}_m^{\alpha\beta} = \frac{\mathrm{dn}_m^{\beta}}{\mathrm{dv}^{\boldsymbol{\alpha}}} \,. \tag{3.16}$$

The true molar concentration $\mathrm{c}_m^{\alpha\beta}$ is defined as the number of moles dn_m^{β} of component φ^{β} related to its solvent volume $\mathrm{dv}^{\boldsymbol{\alpha}}$. In connection with the eTPM, a partial molar concentration c_m^{β} can be defined analogous to the partial density (3.11) by referring the number of moles to the bulk volume with

$$\mathrm{c}_m^{\beta} = \frac{\mathrm{dn}_m^{\beta}}{\mathrm{dv}} = \frac{\mathrm{dv}^{\boldsymbol{\alpha}}}{\mathrm{dv}} \frac{\mathrm{dn}_m^{\beta}}{\mathrm{dv}^{\boldsymbol{\alpha}}} = \mathrm{n}^{\boldsymbol{\alpha}} \, \mathrm{c}_m^{\alpha\beta} \,. \tag{3.17}$$

The mole fraction $x_m^{\alpha\beta}$ is a dimensionless quantity and introduced to describe the composition of the mixture phase, comparable to the macroscopic volume fraction. Using (3.16), it is defined as

$$x_m^{\alpha\beta} = \frac{\mathrm{dn}_m^{\beta}}{\sum_{\beta} \mathrm{dn}_m^{\beta}} = \frac{\mathrm{c}_m^{\alpha\beta}}{\sum_{\beta} \mathrm{c}_m^{\alpha\beta}} = \frac{\mathrm{c}_m^{\alpha\beta}}{\mathrm{c}_m^{\boldsymbol{\alpha}\mathrm{R}}} \,, \tag{3.18}$$

where the number of moles of constituent φ^β is related to the total amount of moles of all components in the solution $\varphi^{\boldsymbol{\alpha}}$. Out of this, the true molar concentration $\mathrm{c}_m^{\boldsymbol{\alpha}\mathrm{R}}$ of the macroscopic solution phase $\varphi^{\boldsymbol{\alpha}}$ can be derived by summing up all molar concentrations of the components via

$$\mathrm{c}_m^{\boldsymbol{\alpha}\mathrm{R}} = \sum_\beta \mathrm{c}_m^{\alpha\beta}\,, \tag{3.19}$$

resulting in the constraint

$$\sum_\beta x_m^{\alpha\beta} = 1\,. \tag{3.20}$$

Finally, by analogy with (3.14), the partial molar concentration for the solution $\varphi^{\boldsymbol{\alpha}}$ is given with

$$\mathrm{c}_m^{\boldsymbol{\alpha}} = \mathrm{n}^{\boldsymbol{\alpha}}\,\mathrm{c}_m^{\boldsymbol{\alpha}\mathrm{R}}\,, \tag{3.21}$$

so that the total molar concentration of the mixture body c_m is given with

$$\mathrm{c}_m = \sum_{\boldsymbol{\alpha}} \mathrm{c}_m^{\boldsymbol{\alpha}}\,. \tag{3.22}$$

3.2.2. Mass concentrations

Often mass units are more useful to solve diffusion equations in context with the balance equation of momentum. In analogy to (3.16), the true mass concentration $\rho^{\alpha\beta}$ of component φ^β in mixture $\varphi^{\boldsymbol{\alpha}}$ is defined as

$$\rho^{\alpha\beta} = \frac{\mathrm{dm}^\beta}{\mathrm{dv}^{\boldsymbol{\alpha}}}\,, \tag{3.23}$$

wherein the mass dm^β of component φ^β is referred to its solvent volume $\mathrm{dv}^{\boldsymbol{\alpha}}$. Using again (3.3), the partial mass concentration ρ^β reads

$$\rho^\beta = \frac{\mathrm{dm}^\beta}{\mathrm{dv}} = \frac{\mathrm{dv}^{\boldsymbol{\alpha}}}{\mathrm{dv}}\,\frac{\mathrm{dm}^\beta}{\mathrm{dv}^{\boldsymbol{\alpha}}} = \mathrm{n}^{\boldsymbol{\alpha}}\rho^{\alpha\beta}\,. \tag{3.24}$$

The mass fraction $\omega^{\alpha\beta}$ can be defined using (3.23) with

$$\omega^{\alpha\beta} = \frac{\mathrm{dm}^\beta}{\sum_\beta \mathrm{dm}^\beta} = \frac{\rho^{\alpha\beta}}{\sum_\beta\, \rho^{\alpha\beta}} = \frac{\rho^{\alpha\beta}}{\rho^{\boldsymbol{\alpha}\mathrm{R}}}\,, \tag{3.25}$$

where the relations

$$\rho^{\boldsymbol{\alpha}\mathrm{R}} = \sum_{\beta} \rho^{\alpha\beta} \quad \text{and} \quad \sum_{\beta} \omega^{\alpha\beta} = 1\,. \tag{3.26}$$

are valid.

3.2.3. Correlation between molar and mass concentration

The mass and molar concentration, respectively, can be converted into each other with the help of the molar mass M_m^β, a constant defined with

$$\mathrm{M}_m^\beta = \frac{\mathrm{dm}^\beta}{\mathrm{dn}_m^\beta}\,. \tag{3.27}$$

Using this quantity, the relation between mass and molar concentration reads

$$\rho^{\alpha\beta} = \mathrm{M}_m^\beta\, \mathrm{c}_m^{\alpha\beta}\,. \tag{3.28}$$

Furthermore, the molar mass of the macroscopic mixture, $\mathrm{M}_m^{\boldsymbol{\alpha}}$, can be calculated by means of the molar fractions with

$$\mathrm{M}_m^{\boldsymbol{\alpha}} = \sum_{\beta} x_m^{\alpha\beta}\, \mathrm{M}_m^\beta \tag{3.29}$$

and hence the macroscopic mass density $\rho^{\boldsymbol{\alpha}\mathrm{R}}$ via

$$\rho^{\boldsymbol{\alpha}\mathrm{R}} = \mathrm{M}_m^{\boldsymbol{\alpha}}\, \mathrm{c}_m^{\boldsymbol{\alpha}\mathrm{R}}\,. \tag{3.30}$$

3.3. Kinematics

3.3.1. Motion of main phases

In the framework of the Theory of Porous Media, the multiphasic body is treated as a smeared model of superimposed continua with mutual interactions with the following underlying assumptions:

Table 3.1.: Overview of true and partial densities.

density	mass units			molar units		
true pore	$\rho^{\alpha\beta}$	$= \dfrac{\mathrm{dm}^{\beta}}{\mathrm{dv}^{\boldsymbol{\alpha}}}$	$= \mathrm{M}_m^{\beta}\mathrm{c}_m^{\alpha\beta}$	$\mathrm{c}_m^{\alpha\beta}$	$= \dfrac{\mathrm{dn}_m^{\beta}}{\mathrm{dv}^{\boldsymbol{\alpha}}}$	$= \dfrac{\rho^{\alpha\beta}}{\mathrm{M}_m^{\beta}}$
partial pore	ρ^{β}	$= \dfrac{\mathrm{dm}^{\beta}}{\mathrm{dv}}$	$= \mathrm{n}^{\boldsymbol{\alpha}}\,\rho^{\alpha\beta}$	c_m^{β}	$= \dfrac{\mathrm{dn}_m^{\beta}}{\mathrm{dv}}$	$= \mathrm{n}^{\boldsymbol{\alpha}}\,\mathrm{c}_m^{\alpha\beta}$
true mixture	$\rho^{\boldsymbol{\alpha}\mathrm{R}}$	$= \sum_{\beta}\rho^{\alpha\beta}$	$= \mathrm{M}_m^{\boldsymbol{\alpha}}\mathrm{c}_m^{\boldsymbol{\alpha}}$	$\mathrm{c}_m^{\boldsymbol{\alpha}\mathrm{R}}$	$= \sum_{\beta}\mathrm{c}_m^{\alpha\beta}$	$= \dfrac{\rho^{\boldsymbol{\alpha}\mathrm{R}}}{\mathrm{M}_m^{\boldsymbol{\alpha}}}$
fraction	$\omega^{\alpha\beta}$	$= \dfrac{\rho^{\alpha\beta}}{\rho^{\boldsymbol{\alpha}\mathrm{R}}}$		$x_m^{\alpha\beta}$	$= \dfrac{\mathrm{c}_m^{\alpha\beta}}{\mathrm{c}_m^{\boldsymbol{\alpha}\mathrm{R}}}$	

- At any time t each spatial point $\mathbf{x}$ of the actual configuration is simultaneously occupied by the material points $\mathrm{X}_{\boldsymbol{\alpha}}$ of the $\boldsymbol{\kappa}$ constituents $\varphi^{\boldsymbol{\alpha}}$.

- The material points proceed from different reference positions $\mathbf{X}_{\boldsymbol{\alpha}}$ at time $\mathrm{t} = \mathrm{t}_0$ and thus, each constituent is assigned its own independent motion function $\boldsymbol{\chi}_{\boldsymbol{\alpha}}(\mathbf{X}_{\boldsymbol{\alpha}}, \mathrm{t})$.

Considering these assumption, the placement vector in the actual configuration is given with

$$\mathbf{x} = \boldsymbol{\chi}_{\boldsymbol{\alpha}}(\mathbf{X}_{\boldsymbol{\alpha}}, \mathrm{t})\,, \tag{3.31}$$

where the material points are identified by their initial position, cf. Fig. 3.2. This definition, referring to the reference position of the material points, represents the LAGRANGEAN description of motion, which is understood as a chronological succession of placements $\chi_{\boldsymbol{\alpha}}$. The velocity and acceleration field of the material points $\mathrm{X}_{\boldsymbol{\alpha}}$ are then given as the partial derivatives of (3.31) with respect to time t:

$$\mathbf{x}'_{\boldsymbol{\alpha}} = \frac{\partial \boldsymbol{\chi}_{\boldsymbol{\alpha}}(\mathbf{X}_{\boldsymbol{\alpha}}, \mathrm{t})}{\partial \mathrm{t}}\,, \qquad \mathbf{x}''_{\boldsymbol{\alpha}} = \frac{\partial^2 \boldsymbol{\chi}_{\boldsymbol{\alpha}}(\mathbf{X}_{\boldsymbol{\alpha}}, \mathrm{t})}{\partial^2 \mathrm{t}}\,. \tag{3.32}$$

The assumption, that each material point has an individual reference position, requires the motion $\boldsymbol{\chi}_{\boldsymbol{\alpha}}$ to be unique and uniquely invertible. A mathematically necessary and sufficient condition for the existence of the inverse motion function $\boldsymbol{\chi}_{\boldsymbol{\alpha}}^{-1}$ is given, if the JACOBIAN

$$\mathrm{J}_{\boldsymbol{\alpha}} = \det \frac{\partial \boldsymbol{\chi}_{\boldsymbol{\alpha}}(\mathbf{X}_{\boldsymbol{\alpha}}, \mathrm{t})}{\partial \mathbf{X}_{\boldsymbol{\alpha}}} \neq 0 \tag{3.33}$$

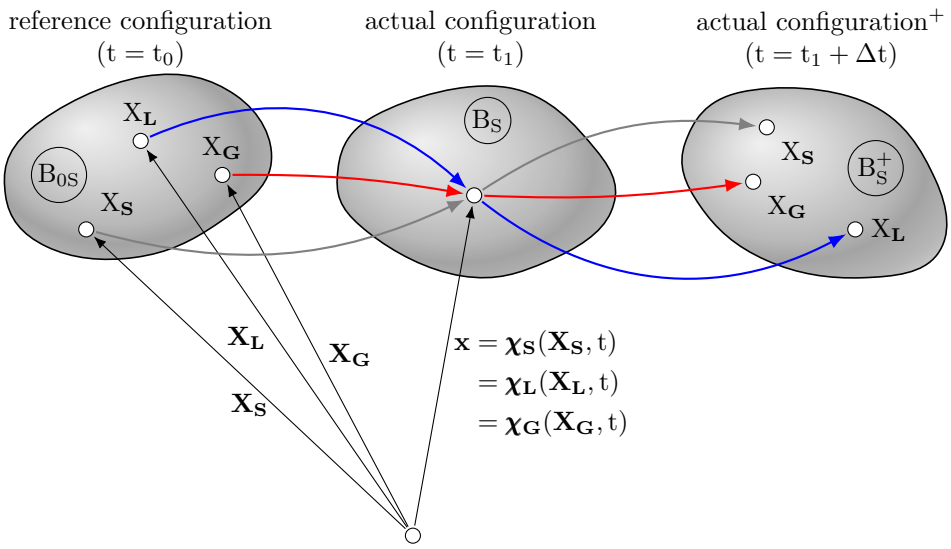

Figure 3.2.: Kinematics of the macroscopic constituents $\varphi^{\boldsymbol{\alpha}}$

differs from zero. Eq. (3.33) enables the EULERIAN description of motion, in which a material point is observed at time t at the spatial position $\mathbf{x}$:

$$\mathbf{X}_{\boldsymbol{\alpha}} = \boldsymbol{\chi}_{\boldsymbol{\alpha}}^{-1}(\mathbf{x}, \mathrm{t})\,. \tag{3.34}$$

To obtain the EULER formulation of the velocity and acceleration field, the inverse motion function (3.34) is used to replace the reference position vector in (3.32), which yields

$$\mathbf{x}'_{\boldsymbol{\alpha}} = \mathbf{x}'_{\boldsymbol{\alpha}}[\boldsymbol{\chi}_{\boldsymbol{\alpha}}^{-1}(\mathbf{x}, \mathrm{t}), \mathrm{t}] = \mathbf{x}'_{\boldsymbol{\alpha}}(\mathbf{x}, \mathrm{t})\,, \quad \mathbf{x}''_{\boldsymbol{\alpha}} = \mathbf{x}''_{\boldsymbol{\alpha}}[\boldsymbol{\chi}_{\boldsymbol{\alpha}}^{-1}(\mathbf{x}, \mathrm{t}), \mathrm{t}] = \mathbf{x}''_{\boldsymbol{\alpha}}(\mathbf{x}, \mathrm{t})\,. \tag{3.35}$$

3.3.2. Material time derivative

Eq. (3.35) depends on time both explicitly and implicitly through the position vector $\mathbf{x}$ of the current configuration. Therefor, the material time derivative for arbitrary field functions ($\Gamma(\mathbf{x}, \mathrm{t}) \mathrel{\hat{=}}$ scalar-valued, $\boldsymbol{\Gamma}(\mathbf{x}, \mathrm{t}) \mathrel{\hat{=}}$ vector/tensor-valued) is defined, which is composed of the local contribution, which describes explicitly the temporal change of a field variable at a fixed spatial point, and of the convective part, which results implicitly from the motion. The material time derivative corresponds mathematically to the total time derivative and can be defined in the multi-phase and multi-component

description with reference to the different motions of constituent $\varphi^{\boldsymbol{\alpha}}$ or component φ^{β} or with respect to the barycentric velocity $\dot{\mathbf{x}}$ of the overall continuum body φ:

$$\dot{\Gamma} = \frac{\mathrm{d}}{\mathrm{dt}}\,\Gamma(\mathbf{x},\mathrm{t}) = \frac{\partial\,\Gamma}{\partial\,\mathrm{t}} + \operatorname{grad}\Gamma\cdot\dot{\mathbf{x}} \qquad \dot{\boldsymbol{\Gamma}} = \frac{\mathrm{d}}{\mathrm{dt}}\,\boldsymbol{\Gamma}(\mathbf{x},\mathrm{t}) = \frac{\partial\,\boldsymbol{\Gamma}}{\partial\,\mathrm{t}} + (\operatorname{grad}\boldsymbol{\Gamma})\;\dot{\mathbf{x}}\,, \tag{3.36}$$

$$(\Gamma)'_{\boldsymbol{\alpha}} = \frac{\mathrm{d}_{\boldsymbol{\alpha}}}{\mathrm{dt}}\,\Gamma(\mathbf{x},\mathrm{t}) = \frac{\partial\,\Gamma}{\partial\,\mathrm{t}} + \operatorname{grad}\Gamma\cdot\mathbf{x}'_{\boldsymbol{\alpha}} \quad (\boldsymbol{\Gamma})'_{\boldsymbol{\alpha}} = \frac{\mathrm{d}_{\boldsymbol{\alpha}}}{\mathrm{t}}\,\boldsymbol{\Gamma}(\mathbf{x},\mathrm{t}) = \frac{\partial\,\boldsymbol{\Gamma}}{\partial\,\mathrm{t}} + (\operatorname{grad}\boldsymbol{\Gamma})\;\mathbf{x}'_{\boldsymbol{\alpha}}\,, \tag{3.37}$$

$$(\Gamma)'_{\beta} = \frac{\mathrm{d}_{\beta}}{\mathrm{dt}}\,\Gamma(\mathbf{x},\mathrm{t}) = \frac{\partial\,\Gamma}{\partial\,\mathrm{t}} + \operatorname{grad}\Gamma\cdot\mathbf{x}'_{\beta} \quad (\boldsymbol{\Gamma})'_{\beta} = \frac{\mathrm{d}_{\beta}}{\mathrm{dt}}\,\boldsymbol{\Gamma}(\mathbf{x},\mathrm{t}) = \frac{\partial\,\boldsymbol{\Gamma}}{\partial\,\mathrm{t}} + (\operatorname{grad}\boldsymbol{\Gamma})\;\mathbf{x}'_{\beta}\,. \tag{3.38}$$

Moreover, the spatial differential operator 'grad $(\cdot)$' denotes the partial derivative of quantity $(\cdot)$ with respect to the spatial position $\mathbf{x}$.

3.3.3. Deformation, transport and strain measures

Deformation gradient

For the description of local deformations at a spatial point $\mathbf{x}$, the material deformation gradient $\mathbf{F}_{\boldsymbol{\alpha}}$ is introduced with

$$\mathbf{F}_{\boldsymbol{\alpha}} = \frac{\partial\boldsymbol{\chi}_{\boldsymbol{\alpha}}(\mathbf{X}_{\boldsymbol{\alpha}},\mathrm{t})}{\partial\mathbf{X}_{\boldsymbol{\alpha}}} = \frac{\partial\mathbf{x}}{\partial\mathbf{X}_{\boldsymbol{\alpha}}} = \operatorname{Grad}_{\boldsymbol{\alpha}}\mathbf{x}\,, \tag{3.39}$$

where the operator 'Grad$_{\boldsymbol{\alpha}}\,(\cdot)$' defines the partial derivative of a quantity $(\cdot)$ with respect to the reference position $\mathbf{X}_{\boldsymbol{\alpha}}$. Using (3.34), the inverse of the deformation gradient $\mathbf{F}_{\boldsymbol{\alpha}}$ can be defined as well as

$$\mathbf{F}_{\boldsymbol{\alpha}}^{-1} = \frac{\partial\boldsymbol{\chi}_{\boldsymbol{\alpha}}^{-1}(\mathbf{x},\mathrm{t})}{\partial\mathbf{x}} = \frac{\partial\mathbf{X}_{\boldsymbol{\alpha}}}{\partial\mathbf{x}} = \operatorname{grad}\mathbf{X}_{\boldsymbol{\alpha}}\,. \tag{3.40}$$

For an undeformed configuration at t=t$_0$ the deformation gradient is equal to the identity $\mathbf{I}$, i.e.

$$\mathbf{F}_{\boldsymbol{\alpha}}(\mathrm{t}=\mathrm{t}_0) = \frac{\partial\mathbf{X}_{\boldsymbol{\alpha}}}{\partial\mathbf{X}_{\boldsymbol{\alpha}}} = \operatorname{Grad}_{\boldsymbol{\alpha}}\mathbf{X}_{\boldsymbol{\alpha}} = \mathbf{I} \quad \rightarrow \quad \det\mathbf{F}_{\boldsymbol{\alpha}}(\mathrm{t}_0) = \det\mathbf{I} = 1 \tag{3.41}$$

and hence, its determinant equal to 1. Comparing (3.39) to (3.33) yields

$$\mathrm{J}_{\boldsymbol{\alpha}} = \det \mathbf{F}_{\boldsymbol{\alpha}} > 0\,, \tag{3.42}$$

which is restricted to be greater than zero during deformation processes.

Transport theorems

The deformation gradient can be utilized for the mapping of differential line elements $\mathrm{d}\mathbf{x}$ of $\varphi^{\boldsymbol{\alpha}}$ between the reference and actual configuration via

$$\mathrm{d}\mathbf{x} = \mathbf{F}_{\boldsymbol{\alpha}}\,\mathrm{d}\mathbf{X}_{\boldsymbol{\alpha}} \quad \text{and} \quad \mathrm{d}\mathbf{X}_{\boldsymbol{\alpha}} = \mathbf{F}_{\boldsymbol{\alpha}}^{-1}\mathrm{d}\mathbf{x}. \tag{3.43}$$

Based on (3.43), a differential area element $\mathrm{d}\mathbf{a}$ can be mapped between the configurations via

$$\begin{aligned} \mathrm{d}\mathbf{a} = \mathrm{d}\mathbf{x}^1 \times \mathrm{d}\mathbf{x}^2 &= \mathbf{F}_{\boldsymbol{\alpha}}\,\mathrm{d}\mathbf{X}_{\boldsymbol{\alpha}}{}^1 \times \mathbf{F}_{\boldsymbol{\alpha}}\,\mathrm{d}\mathbf{X}_{\boldsymbol{\alpha}}{}^2 \\ &= (\det\mathbf{F}_{\boldsymbol{\alpha}})\,\mathbf{F}_{\boldsymbol{\alpha}}^{\mathrm{T}-1}\mathrm{d}\mathbf{A}_{0\boldsymbol{\alpha}} = \mathrm{J}_{\boldsymbol{\alpha}}\,\mathbf{F}_{\boldsymbol{\alpha}}^{\mathrm{T}-1}\mathrm{d}\mathbf{A}_{0\boldsymbol{\alpha}} = \mathrm{cof}\mathbf{F}_{\boldsymbol{\alpha}}\mathrm{d}\mathbf{A}_{0\boldsymbol{\alpha}}\,, \end{aligned} \tag{3.44}$$

where $\mathbf{F}_{\boldsymbol{\alpha}}^{\mathrm{T}-1}$ denotes the inverse of the transposed deformation gradient $\mathbf{F}_{\boldsymbol{\alpha}}^{\mathrm{T}-1}$ and $\mathrm{d}\mathbf{A}_{0\boldsymbol{\alpha}}$ the differential area element in the reference configuration. Finally, the transport of a differential volume element dv to the reference $\mathrm{dV}_{0\boldsymbol{\alpha}}$ can be derived with

$$\begin{aligned} \mathrm{dv} = \mathrm{d}\mathbf{x}^3(\mathrm{d}\mathbf{x}^1 \times \mathrm{d}\mathbf{x}^2) &= \mathbf{F}_{\boldsymbol{\alpha}}\,\mathrm{d}\mathbf{X}_{\boldsymbol{\alpha}}^3\,(\mathbf{F}_{\boldsymbol{\alpha}}\,\mathrm{d}\mathbf{X}_{\boldsymbol{\alpha}}^1 \times \mathbf{F}_{\boldsymbol{\alpha}}\,\mathrm{d}\mathbf{X}_{\boldsymbol{\alpha}}^2) \\ &= \det\mathbf{F}_{\boldsymbol{\alpha}}\,[\mathrm{d}\mathbf{X}_{\boldsymbol{\alpha}}^3\,(\mathrm{d}\mathbf{X}_{\boldsymbol{\alpha}}^1 \times \mathbf{F}_{\boldsymbol{\alpha}}\,\mathrm{d}\mathbf{X}_{\boldsymbol{\alpha}}^2)] = \mathrm{J}_{\boldsymbol{\alpha}}\,\mathrm{dV}_{0\boldsymbol{\alpha}}\,. \end{aligned} \tag{3.45}$$

Thus, a change in volume of the deforming body starting at reference configuration $\mathrm{dV}_{0\boldsymbol{\alpha}}$ is indicated by the Jacobian $\mathrm{J}_{\boldsymbol{\alpha}} = \det\mathbf{F}_{\boldsymbol{\alpha}}$.

Deformation tensors

Deformation measures are derived by calculating the square of the differential line elements for the reference and actual configuration with

$$\begin{aligned} \mathrm{d}\mathbf{x}\cdot\mathrm{d}\mathbf{x} &= \mathrm{d}\mathbf{X}_{\boldsymbol{\alpha}}\cdot(\mathbf{F}_{\boldsymbol{\alpha}}^{\mathrm{T}}\,\mathbf{F}_{\boldsymbol{\alpha}})\,\mathrm{d}\mathbf{X}_{\boldsymbol{\alpha}} &&= \mathrm{d}\mathbf{X}_{\boldsymbol{\alpha}}\cdot(\mathbf{C}_{\boldsymbol{\alpha}})\,\mathrm{d}\mathbf{X}_{\boldsymbol{\alpha}} &&\rightarrow \mathbf{C}_{\boldsymbol{\alpha}}=\mathbf{F}_{\boldsymbol{\alpha}}^{\mathrm{T}}\,\mathbf{F}_{\boldsymbol{\alpha}}\,,\\ \mathrm{d}\mathbf{X}_{\boldsymbol{\alpha}}\cdot\mathrm{d}\mathbf{X}_{\boldsymbol{\alpha}} &= \mathrm{d}\mathbf{x}\cdot(\mathbf{t}\mathrm{ba}^{\mathrm{T}-1}\,\mathbf{F}_{\boldsymbol{\alpha}}^{-1})\,\mathrm{d}\mathbf{x} &&= \mathrm{d}\mathbf{x}\cdot(\mathbf{B}_{\boldsymbol{\alpha}}^{-1})\,\mathrm{d}\mathbf{x} &&\rightarrow \mathbf{B}_{\boldsymbol{\alpha}}=\mathbf{F}_{\boldsymbol{\alpha}}\,\mathbf{F}_{\boldsymbol{\alpha}}^{\mathrm{T}}\,. \end{aligned} \tag{3.46}$$

These equations yield the definitions for the right and left Cauchy-Green deformation tensors $\mathbf{C}_{\boldsymbol{\alpha}}$ and $\mathbf{B}_{\boldsymbol{\alpha}}$, which are a measure for stretch or compression of the line elements. For a deformation free situation they are equal to the identity tensor $\mathbf{I}$.

The underlying definition for 'right' and 'left', respectively, is given by the polar decomposition[2] of the deformation gradient

$$\mathbf{F}_{\boldsymbol{\alpha}}=\mathbf{R}_{\boldsymbol{\alpha}}\,\mathbf{U}_{\boldsymbol{\alpha}}=\mathbf{V}_{\boldsymbol{\alpha}}\,\mathbf{R}_{\boldsymbol{\alpha}}\,, \tag{3.47}$$

where $\mathbf{R}_{\boldsymbol{\alpha}}$ defines the proper orthogonal rotation tensor ($\mathbf{R}_{\boldsymbol{\alpha}}^{-1}=\mathbf{R}_{\boldsymbol{\alpha}}^{\mathrm{T}}$), $\mathbf{U}_{\boldsymbol{\alpha}}$ the material right stretch tensor and $\mathbf{V}_{\boldsymbol{\alpha}}$ the spatial left stretch tensor. Therewith, the deformation gradient can be seen as a series of two transformations: on the one hand a stretch $\mathbf{U}_{\boldsymbol{\alpha}}$[3] followed by a rigid rotation $\mathbf{R}_{\boldsymbol{\alpha}}$, and on the other hand a rigid rotation $\mathbf{R}_{\boldsymbol{\alpha}}$ followed by a stretch $\mathbf{V}_{\boldsymbol{\alpha}}$. The right and left stretch tensors are derived via

$$\mathbf{U}_{\boldsymbol{\alpha}}=\sqrt{\mathbf{F}_{\boldsymbol{\alpha}}^{\mathrm{T}}\,\mathbf{F}_{\boldsymbol{\alpha}}},\quad \mathbf{V}_{\boldsymbol{\alpha}}=\sqrt{\mathbf{F}_{\boldsymbol{\alpha}}\,\mathbf{F}_{\boldsymbol{\alpha}}^{\mathrm{T}}}\,, \tag{3.48}$$

which yields the relation to the right and left Cauchy-Green deformation tensors with

$$\mathbf{C}_{\boldsymbol{\alpha}}=\mathbf{U}_{\boldsymbol{\alpha}}^{2},\quad \mathbf{B}_{\boldsymbol{\alpha}}=\mathbf{V}_{\boldsymbol{\alpha}}^{2}\,. \tag{3.49}$$

Hence, the right Cauchy-Green deformation tensor $\mathbf{C}_{\boldsymbol{\alpha}}$ is applying to the reference configuration, whereas the left Cauchy-Green tensor $\mathbf{B}_{\boldsymbol{\alpha}}$ refers to the actual placement. Both deformation tensors are a measure independent of rotation, since pure rotations should not induce any strains in a deformable body. By multiplying $\mathbf{F}_{\boldsymbol{\alpha}}$

[2] Any second-order tensor can be decomposed into a product of pure rotation and a symmetric tensor.

[3] A pure stretch only for the special case that the dilatation or contraction is towards the main axis with $\mathrm{d}\mathbf{X}_{\boldsymbol{\alpha}}||\mathbf{u}_{\boldsymbol{\alpha}}$ with $\mathbf{u}_{\boldsymbol{\alpha}}\hat{=}$ orthonormal eigenvector of $\mathbf{U}_{\boldsymbol{\alpha}}$

with its transpose, cf. (3.46), the rotation can be excluded with $\mathbf{R}_{\boldsymbol{\alpha}}\mathbf{R}_{\boldsymbol{\alpha}}^{\mathrm{T}} = \mathbf{R}_{\boldsymbol{\alpha}}^{\mathrm{T}}\mathbf{R}_{\boldsymbol{\alpha}} = \mathbf{I}$.

Strain tensors

Strain measures define a dimensionless relative change in length and also angle of the line elements. They are commonly obtained by the squared difference of the line elements between the configurations, viz

$$\begin{aligned} \mathrm{d}\mathbf{x}\cdot\mathrm{d}\mathbf{x} - \mathrm{d}\mathbf{X}_{\boldsymbol{\alpha}}\cdot\mathrm{d}\mathbf{X}_{\boldsymbol{\alpha}} &= \mathrm{d}\mathbf{X}_{\boldsymbol{\alpha}}\cdot(\mathbf{C}_{\boldsymbol{\alpha}}-\mathbf{I})\,\mathrm{d}\mathbf{X}_{\boldsymbol{\alpha}} = \mathrm{d}\mathbf{X}_{\boldsymbol{\alpha}}\cdot 2\,\mathbf{E}_{\boldsymbol{\alpha}}\,\mathrm{d}\mathbf{X}_{\boldsymbol{\alpha}}\,, \\ &= \mathrm{d}\mathbf{x}\cdot(\mathbf{I}-\mathbf{B}_{\boldsymbol{\alpha}}^{-1})\,\mathrm{d}\mathbf{x} = \mathrm{d}\mathbf{x}\cdot 2\,\mathbf{A}_{\boldsymbol{\alpha}}\,\mathrm{d}\mathbf{x}\,. \end{aligned} \tag{3.50}$$

Therein, (3.39) is utilized and the Green-Lagrange strain tensor $\mathbf{E}_{\boldsymbol{\alpha}}$ as well as Almansi strain tensor $\mathbf{A}_{\boldsymbol{\alpha}}$ is introduced with

$$\mathbf{E}_{\boldsymbol{\alpha}} = \frac{1}{2}(\mathbf{C}_{\boldsymbol{\alpha}}-\mathbf{I})\,, \quad \mathbf{A}_{\boldsymbol{\alpha}} = \frac{1}{2}(\mathbf{I}-\mathbf{B}_{\boldsymbol{\alpha}}^{-1})\,. \tag{3.51}$$

In case of an undeformed configurations, these strain measures are equal to zero.

Further strain measurements can be defined by applying a forward rotation on $\mathbf{E}_{\boldsymbol{\alpha}}$ and a backward rotation of $\mathbf{A}_{\boldsymbol{\alpha}}$, respectively, yielding the Karni-Reiner strain tensors in referential and current configuration as

$$\overset{\mathrm{R}}{\mathbf{K}}_{\boldsymbol{\alpha}} = \frac{1}{2}(\mathbf{I}-\mathbf{C}_{\boldsymbol{\alpha}}^{-1})\,, \quad \mathbf{K}_{\boldsymbol{\alpha}} = \frac{1}{2}(\mathbf{B}_{\boldsymbol{\alpha}}-\mathbf{I})\,, \tag{3.52}$$

where

$$\mathbf{K}_{\boldsymbol{\alpha}} = \mathbf{F}_{\boldsymbol{\alpha}}\,\overset{\mathrm{R}}{\mathbf{K}}_{\boldsymbol{\alpha}}\,\mathbf{F}_{\boldsymbol{\alpha}}^{\mathrm{T}} \tag{3.53}$$

is valid.

3.3.4. Deformation and strain rate

Material time derivatives of the introduced deformation and strain measures are considered to specify the deformation and strain rates. The material velocity gradient

as the rate of the deformation gradient in LAGRANGE description is given with

$$(\mathbf{F}_{\boldsymbol{\alpha}})'_{\boldsymbol{\alpha}} = \frac{\mathrm{d}_{\boldsymbol{\alpha}}}{\mathrm{dt}} \left(\frac{\partial \mathbf{x}}{\partial \mathbf{X}_{\boldsymbol{\alpha}}} \right) = \frac{\partial \mathbf{x}'_{\boldsymbol{\alpha}}(\mathbf{X}_{\boldsymbol{\alpha}}, \mathrm{t})}{\partial \mathbf{X}_{\boldsymbol{\alpha}}} = \mathrm{Grad}_{\boldsymbol{\alpha}} \mathbf{x}'_{\boldsymbol{\alpha}} \,. \tag{3.54}$$

It is correlated to the spatial velocity gradient $\mathbf{L}_{\boldsymbol{\alpha}}$ of the current configuration with

$$(\mathbf{F}_{\boldsymbol{\alpha}})'_{\boldsymbol{\alpha}} = \frac{\partial \mathbf{x}'_{\boldsymbol{\alpha}}}{\partial \mathbf{x}} \frac{\partial \mathbf{x}}{\partial \mathbf{X}_{\boldsymbol{\alpha}}} = \mathbf{L}_{\boldsymbol{\alpha}} \mathbf{F}_{\boldsymbol{\alpha}} \,, \tag{3.55}$$

where $\mathbf{L}_{\boldsymbol{\alpha}}$ is introduced as

$$\mathbf{L}_{\boldsymbol{\alpha}} = \frac{\partial \mathbf{x}'_{\boldsymbol{\alpha}}(\mathbf{x}, \mathrm{t})}{\partial \mathbf{x}} = \mathrm{grad}\, \mathbf{x}'_{\boldsymbol{\alpha}} = (\mathbf{F}_{\boldsymbol{\alpha}})'_{\boldsymbol{\alpha}} \, \mathbf{F}_{\boldsymbol{\alpha}}^{-1} \,. \tag{3.56}$$

Furthermore, the relation

$$\mathbf{L}_{\boldsymbol{\alpha}} \cdot \mathbf{I} = \mathrm{tr}\, \mathbf{L}_{\boldsymbol{\alpha}} = (\mathrm{grad}\, \mathbf{x}'_{\boldsymbol{\alpha}}) \cdot \mathbf{I} = \mathrm{div}\, \mathbf{x}'_{\boldsymbol{\alpha}} \tag{3.57}$$

is valid, where 'tr' denotes the trace of a tensor, and 'div' the divergence operator. Additionally, the velocity gradient can be additively decomposed into a symmetric $\mathbf{D}_{\boldsymbol{\alpha}} = \mathbf{D}_{\boldsymbol{\alpha}}^{\mathrm{T}}$ and skew-symmetric part $\mathbf{W}_{\boldsymbol{\alpha}} = -\mathbf{W}_{\boldsymbol{\alpha}}^{\mathrm{T}}$ with

$$\mathbf{L}_{\boldsymbol{\alpha}} = \mathbf{D}_{\boldsymbol{\alpha}} + \mathbf{W}_{\boldsymbol{\alpha}} \quad \text{with} \quad \mathbf{D}_{\boldsymbol{\alpha}} = \frac{1}{2}(\mathbf{L}_{\boldsymbol{\alpha}} + \mathbf{L}_{\boldsymbol{\alpha}}^{\mathrm{T}}) \quad \text{and} \quad \mathbf{W}_{\boldsymbol{\alpha}} = \frac{1}{2}(\mathbf{L}_{\boldsymbol{\alpha}} - \mathbf{L}_{\boldsymbol{\alpha}}^{\mathrm{T}}) \,. \tag{3.58}$$

The material time derivative of the right CAUCHY-GREEN deformation tensor is then given as

$$(\mathbf{C}_{\boldsymbol{\alpha}})'_{\boldsymbol{\alpha}} = (\mathbf{F}_{\boldsymbol{\alpha}}^{\mathrm{T}} \, \mathbf{F}_{\boldsymbol{\alpha}})'_{\boldsymbol{\alpha}} = 2 \, \mathbf{F}_{\boldsymbol{\alpha}}^{\mathrm{T}} \, \mathbf{D}_{\boldsymbol{\alpha}} \mathbf{F}_{\boldsymbol{\alpha}} \,. \tag{3.59}$$

3.3.5. Displacement, relative velocities and types of fluxes

The barycentric velocity[4], denoting the mean velocity $\dot{\mathbf{x}}$ of the overall mixture body φ and the mean molar velocity ${}_m\mathbf{x}'_{\boldsymbol{\alpha}}$ are defined with

$$\dot{\mathbf{x}} = \frac{1}{\rho} \sum_{\boldsymbol{\alpha}} \rho^{\boldsymbol{\alpha}} \, \mathbf{x}'_{\boldsymbol{\alpha}} \quad \text{and} \quad {}_m\dot{\mathbf{x}} = \frac{1}{\mathrm{c}_m} \sum_{\boldsymbol{\alpha}} \mathrm{c}_m^{\boldsymbol{\alpha}} \, {}_m\mathbf{x}'_{\boldsymbol{\alpha}} \,. \tag{3.60}$$

[4]local velocity referring to center of gravity

Each component φ^{β} solved in main phase $\varphi^{\boldsymbol{\alpha}}$ obtains an independent velocity $\mathbf{x}'_{\beta}$, so that the solution velocities $\mathbf{x}'_{\boldsymbol{\alpha}}$ and ${}_m\mathbf{x}'_{\boldsymbol{\alpha}}$ are given as averaged velocities of the dissolved components with

$$\begin{aligned} \mathbf{x}'_{\boldsymbol{\alpha}} &= \frac{1}{\rho^{\boldsymbol{\alpha}}} \sum_{\beta} \rho^{\beta}\, \mathbf{x}'_{\beta} \quad = \frac{1}{\rho^{\boldsymbol{\alpha}\mathrm{R}}} \sum_{\beta} \rho^{\alpha\beta}\, \mathbf{x}'_{\beta} = \sum_{\beta} \omega^{\alpha\beta} \mathbf{x}'_{\beta}\,, \\ {}_m\mathbf{x}'_{\boldsymbol{\alpha}} &= \frac{1}{\mathrm{c}^{\boldsymbol{\alpha}}_m} \sum_{\beta} \mathrm{c}^{\beta}_m\, \mathbf{x}'_{\beta} \quad = \frac{1}{\mathrm{c}^{\boldsymbol{\alpha}\mathrm{R}}_m} \sum_{\beta} \mathrm{c}^{\alpha\beta}_m\, \mathbf{x}'_{\beta} = \sum_{\beta} x^{\alpha\beta}_m\, \mathbf{x}'_{\beta}\,, \end{aligned} \tag{3.61}$$

where use has been made of (3.25) and (3.18). The averaged solution velocities are subsequently used to define advective and diffusive fluxes in mass or molar units.

Moreover, the solid skeleton $\varphi^{\mathbf{S}}$ serves as reference configuration for the fluid flow in the multiphasic eTPM description, whereas the solid skeleton itself can be subject to deformations. For that, the LAGRANGE formulation of the solid displacement $\mathbf{u}_{\mathrm{S}}$ is defined as the primary kinematic variable of the solid displacement field with

$$\mathbf{u}_{\mathrm{S}} = \mathbf{x} - \mathbf{X}_{\mathrm{S}}\,. \tag{3.62}$$

The fluid flow of the solution with respect to the deforming solid, denoted as seepage velocity, is defined in mass and molar units with[5]:

$$\mathbf{w}_{\boldsymbol{\alpha}\mathbf{S}} = \mathbf{x}'_{\boldsymbol{\alpha}} - \mathbf{x}'_{\mathbf{S}} \quad \text{and} \quad {}_m\mathbf{w}_{\boldsymbol{\alpha}\mathbf{S}} = {}_m\mathbf{x}'_{\boldsymbol{\alpha}} - \mathbf{x}'_{\mathbf{S}}\,, \tag{3.63}$$

Similarly, the difference velocity of the dissolved components φ^{β} with respect to the deforming solid is defined as

$$\mathbf{w}_{\beta\mathbf{S}} = \mathbf{x}'_{\beta} - \mathbf{x}'_{\mathbf{S}}\,. \tag{3.64}$$

The diffusion velocity, namely the components' velocity with respect to the moving solution, can again be defined in mass or molar units with (3.63) and (3.64) with

$$\mathbf{d}_{\beta\boldsymbol{\alpha}} = \mathbf{w}_{\beta\mathbf{S}} - \mathbf{w}_{\boldsymbol{\alpha}\mathbf{S}} = \mathbf{x}'_{\beta} - \mathbf{x}'_{\boldsymbol{\alpha}} \quad \text{and} \quad {}_m\mathbf{d}_{\beta\boldsymbol{\alpha}} = \mathbf{w}_{\beta\mathbf{S}} - {}_m\mathbf{w}_{\boldsymbol{\alpha}\mathbf{S}} = \mathbf{x}'_{\beta} - {}_m\mathbf{x}'_{\boldsymbol{\alpha}}\,. \tag{3.65}$$

Regarding the overall mixture, the diffusion velocities of constituent $\varphi^{\boldsymbol{\alpha}}$ related to the barycentric and molar averaged velocity of the mixture body φ, respectively, are

[5]Note, that $\mathbf{w}_{\boldsymbol{\alpha}\mathbf{S}} = \mathbf{0}$ for $\boldsymbol{\alpha} = \mathbf{S}$, so that automatically only the pore fluid flow is captured by (3.63)

defined with

$$\mathbf{d}_{\boldsymbol{\alpha}} = \mathbf{x}'_{\boldsymbol{\alpha}} - \dot{\mathbf{x}} \quad \text{and} \quad {}_m\mathbf{d}_{\boldsymbol{\alpha}} = {}_m\mathbf{x}'_{\boldsymbol{\alpha}} - \dot{\mathbf{x}}_m \,. \tag{3.66}$$

Table 3.2.: Overview true and partial mass and molar fluxes.

flux	mass units		molar units	
true total	$\mathbf{j}^{\alpha\beta}_{tot}$	$= \rho^{\alpha\beta}\,\mathbf{w}_{\beta\mathbf{S}}$	${}_m\mathbf{j}^{\alpha\beta}_{tot}$	$= \mathrm{c}^{\alpha\beta}_m\,\mathbf{w}_{\beta\mathbf{S}}$
partial total	$\mathbf{j}^{\beta}_{tot}$	$= \mathrm{n}^{\boldsymbol{\alpha}}\,\rho^{\alpha\beta}\mathbf{w}_{\beta\mathbf{S}}$	${}_m\mathbf{j}^{\beta}_{tot}$	$= \mathrm{n}^{\boldsymbol{\alpha}}\,\mathrm{c}^{\alpha\beta}_m\,\mathbf{w}_{\beta\mathbf{S}}$
true diffusive	$\mathbf{j}^{\alpha\beta}_{diff}$	$= \rho^{\alpha\beta}\,\mathbf{d}_{\beta\boldsymbol{\alpha}}$	${}_m\mathbf{j}^{\alpha\beta}_{diff}$	$= \mathrm{c}^{\alpha\beta}_m\;{}_m\mathbf{d}_{\beta\boldsymbol{\alpha}}$
partial diffusive	$\mathbf{j}^{\beta}_{diff}$	$= \mathrm{n}^{\boldsymbol{\alpha}}\,\rho^{\alpha\beta}\mathbf{d}_{\beta\boldsymbol{\alpha}}$	${}_m\mathbf{j}^{\beta}_{diff}$	$= \mathrm{n}^{\boldsymbol{\alpha}}\,\mathrm{c}^{\alpha\beta}_m\;{}_m\mathbf{d}_{\beta\boldsymbol{\alpha}}$

In order to derive a formulation for the split into advective and diffusive flow, considering also the multi-phase description with respect to the solid coordinates, one starts with the definition for the partial total mass flux $\mathbf{n}^{\beta} = \mathrm{n}^{\boldsymbol{\alpha}}\,\mathbf{n}^{\alpha\beta}$ of component φ^{β}, where the true mass flux $\mathbf{n}^{\alpha\beta}$ is introduced by

$$\begin{aligned} \mathbf{n}^{\beta} = \mathrm{n}^{\boldsymbol{\alpha}}\,\mathbf{n}^{\alpha\beta} = \rho^{\beta}\,\mathbf{x}'_{\beta} = \mathrm{n}^{\boldsymbol{\alpha}}\,\rho^{\alpha\beta}\,\mathbf{x}'_{\beta}\,, \\ = \mathrm{n}^{\boldsymbol{\alpha}}\,\omega^{\alpha\beta}\rho^{\boldsymbol{\alpha}\mathrm{R}}\,\mathbf{x}'_{\beta}\,. \end{aligned} \tag{3.67}$$

Summing up the true total mass fluxes $\mathbf{n}^{\alpha\beta}$ yields the real total mass flux of solution $\varphi^{\boldsymbol{\alpha}}$ with

$$\mathbf{n}^{\boldsymbol{\alpha}\mathrm{R}} = \sum_{\beta} \mathbf{n}^{\alpha\beta} = \sum_{\beta} \rho^{\alpha\beta}\,\mathbf{x}'_{\beta} = \rho^{\boldsymbol{\alpha}\mathrm{R}}\,\mathbf{x}'_{\boldsymbol{\alpha}}\,. \tag{3.68}$$

Therein, the relation to the deforming solid is not yet considered. Likewise, the partial total molar flux ${}_m\mathbf{n}^{\beta} = \mathrm{n}^{\boldsymbol{\alpha}}\,{}_m\mathbf{n}^{\alpha\beta}$ is defined with

$$\begin{aligned} {}_m\mathbf{n}^{\beta} = \mathrm{n}^{\boldsymbol{\alpha}}\,{}_m\mathbf{n}^{\alpha\beta} = \mathrm{c}^{\beta}_m\,\mathbf{x}'_{\beta} = \mathrm{n}^{\boldsymbol{\alpha}}\,\mathrm{c}^{\alpha\beta}_m\,\mathbf{x}'_{\beta} \\ = \mathrm{n}^{\boldsymbol{\alpha}}\,x^{\alpha\beta}\mathrm{c}^{\boldsymbol{\alpha}\mathrm{R}}_m\,\mathbf{x}'_{\beta} \end{aligned} \tag{3.69}$$

and summation yields the real total molar flux of the solution ${}_m\mathbf{n}^{\boldsymbol{\alpha}\mathrm{R}}$

$${}_m\mathbf{n}^{\boldsymbol{\alpha}\mathrm{R}} = \sum_{\beta} {}_m\mathbf{n}^{\alpha\beta} = \sum_{\beta} \mathrm{c}^{\alpha\beta}_m\,\mathbf{x}'_{\beta} = \mathrm{c}^{\boldsymbol{\alpha}\mathrm{R}}_m\;{}_m\mathbf{x}'_{\boldsymbol{\alpha}}\,. \tag{3.70}$$

Proceeding from that, the total flux is composed of an advective part, where the particle is carried with the solution velocity, and the diffusive flux, which physically describes the motion of the particles by their own motion. The difference between total and advective flux yields the diffusive part and, depending on the chosen reference velocity, the mass and molar diffusive fluxes are defined with

$$\begin{aligned}
\mathbf{j}^{\alpha\beta}_{diff} &= \mathbf{n}^{\alpha\beta} - \rho^{\alpha\beta}\,\mathbf{x}'_{\boldsymbol{\alpha}} && \text{and} && {}_m\mathbf{j}^{\alpha\beta}_{diff} &= {}_m\mathbf{n}^{\alpha\beta} - \mathrm{c}^{\alpha\beta}_m\,{}_m\mathbf{x}'_{\boldsymbol{\alpha}} \\
&= \mathbf{n}^{\alpha\beta} - \omega^{\alpha\beta}\mathbf{n}^{\boldsymbol{\alpha}\mathrm{R}} && && &= {}_m\mathbf{n}^{\alpha\beta} - x^{\alpha\beta}\,{}_m\mathbf{n}^{\boldsymbol{\alpha}\mathrm{R}} \\
&= \rho^{\alpha\beta}\,(\mathbf{x}'_\beta - \mathbf{x}'_{\boldsymbol{\alpha}}) && && &= \mathrm{c}^{\alpha\beta}_m\,(\mathbf{x}'_\beta - {}_m\mathbf{x}'_{\boldsymbol{\alpha}}) \\
&= \rho^{\alpha\beta}\,\mathbf{d}_{\beta\boldsymbol{\alpha}} && && &= \mathrm{c}^{\alpha\beta}_m\,{}_m\mathbf{d}_{\beta\boldsymbol{\alpha}}
\end{aligned} \tag{3.71}$$

Therein, the expressions containing the diffusion velocities $(3.71)_{7,8}$ are obtained by considering the previous definitions for the difference velocities (3.65). Mixture terms, e.g. the difference between the total molar and advective mass flux, can also be defined, but will be neglected in this work.

Since the solid's movement (3.62) serves as a fixed frame, all fluxes can be given in terms of the seepage and difference velocities, respectively. With respect to the solid coordinates (3.64) the true total fluxes in mass and molar units of component φ^β read

$$\mathbf{j}^{\alpha\beta}_{tot} = \rho^{\alpha\beta}\,\mathbf{w}_{\beta\mathbf{S}} \quad \text{and} \quad {}_m\mathbf{j}^{\alpha\beta}_{tot} = \mathrm{c}^{\alpha\beta}_m\,\mathbf{w}_{\beta\mathbf{S}}\,. \tag{3.72}$$

Analogously, the diffusive fluxes are defined in dependence to the advective flux given with the seepage velocity (3.63). Hence, $(3.71)_{7,8}$ can also be written as

$$\mathbf{j}^{\alpha\beta}_{diff} = \rho^{\alpha\beta}\,(\mathbf{w}_{\beta\mathbf{S}} - \mathbf{w}_{\boldsymbol{\alpha}\mathbf{S}}) \quad \text{and} \quad {}_m\mathbf{j}^{\alpha\beta}_{diff} = \mathrm{c}^{\alpha\beta}_m\,(\mathbf{w}_{\beta\mathbf{S}} - {}_m\mathbf{w}_{\boldsymbol{\alpha}\mathbf{S}})\,, \tag{3.73}$$

where the connection to the solid deformation becomes clear. In addition, partial quantities can be defined for the multi-phase description, which are summarized in Tab. 3.2.

Building the sum of (3.73) yields zero and thus verifies, that the diffusive fluxes balance each other:

$$\sum_\beta \mathbf{j}^{\alpha\beta}_{diff} = \sum_\beta \rho^{\alpha\beta}\mathbf{d}_{\beta\boldsymbol{\alpha}} = 0 \quad \text{and} \quad \sum_\beta {}_m\mathbf{j}^{\alpha\beta}_{diff} = \sum_\beta \mathrm{c}^{\alpha\beta}_m\,{}_m\mathbf{d}_{\beta\boldsymbol{\alpha}} = 0\,. \tag{3.74}$$

Therein, some reformulations need to be done by using (3.18) and (3.20), (3.25) and $(3.26)_2$ as well as (3.68) and (3.70). Finally, for the overall mixture φ the relations

$$\sum_{\boldsymbol{\alpha}} \rho^{\boldsymbol{\alpha}}\, \mathbf{d}_{\boldsymbol{\alpha}} = 0 \quad \text{and} \quad \sum_{\boldsymbol{\alpha}} \mathrm{c}_m^{\boldsymbol{\alpha}}\, {}_m\mathbf{d}_{\boldsymbol{\alpha}} = 0\,, \tag{3.75}$$

have to be considered by using (3.60), (3.14) and (3.22).

3.4. Concept of stress

The link between deformation and material is given by the stress tensors. For that, the traction vector $\mathbf{t} = \mathbf{t}(\mathbf{x}, \mathrm{t}, \mathbf{n})$ is introduced, depending on the current configuration $\mathbf{x}$, time t and the outward orientated surface normal vector $\mathbf{n}$ on $\partial \mathrm{B}_{\mathbf{S}}$, which is defined as the force measured per unit surface area d$\mathbf{a}$ of the free cut body, see Fig. 3.3.

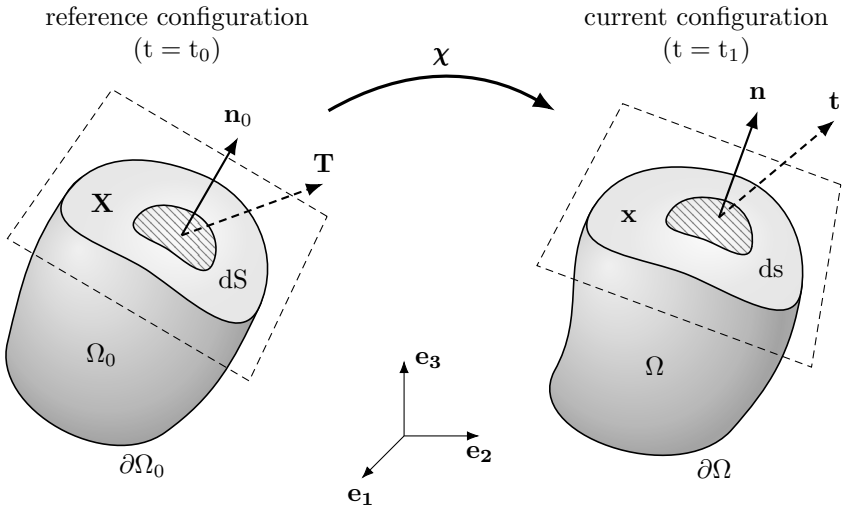

Figure 3.3.: Stresses

The number of all possible intersections through a material point of the body defines the stress state at the material point. For a complete description of the stress state, three perpendicular sectional surfaces are sufficient and are described with the CAUCHY stress tensor $\mathbf{T}(\mathbf{x}, \mathrm{t})$ in the current configuration. The CAUCHY stress theorem connects the traction vector with the cutting direction by

$$\mathbf{t}(\mathbf{x}, \mathrm{t}, \mathbf{n}) = \mathbf{T}\,\mathbf{n} \quad \text{and} \quad \mathbf{t}^{\boldsymbol{\alpha}}(\mathbf{x}, \mathrm{t}, \mathbf{n}) = \mathbf{T}^{\boldsymbol{\alpha}}\,\mathbf{n}\,, \tag{3.76}$$

which can be referred to each phase, yielding the partial traction vector and partial stress tensor $(3.76)_2$. The LAGRANGE counterpart for a surface element in the reference configuration $\mathrm{d}\mathbf{A}_{0\mathbf{S}}$ to the EULER setting on $\mathrm{d}\mathbf{a}$ is introduced with

$$\mathbf{t}_0^{\boldsymbol{\alpha}}(\mathbf{X}_{\boldsymbol{\alpha}}, \mathrm{t}, \mathbf{n}_0) = \mathbf{P}^{\boldsymbol{\alpha}}\left(\mathbf{X}_{\boldsymbol{\alpha}}, \mathrm{t}\right) \mathbf{n}_0 \tag{3.77}$$

where $\mathbf{P}^{\boldsymbol{\alpha}}$ denotes the partial first PIOLA-KIRCHHOFF (1. PK) stress tensor. From that, and utilizing the surface mapping from current to reference configuration (3.44) the transformation rule for the 1. PK stress tensor can be derived with

$$\mathbf{P}^{\boldsymbol{\alpha}} = \mathrm{J}_{\mathbf{S}}\, \mathbf{T}^{\boldsymbol{\alpha}}\, \mathbf{F}_{\mathbf{S}}^{\mathrm{T\text{-}1}}\,. \tag{3.78}$$

Thus, the 1. PK stress tensor describes stresses resulting from forces applied on the current placement but related to the geometric reference configuration. Performing another pull-back operation leads to the definition for the second PIOLA-KIRCHHOFF (2. PK) stress tensor with

$$\mathbf{S}^{\boldsymbol{\alpha}} = \mathbf{F}_{\boldsymbol{\alpha}}^{-1}\, \mathbf{P}^{\boldsymbol{\alpha}}\,. \tag{3.79}$$

This tensor applies the forces projected on the reference to the geometric reference configuration and thus is a fully referential placement tensor.

3.5. Master balance principle

Balance equations describe the universally valid principles and natural laws, respectively, independent of the individual characteristics of the continuum and thus, they are valid for all materials and their related constitutive laws. For the thermodynamic continuum, the balance equations are all of the same kind of mathematical structure, and the generalized relation is known as the **master balance principle**, cf. HOLZAPFEL [65].

Together with the constitutive equations, balance equations of continuum mechanics form the set of required field equations to solve the initial boundary value problem (IBVP)[6]. In the framework of the eTPM, the set is given, besides for the overall body

[6] A solution to an initial boundary value problem is the solution to a set of differential equations, which satisfies both the boundary conditions (additional constraints for the set of differential

φ, for each constituent $\varphi^{\boldsymbol{\alpha}}$ as well as for the dissolved components φ^{β}.

Following the metaphysical principles[7] by Truesdell [103], the balance relations for the overall aggregate φ must show identical mechanical behavior as the summation of the balance equations of constituents $\varphi^{\boldsymbol{\alpha}}$. The same applies for balance equations of $\varphi^{\boldsymbol{\alpha}}$ itself, which have to yield same results as the summation of the balance equations of the dissolved components φ^{β}. This yields the correlation between the scalar- or vector-valued field quantity[8] (Υ, $\boldsymbol{\Upsilon}$) of the overall mixture body and its partial ($\Upsilon^{\boldsymbol{\alpha}}$, $\boldsymbol{\Upsilon}^{\boldsymbol{\alpha}}$) and component-wise ($\Upsilon^{\beta}$, $\boldsymbol{\Upsilon}^{\beta}$) composition with

$$\Upsilon = \sum_{\boldsymbol{\alpha}} \Upsilon^{\boldsymbol{\alpha}} = \sum_{\boldsymbol{\alpha}} \sum_{\beta} \Upsilon^{\beta} \quad \text{and} \quad \boldsymbol{\Upsilon} = \sum_{\boldsymbol{\alpha}} \boldsymbol{\Upsilon}^{\boldsymbol{\alpha}} = \sum_{\boldsymbol{\alpha}} \sum_{\beta} \boldsymbol{\Upsilon}^{\beta} \,. \tag{3.80}$$

3.5.1. Global master formulation

Based on the classical continuum mechanical formulation for a single-phase material, cf. e.g. Altenbach [8], the global master balance equation for the density distribution of a field quantity over the whole body is given with

$$\begin{aligned} \frac{\mathrm{d}}{\mathrm{dt}} \int_{\mathrm{B}} \Upsilon \,\mathrm{dv} &= \int_{\partial \mathrm{B}} (\boldsymbol{\phi} \cdot \mathbf{n}) \,\mathrm{da} + \int_{\mathrm{B}} \xi \,\mathrm{dv} + \int_{\mathrm{B}} \hat{\Upsilon} \,\mathrm{dv} \,, \\ &\qquad\qquad\qquad\qquad\qquad\qquad 0 \,(\text{for closed systems}) \\ \frac{\mathrm{d}}{\mathrm{dt}} \int_{\mathrm{B}} \boldsymbol{\Upsilon} \,\mathrm{dv} &= \int_{\partial \mathrm{B}} (\boldsymbol{\Phi}\, \mathbf{n}) \,\mathrm{da} + \int_{\mathrm{B}} \boldsymbol{\xi} \,\mathrm{dv} + \int_{\mathrm{B}} \hat{\boldsymbol{\Upsilon}} \,\mathrm{dv} \,. \\ &\qquad\qquad\qquad\qquad\qquad\qquad 0 \,(\text{for closed systems}) \end{aligned} \tag{3.81}$$

Therein, the temporal change of state of the scalar-, vector- or tensor-valued field quantity (Υ / $\boldsymbol{\Upsilon}$) per unit current volume dv is balanced with the density of effluxes of this quantity over the surface ($\boldsymbol{\phi} \cdot \mathbf{n}$ / $\boldsymbol{\Phi}\, \mathbf{n}$), and the supply for the volume density (ξ / $\boldsymbol{\xi}$), caused by an external source. Furthermore, $\mathbf{n}$ denotes the outward orientated surface normal.

The terms $\hat{\Upsilon}$ and $\hat{\boldsymbol{\Upsilon}}$ represent production terms of the field quantity due to couplings with its environment. For a single-phase material or the overall mixture body φ

equations) of the field variable and its initial specified values.

[7] The balance equations for φ, $\varphi^{\boldsymbol{\alpha}}$ and φ^{β} are given analogously to balance relations of classical continuum mechanics for single-phase materials while considering the interaction mechanisms between the constituents and components by introduction of production terms.

[8] A mechanical, thermodynamic, chemical, electrical etc. quantity, depending on the problem to solve.

considered in a closed system, this production is equal to zero. Only exception is the entropy, which is always greater or equal to zero, which will be discussed later in Sect. 3.7.

Recalling (3.80), the balance equations can also be set up in general for each field quantity of each constituent $\varphi^{\boldsymbol{\alpha}}$ of the mixture

$$\begin{aligned} \frac{\mathrm{d}_{\boldsymbol{\alpha}}}{\mathrm{dt}} \int_{\mathrm{B}} \Upsilon^{\boldsymbol{\alpha}} \,\mathrm{dv} &= \int_{\partial \mathrm{B}} (\boldsymbol{\phi}^{\boldsymbol{\alpha}} \cdot \mathbf{n}) \,\mathrm{da} + \int_{\mathrm{B}} \xi^{\boldsymbol{\alpha}} \,\mathrm{dv} + \int_{\mathrm{B}} \hat{\Upsilon}^{\boldsymbol{\alpha}} \,\mathrm{dv} \,, \\ \frac{\mathrm{d}_{\boldsymbol{\alpha}}}{\mathrm{dt}} \int_{\mathrm{B}} \boldsymbol{\Upsilon}^{\boldsymbol{\alpha}} \,\mathrm{dv} &= \int_{\partial \mathrm{B}} (\boldsymbol{\Phi}^{\boldsymbol{\alpha}} \,\mathbf{n}) \,\mathrm{da} + \int_{\mathrm{B}} \boldsymbol{\xi}^{\boldsymbol{\alpha}} \,\mathrm{dv} + \int_{\mathrm{B}} \hat{\boldsymbol{\Upsilon}}^{\boldsymbol{\alpha}} \,\mathrm{dv} \,, \end{aligned} \tag{3.82}$$

and for each component φ^{β}

$$\begin{aligned} \frac{\mathrm{d}_{\beta}}{\mathrm{dt}} \int_{\mathrm{B}} \Upsilon^{\beta} \,\mathrm{dv} &= \int_{\partial \mathrm{B}} (\boldsymbol{\phi}^{\beta} \cdot \mathbf{n}) \,\mathrm{da} + \int_{\mathrm{B}} \xi^{\beta} \,\mathrm{dv} + \int_{\mathrm{B}} \hat{\Upsilon}^{\beta} \,\mathrm{dv} \,, \\ \frac{\mathrm{d}_{\beta}}{\mathrm{dt}} \int_{\mathrm{B}} \boldsymbol{\Upsilon}^{\beta} \,\mathrm{dv} &= \int_{\partial \mathrm{B}} (\boldsymbol{\Phi}^{\beta} \,\mathbf{n}) \,\mathrm{da} + \int_{\mathrm{B}} \boldsymbol{\xi}^{\beta} \,\mathrm{dv} + \int_{\mathrm{B}} \hat{\boldsymbol{\Upsilon}}^{\beta} \,\mathrm{dv} \,. \end{aligned} \tag{3.83}$$

3.5.2. Local master formulation

Assuming sufficiently smooth fields of $\Upsilon/\boldsymbol{\Upsilon}$ as well as $\Upsilon^{\boldsymbol{\alpha}}/\boldsymbol{\Upsilon}^{\boldsymbol{\alpha}}$ and $\Upsilon^{\beta}/\boldsymbol{\Upsilon}^{\beta}$, the local balance equations can be established for the overall mixture with

$$\dot{\Upsilon} + \Upsilon \operatorname{div} \dot{\mathbf{x}} = \operatorname{div} \boldsymbol{\phi} + \xi + \hat{\Upsilon} \,, \quad \dot{\boldsymbol{\Upsilon}} + \boldsymbol{\Upsilon} \operatorname{div} \dot{\mathbf{x}} = \operatorname{div} \boldsymbol{\Phi} + \boldsymbol{\xi} + \hat{\boldsymbol{\Upsilon}} \,, \tag{3.84}$$

and for the constituents $\varphi^{\boldsymbol{\alpha}}$ and components φ^{β} with

$$\begin{aligned} (\Upsilon^{\boldsymbol{\alpha}})'_{\boldsymbol{\alpha}} + \Upsilon^{\boldsymbol{\alpha}} \operatorname{div} \mathbf{x}'_{\boldsymbol{\alpha}} &= \operatorname{div} \boldsymbol{\phi}^{\boldsymbol{\alpha}} + \xi^{\boldsymbol{\alpha}} + \hat{\Upsilon}^{\boldsymbol{\alpha}} \,, \quad (\boldsymbol{\Upsilon}^{\boldsymbol{\alpha}})'_{\boldsymbol{\alpha}} + \boldsymbol{\Upsilon}^{\boldsymbol{\alpha}} \operatorname{div} \mathbf{x}'_{\boldsymbol{\alpha}} &= \operatorname{div} \boldsymbol{\Phi}^{\boldsymbol{\alpha}} + \boldsymbol{\xi}^{\boldsymbol{\alpha}} + \hat{\boldsymbol{\Upsilon}}^{\boldsymbol{\alpha}} \,, \\ (\Upsilon^{\beta})'_{\beta} + \Upsilon^{\beta} \operatorname{div} \mathbf{x}'_{\beta} &= \operatorname{div} \boldsymbol{\phi}^{\beta} + \xi^{\beta} + \hat{\Upsilon}^{\beta} \,, \quad (\boldsymbol{\Upsilon}^{\beta})'_{\beta} + \boldsymbol{\Upsilon}^{\beta} \operatorname{div} \mathbf{x}'_{\beta} &= \operatorname{div} \boldsymbol{\Phi}^{\beta} + \boldsymbol{\xi}^{\beta} + \hat{\boldsymbol{\Upsilon}}^{\beta} \,. \end{aligned} \tag{3.85}$$

To gain the local master formulations, the total time derivatives of the left-hand side of the global integral formulations given in Sect. 3.5.1 have been evaluated and moreover, the Gauss divergence theorem [65] has been applied to the right-hand side surface terms. A more detailed derivation is given in Appendix A.2.

3.5.3. Constraints in multi-phase and multi-component framework

Considering the different levels of balance equations for φ, $\varphi^{\boldsymbol{\alpha}}$ and φ^{β}, and the corresponding correlations of the field quantity to be balanced (3.80), it becomes clear that the right-hand side parts of the balance equations are also subject to constraints, which have to be fulfilled to comply with the behavior of a single-phase material. The constraints are derived by analyzing the summation of the balance equations of φ^{β} to gain the balance for $\varphi^{\boldsymbol{\alpha}}$, and as well as summing over $\varphi^{\boldsymbol{\alpha}}$ to gain the balance equation for φ. The derivations are given in Appendix A.4.

For the effluxes through the surface the constraints are given in general form with

$$\begin{aligned} \boldsymbol{\phi} &= \sum_{\boldsymbol{\alpha}} \left(\boldsymbol{\phi}^{\boldsymbol{\alpha}} - \Upsilon^{\boldsymbol{\alpha}}\, \mathbf{d}_{\boldsymbol{\alpha}}\right) &&= \sum_{\boldsymbol{\alpha}} \sum_{\beta} \left(\boldsymbol{\phi}^{\beta} - \Upsilon^{\beta} \mathbf{d}_{\beta\boldsymbol{\alpha}}\right), \\ \boldsymbol{\Phi} &= \sum_{\boldsymbol{\alpha}} \left(\boldsymbol{\Phi}^{\boldsymbol{\alpha}} - \boldsymbol{\Upsilon}^{\boldsymbol{\alpha}} \otimes \mathbf{d}_{\boldsymbol{\alpha}}\right) &&= \sum_{\boldsymbol{\alpha}} \sum_{\beta} \left(\boldsymbol{\Phi}^{\beta} - \boldsymbol{\Upsilon}^{\beta} \otimes \mathbf{d}_{\beta\boldsymbol{\alpha}}\right), \end{aligned} \tag{3.86}$$

and for the volume density productions and interaction supply terms the constraints are given via

$$\xi = \sum_{\boldsymbol{\alpha}} \xi^{\boldsymbol{\alpha}} = \sum_{\boldsymbol{\alpha}} \sum_{\beta} \xi^{\beta}, \qquad \boldsymbol{\xi} = \sum_{\boldsymbol{\alpha}} \boldsymbol{\xi}^{\boldsymbol{\alpha}} = \sum_{\boldsymbol{\alpha}} \sum_{\beta} \boldsymbol{\xi}^{\beta} \tag{3.87}$$

$$\hat{\Upsilon} = \sum_{\boldsymbol{\alpha}} \hat{\Upsilon}^{\boldsymbol{\alpha}} = \sum_{\boldsymbol{\alpha}} \sum_{\beta} \hat{\Upsilon}^{\beta}, \qquad \hat{\boldsymbol{\Upsilon}} = \sum_{\boldsymbol{\alpha}} \hat{\boldsymbol{\Upsilon}}^{\boldsymbol{\alpha}} = \sum_{\boldsymbol{\alpha}} \sum_{\beta} \hat{\boldsymbol{\Upsilon}}^{\beta}. \tag{3.88}$$

3.6. Mechanical balance equations

For purely mechanical problem definitions, the fields of density ρ and motion $\boldsymbol{\chi}$ are evaluated as a function of time t for all material points of the body within the continuum mechanical description. For that, the material-independent balance equations are derived for the density ρ, the linear momentum $\mathbf{l}$, and the angular momentum $\mathbf{h}$. In the following, the balance of mass, balance of linear momentum and balance of angular momentum are established for the overall mixture body φ, each main phase $\varphi^{\boldsymbol{\alpha}}$ and each component φ^{β}.

3.6.1. Balance equation of mass

The axiom for a single-phase material in a closed system states, that the mass $\mathrm{M} = \int_{\mathrm{B_S}} \rho \,\mathrm{dv}$ of body φ is constant and thus the temporal change equal to zero. At the same time, the partial mass $\mathrm{M}^{\boldsymbol{\alpha}} = \int_{\mathrm{B_S}} \rho^{\boldsymbol{\alpha}} \,\mathrm{dv}$ of constituent $\varphi^{\boldsymbol{\alpha}}$ as well as mass $\mathrm{M}^{\beta} = \int_{\mathrm{B_S}} \rho^{\beta} \,\mathrm{dv}$ of component φ^{β} is variable due to exchange and/or reaction with the remaining constituents and components, respectively. Proceeding from that, the global mass balances are postulated with

$$\frac{\mathrm{d}}{\mathrm{dt}} \int_{\mathrm{B}} \rho \,\mathrm{dv} = 0 \,, \qquad \frac{\mathrm{d}_{\boldsymbol{\alpha}}}{\mathrm{dt}} \int_{\mathrm{B}} \rho^{\boldsymbol{\alpha}} \,\mathrm{dv} = \int_{\mathrm{B}} \hat{\rho}^{\boldsymbol{\alpha}} \,\mathrm{dv} \,, \qquad \frac{\mathrm{d}_{\beta}}{\mathrm{dt}} \int_{\mathrm{B}} \rho^{\beta} \,\mathrm{dv} = \int_{\mathrm{B}} \hat{\rho}^{\beta} \,\mathrm{dv} \,, \tag{3.89}$$

wherein $\hat{\rho}^{\boldsymbol{\alpha}}$ and $\hat{\rho}^{\beta}$ denote the mass production terms per volume element dv. Mass production occurs in case of e.g. growth of biological tissue, phase transformation (liquid to ice), or chemical reactions.

Considering the introduced global master balances, the components of the mass balances (3.89) are identified with

$$\begin{array}{llllllll}
\Upsilon & \to \rho & \boldsymbol{\phi} & \to 0 & \xi & \to 0 & \hat{\Upsilon} & \to 0 \\
\Upsilon^{\boldsymbol{\alpha}} & \to \rho^{\boldsymbol{\alpha}} & \boldsymbol{\phi}^{\boldsymbol{\alpha}} & \to 0 & \xi^{\boldsymbol{\alpha}} & \to 0 & \hat{\Upsilon}^{\boldsymbol{\alpha}} & \to \hat{\rho}^{\boldsymbol{\alpha}} \\
\Upsilon^{\beta} & \to \rho^{\beta} & \boldsymbol{\phi}^{\beta} & \to 0 & \xi^{\beta} & \to 0 & \hat{\Upsilon}^{\beta} & \to \hat{\rho}^{\beta} \,,
\end{array} \tag{3.90}$$

so that the local balance equations read according to (3.84) and (3.85)

$$\dot{\rho} + \rho \operatorname{div} \dot{\mathbf{x}} = 0 \,, \qquad (\rho^{\boldsymbol{\alpha}})'_{\boldsymbol{\alpha}} + \rho^{\boldsymbol{\alpha}} \operatorname{div} \mathbf{x}'_{\boldsymbol{\alpha}} = \hat{\rho}^{\boldsymbol{\alpha}} \,, \qquad (\rho^{\beta})'_{\beta} + \rho^{\beta} \operatorname{div} \mathbf{x}'_{\beta} = \hat{\rho}^{\beta} \,. \tag{3.91}$$

Implementing (3.90) into the general constraint formulations (3.80), (3.86) and (3.88) provides the specific constraints for density, effluxes and mass fluxes with

$$\begin{gathered} \rho = \sum_{\boldsymbol{\alpha}} \rho^{\boldsymbol{\alpha}} = \sum_{\boldsymbol{\alpha}} \sum_{\beta} \rho^{\beta} \,, \quad \boldsymbol{\phi} = - \sum_{\boldsymbol{\alpha}} \rho^{\boldsymbol{\alpha}} \mathbf{d}_{\boldsymbol{\alpha}} = - \sum_{\boldsymbol{\alpha}} \sum_{\beta} \rho^{\beta} \mathbf{d}_{\beta\boldsymbol{\alpha}} = \mathbf{0} \,, \\ \hat{\rho} = \sum_{\boldsymbol{\alpha}} \hat{\rho}^{\boldsymbol{\alpha}} = \sum_{\boldsymbol{\alpha}} \sum_{\beta} \hat{\rho}^{\beta} = 0 \,. \end{gathered} \tag{3.92}$$

This coincides with the preliminary assumptions regarding the composition of the densities (3.14) and (3.26) as well as the stated requirements for the diffusive mass fluxes, cf. (3.74) and (3.75). Moreover, since the overall body is idealized as closed system for mass exchange, whereas the boundaries of the constituents and their composition are considered to be open fo mass exchange, eq. $(3.92)_3$ applies.

Different representations of the mass balance

Inserting the definition of the partial density (3.11), the local mass balance $(3.91)_2$ reads

$$(\mathrm{n}^{\boldsymbol{\alpha}} \rho^{\boldsymbol{\alpha}\mathrm{R}})'_{\boldsymbol{\alpha}} + (\mathrm{n}^{\boldsymbol{\alpha}} \rho^{\boldsymbol{\alpha}\mathrm{R}}) \operatorname{div} \mathbf{x}'_{\boldsymbol{\alpha}} = \hat{\rho}^{\boldsymbol{\alpha}} \,. \tag{3.93}$$

A change in mass indicated by $\hat{\rho}^{\boldsymbol{\alpha}}$ can be caused either by change in volume with $\hat{\rho}^{\boldsymbol{\alpha}} = \hat{\mathrm{n}}^{\boldsymbol{\alpha}} \, \rho^{\boldsymbol{\alpha}\mathrm{R}}$ or by a change of the true density with $\hat{\rho}^{\boldsymbol{\alpha}} = \mathrm{n}^{\boldsymbol{\alpha}} \, \hat{\rho}^{\boldsymbol{\alpha}\mathrm{R}}$. In case of a constant true density $\rho^{\boldsymbol{\alpha}\mathrm{R}} = \mathit{const.} \rightarrow (\rho^{\boldsymbol{\alpha}\mathrm{R}})'_{\boldsymbol{\alpha}} = 0$, (3.93) reduces to

$$(\mathrm{n}^{\boldsymbol{\alpha}})'_{\boldsymbol{\alpha}} + \mathrm{n}^{\boldsymbol{\alpha}} \operatorname{div} \mathbf{x}'_{\boldsymbol{\alpha}} = \hat{\mathrm{n}}^{\boldsymbol{\alpha}} \,, \tag{3.94}$$

and moreover, when mass exchange is excluded ($\hat{\rho}^{\boldsymbol{\alpha}} = 0$ or $\hat{\mathrm{n}}^{\boldsymbol{\alpha}} = 0$, respectively) to the volume balance

$$(\mathrm{n}^{\boldsymbol{\alpha}})'_{\boldsymbol{\alpha}} + \mathrm{n}^{\boldsymbol{\alpha}} \operatorname{div} \mathbf{x}'_{\boldsymbol{\alpha}} = 0 \,. \tag{3.95}$$

The local mass balances (3.91) can also be reformulated in an EULERian description, here showing exemplarily the mass balance for the solution, by applying the material

time derivative $(3.37)_1$ and the divergence calculation rule (A.1), so that

$$\frac{\partial \rho^{\boldsymbol{\alpha}}}{\partial \mathrm{t}} + \operatorname{div}(\rho^{\boldsymbol{\alpha}} \, \mathbf{x}'_{\boldsymbol{\alpha}}) = \hat{\rho}^{\boldsymbol{\alpha}} \tag{3.96}$$

is obtained. For stationary conditions, i.e. $\partial \rho^{\boldsymbol{\alpha}} / \partial \mathrm{t} = 0$, and excluding mass exchanges, the continuity equation known from fluid mechanics can be specified with

$$\operatorname{div}\left(\rho^{\boldsymbol{\alpha}} \, \mathbf{x}'_{\boldsymbol{\alpha}}\right) = 0 \,. \tag{3.97}$$

Likewise, these mass balance equations can be formulated also for the components φ^{β}.

3.6.2. Balance equation of linear momentum

Referring to the second axiom of NEWTON's laws of motion, which states, that the temporal change of the linear momentum $\mathbf{l} = \rho \dot{\mathbf{x}}$ equals the sum of all external forces $\mathbf{k}$ acting in the volume and the surface, the global balances of momentum can be formulated. The external forces are composed of the local volume force $\rho \, \mathbf{b}$ and the surface force $\mathbf{t} = \mathbf{T} \, \mathbf{n}$, cf. (3.76). As a consequence from the multi-phase and -component description, an additional momentum production term has to be considered for $\varphi^{\boldsymbol{\alpha}}$ and φ^{β}. Thus, the linear momentum balances are postulated with

$$\begin{aligned}
\frac{\mathrm{d}}{\mathrm{dt}} \int_{\mathrm{B}} \rho \, \dot{\mathbf{x}} \, \mathrm{dv} &= \int_{\partial \mathrm{B}} \mathbf{T} \, \mathbf{n} \, \mathrm{da} + \int_{\mathrm{B}} \rho \, \mathbf{b} \, \mathrm{dv} \\
\frac{\mathrm{d}_{\boldsymbol{\alpha}}}{\mathrm{dt}} \int_{\mathrm{B}} \rho^{\boldsymbol{\alpha}} \, \mathbf{x}'_{\boldsymbol{\alpha}} \, \mathrm{dv} &= \int_{\partial \mathrm{B}} \mathbf{T}^{\boldsymbol{\alpha}} \, \mathbf{n} \, \mathrm{da} + \int_{\mathrm{B}} \rho^{\boldsymbol{\alpha}} \, \mathbf{b} \, \mathrm{dv} + \int_{\mathrm{B}} \hat{\mathbf{s}}^{\boldsymbol{\alpha}} \, \mathrm{dv} \\
\frac{\mathrm{d}_{\beta}}{\mathrm{dt}} \int_{\mathrm{B}} \rho^{\beta} \, \mathbf{x}'_{\beta} \, \mathrm{dv} &= \int_{\partial \mathrm{B}} \mathbf{T}^{\beta} \, \mathbf{n} \, \mathrm{da} + \int_{\mathrm{B}} \rho^{\beta} \, \mathbf{b} \, \mathrm{dv} + \int_{\mathrm{B}} \hat{\mathbf{s}}^{\beta} \, \mathrm{dv} \,.
\end{aligned} \tag{3.98}$$

Therein, the terms $\hat{\mathbf{s}}^{\boldsymbol{\alpha}}$ and $\hat{\mathbf{s}}^{\beta}$ define the total momentum supply terms between the phases and components, also denoted as interaction forces. Considering the global master balance equations $(3.81)_2$, $(3.82)_2$ and $(3.83)_2$ together with the specific ones (3.98), the associated quantities of the linear momentum balance for overall mixture

φ, main phase $\varphi^{\boldsymbol{\alpha}}$ and component φ^{β} are identified with

$$\begin{array}{llllllll} \Upsilon & \to \rho\,\dot{\mathbf{x}} & \boldsymbol{\phi} & \to \mathbf{T} & \boldsymbol{\xi} & \to \rho\,\mathbf{b} & \hat{\Upsilon} & \to 0 \\ \Upsilon^{\boldsymbol{\alpha}} & \to \rho^{\boldsymbol{\alpha}}\,\mathbf{x}'_{\boldsymbol{\alpha}} & \boldsymbol{\phi}^{\boldsymbol{\alpha}} & \to \mathbf{T}^{\boldsymbol{\alpha}} & \boldsymbol{\xi}^{\boldsymbol{\alpha}} & \to \rho^{\boldsymbol{\alpha}}\,\mathbf{b} & \hat{\Upsilon}^{\boldsymbol{\alpha}} & \to \hat{\mathbf{s}}^{\boldsymbol{\alpha}} \\ \Upsilon^{\beta} & \to \rho^{\beta}\mathbf{x}'_{\beta} & \boldsymbol{\phi}^{\beta} & \to \mathbf{T}^{\beta} & \boldsymbol{\xi}^{\beta} & \to \rho^{\beta}\,\mathbf{b} & \hat{\Upsilon}^{\beta} & \to \hat{\mathbf{s}}^{\beta} \end{array} \tag{3.99}$$

Furthermore, the local balances of momentum read, proceeding from $(3.84)_2$ and $(3.85)_{2,4}$, and moreover by implementing the local mass balances (3.91)

$$\rho\,\ddot{\mathbf{x}} = \operatorname{div}\mathbf{T}+\rho\,\mathbf{b}\,, \quad \rho^{\boldsymbol{\alpha}}\,\mathbf{x}''_{\boldsymbol{\alpha}} = \operatorname{div}\mathbf{T}^{\boldsymbol{\alpha}}+\rho^{\boldsymbol{\alpha}}\,\mathbf{b}+\hat{\mathbf{p}}^{\boldsymbol{\alpha}}\,, \quad \rho^{\beta}\,\mathbf{x}''_{\beta} = \operatorname{div}\mathbf{T}^{\beta}+\rho^{\beta}\,\mathbf{b}+\hat{\mathbf{p}}^{\beta}\,, \tag{3.100}$$

see also App. A.5. In (3.100), the direct local momentum supply $\hat{\mathbf{p}}^{\boldsymbol{\alpha}}$ and $\hat{\mathbf{p}}^{\beta}$, respectively, are introduced with

$$\hat{\mathbf{p}}^{\boldsymbol{\alpha}} = \hat{\mathbf{s}}^{\boldsymbol{\alpha}} - \hat{\rho}^{\boldsymbol{\alpha}}\,\mathbf{x}'_{\boldsymbol{\alpha}} \quad \text{and} \quad \hat{\mathbf{p}}^{\beta} = \hat{\mathbf{s}}^{\beta} - \hat{\rho}^{\beta}\,\mathbf{x}'_{\beta}\,. \tag{3.101}$$

Equation (3.101) shows, that the total momentum production $\hat{\mathbf{s}}^{\boldsymbol{\alpha}}$ and $\hat{\mathbf{s}}^{\beta}$ result from a direct part $\hat{\mathbf{p}}^{\boldsymbol{\alpha}}$ and $\hat{\mathbf{p}}^{\beta}$, and a possible additional supply term produced by a density production $\hat{\rho}^{\boldsymbol{\alpha}}$ and $\hat{\rho}^{\beta}$, respectively.

Considering the general constraints $(3.80)_2$ and $(3.88)_2$, the requirements for the balance equations of linear momentum read

$$\begin{array}{lcll} \dot{\mathbf{x}} & = & \dfrac{1}{\rho}\displaystyle\sum_{\boldsymbol{\alpha}} \rho^{\boldsymbol{\alpha}}\,\mathbf{x}'_{\boldsymbol{\alpha}} & = \dfrac{1}{\rho}\displaystyle\sum_{\boldsymbol{\alpha}}\sum_{\beta} \rho^{\beta}\,\mathbf{x}'_{\beta}\,, \\ \mathbf{T} & = & \displaystyle\sum_{\boldsymbol{\alpha}} (\mathbf{T}^{\boldsymbol{\alpha}} - \rho^{\boldsymbol{\alpha}}\,\mathbf{d}_{\boldsymbol{\alpha}} \otimes \mathbf{d}_{\boldsymbol{\alpha}}) & = \displaystyle\sum_{\boldsymbol{\alpha}}\sum_{\beta} (\mathbf{T}^{\beta} - \rho^{\beta}\mathbf{d}_{\beta\boldsymbol{\alpha}} \otimes \mathbf{d}_{\beta\boldsymbol{\alpha}})\,, \\ \rho\,\mathbf{b} & = & \displaystyle\sum_{\boldsymbol{\alpha}} \rho^{\boldsymbol{\alpha}}\,\mathbf{b} & = \displaystyle\sum_{\boldsymbol{\alpha}}\sum_{\beta} \rho^{\beta}\,\mathbf{b}\,, \end{array} \tag{3.102}$$

Equation $(3.102)_1$ is in accordance with the postulated relations for the mass average velocities, cf. $(3.60)_1$ and $(3.61)_1$. To obtain $(3.102)_2$, the relations (3.65) and (3.66) have to be considered. Finally, the interaction forces need to fulfill

$$\hat{\mathbf{s}} = \sum_{\boldsymbol{\alpha}} \hat{\mathbf{s}}^{\boldsymbol{\alpha}} = \sum_{\boldsymbol{\alpha}}\sum_{\beta} \hat{\mathbf{s}}^{\beta} = \mathbf{0}\,. \tag{3.103}$$

3.6.3. Balance equation of angular momentum

The balance equation of angular momentum again bases on NEWTON's second law of motion. It postulates, that the temporal change of the overall angular momentum $\mathbf{h} = \mathbf{x} \times \rho \dot{\mathbf{x}}$ with regard to an arbitrary but spatial fixed reference point is balanced with the total angular momentum caused by all external forces $\mathbf{k}$ acting on the body B and surface ∂B with regard to the same spatial fixed point. Proceeding from this, the global angular momentum balances for φ, $\varphi^{\boldsymbol{\alpha}}$ and φ^{β} are postulated with

$$\begin{aligned}
\frac{\mathrm{d}}{\mathrm{dt}} \int_{\mathrm{B}} \mathbf{x} \times \rho \, \dot{\mathbf{x}} \, \mathrm{dv} &= \int_{\partial \mathrm{B}} \mathbf{x} \times \mathbf{T} \, \mathbf{n} \, \mathrm{da} + \int_{\mathrm{B}} \mathbf{x} \times \rho \, \mathbf{b} \, \mathrm{dv} \\
\frac{\mathrm{d}_{\boldsymbol{\alpha}}}{\mathrm{dt}} \int_{\mathrm{B}} \mathbf{x} \times \rho^{\boldsymbol{\alpha}} \, \mathbf{x}'_{\boldsymbol{\alpha}} \, \mathrm{dv} &= \int_{\partial \mathrm{B}} \mathbf{x} \times \mathbf{T}^{\boldsymbol{\alpha}} \, \mathbf{n} \, \mathrm{da} + \int_{\mathrm{B}} \mathbf{x} \times \rho^{\boldsymbol{\alpha}} \, \mathbf{b} \, \mathrm{dv} + \int_{\mathrm{B}} \hat{\mathbf{h}}^{\boldsymbol{\alpha}} \, \mathrm{dv} \\
\frac{\mathrm{d}_{\beta}}{\mathrm{dt}} \int_{\mathrm{B}} \mathbf{x} \times \rho^{\beta} \, \mathbf{x}'_{\beta} \, \mathrm{dv} &= \int_{\partial \mathrm{B}} \mathbf{x} \times \mathbf{T}^{\beta} \, \mathbf{n} \, \mathrm{da} + \int_{\mathrm{B}} \mathbf{x} \times \rho^{\beta} \, \mathbf{b} \, \mathrm{dv} + \int_{\mathrm{B}} \hat{\mathbf{h}}^{\beta} \, \mathrm{dv} \, .
\end{aligned} \tag{3.104}$$

Therein, the total production terms $\hat{\mathbf{h}}^{\boldsymbol{\alpha}}$ and $\hat{\mathbf{h}}^{\beta}$ for the moment of momentum are introduced for the multi-phase and -component description. Comparing again (3.104) to the master global balances $(3.81)_2$, $(3.82)_2$, and $(3.83)_2$, the specific field quantities are obtained with

$$\begin{array}{llllllll}
\Upsilon & \to \mathbf{x} \times \rho \, \dot{\mathbf{x}} & \boldsymbol{\phi} & \to \mathbf{x} \times \mathbf{T} & \boldsymbol{\xi} & \to \mathbf{x} \times \rho \, \mathbf{b} & \hat{\Upsilon} & \to 0 \\
\Upsilon^{\boldsymbol{\alpha}} & \to \mathbf{x} \times \rho^{\boldsymbol{\alpha}} \, \mathbf{x}'_{\boldsymbol{\alpha}} & \boldsymbol{\phi}^{\boldsymbol{\alpha}} & \to \mathbf{x} \times \mathbf{T}^{\boldsymbol{\alpha}} & \boldsymbol{\xi}^{\boldsymbol{\alpha}} & \to \mathbf{x} \times \rho^{\boldsymbol{\alpha}} \, \mathbf{b} & \hat{\Upsilon}^{\boldsymbol{\alpha}} & \to \hat{\mathbf{h}}^{\boldsymbol{\alpha}} \\
\Upsilon^{\beta} & \to \mathbf{x} \times \rho^{\beta} \mathbf{x}'_{\beta} & \boldsymbol{\phi}^{\beta} & \to \mathbf{x} \times \mathbf{T}^{\beta} & \boldsymbol{\xi}^{\beta} & \to \mathbf{x} \times \rho^{\beta} \, \mathbf{b} & \hat{\Upsilon}^{\beta} & \to \hat{\mathbf{h}}^{\beta} \, .
\end{array} \tag{3.105}$$

With that, and by using the local mass balances (3.91) as well as the local linear momentum balances (3.100), the local balances for angular momentum can be derived in accordance to $(3.84)_2$ and $(3.85)_{2,4}$ as

$$\mathbf{0} = \mathbf{I} \times \mathbf{T} \, , \qquad \mathbf{0} = \mathbf{I} \times \mathbf{T}^{\boldsymbol{\alpha}} + \hat{\mathbf{m}}^{\boldsymbol{\alpha}} \, , \qquad \mathbf{0} = \mathbf{I} \times \mathbf{T}^{\beta} + \hat{\mathbf{m}}^{\beta} \, , \tag{3.106}$$

where the direct angular momentum production is given with

$$\hat{\mathbf{m}}^{\boldsymbol{\alpha}} = \hat{\mathbf{h}}^{\boldsymbol{\alpha}} - \mathbf{x} \times \hat{\mathbf{s}}^{\boldsymbol{\alpha}} \quad \text{and} \quad \hat{\mathbf{m}}^{\beta} = \hat{\mathbf{h}}^{\beta} - \mathbf{x} \times \hat{\mathbf{s}}^{\beta} \, . \tag{3.107}$$

In analogy to (3.101), the total angular momentum production $\hat{\mathbf{h}}^{\boldsymbol{\alpha}}$ and $\hat{\mathbf{h}}^{\beta}$ is composed of a direct part $\hat{\mathbf{m}}^{\boldsymbol{\alpha}}$ and $\hat{\mathbf{m}}^{\beta}$, and an additional term due to linear momentum production $\hat{\mathbf{s}}^{\boldsymbol{\alpha}}$ and $\hat{\mathbf{s}}^{\beta}$, respectively. The derivation is given in App. A.6. From (3.106) can be concluded, that the CAUCHY stress tensor is symmetric, viz

$$\mathbf{T} = \mathbf{T}^{\mathrm{T}}\,, \tag{3.108}$$

whereas the partial stress tensors $\mathbf{T}^{\boldsymbol{\alpha}}$ and $\mathbf{T}^{\beta}$ are only symmetric in case of $\hat{\mathrm{m}}^{\boldsymbol{\alpha}} = 0$ and $\hat{\mathrm{m}}^{\beta} = 0$, respectively, which is the case for non-polar materials, cf. Ehlers [45] or Hassanizadeh and Gray [59].

Considering again $(3.80)_2$, $(3.86)_2$ and $(3.88)_2$, the constraints for the balance of angular momentum read for the angular momentum

$$\begin{aligned}
\mathbf{x} \times \rho\,\dot{\mathbf{x}} &= \mathbf{x} \times \sum_{\boldsymbol{\alpha}} \rho^{\boldsymbol{\alpha}}\,\mathbf{x}'_{\boldsymbol{\alpha}} &&= \mathbf{x} \times \sum_{\boldsymbol{\alpha}} \sum_{\beta} \rho^{\beta}\,\mathbf{x}'_{\beta}\,,\\
\mathbf{x} \times \mathbf{T} &= \mathbf{x} \times \sum_{\boldsymbol{\alpha}} \left(\mathbf{T}^{\boldsymbol{\alpha}} - \rho^{\boldsymbol{\alpha}}\,\mathrm{d}_{\boldsymbol{\alpha}} \otimes \mathrm{d}_{\boldsymbol{\alpha}}\right) &&= \mathbf{x} \times \sum_{\boldsymbol{\alpha}} \sum_{\beta} \left(\mathbf{T}^{\beta} - \mathbf{d}_{\beta\boldsymbol{\alpha}} \otimes \mathbf{d}_{\beta\boldsymbol{\alpha}}\right),\\
\mathbf{x} \times \rho\,\mathbf{b} &= \mathbf{x} \times \sum_{\boldsymbol{\alpha}} \rho^{\boldsymbol{\alpha}}\,\mathbf{b} &&= \mathbf{x} \times \sum_{\boldsymbol{\alpha}} \sum_{\beta} \rho^{\beta}\,\mathbf{b}\,,
\end{aligned} \tag{3.109}$$

The angular momentum production is constrained with

$$\hat{\mathbf{h}} = \sum_{\boldsymbol{\alpha}} \hat{\mathbf{h}}^{\boldsymbol{\alpha}} = \sum_{\boldsymbol{\alpha}} \sum_{\beta} \hat{\mathbf{h}}^{\beta} = \mathbf{0}\,. \tag{3.110}$$

3.7. Thermodynamical balance equations

Several problem definitions in continuum mechanics contain also non-mechanical, like thermal, electromagnetic or chemical, influences. Their description is possible by defining corresponding field variables, and the effects of all physical fields can be coupled and balanced. All of these processes are accompanied by the thermal effects of temporal and spatial temperature change and heat flux. Hence, for non-isothermal investigations, as given in this contribution, the balance equation of energy is required as a governing equation. The balance equation can be derived axiomatically from the first law of thermodynamics, which postulates, that the total energy U in a closed systems stays constant, cf. also (2.1).

Nevertheless, the laws of thermodynamics have to be considered likewise also for isothermal problem investigations to ensure a thermodynamical consistent material description. This is done by evaluating the second law of thermodynamics, cf. (2.6), the entropy inequality, which is not a balance equation in the proper sense. It reflects the fact, that thermal energy is only convertible into mechanical energy up to a certain degree of efficiency, and thus reveals, if a process is reversible or dissipative. It also implies, e.g., that heat is not transferable spontaneously from a system with lower temperature to a system with higher temperature.

3.7.1. Balance equation of energy

The first law of thermodynamics balances the rate of energy change in the system. The total energy of a body is composed of the kinetic energy K and internal energy U, cf. Sect. 2.2,

$$K = \int_{\mathrm{B_S}} \frac{1}{2}\,\rho\,\dot{\mathbf{x}}\cdot\dot{\mathbf{x}}\,\mathrm{dv}\,, \qquad U = \int_{\mathrm{B_S}} \rho\,\varepsilon\,\mathrm{dv}\,, \tag{3.111}$$

where ε denotes the specific internal energy, cf. (2.50). The temporal change of the total energy is balanced with the sum of external mechanical work[9] W and heat Q with

$$W = \int_{\partial\mathrm{B_S}} \mathbf{T}^{\mathrm{T}}\dot{\mathbf{x}}\cdot\mathbf{n}\,\mathrm{da} + \int_{\mathrm{B_S}} \rho\,\mathbf{b}\cdot\dot{\mathbf{x}}\,\mathrm{dv}\,, \quad Q = \int_{\partial\mathrm{B_S}} -\mathbf{q}\cdot\mathbf{n}\,\mathrm{da} + \int_{\mathrm{B_S}} \rho\,\mathrm{r}\,\mathrm{dv} \tag{3.112}$$

The non-mechanical power in the form of heat is contains the heat flux vector $\mathbf{q}$, which is positive when entering the body, and an external specific energy source r. Again, all definitions can be transferred to its partial and component-wise quantities. The global balance equations are then postulated for φ, $\varphi^{\boldsymbol{\alpha}}$ and φ^{β} with

[9] Use has been made of the CAUCHY theorem via $W = \int_{\partial\mathrm{B_S}} \dot{\mathbf{x}}\cdot\mathbf{t}\,\mathrm{da} = \dot{\mathbf{x}}\cdot\mathbf{T}\,\mathbf{n}\,\mathrm{da} = \mathbf{T}^{\mathrm{T}}\dot{\mathbf{x}}\cdot\mathbf{n}\,\mathrm{da} + \ldots$

$$
\begin{aligned}
\frac{\mathrm{d}}{\mathrm{dt}} \int_{\mathrm{B}} \rho \left(\varepsilon + \frac{1}{2} \dot{\mathbf{x}} \cdot \dot{\mathbf{x}}\right) \mathrm{dv} \quad &= \int_{\partial \mathrm{B}} (\mathbf{T}^{\mathrm{T}} \dot{\mathbf{x}} - \mathbf{q}) \cdot \mathbf{n} \, \mathrm{da} \quad && + \int_{\mathrm{B}} \rho \left(\mathbf{b} \cdot \dot{\mathbf{x}} + \mathrm{r}\right) \mathrm{dv} \\
\frac{\mathrm{d}_{\boldsymbol{\alpha}}}{\mathrm{dt}} \int_{\mathrm{B}} \rho^{\boldsymbol{\alpha}} \left(\varepsilon^{\boldsymbol{\alpha}} + \frac{1}{2} \mathbf{x}'_{\boldsymbol{\alpha}} \cdot \mathbf{x}'_{\boldsymbol{\alpha}}\right) \mathrm{dv} \quad &= \int_{\partial \mathrm{B}} ((\mathbf{T}^{\boldsymbol{\alpha}})^{\mathrm{T}} \mathbf{x}'_{\boldsymbol{\alpha}} - \mathbf{q}^{\boldsymbol{\alpha}}) \cdot \mathbf{n} \, \mathrm{da} \quad && + \int_{\mathrm{B}} \rho^{\boldsymbol{\alpha}} \left(\mathbf{b} \cdot \mathbf{x}'_{\boldsymbol{\alpha}} + \mathrm{r}^{\boldsymbol{\alpha}}\right) \mathrm{dv} \\
& && + \int_{\mathrm{B}} \hat{\mathrm{e}}^{\boldsymbol{\alpha}} \, \mathrm{dv} \\
\frac{\mathrm{d}_{\beta}}{\mathrm{dt}} \int_{\mathrm{B}} \rho^{\beta} \left(\varepsilon^{\beta} + \frac{1}{2} \mathbf{x}'_{\beta} \cdot \mathbf{x}'_{\beta}\right) \mathrm{dv} \quad &= \int_{\partial \mathrm{B}} ((\mathbf{T}^{\beta})^{\mathrm{T}} \mathbf{x}'_{\beta} - \mathbf{q}^{\beta}) \cdot \mathbf{n} \, \mathrm{da} \quad && + \int_{\mathrm{B}} \rho^{\beta} \left(\mathbf{b} \cdot \mathbf{x}'_{\beta} + \mathrm{r}^{\beta}\right) \mathrm{dv} \\
& && + \int_{\mathrm{B}} \hat{\mathrm{e}}^{\beta} \, \mathrm{dv}
\end{aligned}
\tag{3.113}
$$

The local energy supply between the phases and components due to a multi-phase and -component framework is considered via $\hat{\mathrm{e}}^{\boldsymbol{\alpha}}$ and $\hat{\mathrm{e}}^{\beta}$, respectively. Comparing the global energy balances (3.113) to $(3.81)_1$, $(3.82)_1$ and $(3.83)_1$ yields the specific field quantities of the energy balance with

$$
\begin{aligned}
&\Upsilon \to \rho \left(\varepsilon + \frac{1}{2} \dot{\mathbf{x}} \cdot \dot{\mathbf{x}}\right) && \boldsymbol{\phi} \to \mathbf{T}^{\mathrm{T}} \dot{\mathbf{x}} - \mathbf{q} && \xi \to \rho \left(\mathbf{b} \cdot \dot{\mathbf{x}} + \mathrm{r}\right) && \hat{\Upsilon} \to 0 \\
&\Upsilon^{\boldsymbol{\alpha}} \to \rho^{\boldsymbol{\alpha}} \left(\varepsilon^{\boldsymbol{\alpha}} + \frac{1}{2} \mathbf{x}'_{\boldsymbol{\alpha}} \cdot \mathbf{x}'_{\boldsymbol{\alpha}}\right) && \boldsymbol{\phi}^{\boldsymbol{\alpha}} \to (\mathbf{T}^{\boldsymbol{\alpha}})^{\mathrm{T}} \mathbf{x}'_{\boldsymbol{\alpha}} - \mathbf{q}^{\boldsymbol{\alpha}} && \xi^{\boldsymbol{\alpha}} \to \rho^{\boldsymbol{\alpha}} \left(\mathbf{b} \cdot \mathbf{x}'_{\boldsymbol{\alpha}} + \mathrm{r}^{\boldsymbol{\alpha}}\right) && \hat{\Upsilon}^{\boldsymbol{\alpha}} \to \hat{\mathrm{e}}^{\boldsymbol{\alpha}} \\
&\Upsilon^{\beta} \to \rho^{\beta} \left(\varepsilon^{\beta} + \frac{1}{2} \mathbf{x}'_{\beta} \cdot \mathbf{x}'_{\beta}\right) && \boldsymbol{\phi}^{\beta} \to (\mathbf{T}^{\beta})^{\mathrm{T}} \mathbf{x}'_{\beta} - \mathbf{q}^{\beta} && \xi^{\beta} \to \rho^{\beta} \left(\mathbf{b} \cdot \mathbf{x}'_{\beta} + \mathrm{r}^{\beta}\right) && \hat{\Upsilon}^{\beta} \to \hat{\mathrm{e}}^{\beta}
\end{aligned}
\tag{3.114}
$$

With (3.114) and by using (3.91) and (3.100), the local balances of energy can be derived in accordance to the general formulations $(3.84)_1$ and $(3.85)_{1,3}$ with

$$
\begin{aligned}
\rho \, \dot{\varepsilon} &= \mathbf{T} \cdot \mathbf{L} - \operatorname{div} \mathbf{q} + \rho \, \mathrm{r} \\
\rho^{\boldsymbol{\alpha}} \left(\varepsilon^{\boldsymbol{\alpha}}\right)'_{\boldsymbol{\alpha}} &= \mathbf{T}^{\boldsymbol{\alpha}} \cdot \mathbf{L}_{\boldsymbol{\alpha}} - \operatorname{div} \mathbf{q}^{\boldsymbol{\alpha}} + \rho^{\boldsymbol{\alpha}} \, \mathrm{r}^{\boldsymbol{\alpha}} + \hat{\varepsilon}^{\boldsymbol{\alpha}} \\
\rho^{\beta} \left(\varepsilon^{\beta}\right)'_{\beta} &= \mathbf{T}^{\beta} \cdot \mathbf{L}_{\beta} - \operatorname{div} \mathbf{q}^{\beta} + \rho^{\beta} \, \mathrm{r}^{\beta} + \hat{\varepsilon}^{\beta} \, ,
\end{aligned}
\tag{3.115}
$$

where the direct energy production terms $\hat{\varepsilon}^{\boldsymbol{\alpha}}$ and $\hat{\varepsilon}^{\beta}$ are introduced, cf. App. A.7. The total energy production terms $\hat{\mathrm{e}}^{\boldsymbol{\alpha}}$ and $\hat{\mathrm{e}}^{\beta}$, respectively, are the sum of mechanical and non-mechanical energy production with

$$\begin{aligned} \hat{\mathrm{e}}^{\boldsymbol{\alpha}} &= \hat{\varepsilon}^{\boldsymbol{\alpha}} + \hat{\mathbf{p}}^{\boldsymbol{\alpha}} \cdot \mathbf{x}'_{\boldsymbol{\alpha}} + \hat{\rho}^{\boldsymbol{\alpha}} (\varepsilon^{\boldsymbol{\alpha}} + \frac{1}{2}\, \mathbf{x}'_{\boldsymbol{\alpha}} \cdot \mathbf{x}'_{\boldsymbol{\alpha}}) \\ \hat{\mathrm{e}}^{\beta} &= \hat{\varepsilon}^{\beta} + \hat{\mathbf{p}}^{\beta} \cdot \mathbf{x}'_{\beta} + \hat{\rho}^{\beta} (\varepsilon^{\beta} + \frac{1}{2}\, \mathbf{x}'_{\beta} \cdot \mathbf{x}'_{\beta})\,. \end{aligned} \tag{3.116}$$

Equation (3.116) shows, that the total energy production results from a direct energy production part $\hat{\varepsilon}^{\boldsymbol{\alpha}}$ and $\hat{\varepsilon}^{\beta}$, a part from direct momentum production $\hat{\mathbf{p}}^{\boldsymbol{\alpha}}$ and $\hat{\mathbf{p}}^{\beta}$, and a part due to exchange of specific internal and kinetic energy caused by a density production connected with $\hat{\rho}^{\boldsymbol{\alpha}}$ and $\hat{\rho}^{\beta}$, respectively.

To comply with the constraints based on Truesdell's metaphysical principles given in (3.80), (3.88) and $(3.92)_3$, the following relations have to considered

$$\begin{aligned} \rho\, \varepsilon &= \sum_{\boldsymbol{\alpha}} \rho^{\boldsymbol{\alpha}} (\varepsilon^{\boldsymbol{\alpha}} + \frac{1}{2}\, \mathbf{d}_{\boldsymbol{\alpha}} \cdot \mathbf{d}_{\boldsymbol{\alpha}}) \quad = \sum_{\boldsymbol{\alpha}} \sum_{\beta} \rho^{\beta} (\varepsilon^{\beta} + \frac{1}{2}\, \mathbf{d}_{\beta\boldsymbol{\alpha}} \cdot \mathbf{d}_{\beta\boldsymbol{\alpha}}) \\ \rho\, \mathrm{r} &= \sum_{\boldsymbol{\alpha}} \rho^{\boldsymbol{\alpha}} (\mathrm{r}^{\boldsymbol{\alpha}} + \mathbf{b} \cdot \mathbf{d}_{\boldsymbol{\alpha}}) \qquad = \sum_{\boldsymbol{\alpha}} \sum_{\beta} \rho^{\beta} (\mathrm{r}^{\beta} + \mathbf{b} \cdot \mathbf{d}_{\beta\boldsymbol{\alpha}}) \qquad . \end{aligned} \tag{3.117}$$

and

$$\begin{aligned} \mathbf{q} =& \sum_{\boldsymbol{\alpha}} \mathbf{q}^{\boldsymbol{\alpha}} - [(\mathbf{T}^{\boldsymbol{\alpha}})^{\mathrm{T}} - \rho^{\boldsymbol{\alpha}} (\varepsilon^{\boldsymbol{\alpha}} + \frac{1}{2}\, \mathbf{d}_{\boldsymbol{\alpha}} \cdot \mathbf{d}_{\boldsymbol{\alpha}})\, \mathbf{I}]\, \mathbf{d}_{\boldsymbol{\alpha}} \\ =& \sum_{\boldsymbol{\alpha}} \sum_{\beta} \mathbf{q}^{\beta} - [(\mathbf{T}^{\beta})^{\mathrm{T}} - \rho^{\beta} (\varepsilon^{\beta} + \frac{1}{2}\, \mathbf{d}_{\beta\boldsymbol{\alpha}} \cdot \mathbf{d}_{\beta\boldsymbol{\alpha}})\, \mathbf{I}]\, \mathbf{d}_{\beta\boldsymbol{\alpha}} \end{aligned} \tag{3.118}$$

To derive the rearranged constraints specified in (3.117) and (3.118), use has been made of the definitions for the diffusion velocities (3.65) and (3.66), as well as the relations of the diffusive fluxes (3.74) and (3.75)[10].

Therein, the parts connected with the diffusion velocities $\mathbf{d}_{\boldsymbol{\alpha}}$ and $\mathbf{d}_{\beta\boldsymbol{\alpha}}$ describe the entries of the kinetic diffusion energy to the internal energy, the heat flux or source, compare also the constraint for the stress tensor $(3.102)_2$. Physically interpreted,

[10] A detailed derivation is not provided here

these diffusive initiated parts come into play for turbulent flow situations, so that they are neglected in the application in the further course of this work.

Finally, the constraint for the energy supply is given with

$$\hat{\mathrm{e}} = \sum_{\boldsymbol{\alpha}} \hat{\mathrm{e}}^{\boldsymbol{\alpha}} = \sum_{\boldsymbol{\alpha}} \sum_{\beta} \hat{\mathrm{e}}^{\beta} = 0. \tag{3.119}$$

3.7.2. Entropy inequality

As described in the introductory part of Sect. 3.7, the entropy balance is not utilized as governing equation during model setup, but for the thermodynamical consistent material modeling. In general, material laws have to be constrained, so that they don't violate basic physical principles, e.g., that heat cannot spontaneously flow from cold to hot, or heat can't be turned entirely into mechanical work. This is described with the second law of thermodynamics, which has to be fulfilled for any admissible thermo-mechanical process.

The entropy balance relation equals the temporal change of the specific entropy η in the mixture body φ with external influences. The global balances for φ, $\varphi^{\boldsymbol{\alpha}}$ and φ^{β} are postulated with

$$\begin{aligned}
\frac{\mathrm{d}}{\mathrm{dt}} \int_{\mathrm{B}} \rho\, \eta \,\mathrm{dv} &= -\int_{\partial \mathrm{B}} \boldsymbol{\phi}_{\eta} \cdot \mathbf{n} \,\mathrm{da} + \int_{\mathrm{B}} \xi_{\eta} \,\mathrm{dv} + \int_{\mathrm{B}} \hat{\eta} \,\mathrm{dv} \\
\frac{\mathrm{d}_{\boldsymbol{\alpha}}}{\mathrm{dt}} \int_{\mathrm{B}} \rho^{\boldsymbol{\alpha}} \eta^{\boldsymbol{\alpha}} \,\mathrm{dv} &= -\int_{\partial \mathrm{B}} (\frac{1}{\theta^{\boldsymbol{\alpha}}} \mathbf{q}^{\boldsymbol{\alpha}} \cdot \mathbf{n}) \,\mathrm{da} + \int_{\mathrm{B}} \frac{1}{\theta^{\boldsymbol{\alpha}}} \rho^{\boldsymbol{\alpha}}\, \mathrm{r}^{\boldsymbol{\alpha}} \,\mathrm{dv} + \int_{\mathrm{B}} \hat{\eta}^{\boldsymbol{\alpha}} \,\mathrm{dv} \\
\frac{\mathrm{d}_{\beta}}{\mathrm{dt}} \int_{\mathrm{B}} \rho^{\beta} \eta^{\beta} \,\mathrm{dv} &= -\int_{\partial \mathrm{B}} (\frac{1}{\theta^{\beta}} \mathbf{q}^{\beta} \cdot \mathbf{n}) \,\mathrm{da} + \int_{\mathrm{B}} \frac{1}{\theta^{\beta}} \rho^{\beta}\, \mathrm{r}^{\beta} \,\mathrm{dv} + \int_{\mathrm{B}} \hat{\eta}^{\beta} \,\mathrm{dv}\,,
\end{aligned} \tag{3.120}$$

wherein the negative sign of the efflux term denotes entropy supply, when the flux vector is directed into the body. In contrast to the former introduced balance equations for the mixture, eq. $(3.120)_1$ contains the entropy production term $\hat{\eta}$ for the overall mixture, which is restricted to be ≥ 0 by the second law of thermodynamics. The 2nd law expresses the experience that mechanical work can be completely transformed into heat, but the transformation of heat into mechanical energy is only partially

successful. Hence, the dissipation of mechanical work into heat is accompanied by an entropy production, which must not be negative[11].

This restriction is postulated in a multiphasic and multi-component framework only for the overall mixture body, since it is too restrictive to be claimed for $\varphi^{\boldsymbol{\alpha}}$ and φ^{β} as historically experienced. For more detailed explanations see e.g. EHLERS [45]. Proceeding from that, the entropy fluxes of $\varphi^{\boldsymbol{\alpha}}$ and φ^{β} are introduced a priori with

$$\boldsymbol{\phi}_{\eta}^{\boldsymbol{\alpha}} = \mathbf{q}^{\boldsymbol{\alpha}}/\theta^{\boldsymbol{\alpha}} \quad \text{and} \quad \boldsymbol{\phi}_{\eta}^{\beta} = \mathbf{q}^{\beta}/\theta^{\beta}\,, \tag{3.121}$$

and the entropy supply with

$$\xi_{\eta}^{\boldsymbol{\alpha}} = \rho^{\boldsymbol{\alpha}}\mathrm{r}^{\boldsymbol{\alpha}}/\theta^{\boldsymbol{\alpha}} \quad \text{and} \quad \xi_{\eta}^{\beta} = \rho^{\beta}\mathrm{r}^{\beta}/\theta^{\beta}\,. \tag{3.122}$$

The entropy efflux of the overall mixture as well as the supply $\boldsymbol{\phi}_{\eta}$ and ξ_{η} are then derived from the summation over $\varphi^{\boldsymbol{\alpha}}$ and φ^{β}, respectively. With that, the following quantities can be identified for the entropy balances:

$$\begin{array}{llllllll}
\Upsilon & \to \rho\,\eta & \boldsymbol{\phi} & \to -\boldsymbol{\phi}_{\eta} & \xi & \to \xi_{\eta} & \hat{\Upsilon} & \to \hat{\eta} \geq 0 \\
\Upsilon^{\boldsymbol{\alpha}} & \to \rho^{\boldsymbol{\alpha}}\,\eta^{\boldsymbol{\alpha}} & \boldsymbol{\phi}^{\boldsymbol{\alpha}} & \to -\dfrac{\mathbf{q}^{\boldsymbol{\alpha}}}{\theta^{\boldsymbol{\alpha}}} & \xi^{\boldsymbol{\alpha}} & \to \dfrac{\rho^{\boldsymbol{\alpha}}\,\mathrm{r}^{\boldsymbol{\alpha}}}{\theta^{\boldsymbol{\alpha}}} & \hat{\Upsilon}^{\boldsymbol{\alpha}} & \to \hat{\eta}^{\boldsymbol{\alpha}} \\
\Upsilon^{\beta} & \to \rho^{\beta}\,\eta^{\beta} & \boldsymbol{\phi}^{\beta} & \to -\dfrac{\mathbf{q}^{\beta}}{\theta^{\beta}} & \xi^{\beta} & \to \dfrac{\rho^{\beta}\,\mathrm{r}^{\beta}}{\theta^{\beta}} & \hat{\Upsilon}^{\beta} & \to \hat{\eta}^{\beta}
\end{array} \tag{3.123}$$

With (3.123) and $(3.91)_1$ the local entropy balances for $\varphi^{\boldsymbol{\alpha}}$ and φ^{β} are formulated as

$$\rho^{\boldsymbol{\alpha}}\,(\eta^{\boldsymbol{\alpha}})'_{\boldsymbol{\alpha}} + \operatorname{div}\big(\frac{\mathbf{q}^{\boldsymbol{\alpha}}}{\theta^{\boldsymbol{\alpha}}}\big) - \frac{\rho^{\boldsymbol{\alpha}}\,\mathrm{r}^{\boldsymbol{\alpha}}}{\theta^{\boldsymbol{\alpha}}} = \hat{\zeta}^{\boldsymbol{\alpha}}\,, \quad \rho^{\beta}\,(\eta^{\beta})'_{\beta} + \operatorname{div}\big(\frac{\mathbf{q}^{\beta}}{\theta^{\beta}}\big) - \frac{\rho^{\beta}\,\mathrm{r}^{\beta}}{\theta^{\beta}} = \hat{\zeta}^{\beta}\,, \tag{3.124}$$

cf. also App. A.8. Therein, the direct entropy production terms $\hat{\zeta}^{\boldsymbol{\alpha}}$ and $\hat{\zeta}^{\beta}$ are introduced, which build, together with the entropy increase caused by density production, the total entropy production:

$$\hat{\eta}^{\boldsymbol{\alpha}} = \hat{\zeta}^{\boldsymbol{\alpha}} + \hat{\rho}^{\boldsymbol{\alpha}}\,\eta^{\boldsymbol{\alpha}} \quad \text{and} \quad \hat{\eta}^{\beta} = \hat{\zeta}^{\beta} + \hat{\rho}^{\beta}\,\eta^{\beta}\,. \tag{3.125}$$

[11] From dissipation inequality: $\displaystyle\int_{\mathrm{B}} \hat{\eta}\,\mathrm{dv} = \frac{\mathrm{d}}{\mathrm{dt}}\int_{\mathrm{B}} \rho\,\eta\,\mathrm{dv} - \int_{\mathrm{B}} \xi_{\eta}\,\mathrm{dv} + \int_{\partial\mathrm{B}} \boldsymbol{\phi}_{\eta}\cdot\mathrm{d}\mathbf{a} \geq 0$

The local entropy balance for φ is derived by summation of the local balances of the constituents $\varphi^{\boldsymbol{\alpha}}$ $(3.124)_1$ and by considering the constraint $\hat{\eta} = \sum_{\boldsymbol{\alpha}} \hat{\eta}^{\boldsymbol{\alpha}} \geq 0$, so that

$$\sum_{\boldsymbol{\alpha}} [\, \rho^{\boldsymbol{\alpha}} \, (\eta^{\boldsymbol{\alpha}})'_{\boldsymbol{\alpha}} + \hat{\rho}^{\boldsymbol{\alpha}} \, \eta^{\boldsymbol{\alpha}} + \operatorname{div} (\frac{\mathbf{q}^{\boldsymbol{\alpha}}}{\theta^{\boldsymbol{\alpha}}}) - \frac{\rho^{\boldsymbol{\alpha}} \, \mathrm{r}^{\boldsymbol{\alpha}}}{\theta^{\boldsymbol{\alpha}}}] \geq 0 \tag{3.126}$$

is obtained. The constraints for the multiphasic and multi-component entropy principle can finally be specified in accordance to $(3.80)_1$ and $(3.88)_1$ with

$$\begin{aligned}
\eta &= \frac{1}{\rho} \sum_{\boldsymbol{\alpha}} \rho^{\boldsymbol{\alpha}} \, \eta^{\boldsymbol{\alpha}} &&= \frac{1}{\rho} \sum_{\boldsymbol{\alpha}} \sum_{\beta} \rho^{\beta} \, \eta^{\beta} \\
\boldsymbol{\phi}_{\eta} &= \sum_{\boldsymbol{\alpha}} (\frac{\mathbf{q}^{\boldsymbol{\alpha}}}{\theta^{\boldsymbol{\alpha}}} + \rho^{\boldsymbol{\alpha}} \, \eta^{\boldsymbol{\alpha}} \, \mathbf{d}_{\boldsymbol{\alpha}}) &&= \sum_{\boldsymbol{\alpha}} \sum_{\beta} (\frac{\mathbf{q}^{\beta}}{\theta^{\beta}} + \rho^{\beta} \, \eta^{\beta} \, \mathbf{d}_{\beta\boldsymbol{\alpha}}) \\
\xi_{\eta} &= \sum_{\boldsymbol{\alpha}} \frac{\rho^{\boldsymbol{\alpha}} \, \mathrm{r}^{\boldsymbol{\alpha}}}{\theta^{\boldsymbol{\alpha}}} &&= \sum_{\boldsymbol{\alpha}} \sum_{\beta} \frac{\rho^{\beta} \, \mathrm{r}^{\beta}}{\theta^{\beta}}
\end{aligned} \tag{3.127}$$

and

$$\hat{\eta} = \sum_{\boldsymbol{\alpha}} \hat{\eta}^{\boldsymbol{\alpha}} = \sum_{\boldsymbol{\alpha}} \sum_{\beta} \hat{\eta}^{\beta} \geq 0 \, . \tag{3.128}$$

Clausius-Duhem inequality

For another representation of (3.126), the partial specific HELMHOLTZ free energy ψ and its derivative are chosen as energy potential with

$$\psi^{\boldsymbol{\alpha}} = \varepsilon^{\boldsymbol{\alpha}} - \theta^{\boldsymbol{\alpha}}\,\eta^{\boldsymbol{\alpha}} \quad \text{and} \quad (\psi^{\boldsymbol{\alpha}})'_{\boldsymbol{\alpha}} = (\varepsilon^{\boldsymbol{\alpha}})'_{\boldsymbol{\alpha}} - (\theta^{\boldsymbol{\alpha}})'_{\boldsymbol{\alpha}}\,\eta^{\boldsymbol{\alpha}} - \theta^{\boldsymbol{\alpha}}\,(\eta^{\boldsymbol{\alpha}})'_{\boldsymbol{\alpha}}\,, \tag{3.129}$$

cf. (2.7). As the entropy $\eta^{\boldsymbol{\alpha}}$ is the primary natural variable of the internal energy $\varepsilon^{\boldsymbol{\alpha}}$, whereas for the free energy $\psi^{\boldsymbol{\alpha}}$ it is the temperature $\theta^{\boldsymbol{\alpha}}$, this formulation provides a more useful quantity to observe and measure. Implementing (3.129) into the local balance equation of energy $(3.115)_2$, rearranging the new formulated energy balance with respect to $\rho^{\boldsymbol{\alpha}}\,\mathrm{r}^{\boldsymbol{\alpha}}$ and finally inserting[12] it into (3.126) yields

$$\begin{aligned}\sum_{\boldsymbol{\alpha}} \frac{1}{\theta^{\boldsymbol{\alpha}}}\{\mathbf{T}^{\boldsymbol{\alpha}} \cdot \mathbf{L}_{\boldsymbol{\alpha}} - \rho^{\boldsymbol{\alpha}}[(\psi^{\boldsymbol{\alpha}})'_{\boldsymbol{\alpha}} + (\theta^{\boldsymbol{\alpha}})'_{\boldsymbol{\alpha}}\,\eta^{\boldsymbol{\alpha}}] - \hat{\mathbf{p}}^{\boldsymbol{\alpha}} \cdot \mathbf{x}'_{\boldsymbol{\alpha}} \\ - \hat{\rho}^{\boldsymbol{\alpha}}(\psi^{\boldsymbol{\alpha}} + \frac{1}{2}\mathbf{x}'_{\boldsymbol{\alpha}} \cdot \mathbf{x}'_{\boldsymbol{\alpha}}) - \frac{1}{\theta^{\boldsymbol{\alpha}}}\,\mathrm{grad}\,\theta^{\boldsymbol{\alpha}} \cdot \mathbf{q}^{\boldsymbol{\alpha}} + \hat{\mathrm{e}}^{\boldsymbol{\alpha}}\} \geq 0\,,\end{aligned} \tag{3.130}$$

which represents the well-known Clausius-Duhem inequality. This form of the entropy inequality is sufficient and convenient in order to obtain restrictions for the constitutive modeling.

[12] with calculation rule $\mathrm{div}\,(\frac{1}{\theta^{\boldsymbol{\alpha}}}\mathbf{q}^{\boldsymbol{\alpha}}) = \frac{1}{\theta^{\boldsymbol{\alpha}}}\mathrm{div}\,\mathbf{q}^{\boldsymbol{\alpha}} - \frac{1}{(\theta^{\boldsymbol{\alpha}})^2}\,\mathrm{grad}\,\theta^{\boldsymbol{\alpha}} \cdot \mathbf{q}^{\boldsymbol{\alpha}}$

4. Mass transport in multi-component porous media

Section 3.3.5 introduced the different types of fluxes contributing to mass transport that can arise in multi-component systems. On the one hand, mass can be transported and carried along by the bulk motion of the solvent $\varphi^{\boldsymbol{\alpha}}$. On the other hand, differences in concentration can be balanced out by the molecular motion of the components φ^{β}. Commonly, these phenomena are denoted with advection and diffusion, and well-established material equations exist for the implementation into computational models.

Furthermore, the interaction of the advective and diffusive components may become important, depending on the issue under investigation. If one considers for example a light and a heavy gas (depending on its molar mass) separated at first in a tube, the diffusion of the light gas is faster due to higher molecule velocity. When the barrier between the light and heavy gas section is removed, the net flow of the molecules is towards the heavy gas section. This leads to a pressure increase in the heavy gas section, so that the arising pressure gradient causes in turn advection from the heavy to light gas section. It is clear from the example, that diffusion is always followed by advection, except for equimolar diffusion.

Another mechanism of mass transport in porous media is dispersion, which describes the mechanical mixing of mass due to different relative movements of the fluid through the pore network. Dispersion arises on the one hand through different fluid velocities across the pores, on the other hand through the different characteristic lengths due to the tortuosity of the pore network resulting in long or short pathways, see Fig. 4.1, or also by friction.

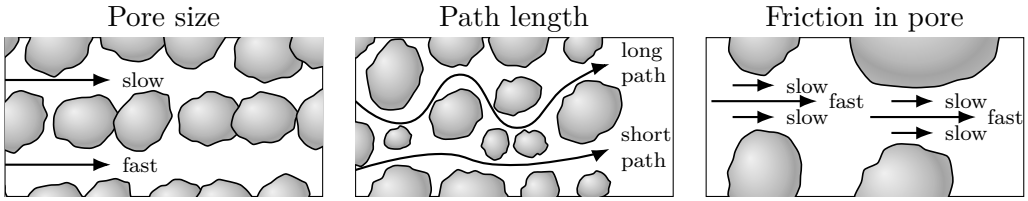

Figure 4.1.: Microscopic dispersion at pore scale.

A distinction, if a transport process is driven by diffusion or advection/dispersion can be made with the help of the dimensionless PECLÉT number, which relates the advective to diffusive flow. A general calculation is given with

$$Pe' = \frac{L\,v}{D}\,, \tag{4.1}$$

where L denotes the characteristic flow length, v the average flow velocity and D the binary diffusion coefficient. Small PECLÉT numbers indicate, that a process is diffusion dominated whereas higher PECLÉT numbers show increasing dispersion driven mixing.

For modeling of the advection-diffusion interaction, one simple and intuitive ansatz is to use an additive approach for advection and diffusion. The classical constitutive descriptions of these fluxes go back to DARCY's equation, cf. Darcy [32], for flow through porous media and FICK's law of diffusion, see e.g. Atkins and de Paula [9].

In view of the constitutive material modeling presented in Sect. 5.4, which relate to multi-component gas transport in porous media, the equations describing diffusion and advection in porous media are presented in advance in the following paragraphs.

4.1. Diffusion

The generalized FICK's law for a multi-component mixture is given with

$${}_m\mathbf{j}^{\alpha\beta}_{diff} = -\mathrm{c}^{\boldsymbol{\alpha}}_m \sum_{\beta=1}^{\nu-1} {}_mD_{\beta\nu}\,\mathrm{grad}\,x^{\alpha\beta}_m\,, \quad \mathbf{j}^{\alpha\beta}_{diff} = -\rho^{\boldsymbol{\alpha}\mathrm{R}} \sum_{\beta=1}^{\nu-1} D_{\beta\nu}\,\mathrm{grad}\,\omega^{\alpha\beta}\,, \tag{4.2}$$

see e.g. De Groot [37]. The coefficients ${}_mD_{\beta\nu}$ and $D_{\beta\nu}$ define the multi-component diffusion coefficients for the $(\nu-1)$ independent fluxes, resulting from the complex

interactions between all components of the mixture, and should not to be mistaken with the FICK binary diffusion coefficients known from literature, e.g. [74]. Additionally, they depend on the the chosen reference frame, which is set up by choosing the mass or molar averaged velocity, cf. (3.61).

The generalized form (4.2) indicates, that in case of a multi-component mixture the diffusion of component φ^β is not only driven by its own concentration gradient as in classical binary FICK diffusion, but also by the concentration gradients of the remaining mixture components. This idea was first formulated by MAXWELL and STEFAN, which used another formalism based on the kinetic theory of gases and hydromechanics[1]. However, both theories are equivalent, cf. Juncu et al. [68]. Detailed derivations of both can e.g. be found in Taylor and Krishna [97]. Furthermore, it should be noted that FICK's approach to diffusion is most popular in experiments, since chemical potentials in a multi-component mixture can only be obtained indirectly, while concentrations can directly be measured. Additionally, FICK's approach combines more naturally with the concentration balance in multi-component fluid flow, cf. Sect. 5.4.3.

A closer look has to be taken on the calculation of the diffusion coefficients, on the one hand due to the multi-component composition, and on the other hand due to porous media interaction. The multi-component diffusion coefficients given in (4.2) can just be derived by experimental measures, and all in all, a non-symmetric matrix of $(\nu-1)^2$ independent diffusion coefficients, highly dependent on the reference frame, arises, cf. Taylor and Krishna [97]. A more suitable approach from a modeler's point of view to account for the multi-component nature of a liquid mixture is given with the sometimes called Blanc's law as

$$ {}_mD_{\alpha\beta} = \frac{1-x_m^{\alpha\beta}}{\sum\limits_{\substack{\beta=1\\ \iota\neq\beta}}^{\nu} \frac{x_m^{\alpha\beta}}{{}_mD_{\beta\iota}}} \quad \text{and} \quad D_{\alpha\beta} = \frac{1-\omega^{\alpha\beta}}{\sum\limits_{\substack{\beta=1\\ \iota\neq\beta}}^{\nu} \frac{\omega^{\alpha\beta}}{D_{\beta\iota}}} \tag{4.3} $$

see e.g. Reid, Prausnitz, and Poling [87]. This relation bases on the MAXWELL-STEFAN equations, cf. Bird, Stewart, and Lightfoot [12], which illustrates the equality of the common diffusion formulations by MAXWELL-STEFAN and FICK. In (4.3),

[1]The thermodynamical driving force, the chemical potential μ^β, see also Sect. 2.5, of φ^β is in equilibrium with the friction forces between molecules, see e.g. Bothe [17].

${}_mD_{\beta\iota}$ and $D_{\beta\iota}$ denotes the binary diffusion coefficient of the binary mixture β and ι. These values can be derived either by experimental measurements or otherwise by empirical derived formulas, which mainly base on temperature, pressure, and molar weights. Relations are given e.g. in Marrero and Mason [74], Stein, Hettiratchi, and Achari [95], Ng, Feng, and Liu [83] or Novaresioa et al. [84].

Furthermore, (4.3) is only valid for diffusion in free air. For a porous medium, a factor accounting for the limited pore space for gas diffusion and tortuosity of the soil channels (see Fig. 4.1) is introduced with

$$\tau = \frac{[(1 - \mathrm{s}^{\mathbf{L}})\,\mathrm{n}^{\mathbf{F}}]^{10/3}}{(\mathrm{n}^{\mathbf{F}})^2}\,, \tag{4.4}$$

cf. Millington and Quirk [76]. Therein, the influence by liquid and solid obstacles are captured by the saturation $\mathrm{s}^{\mathbf{L}}$ and porosity $\mathrm{n}^{\mathbf{F}}$, cf. (3.5). Moreover, when the mean-free path of molecules is of the same order as the pore diameter of the porous media, the so-called Knudsen diffusion becomes important, which captures wall-molecule interaction. A correlation for that factor can also be found in e.g. [84]. However, in this work Knudsen diffusion will be disregarded as it is of negligible influence. With (4.3) and (4.4) the diffusive flux of a gas mixture[2] can finally be obtained with

$${}_m\mathbf{j}^{\mathrm{G}\gamma}_{diff} = -\tau\, {}_mD_{\mathrm{G}\gamma}\,\mathrm{grad}\,\mathrm{c}^{\mathrm{G}\gamma}_m \quad \text{and} \quad \mathbf{j}^{\mathrm{G}\gamma}_{diff} = -\tau D_{\mathrm{G}\gamma}\,\mathrm{grad}\,\rho^{\mathrm{G}\gamma}\,, \tag{4.5}$$

wherein additionally use has been made of relation (3.25).

4.2. Advection

A common description for advective flow in porous media is to use an approach founding on Darcy's equation, who found a linear proportionality of a volumetric flow passing through a cross-sectional area of a porous medium. Darcy's law is applicable to low velocity, yielding laminar flow[3], which is usually the case in porous media, see Webb [107]. For this work, only laminar flow will be considered, so that

[2] The gas main phase is denoted with $\varphi^{\mathbf{G}}$ with ν mixture components φ^{γ} so that $\varphi^{\mathbf{G}} = \bigcup_{\gamma} \varphi^{\mathrm{G}\gamma}$.

[3] The indicator for laminar or turbulent flow is given by the Reynold number Re. For values below a critical value Re_{crit}, where destabilizing inertia forces are stabilized by friction forces, laminar flow prevails, while values above Re_{crit} yield turbulent flow.

the BRINKMAN extension for boundary shear [23] and the FORCHHEIMER extension for turbulent flow [52] can be neglected. The DARCY-like weighted seepage velocity for porous media is denoted as filter velocity and stated for each of the macroscopic fluid main phases $\varphi^{\mathbf{F}}$, distinguished with $\varphi^{\boldsymbol{\beta}}$ with $\boldsymbol{\beta} \in \{\mathbf{L}, \mathbf{G}\}$, as

$$\mathrm{n}^{\boldsymbol{\beta}} \mathbf{w}_{\beta\mathbf{S}} = -\mathrm{k}_0^{\boldsymbol{\beta}} \left(\operatorname{grad} \mathrm{p}^{\boldsymbol{\beta}\mathrm{R}} - \rho^{\boldsymbol{\beta}\mathrm{R}} \mathbf{b} \right) \tag{4.6}$$

with respect to the deforming solid $\varphi^{\mathbf{S}}$. The filer velocity contains the coefficient $\mathrm{k}_0^{\boldsymbol{\beta}}$, which can either be derived by the quotient of the intrinsic permeability $\mathrm{K}^{\mathbf{S}}$ of the solid matrix and the dynamic viscosity $\eta^{\boldsymbol{\beta}\mathrm{R}}$ of the fluid passing through, or by the permeability coefficient $\mathrm{k}^{\boldsymbol{\beta}}$ and the specific weight $\gamma^{\boldsymbol{\beta}\mathrm{R}} = \rho^{\boldsymbol{\beta}}\, \mathbf{b}$:

$$\mathrm{k}_0^{\boldsymbol{\beta}} = \frac{\mathrm{K}^{\mathbf{S}}}{\eta^{\boldsymbol{\beta}\mathrm{R}}} = \frac{\mathrm{k}^{\boldsymbol{\beta}}}{\gamma^{\boldsymbol{\beta}\mathrm{R}}} \,. \tag{4.7}$$

Which formulation is used depends on the available values. Furthermore, the DARCY coefficient $\mathrm{k}_{\mathrm{D}}^{\boldsymbol{\beta}}$ is introduced and adjusted to account for the deformable nature of the porous medium with a pre-factor according to Ehlers and Eipper [47] with

$$\mathrm{k}_{\mathrm{D}}^{\boldsymbol{\beta}} = \left(\frac{\mathrm{n}^{\mathbf{F}}}{\mathrm{n}_{0\mathrm{S}}^{\mathbf{F}}}\right)^{m} \mathrm{k}_0^{\boldsymbol{\beta}} \,, \tag{4.8}$$

where $\mathrm{k}_{\mathrm{D}}^{\boldsymbol{\beta}}$ denotes the permeability coefficient in the actual configuration for a fully saturated condition. The deformation dependence can be controlled via the exponent $m \geq 0$, which for $m = 0$ yields the permeability factor of the reference configuration. For a triphasic constitutive formulation the DARCY factor (4.8) will further be enhanced by the relative permeability factor $\kappa_r^{\boldsymbol{\beta}}$ depending on the respective saturation of the mobile fluid phases.

4.3. Concentration profiles for transport mechanisms

In the following typical concentration profiles are shown that can be taken to identify the prevailing mass transport mechanism, advective or diffusive, or if both phenomena seem to be involved. The plots are taken from an academic example to show the trends of the respective curves. Thus, Fig. 4.2 shows principle diagrams of concentrations,

whose values are plotted on the ordinate, over a certain path, plotted on the abscissa. The curves can be followed for an amount of time steps starting with the black curves and proceeding to the dark blue curves. The applied concentration at the left path boundary redistributes from the left to the right edge, which serves as an outflow. The redistribution is either purely diffusion-driven with no induced filter velocity, or purely advection-driven by applying a pressure induced filter velocity and at the same time zero diffusion coefficients. In the case of Fig. 4.2c both mechanisms apply by induced flow as well as diffusion.

While the diffusion curves, cf. Fig. 4.2a, are slightly convexly curved in the direction of the outflow, the advection curves, cf. 4.2b show more of a concave curvature. When both mechanisms are involved, Fig. 4.2c, the curve opens convexly to both sides. From a physical point of view, mass transport always includes diffusion, whereas purely advective processes are not occuring. However, the advective processes can dominate the whole transport.

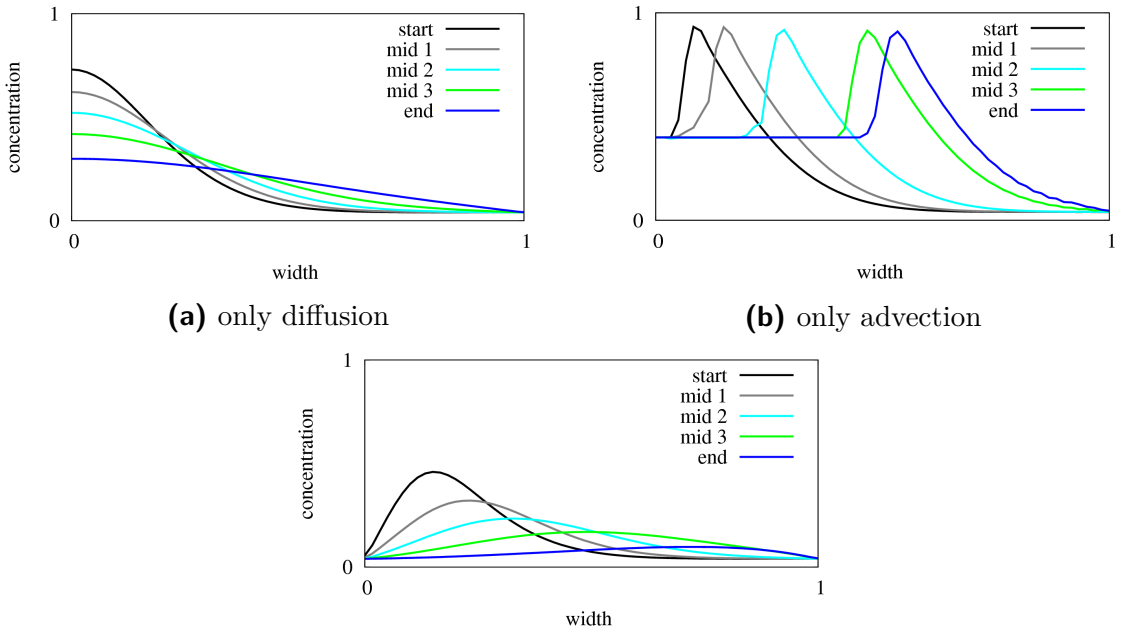

(a) only diffusion

(b) only advection

(c) both diffusion and advection

Figure 4.2.: Comparison of mass transport driven by (a) solely diffusion, (b) solely advection, and (c) both transport mechanisms.

5. Biphasic solid - gas mixture model

Building on the previously derived theoretical description for a multi-component porous medium, the specific model for a biphasic mixture consisting of a solid and a multi-component gas phase is presented. The liquid phase is considered as trapped liquid in the solid phase $\varphi^{\mathbf{S}}$, providing optimum moisture conditions with regard to the later application example. Of course, soil mechanical problems can be modeled and calculated more realistically invoking a triphasic model, but however, this would lead to a higher computational effort. This is avoided with regard to the later application of methane oxidation in landfill cover layers, where the focus is on gas production, transport and reaction, and the highly complex problem is investigated initially without influences of the liquid content.

Subsequently, this chapter is concerned with the application of the general model equations to the two-phase problem and the derivation of thermodynamically consistent material equations for a biphasic compressible model.

5.1. Modeling approach

The biphasic model is composed of the macroscopic immiscible solid phase $\varphi^{\mathbf{S}}$ and the gas mixture phase $\varphi^{\mathbf{G}}$, which is given the framework of the eTPM with

$$\varphi = \bigcup_{\boldsymbol{\alpha}} \varphi^{\boldsymbol{\alpha}} = \varphi^{\mathbf{S}} \cup \varphi^{\mathbf{G}} \quad \text{and} \quad \varphi^{\mathbf{G}} = \bigcup_{\gamma} \varphi^{\gamma} \,, \tag{5.1}$$

cf. (3.1) and (3.15). Therein, the general mixture components φ^{β} are now denoted with φ^{γ} with $\gamma = \{1,...,\nu\}$ to show unambiguously that they are the components

that make up the gas phase. According to (3.3) and (3.4) the macroscopic saturation condition reads

$$\sum_{\boldsymbol{\alpha}} \mathrm{n}^{\boldsymbol{\alpha}} = \mathrm{n}^{\mathbf{S}} + \mathrm{n}^{\mathbf{G}} = 1\,, \tag{5.2}$$

and its material time derivative

$$(\mathrm{n}^{\mathbf{S}})'_{\mathbf{S}} + (\mathrm{n}^{\mathbf{G}})'_{\mathbf{S}} = 0\,, \tag{5.3}$$

which clarifies, that changes in volume fractions have to balance each other so that (5.2) is fulfilled. Furthermore, the partial densities for solid and gas are given with

$$\rho^{\mathbf{S}} = \mathrm{n}^{\mathbf{S}}\,\rho^{\mathbf{S}\mathrm{R}} \quad \text{and} \quad \rho^{\mathbf{G}} = \mathrm{n}^{\mathbf{G}}\,\rho^{\mathbf{G}\mathrm{R}}\,. \tag{5.4}$$

The overall gas phase is composed of different components, i.e. gases, assumed to be ideal gases each, which together form a compressible gas mixture. The required density definitions formulated in mass and molar units, cf. Sect. 3.2, are collected for the gas mixture in Tab. 5.1.

Moreover, both densities, molar and mass, are connected by the molar mass constant $\mathrm{M}^{\mathbf{G}}_m = \sum_\gamma \mathrm{M}^{\gamma}_m$, calculated by the sum of each molar mass of φ^γ, with

$$\rho^{\mathrm{G}\gamma} = \mathrm{M}^{\gamma}_m\,\mathrm{c}^{\mathrm{G}\gamma}_m \quad \text{and} \quad \rho^{\mathbf{G}\mathrm{R}} = \mathrm{M}^{\mathbf{G}}_m\,\mathrm{c}^{\mathbf{G}}_m\,. \tag{5.5}$$

Summation of the molar and mass fraction, respectively, yields

$$\sum_\gamma x^{\mathrm{G}\gamma}_m = 1 \quad \text{and} \quad \sum_\gamma \omega^{\mathrm{G}\gamma} = 1\,. \tag{5.6}$$

Furthermore, the following relation for the partial density $\rho^{\mathbf{G}}$ of the gas mixture

Table 5.1.: Density definitions for gas mixture.

density	true	partial	total	fraction
molar	$\mathrm{c}^{\mathrm{G}\gamma}_m = \dfrac{\mathrm{dn}^{\gamma}_{\mathrm{m}}}{\mathrm{dv}^{\mathbf{G}}}$	$\mathrm{c}^{\gamma}_m = \mathrm{n}^{\mathbf{G}}\,\mathrm{c}^{\mathrm{G}\gamma}_m$	$\mathrm{c}^{\mathbf{G}}_m = \sum_\gamma \mathrm{c}^{\mathrm{G}\gamma}_m$	$x^{\mathrm{G}\gamma}_m = \dfrac{\mathrm{c}^{\mathrm{G}\gamma}_m}{\mathrm{c}^{\mathbf{G}}_m}$
mass	$\rho^{\mathrm{G}\gamma} = \dfrac{\mathrm{dm}^{\gamma}}{\mathrm{dv}^{\mathbf{G}}}$	$\rho^{\gamma} = \mathrm{n}^{\mathbf{G}}\,\rho^{\mathrm{G}\gamma}$	$\rho^{\mathbf{G}\mathrm{R}} = \sum_\gamma \rho^{\mathrm{G}\gamma}$	$\omega^{\mathrm{G}\gamma} = \dfrac{\rho^{\mathrm{G}\gamma}}{\rho^{\mathbf{G}\mathrm{R}}}$

resulting from the multiphasic and multi-component description can be obtained:

$$\rho^{\mathbf{G}} = \mathrm{n}^{\mathbf{G}} \rho^{\mathbf{G}\mathrm{R}} = \mathrm{n}^{\mathbf{G}} \sum_{\gamma} \rho^{\mathrm{G}\gamma} = \mathrm{n}^{\mathbf{G}} \sum_{\gamma} \frac{\rho^{\gamma}}{\mathrm{n}^{\mathbf{G}}} = \sum_{\gamma} \rho^{\gamma} \,. \tag{5.7}$$

The basic definitions for displacement, diffusion and difference velocities, cf. Sect. 3.3.5, for the applied problem are collected in Tab. 5.2 with the mass and molar averaged mixture velocities

$$\mathbf{x}'_{\mathbf{G}} = \frac{1}{\rho^{\mathbf{G}\mathrm{R}}} \sum_{\gamma} \rho^{\mathrm{G}\gamma} \, \mathbf{x}'_{\gamma} \quad \text{and} \quad {}_{m}\mathbf{x}'_{\mathbf{G}} = \frac{1}{\mathrm{c}^{\mathbf{G}}_{m}} \sum_{\gamma} \mathrm{c}^{\mathrm{G}\gamma}_{m} \, \mathbf{x}'_{\gamma} \,. \tag{5.8}$$

Therein, the constraints concerning the diffusion velocity have to be obtained with

Table 5.2.: Kinematic definitions for solid - gas mixture.

	mass averaged		molar averaged
diffusion velocity	$\mathbf{d}_{\gamma\mathbf{G}} = \mathbf{x}'_{\gamma} - \mathbf{x}'_{\mathbf{G}}$		${}_{m}\mathbf{d}_{\gamma\mathbf{G}} = \mathbf{x}'_{\gamma} - {}_{m}\mathbf{x}'_{\mathbf{G}}$
seepage velocity	$\mathbf{w}_{\mathbf{GS}} = \mathbf{x}'_{\mathbf{G}} - \mathbf{x}'_{\mathbf{S}}$		${}_{m}\mathbf{w}_{\mathbf{GS}} = {}_{m}\mathbf{x}'_{\mathbf{G}} - \mathbf{x}'_{\mathbf{S}}$
relative velocity	$\mathbf{w}_{\gamma\mathbf{S}} = \mathbf{d}_{\gamma\mathbf{G}} + \mathbf{w}_{\mathbf{GS}}$	or	$\mathbf{w}_{\gamma\mathbf{S}} = {}_{m}\mathbf{d}_{\gamma\mathbf{G}} + {}_{m}\mathbf{w}_{\mathbf{GS}}$

$$\sum_{\gamma} \rho^{\mathrm{G}\gamma} \mathbf{d}_{\gamma\mathbf{G}} = 0 \quad \text{and} \quad \sum_{\gamma} \mathrm{c}^{\mathbf{G}}_{m} \, {}_{m}\mathbf{d}_{\gamma\mathbf{G}} = 0 \,. \tag{5.9}$$

5.2. Preliminary assumptions

Any problem under investigation should be approximated as physically accurate as possible by a computational model, but by taking also into account the time and effort required for the calculation, so that reasonable assumptions are made in advance. These are, for a mentioned soil mechanical problem with focus on the gas mixture

and interaction to the solid matrix, given with:

$$
\begin{array}{rrcl}
\text{incompressible solid phase:} & (\rho^{\mathbf{S}\mathrm{R}})'_{\mathbf{S}} & = & 0 \\
\text{compressible gas mixture:} & (\rho^{\mathbf{G}\mathrm{R}})'_{\mathbf{G}} & \neq & 0 \\
 & & \rightarrow & \rho^{\mathbf{G}\mathrm{R}}\left(\mathbf{x}, \mathrm{t}, \rho^{\mathrm{G}\gamma}\right) \\
\text{equal temperature:} & \theta & = & \theta^{\boldsymbol{\alpha}} = \theta^{\mathrm{G}\gamma} \\
 & & \rightarrow & \hat{\mathrm{e}}^{\boldsymbol{\alpha}} = \hat{\mathrm{e}}^{\mathrm{G}\gamma} = 0 \\
\text{non-isothermal calculation:} & (\theta)'_{\boldsymbol{\alpha}} & \neq & 0 \\
\text{no external heat supply:} & \mathrm{r} = \mathrm{r}^{\boldsymbol{\alpha}} = \mathrm{r}^{\mathrm{G}\gamma} & = & 0 \\
\text{no mass exchange of main phases:} & \hat{\rho}^{\mathbf{S}} = \hat{\rho}^{\mathbf{G}} & = & 0 \\
\text{quasi-static investigation:} & \ddot{\mathbf{x}} = \mathbf{x}''_{\boldsymbol{\alpha}} = \mathbf{x}''_{\gamma} & = & 0
\end{array}
\tag{5.10}
$$

Considering the incompressible solid phase the derivatives of the true and partial density read as

$$
\rho^{\mathbf{S}\mathrm{R}} = \rho^{\mathbf{S}\mathrm{R}}_{0\mathbf{S}} = \text{const.} \quad \rightarrow \quad (\rho^{\mathbf{S}\mathrm{R}})'_{\mathbf{S}} = 0 \quad \rightarrow \quad (\rho^{\mathbf{S}})'_{\mathbf{S}} = (\mathrm{n}^{\mathbf{S}})'_{\mathbf{S}}\, \rho^{\mathbf{S}\mathrm{R}}_{0\mathbf{S}}\,, \tag{5.11}
$$

whereas for the compressible gas phase the material time derivative for the partial density reads

$$
(\rho^{\mathbf{G}})'_{\mathbf{G}} = (\mathrm{n}^{\mathbf{G}}\rho^{\mathbf{G}\mathrm{R}})'_{\mathbf{G}} = (\mathrm{n}^{\mathbf{G}})'_{\mathbf{G}}\, \rho^{\mathbf{G}\mathrm{R}} + \mathrm{n}^{\mathbf{G}}(\rho^{\mathbf{G}\mathrm{R}})'_{\mathbf{G}}\,. \tag{5.12}
$$

Temperature changes are permitted for the non-isothermal calculation, but only considering the same temperature for the whole mixture. The body is neither heated nor cooled by external heat sources or sinks. Furthermore, mass exchange is excluded between the main phases $\varphi^{\boldsymbol{\alpha}}$, but existent for the components of the gas mixture due to bio-chemical reactions following the constraint

$$
\sum_{\gamma} \hat{\rho}^{\gamma} = 0. \tag{5.13}
$$

The momentum induced by density production $\hat{\rho}^{\boldsymbol{\alpha}}\mathbf{x}'_{\boldsymbol{\alpha}}$ and $\hat{\rho}^{\gamma}\mathbf{x}'_{\gamma}$ will be neglected, since its amount is small in comparison to the direct momentum production $\hat{\mathbf{p}}^{\boldsymbol{\alpha}}$ with

$\hat{\rho}^{\boldsymbol{\alpha}}\,\mathbf{x}'_{\boldsymbol{\alpha}} \ll \hat{\mathbf{p}}^{\boldsymbol{\alpha}}$ and $\hat{\rho}^{\gamma}\mathbf{x}'_{\gamma} \ll \hat{\mathbf{p}}^{\gamma}$. From that, (3.101) can be reformulated to

$$\hat{\mathbf{p}}^{\boldsymbol{\alpha}} = \hat{\mathbf{s}}^{\boldsymbol{\alpha}} \quad \text{and} \quad \hat{\mathbf{p}}^{\gamma} = \hat{\mathbf{s}}^{\gamma} \tag{5.14}$$

constrained for the overall mixture by

$$\hat{\mathbf{p}} = \sum_{\boldsymbol{\alpha}} \hat{\mathbf{p}}^{\boldsymbol{\alpha}} = \hat{\mathbf{p}}^{\mathbf{S}} + \sum_{\gamma} \hat{\mathbf{p}}^{\gamma} = \mathbf{o}\,. \tag{5.15}$$

Finally, laminar flow conditions are assumed, cf. Chapter 4.2, free of accelerations.

5.3. Field equations

The required field equations to set up the model can be derived by adapting the introduced general balance equations, cf. Sec. 3.5.

5.3.1. Volume and concentration balances

The local volume balance equation for the solid main phase $\varphi^{\mathbf{S}}$, considering the assumptions of incompressibility (5.11) and exclusion of mass exchange, reads

$$(\mathrm{n}^{\mathbf{S}})'_{\mathbf{S}} + \mathrm{n}^{\mathbf{S}}\,\mathrm{div}\,\mathbf{x}'_{\mathbf{S}} = 0 \quad \Rightarrow \quad \mathrm{n}^{\mathbf{S}} = \mathrm{n}^{\mathbf{S}}_{0\mathbf{S}}\,\mathrm{J}_{\mathbf{S}}^{-1}\,, \tag{5.16}$$

see also App. B.1. The local mass balance equation for the gas main phase $\varphi^{\mathbf{G}}$ reads, cf. $(3.91)_2$,

$$(\mathrm{n}^{\mathbf{G}})'_{\mathbf{G}} + \frac{\mathrm{n}^{\mathbf{G}}}{\rho^{\mathbf{G}\mathrm{R}}}(\rho^{\mathbf{G}\mathrm{R}})'_{\mathbf{G}} + \mathrm{n}^{\mathbf{G}}\,\mathrm{div}\,\mathbf{x}'_{\mathbf{G}} = 0\,, \tag{5.17}$$

where (5.12) has been considered. Proceeding from $(3.91)_3$, the concentration balance for the gas mixture components reads

$$(\rho^{\gamma})'_{\gamma} + \rho^{\gamma}\,\mathrm{div}\,\mathbf{x}'_{\gamma} = \hat{\rho}^{\gamma}\,. \tag{5.18}$$

Implementing the partial mass definition for ρ^γ, see Tab. (5.1), as well as (5.5), and furthermore truncating the molar mass constant leads to

$$(\mathrm{n}^{\mathbf{G}}\,\mathrm{c}_m^{\mathrm{G}\gamma})'_\gamma + \mathrm{n}^{\mathbf{G}}\,\mathrm{c}_m^{\mathrm{G}\gamma}\,\mathrm{div}\,\mathbf{x}'_\gamma = \mathrm{n}^{\mathbf{G}}\,\hat{\mathrm{c}}_m^{\mathrm{G}\gamma}\,, \tag{5.19}$$

with the molar exchange rate

$$\hat{\mathrm{c}}_m^{\mathrm{G}\gamma} = \frac{1}{\mathrm{M}_m^\gamma}\,\hat{\rho}^{\mathrm{G}\gamma}\,. \tag{5.20}$$

Reformulating the material time derivative of (5.19) with respect to the solid motion[1], and afterwards applying the divergence calculation rule (A.1) yields

$$(\mathrm{n}^{\mathbf{G}}\,\mathrm{c}_m^{\mathrm{G}\gamma})'_{\mathbf{S}} + \mathrm{div}\,(\mathrm{n}^{\mathbf{G}}\,\mathrm{c}_m^{\mathrm{G}\gamma}\,\mathbf{w}_{\gamma\mathbf{S}}) + \mathrm{n}^{\mathbf{G}}\,\mathrm{c}_m^{\mathrm{G}\gamma}\,\mathrm{div}\,\mathbf{x}'_{\mathbf{S}} = \mathrm{n}^{\mathbf{G}}\,\hat{\mathrm{c}}_m^{\mathrm{G}\gamma}\,. \tag{5.21}$$

Moreover, resolving the term $(\mathrm{n}^{\mathbf{G}}\,\mathrm{c}_m^{\mathrm{G}\gamma})'_{\mathbf{S}}$

- by considering (5.3) with $(\mathrm{n}^{\mathbf{G}})'_{\mathbf{S}} = -(\mathrm{n}^{\mathbf{S}})'_{\mathbf{S}}$,
- implementing the solid volume balance $(5.16)_1$ with $(\mathrm{n}^{\mathbf{S}})'_{\mathbf{S}} = -\mathrm{n}^{\mathbf{S}}\,\mathrm{div}\,\mathbf{x}'_{\mathbf{S}}$,
- and considering the saturation condition itself with $\mathrm{n}^{\mathbf{S}} = 1 - \mathrm{n}^{\mathbf{G}}$

the final formulation of the molar concentration balance can be obtained with

$$\mathrm{n}^{\mathbf{G}}(\mathrm{c}_m^{\mathrm{G}\gamma})'_{\mathbf{S}} + \mathrm{div}\,(\mathrm{n}^{\mathbf{G}}\,\mathrm{c}_m^{\mathrm{G}\gamma}\,\mathbf{w}_{\gamma\mathbf{S}}) + \mathrm{c}_m^{\mathrm{G}\gamma}\,\mathrm{div}\,\mathbf{x}'_{\mathbf{S}} = \mathrm{n}^{\mathbf{G}}\,\hat{\mathrm{c}}_m^{\mathrm{G}\gamma}\,. \tag{5.22}$$

Likewise, the concentration balance in mass units can be obtained with

$$\mathrm{n}^{\mathbf{G}}\,(\rho^{\mathrm{G}\gamma})'_{\mathbf{S}} + \mathrm{div}\,(\mathrm{n}^{\mathbf{G}}\,\rho^{\mathrm{G}\gamma}\,\mathbf{w}_{\gamma\mathbf{S}}) + \rho^{\mathrm{G}\gamma}\,\mathrm{div}\,\mathbf{x}'_{\mathbf{S}} = \mathrm{n}^{\mathbf{G}}\,\hat{\rho}^{\mathrm{G}\gamma}\,. \tag{5.23}$$

To comply with the general constraints (3.80), the summation of (5.18) with respect to the average velocity $\mathbf{x}'_{\mathbf{G}}$ has to yield the overall mass balance of the main gas phase (5.17). A more detailed derivation is given in Appendix B.2.

[1] $(\cdot)'_\gamma = (\cdot)'_{\mathbf{S}} + \mathrm{grad}\,(\cdot)\cdot\mathbf{w}_{\gamma\mathbf{S}}$, in analogy to (A.12)

5.3.2. Momentum balances

The local momentum balances for a quasi-static formulation for the immiscible solid and gas phase can be set up according to (3.100) with

$$\operatorname{div} \mathbf{T}^{\mathbf{S}} + \rho^{\mathbf{S}}\, \mathbf{b} = -\hat{\mathbf{p}}^{\mathbf{S}} \quad \text{and} \quad \operatorname{div} \mathbf{T}^{\mathbf{G}} + \rho^{\mathbf{G}}\, \mathbf{b} = -\hat{\mathbf{p}}^{\mathbf{G}} \tag{5.24}$$

as well as

$$\operatorname{div} \mathbf{T}^{\gamma} + \rho^{\gamma}\, \mathbf{b} = -\hat{\mathbf{p}}^{\gamma} \quad \text{with} \quad \mathbf{T}^{\mathbf{G}} = \sum_{\gamma} \mathbf{T}^{\gamma} \tag{5.25}$$

for the gas components. Summing up all single momentum balances yields the local momentum balance for the overall body with

$$\operatorname{div} \mathbf{T} + \rho\, \mathbf{b} = \mathbf{0}\,, \tag{5.26}$$

where the relation (3.103) has been considered.

5.3.3. Energy balance

The problem to investigate requires the energy balance, but only for the mixture, since equal phase and component temperatures are presumed. Proceeding from the general local form according to (3.115) with

$$\rho^{\boldsymbol{\alpha}} (\varepsilon^{\boldsymbol{\alpha}})'_{\boldsymbol{\alpha}} - \mathbf{T}^{\boldsymbol{\alpha}} \cdot \mathbf{D}_{\boldsymbol{\alpha}} - \rho^{\boldsymbol{\alpha}}\, \mathrm{r}^{\boldsymbol{\alpha}} + \operatorname{div} \mathbf{q}^{\boldsymbol{\alpha}} = \hat{\varepsilon}^{\boldsymbol{\alpha}} \tag{5.27}$$

with the direct energy production term

$$\hat{\varepsilon}^{\boldsymbol{\alpha}} = \hat{\mathrm{e}}^{\boldsymbol{\alpha}} - \hat{\mathbf{p}}^{\boldsymbol{\alpha}} \cdot \mathbf{x}'_{\boldsymbol{\alpha}} - \hat{\rho}^{\boldsymbol{\alpha}} \left(\varepsilon^{\boldsymbol{\alpha}} + \frac{1}{2}\, \mathbf{x}'_{\boldsymbol{\alpha}} \cdot \mathbf{x}'_{\boldsymbol{\alpha}}\right), \tag{5.28}$$

(5.27) can be reformulated to

$$\begin{aligned} \rho^{\boldsymbol{\alpha}} \left\{ (\psi^{\boldsymbol{\alpha}})'_{\boldsymbol{\alpha}} + (\theta)'_{\boldsymbol{\alpha}}\, \eta^{\boldsymbol{\alpha}} + \theta^{\boldsymbol{\alpha}} (\eta^{\boldsymbol{\alpha}})'_{\boldsymbol{\alpha}} \right\} - \mathbf{T}^{\boldsymbol{\alpha}} \cdot \mathbf{D}_{\boldsymbol{\alpha}} - \rho^{\boldsymbol{\alpha}}\, \mathrm{r}^{\boldsymbol{\alpha}} + \operatorname{div} \mathbf{q}^{\boldsymbol{\alpha}} \\ = \hat{\mathrm{e}}^{\boldsymbol{\alpha}} - \hat{\mathbf{p}}^{\boldsymbol{\alpha}} \cdot \mathbf{x}'_{\boldsymbol{\alpha}} - \hat{\rho}^{\boldsymbol{\alpha}} \left(\varepsilon^{\boldsymbol{\alpha}} + \frac{1}{2}\, \mathbf{x}'_{\boldsymbol{\alpha}} \cdot \mathbf{x}'_{\boldsymbol{\alpha}}\right) \end{aligned} \tag{5.29}$$

where the definition of the HELMHOLTZ free energy (3.129) is implemented. Considering (5.7), (5.15), and (5.25), the mixture energy balance reads for the present solid-gas mixture model

$$\rho^{\mathbf{S}} \left\{ (\psi^{\mathbf{S}})'_{\mathbf{S}} + (\theta)'_{\mathbf{S}}\, \eta^{\mathbf{S}} + \theta\, (\eta^{\mathbf{S}})'_{\mathbf{S}} \right\} - \mathbf{T}^{\mathbf{S}} \cdot \mathbf{D}_{\mathbf{S}} + \sum_{\gamma} \rho^{\gamma} \left\{ (\psi^{\gamma})'_{\gamma} + (\theta)'_{\gamma}\, \eta^{\gamma} + \theta (\eta^{\gamma})'_{\gamma} \right\}$$

$$- \sum_{\gamma} \mathbf{T}^{\gamma} \cdot \mathbf{D}_{\gamma} + \operatorname{div} \mathbf{q} + \sum_{\gamma} \hat{\mathbf{p}}^{\gamma} \cdot \mathbf{w}_{\gamma \mathbf{S}} + \sum_{\gamma} \hat{\rho}^{\gamma} \left(\psi^{\gamma} + \theta\, \eta^{\gamma} \right) = 0 \,, \quad (5.30)$$

where use has been made of (3.117) and (5.15) as well as the postulation for the heat flux vector

$$\mathbf{q}^{\mathbf{S}} + \sum_{\gamma} \mathbf{q}^{\gamma} = \mathbf{q} \,. \quad (5.31)$$

Furthermore, for the mass-specific free energy ψ^{γ} as well as the mass-specific entropy η^{γ} the following constraints are valid:

$$\psi^{\mathbf{G}} = \sum_{\gamma} \psi^{\gamma} \qquad \eta^{\mathbf{G}} = \sum_{\gamma} \eta^{\gamma} \,. \quad (5.32)$$

Due to the assumption of creeping flow conditions the square of the velocities $\mathbf{x}'_{\boldsymbol{\alpha}} \cdot \mathbf{x}'_{\boldsymbol{\alpha}}$ is disregarded from (5.29) to (5.30). Thus, the contribution of the kinetic energy, see (3.116), caused by chemical conversion to the mixture energy balance is negligible.

5.4. Constitutive theory

To close the model under consideration, this section provides the derivation for a thermodynamic consistent approach of constitutive equations, which adequately describe the material behavior. For that, the CLAUSIUS-DUHEM inequality (3.130) is invoked and evaluated. Following e.g. Ehlers [45], the set of constitutive variables ($\#\mathcal{CQ}$) is chosen with

$$\mathcal{CQ} = \{\, \mathbf{T}^{\mathbf{S}},\, \mathbf{T}^{\gamma},\, \hat{\mathbf{p}}^{\gamma},\, \hat{\rho}^{\gamma}, \psi^{\mathbf{S}},\, \psi^{\gamma},\, \eta^{\mathbf{S}}, \eta^{\gamma}, \mathbf{q} \,\} := \mathcal{R} \,. \quad (5.33)$$

These variables represent the set of undetermined response functions $\mathcal{R}$, which cannot be computed from the given set of balance equations and the given motion and

temperature fields $\mathbf{x} = \boldsymbol{\chi}_{\boldsymbol{\alpha}}(\mathbf{X}_{\boldsymbol{\alpha}}, t)$ and $\theta = \theta(\mathbf{x}, t)$. The detailed derivation to gain $\mathcal{R}$ is given in App. B.4.

Moreover, each response function is given as a functional of the basic thermo-mechanical process variables density, motion and temperature, or generally speaking as a functional of the set of process variables $\mathcal{P}$ with

$$\mathcal{R} = \mathcal{R}(\mathcal{P})\,. \tag{5.34}$$

The development of constitutive equations in dependence of process variables for the individual material requires the consideration of some basic principles of material modeling in order not to violate physical and thermodynamical laws, and to avoid an arbitrary construction of these. The axioms trace back e.g. to Truesdell and Toupin [105], Truesdell and Noll [104] and Truesdell [103]. The main keypoints are:

- **Principle of determinism**: The current state at a material point depends on the complete thermo-mechanical history of the entire material body and thus, the set of response functions $\mathcal{R}$ is clearly defined by the history of the body.
- **Principle of equipresence**: The set of response functions $\mathcal{R}$ depends basically on the same set of process variables $\mathcal{P}$ with $\mathcal{R} = \mathcal{R}(\mathcal{P})$.
- **Principle of local action**: The set of response functions $\mathcal{R}$ of a material point is determined by the history of only a small neighborhood of that particle.
- **Principle of objectivity and material frame-indifference**: The constitutive equations must be observer-invariant to ensure an identical material response including that the energy of a deformed body should remain unchanged for a rigid-body motion.
- **Principle of dissipation**: The material equations have to be formulated such that they do not violate the 2nd law of thermodynamics.

Based on the mentioned basic thermo-mechanical set, the set of process variables for a multi-phase problem reads

$$\begin{aligned}\mathcal{P} = \{&\theta,\, \mathrm{grad}\theta,\, \mathrm{n}^{\boldsymbol{\alpha}},\, \mathrm{gradn}^{\boldsymbol{\alpha}},\, \rho^{\boldsymbol{\alpha}\mathrm{R}},\, \mathrm{grad}\rho^{\boldsymbol{\alpha}\mathrm{R}},\\ &\mathbf{F}_{\boldsymbol{\alpha}},\, \mathrm{Grad}_{\boldsymbol{\alpha}}\,\mathbf{F}_{\boldsymbol{\alpha}},\, \mathbf{x}'_{\boldsymbol{\alpha}}, \mathrm{Grad}_{\boldsymbol{\alpha}}\,\mathbf{x}'_{\boldsymbol{\alpha}},\, \mathbf{X}_{\boldsymbol{\alpha}}\}\,.\end{aligned} \tag{5.35}$$

With this general set, a porous body can be described regarding its thermal state with θ and gradθ [2], its inhomogenities $\mathbf{X}_{\boldsymbol{\alpha}}$, and its deformation state, see also Bowen [22, 20] and Ehlers [42]. In contrast to a single-phase material, whose state of deformation can totally be described via the deformation gradient $\mathbf{F}$, a multi-phase material needs more variables. Due to possible mass productions, the partial densities cannot be determined by the mass balance with $\rho_0 = \mathrm{J}\rho$ (cf. (5.16)). Hence, the partial densities $\rho^{\boldsymbol{\alpha}}$ are independent variables determined by $\mathrm{n}^{\boldsymbol{\alpha}}$ and $\rho^{\boldsymbol{\alpha}\mathrm{R}}$, where either the partial or true density, and the volume fraction have to be considered in (5.35). Moreover, considering the saturation condition, only one volume fraction is needed as process variable. To capture viscous effects, the velocities $\mathbf{x}'_{\boldsymbol{\alpha}}$ and their gradients $\mathrm{Grad}_{\boldsymbol{\alpha}}\,\mathbf{x}'_{\boldsymbol{\alpha}}$ can be included.

The set of (5.35) can be reduced to adapt more to the biphasic material considered in this work as well as for simplifying reasons regarding the evaluation of the entropy inequality as follows:

- Inhomogenitities, captured by $\mathbf{X}_{\boldsymbol{\alpha}}$, are not considered, neither for the solid nor the gas phase.

- The solid phase itself is considered to behave purely elastically, so $\mathbf{x}'_{\mathbf{S}}$ and its gradient are eliminated from the set, whereas the whole body acts viscous, so that $\mathbf{x}'_{\mathbf{G}}$ is replaced by the seepage velocity $\mathbf{w}_{\mathbf{GS}}$ or relative $\mathbf{w}_{\gamma\mathbf{S}}$, respectively. The gradient of the gas velocity is considered via the symmetric part of the material velocity gradient of the gas components $\mathbf{D}_{\gamma}$, which compose the main gas velocity.

- The deformation gradient of the gas phase $\mathbf{F}_{\mathbf{G}}$ can be replaced by its determinant and finally by $\rho^{\mathbf{G}\mathrm{R}}$, see Acartürk [6]. Proceeding from a multiplicative split of $\mathbf{F}_{\mathbf{G}}$ into a volumetric (det$\mathbf{F}_{\mathbf{G}}$) and isochoric ($\tilde{\mathbf{F}}_{\mathbf{G}}$) part, see e.g. [65], the deformation of the gas phase is only a function of its volumetric change with $\mathbf{F}_{\mathbf{G}} = (\det \mathbf{F}_{\mathbf{G}})^{1/3}\,\mathbf{I}$, where $\tilde{\mathbf{F}}_{\mathbf{G}} = \mathbf{I}$ is stated for the isochoric part of a fluid. Furthermore, the deformation variables of a fluid are not influenced by mass production, so that det$\mathbf{F}_{\mathbf{G}}$ can be replaced by $\rho^{\mathbf{G}\mathrm{R}}$ by considering the overall mass balance .

[2] Gradients are generally considered to account for second grade materials, where the state of a constituent may depend on the state of the others

- The overall gas density $\rho^{\mathbf{GR}}$ is composed of the densities of its components ρ^{γ}, cf. (5.7).
- The volume fraction $\mathrm{n}^{\mathbf{G}}$ can be replaced utilizing the saturation condition and $(5.16)_2$ with $\mathrm{n}^{\mathbf{G}} = 1 - \mathrm{n}^{\mathbf{S}}_{0\mathbf{S}} \, (\det \mathbf{F}_{\mathbf{S}})^{-1}$
- The solid material is assumed to be incompressible and not part of mass exchange, hence, $\rho^{\mathbf{SR}}$ and its gradient can be neglected from (5.35) and the solid deformation gradient is the only describing variable.

Finally, the set of specific process variables for the solid - gas mixture material is defined with

$$\mathcal{P} = \{ \, \theta, \, \mathrm{grad}\theta, \, \mathbf{F}_{\mathbf{S}}, \, \mathrm{Grad}_{\mathbf{S}}\mathbf{F}_{\mathbf{S}}, \, \rho^{\gamma}, \, \mathrm{grad}\rho^{\gamma}, \, \mathbf{w}_{\gamma\mathbf{S}}, \, \mathbf{D}_{\gamma} \} \, . \tag{5.36}$$

5.4.1. Adaption of the entropy inequality

Proceeding from the general Clausius-Duhem inequality (3.130), used for thermo-mechanical constitutive modeling, the entropy inequality for the material under consideration reads

$$\begin{aligned} \mathbf{T}^{\mathbf{S}} \cdot \mathbf{D}_{\mathbf{S}} - \rho^{\mathbf{S}} \, \{ (\psi^{\mathbf{S}})'_{\mathbf{S}} + (\theta)'_{\mathbf{S}} \, \eta^{\mathbf{S}} \} - \sum_{\gamma} \mathbf{T}^{\gamma} \cdot \mathbf{D}_{\gamma} - \sum_{\gamma} \rho^{\gamma} \, \{ \, (\psi^{\gamma})'_{\gamma} + (\theta)'_{\gamma} \, \eta^{\gamma} \, \} \\ - \sum_{\gamma} \hat{\rho}^{\gamma} \, \psi^{\gamma} - \sum_{\gamma} \hat{\mathbf{p}}^{\gamma} \cdot \mathbf{w}_{\gamma\mathbf{S}} - \frac{1}{\theta} \, \mathbf{q} \cdot \mathrm{grad} \, \theta \;\; \geq 0 \, . \end{aligned} \tag{5.37}$$

Therein, the assumption of equal temperatures for mixture, phases and components, see (5.10), is applied, so that the energetically conjugate variables $\theta \leftrightarrow \eta$, cf. Tab. 2.1 are equal to $\theta \leftrightarrow \eta^{\gamma}$. Due to the symmetry of the stress tensor $\mathbf{T}^{\boldsymbol{\alpha}}$ the velocity gradient $\mathbf{L}_{\boldsymbol{\alpha}}$ was replaced by its symmetric part $\mathbf{D}_{\boldsymbol{\alpha}}$. Furthermore, the composition of the gas density was considered via (5.7), the momentum production restriction (3.101) and (3.103) were utilized, the definition for the relative velocity cf. Tab. (5.2) and relation (5.31).

The mixture energy balance (5.30) and the given entropy inequality (5.37) contain the specific Helmholtz free energy ψ^{γ}, which can be related to the main gas phase

volume using the definitions for true and partial densities given in Tab. (5.1):

$$\rho^{\gamma}\psi^{\gamma} = \mathrm{n}^{\mathbf{G}}(\rho^{\mathrm{G}\gamma}\psi^{\gamma}) = \mathrm{n}^{\mathbf{G}}\psi^{\mathrm{G}\gamma} \quad \text{with} \quad \psi^{\mathrm{G}\gamma} = \rho^{\mathrm{G}\gamma}\psi^{\gamma}\,, \tag{5.38}$$

so that the components φ^{γ} are related to their solvent $\varphi^{\mathbf{G}}$. The material time derivative of the specific HELMHOLTZ energy is obtained with

$$\rho^{\gamma}(\psi^{\gamma})'_{\gamma} = \rho^{\gamma}\,(\frac{\psi^{\mathrm{G}\gamma}}{\rho^{\mathrm{G}\gamma}}\,)'_{\gamma} = \frac{\rho^{\gamma}}{\rho^{\mathrm{G}\gamma}}(\psi^{\mathrm{G}\gamma})'_{\gamma} - \frac{\rho^{\gamma}}{(\rho^{\mathrm{G}\gamma})^2}\psi^{\mathrm{G}\gamma}(\rho^{\mathrm{G}\gamma})'_{\gamma}\,, \tag{5.39}$$

which will be needed subsequently. For the thermodynamical consistent description of a multi-phase material the saturation condition has to be included as constraining condition. This restricts the mutual impact of the motion and deformation of the main phases. Hence, the material time derivative of (5.2) following the motion of the solid phase, together with the LAGRANGE multiplier λ will be added to (5.37) with

$$\lambda\,\{(\mathrm{n}^{\mathbf{S}})'_{\mathbf{S}} + (\mathrm{n}^{\mathbf{G}})'_{\mathbf{S}}\} = 0\,. \tag{5.40}$$

In a next step the included material time derivatives of the volume fractions are replaced by their associated mass and volume balances, respectively, and moreover, the multi-component description of $\varphi^{\mathbf{G}}$ is taken into account by using the molar concentration balance (5.19). To obtain an adequate expression for the change of the gas fractions, one starts by summing up the molar concentration balances with

$$\sum_{\gamma}\{(\mathrm{n}^{\mathbf{G}}\,\mathrm{c}_m^{\mathrm{G}\gamma})'_{\gamma} + \mathrm{n}^{\mathbf{G}}\,\mathrm{c}_m^{\mathrm{G}\gamma}\,\mathrm{div}\,\mathbf{x}'_{\gamma}\} = \mathrm{n}^{\mathbf{G}}\sum_{\gamma}\hat{\mathrm{c}}_m^{\mathrm{G}\gamma}\,. \tag{5.41}$$

Rearranging (5.41) according to App. B.3 yields the overall molar balance solved for $(\mathrm{n}^{\mathbf{G}})'_{\mathbf{S}}$ with

$$(\mathrm{n}^{\mathbf{G}})'_{\mathbf{S}} = -\frac{\mathrm{n}^{\mathbf{G}}}{\mathrm{c}_m^{\mathbf{G}}}\sum_{\gamma}(\mathrm{c}_m^{\mathrm{G}\gamma})'_{\gamma} - \mathrm{n}^{\mathbf{G}}\sum_{\gamma}x_m^{\mathrm{G}\gamma}\,\mathbf{D}_{\gamma}\cdot\mathbf{I} - \mathrm{grad}\,\mathrm{n}^{\mathbf{G}}\sum_{\gamma}x_m^{\mathrm{G}\gamma}\cdot\mathbf{w}_{\gamma\mathbf{S}} + \frac{\mathrm{n}^{\mathbf{G}}}{\mathrm{c}_m^{\mathbf{G}}}\sum_{\gamma}\hat{\mathrm{c}}_m^{\mathrm{G}\gamma}\,, \tag{5.42}$$

where use has been made of (3.57). By formulating the overall gas balance in molar units, one derives the dependency on the molar fraction $x_m^{\mathrm{G}\gamma}$, which is necessary in the further course of evaluation regarding partial pressures. The material time derivative

of the solid part is replaced by the volume balance (5.16) via

$$(\mathrm{n}^{\mathbf{S}})'_{\mathbf{S}} = -\mathrm{n}^{\mathbf{S}} \mathrm{div}\, \mathbf{x}'_{\mathbf{S}} = -\mathrm{n}^{\mathbf{S}}\, \mathbf{D_S} \cdot \mathbf{I}\,, \tag{5.43}$$

where again use has been made of (3.57). With (5.42) and (5.43), the LAGRANGE constraint (5.40) for evaluating the entropy inequality reads

$$\lambda \{\, \mathrm{n}^{\mathbf{S}}\, \mathbf{D_S} \,\cdot\, \mathbf{I} + \frac{\mathrm{n}^{\mathbf{G}}}{\mathrm{c}^{\mathbf{G}}_m} \sum_\gamma (\mathrm{c}^{\mathrm{G}\gamma}_m)'_\gamma + \mathrm{n}^{\mathbf{G}} \sum_\gamma x^{\mathrm{G}\gamma}_m\, \mathbf{D}_\gamma \,\cdot\, \mathbf{I} \\ + \operatorname{grad} \mathrm{n}^{\mathbf{G}} \sum_\gamma x^{\mathrm{G}\gamma}_m \cdot \mathbf{w}_{\gamma\mathbf{S}} - \frac{\mathrm{n}^{\mathbf{G}}}{\mathrm{c}^{\mathbf{G}}_m} \sum_\gamma \hat{\mathrm{c}}^{\mathrm{G}\gamma}_m \} = 0\,. \tag{5.44}$$

To comply with the mass formulation of (5.37), the molar parts of (5.44) are reformulated back to mass concentrations by extending both expressions with

$$1 = \frac{(\rho^\gamma)^2\, \mathrm{M}^\gamma_m}{(\rho^\gamma)^2\, \mathrm{M}^\gamma_m}\,,$$

cf. Graf [56]. They read afterwards:

$$\begin{aligned} \sum_\gamma \frac{\mathrm{n}^{\mathbf{G}}}{\mathrm{c}^{\mathbf{G}}_m} (\mathrm{c}^{\mathrm{G}\gamma}_m)'_\gamma &= \sum_\gamma \rho^\gamma \frac{x^{\mathrm{G}\gamma}_m}{(\rho^{\mathrm{G}\gamma})^2} (\rho^{\mathrm{G}\gamma})'_\gamma \\ \sum_\gamma \frac{\mathrm{n}^{\mathbf{G}}}{\mathrm{c}^{\mathbf{G}}_m} \hat{\mathrm{c}}^{\mathrm{G}\gamma}_m &= \sum_\gamma \hat{\rho}^\gamma \frac{x^{\mathrm{G}\gamma}_m}{\rho^{\mathrm{G}\gamma}}\,. \end{aligned} \tag{5.45}$$

Finally, (5.44) including (5.45) is added[3] to the basic entropy inequality (5.37), which yields after implementing as well (5.39) and rearranging

$$(\, \mathbf{T}^{\mathbf{S}} + \mathrm{n}^{\mathbf{S}} \lambda \mathbf{I}\,) \cdot \mathbf{D_S} - \rho^{\mathbf{S}} \{\, (\psi^{\mathbf{S}})'_{\mathbf{S}} + (\theta)'_{\mathbf{S}}\, \eta^{\mathbf{S}} \,\} + \sum_\gamma \{\, \mathbf{T}^\gamma + \mathrm{n}^{\mathbf{G}} x^{\mathrm{G}\gamma}_m \lambda\, \mathbf{I}\,\} \cdot \mathbf{D}_\gamma \\ - \sum_\gamma \rho^\gamma \{\, \frac{1}{\rho^{\mathrm{G}\gamma}} (\psi^{\mathrm{G}\gamma})'_\gamma + (\theta)'_\gamma\, \eta^\gamma \,\} + \sum_\gamma \{\, \frac{\rho^\gamma}{(\rho^{\mathrm{G}\gamma})^2} (\, x^{\mathrm{G}\gamma}_m \lambda + \psi^{\mathrm{G}\gamma}\,) \,\} (\rho^{\mathrm{G}\gamma})'_\gamma \\ - \sum_\gamma \{\, \hat{\mathbf{p}}^\gamma - \operatorname{grad} \mathrm{n}^{\mathbf{G}} x^{\mathrm{G}\gamma}_m \lambda \,\} \cdot \mathbf{w}_{\gamma\mathbf{S}} - \sum_\gamma \hat{\rho}^\gamma \{ \psi^\gamma + \frac{x^{\mathrm{G}\gamma}_m\, \lambda}{\rho^{\mathrm{G}\gamma}} \} - \frac{1}{\theta}\, \mathbf{q} \cdot \operatorname{grad} \theta \quad \geq 0\,. \tag{5.46}$$

[3] Adding the material time derivative of the saturation condition is possible, since it is equal to zero.

5.4.2. Evaluation of the entropy inequality

The entropy inequality (5.46) is evaluated following the procedure according to Coleman and Noll [28], see also Bowen [22, 19, 18]. This procedure presumes that the balance equations for the physical process are satisfied at all times, and only specified mechanical or other physical equations can be considered as a constraining condition (e.g. the rate of the saturation condition for multi-phase problems as given in this work). The more general, but hence more demanding procedure according to Liu [71] and Müller [81] prescribes to add all field equations multiplied by LAGRANGE multipliers to the inequality as constraints. Due to the amount of multipliers, a greater generality of the results arises, since more degrees of freedom are available in the evaluation. On the other hand, the introduced multipliers have to be determined. This is done on the basis of physically motivated assumptions and can be very time-consuming. Based on the experience gained, COLEMAN & NOLL procedure is chosen for this investigation.

The set of process variables $\mathcal{P}$ (5.36) was specified so, that it satisfies the needs to describe the material at hand adequately. With the choice of $\mathcal{P}$ the material change of the HELMHOLTZ free energy can be formulated. For that, a few more findings are taken into account. Following the argumentation of Bowen [18], the gradients of the describing variables in (5.36) only influence the dissipative terms, see also e.g. the derivation by Ghadiani [55]. Furthermore, the experience has shown, that the HELMHOLTZ free energy of the constituents and components, respectively, only depend on the variables brought into the process by the consitituent/component itself, so that

$$\psi^{\mathbf{S}} = \psi^{\mathbf{S}}\left(\mathbf{F}_{\mathbf{S}}, \theta\right) \quad \text{and} \quad \psi^{\gamma} = \psi^{\gamma}\left(\rho^{\gamma}, \theta, \mathbf{w}_{\gamma\mathbf{S}}, \mathbf{D}_{\gamma}\right). \tag{5.47}$$

Moreover, ψ^{γ} is chosen to be independent of $\mathbf{w}_{\gamma\mathbf{S}}$ and $\mathbf{D}_{\gamma}$ in advance, which can be followed e.g. in the derivation made by Ghadiani [55]. Moreover, keeping in mind the *principle of material frame-indifference*, $\mathbf{F}_{\mathbf{S}}$ will be replaced by the right CAUCHY-GREEN deformation tensor $\mathbf{C}_{\mathbf{S}}$, so that rigid body motions are excluded and $\psi^{\mathbf{S}}$ only depends on the stretch component $\mathbf{U}_{\mathbf{S}}$ via $\mathbf{C}_{\mathbf{S}} = \mathbf{U}_{\mathbf{S}}^2 = \mathbf{F}_{\mathbf{S}}^{\mathrm{T}}\,\mathbf{F}_{\mathbf{S}}$, cf. (3.49). Finally, the chosen dependencies are stated with

$$\psi^{\mathbf{S}} = \psi^{\mathbf{S}}\left(\mathbf{C}_{\mathbf{S}}, \theta\right) \quad \text{and} \quad \psi^{\gamma} = \psi^{\gamma}\left(\rho^{\gamma}, \theta\right). \tag{5.48}$$

Hence, the weighted material time derivatives of (5.46) can be calculated via

$$\begin{aligned} \rho^{\mathbf{S}}\,(\psi^{\mathbf{S}})'_{\mathbf{S}} &= 2\,\rho^{\mathbf{S}}\,\mathbf{F}_{\mathbf{S}}\frac{\partial\psi^{\mathbf{S}}}{\partial\mathbf{C}_{\mathbf{S}}}\mathbf{F}_{\mathbf{S}}^{\mathrm{T}}\cdot\mathbf{D}_{\mathbf{S}} + \rho^{\mathbf{S}}\,\frac{\partial\psi^{\mathbf{S}}}{\partial\theta}(\theta)'_{\mathbf{S}} \\ \frac{\rho^{\gamma}}{\rho^{\mathrm{G}\gamma}}\,(\psi^{\mathrm{G}\gamma})'_{\gamma} &= \frac{\rho^{\gamma}}{\rho^{\mathrm{G}\gamma}}\,\frac{\partial\psi^{\mathrm{G}\gamma}}{\partial\rho^{\mathrm{G}\gamma}}(\rho^{\mathrm{G}\gamma})'_{\gamma} + \frac{\rho^{\gamma}}{\rho^{\mathrm{G}\gamma}}\,\frac{\partial\psi^{\mathrm{G}\gamma}}{\partial\theta}\,(\theta)'_{\gamma}\,. \end{aligned} \tag{5.49}$$

Inserting these formulations into (5.46) finally yields the determining entropy inequality with

$$\begin{aligned} &\mathbf{D}_{\mathbf{S}}\cdot\{\,\mathbf{T}^{\mathbf{S}} + \mathrm{n}^{\mathbf{S}}\lambda\mathbf{I} - 2\,\rho^{\mathbf{S}}\mathbf{F}_{\mathbf{S}}\frac{\partial\psi^{\mathbf{S}}}{\partial\mathbf{C}_{\mathbf{S}}}\mathbf{F}_{\mathbf{S}}^{\mathrm{T}}\,\} + \sum_{\gamma}\mathbf{D}_{\gamma}\cdot\{\,\mathbf{T}^{\gamma} + \mathrm{n}^{\mathbf{G}}x_m^{\mathrm{G}\gamma}\lambda\,\mathbf{I}\,\} \\ &\qquad - (\theta)'_{\mathbf{S}}\,\{\rho^{\mathbf{S}}\,(\,\eta^{\mathbf{S}} + \frac{\partial\psi^{\mathbf{S}}}{\partial\theta}\,)\,\} - \sum_{\gamma}(\theta)'_{\gamma}\,\{\rho^{\gamma}\,(\,\eta^{\gamma} + \frac{1}{\rho^{\mathrm{G}\gamma}}\frac{\partial\psi^{\mathrm{G}\gamma}}{\partial\theta}\,)\,\} \\ &\qquad + \sum_{\gamma}(\rho^{\mathrm{G}\gamma})'_{\gamma}\,\{\,\frac{\rho^{\gamma}}{(\rho^{\mathrm{G}\gamma})^2}\,(x_m^{\mathrm{G}\gamma}\,\lambda + \psi^{\mathrm{G}\gamma} - \rho^{\mathrm{G}\gamma}\,\frac{\partial\psi^{\mathrm{G}\gamma}}{\partial\rho^{\mathrm{G}\gamma}}\,)\,\} \\ &- \sum_{\gamma}\mathbf{w}_{\gamma\mathbf{S}}\cdot\{\,\hat{\mathbf{p}}^{\gamma} - \operatorname{grad}\mathrm{n}^{\mathbf{G}}x_m^{\mathrm{G}\gamma}\lambda\,\} - \sum_{\gamma}\hat{\rho}^{\gamma}\,\{\,\psi^{\gamma} + \frac{x_m^{\mathrm{G}\gamma}\lambda}{\rho^{\mathrm{G}\gamma}}\,\} - \frac{1}{\theta}\,\mathbf{q}\cdot\operatorname{grad}\theta \quad \geq 0 \end{aligned} \tag{5.50}$$

This formulation of the inequality has to be fulfilled for any admissible thermodynamical process, cf. Coleman and Noll [28], in other words has to be valid for every applied boundary value problem. The argumentation for the evaluation of the entropy principle is based on the fact that in (5.50) both the process variables and their temporal or spatial derivatives occur. In the context of the thermodynamic process under consideration, the values of the process variables are fixed, but not the values of their temporal and spatial derivatives. The thermodynamic state within the process is completely determined by its process variables, but the process itself can be controlled externally in such a way that for certain values of the process variables their derivatives assume arbitrary values. It follows from this argumentation, that the terms connected with the derivatives of the process variables, in this case $\mathcal{P}' = \{\mathbf{D}_{\mathbf{S}},\, \mathbf{D}_{\gamma},\, (\theta)'_{\mathbf{S}},\, (\theta)'_{\gamma},\, (\rho^{\mathrm{G}\gamma})'_{\gamma}\,\}$, must become zero and thus, are the energy preserving parts.

Equilibrium part

Proceeding from this argumentation, the following relations are obtained from (5.50):

$$\mathbf{T}^{\mathbf{S}} + \mathrm{n}^{\mathbf{S}} \lambda \, \mathbf{I} = 2 \, \rho^{\mathbf{S}} \mathbf{F}_{\mathbf{S}} \frac{\partial \psi^{\mathbf{S}}}{\partial \mathbf{C}_{\mathbf{S}}} \mathbf{F}_{\mathbf{S}}^{\mathrm{T}} \tag{5.51}$$

$$\mathbf{T}^{\gamma} + \mathrm{n}^{\mathbf{G}} \, x_m^{\mathrm{G}\gamma} \, \lambda \, \mathbf{I} = 0 \tag{5.52}$$

$$x_m^{\mathrm{G}\gamma} \, \lambda = \rho^{\mathrm{G}\gamma} \frac{\partial \psi^{\mathrm{G}\gamma}}{\partial \rho^{\mathrm{G}\gamma}} - \psi^{\mathrm{G}\gamma} \tag{5.53}$$

$$\eta^{\mathbf{S}} = -\frac{\partial \psi^{\mathbf{S}}}{\partial \theta} \tag{5.54}$$

$$\eta^{\gamma} = -\frac{1}{\rho^{\mathrm{G}\gamma}} \frac{\partial \psi^{\mathrm{G}\gamma}}{\partial \theta} \, , \tag{5.55}$$

where it becomes clear, that the stresses and entropy are thermodynamic potentials, since they can be deduced from the derivative of the free energy to the defomations and temperature, respectively. The remaining dissipation inequality is given with

$$\mathcal{D} = -\sum_{\gamma} \mathbf{w}_{\gamma \mathbf{S}} \cdot \{ \, \hat{\mathbf{p}}^{\gamma} - \operatorname{grad} \mathrm{n}^{\mathbf{G}} x_m^{\mathrm{G}\gamma} \lambda \, \} - \sum_{\gamma} \hat{\rho}^{\gamma} \{ \, \psi^{\gamma} + \frac{x_m^{\mathrm{G}\gamma} \lambda}{\rho^{\mathrm{G}\gamma}} \, \} - \frac{1}{\theta} \, \mathbf{q} \cdot \operatorname{grad} \theta \geq 0 \, , \tag{5.56}$$

which will be evaluated afterwards. Looking at the thermodynamic potentials, some more assertions can be concluded. Analogously to the Helmholtz free energy of the components φ^{γ} (5.38), a mass- and volume-specific formulation can be found for the entropy (5.55) with

$$\eta^{\mathrm{G}\gamma} = \rho^{\mathrm{G}\gamma} \eta^{\gamma} \, , \tag{5.57}$$

where η^{γ} denotes the mass-specific and $\eta^{\mathrm{G}\gamma}$ the volume-specific definition leading to

$$\eta^{\mathrm{G}\gamma} = -\frac{\partial \psi^{\mathrm{G}\gamma}}{\partial \theta} \, . \tag{5.58}$$

Following the principle of effective stresses founded on Terzaghi [100], which states that the total stresses of the solid matrix $\mathbf{T}^{\mathbf{S}}$ are divided into a mechanical (effective)[4] part $\mathbf{T}_{\mathrm{E}}^{\mathbf{S}}$, and a part arising from the pore fluid pressure $\mathrm{p}^{\mathbf{FR}}$ acting on the solid

[4] Stresses, which are exclusively sustained by the solid grain matrix.

matrix, Eq. (5.51) can be analyzed with

$$\underbrace{\mathbf{T}^{\mathbf{S}} + \mathrm{n}^{\mathbf{S}} \lambda \mathbf{I}}_{= \mathbf{T}_{\mathrm{E}}^{\mathbf{S}}} = 2\rho^{\mathbf{S}} \mathbf{F}_{\mathbf{S}} \frac{\partial \psi^{\mathbf{S}}}{\partial \mathbf{C}_{\mathbf{S}}} \mathbf{F}_{\mathbf{S}}^{\mathrm{T}} , \tag{5.59}$$

leading to the expression for the effective stresses with

$$\mathbf{T}_{\mathrm{E}}^{\mathbf{S}} = 2\rho^{\mathbf{S}} \mathbf{F}_{\mathbf{S}} \frac{\partial \psi^{\mathbf{S}}}{\partial \mathbf{C}_{\mathbf{S}}} \mathbf{F}_{\mathbf{S}}^{\mathrm{T}} . \tag{5.60}$$

Furthermore, from (5.59) the LAGRANGE multiplier λ, connected with the rate of the saturation condition, can be identified as the overall pore pressure $\mathrm{p}^{\mathbf{F}\mathrm{R}}$, which makes sense considering the physical behavior. The pore pressure $\mathrm{p}^{\mathbf{F}\mathrm{R}}$ of a partially saturated medium is additively composed of the different pore fluid pressures from the liquid- and gas-filled pore space with

$$\mathrm{p}^{\mathbf{F}\mathrm{R}} = (1 - \mathrm{s}^{\mathbf{L}})\, \mathrm{p}^{\mathbf{G}\mathrm{R}} + \mathrm{s}^{\mathbf{L}}\, \mathrm{p}^{\mathbf{L}\mathrm{R}} , \tag{5.61}$$

cf. Ehlers [43], which is in accordance to DALTON's law [31]. However, since the liquid phase $\varphi^{\mathbf{L}}$ is assumed to be included into the solid phase $\varphi^{\mathbf{S}}$ for the purpose of this work, for the biphasic investigation

$$\lambda = \mathrm{p}^{\mathbf{F}\mathrm{R}} = \mathrm{p}^{\mathbf{G}\mathrm{R}} \tag{5.62}$$

is valid. Analyzing furthermore restriction (5.52), the gas pressure $\mathrm{p}^{\mathbf{G}\mathrm{R}}$ is given compliant with DALTON's law of partial pressures for ideal gases, cf. (2.45), that states, that the pore pressure is composed of the sum of partial pressures of mixture components. With the knowledge, that the ratio of partial pressures $\mathrm{p}^{\mathrm{G}\gamma}$ equals the ratio of the number of molecules, expressed by the molar fraction $x_m^{\mathrm{G}\gamma}$, DALTON's law for the gas mixture pressures can be found with

$$\mathrm{p}^{\mathrm{G}\gamma} = x_m^{\mathrm{G}\gamma}\, \mathrm{p}^{\mathbf{G}\mathrm{R}} \qquad \text{and} \qquad \sum_{\gamma} \mathrm{p}^{\mathrm{G}\gamma} = \mathrm{p}^{\mathbf{G}\mathrm{R}} . \tag{5.63}$$

With that, restriction (5.52) can be reformulated to

$$\mathbf{T}^{\gamma} = -\mathrm{n}^{\mathbf{G}}\, x_m^{\mathrm{G}\gamma}\, \mathrm{p}^{\mathbf{G}\mathrm{R}}\, \mathbf{I} , \tag{5.64}$$

and furthermore, cf. (5.25),

$$\mathbf{T}^{\mathbf{G}} = \sum_{\gamma} \mathbf{T}^{\gamma} = -\sum_{\gamma} \mathrm{n}^{\mathbf{G}}\, \mathrm{p}^{\mathrm{G}\gamma}\, \mathbf{I} = -\sum_{\gamma} \mathrm{p}^{\gamma}\, \mathbf{I} = -\mathrm{n}^{\mathbf{G}}\, \mathrm{p}^{\mathbf{G}\mathrm{R}}\, \mathbf{I}\,, \tag{5.65}$$

which satisfies the constraints for multi-phase and -component material description (3.80). Further explanations regarding the modeling approach of the gas phase will be given in Sect. 5.4.5.

Dissipative part

Taking into account the findings for the partial pressures (5.53), (5.62) and $(5.63)_1$, the dissipative part of the entropy inequality, cf. (5.56), is now reformulated to

$$\mathcal{D} := \underbrace{-\sum_{\gamma} \mathbf{w}_{\gamma\mathbf{S}} \cdot (\hat{\mathbf{p}}^{\gamma} - \operatorname{grad} \mathrm{n}^{\mathbf{G}} \mathrm{p}^{\mathrm{G}\gamma})}_{\mathcal{D}_{mom}} \underbrace{-\sum_{\gamma} \hat{\rho}^{\gamma}\, (\psi^{\gamma} + \frac{\mathrm{p}^{\mathrm{G}\gamma}}{\rho^{\mathrm{G}\gamma}})}_{\mathcal{D}_{chem}} \underbrace{-\frac{1}{\theta}\, \mathbf{q} \cdot \operatorname{grad} \theta}_{\mathcal{D}_{heat}} \geq 0\,. \tag{5.66}$$

Therein, three parts can be identified by their connection with the process variables $\mathbf{w}_{\gamma\mathbf{S}}$, $\hat{\rho}^{\gamma}$ and $\operatorname{grad}\theta$.[5]

The first term related to the seepage velocity $\mathbf{w}_{\gamma\mathbf{S}}$ describes the dissipative part $\mathcal{D}_{mom}$ resulting from momentum supply and thus reflects friction and damping between the phases. The second term connected with the rate of mass exchange $\hat{\rho}^{\gamma}$ reveals the dissipative part $\mathcal{D}_{chem}$ due to chemical conversion and lastly, the term connected with gradient of temperature governs the dissipation due to temperature change and heat conduction $\mathcal{D}_{heat}$. It is a sufficient demand that each part itself has to be equal or greater than zero, so that

$$\mathcal{D}_{mom} \overset{!}{\geq} 0\,, \quad \mathcal{D}_{chem} \overset{!}{\geq} 0\,, \quad \mathcal{D}_{heat} \overset{!}{\geq} 0 \tag{5.67}$$

is stated. The following relations ensure that (5.67) is satisfied:

$$\hat{\mathbf{p}}^{\gamma}_{\mathrm{E}} = -\delta_{\mathbf{w}_{\gamma\mathbf{S}}}\, \mathbf{w}_{\gamma\mathbf{S}}\,, \quad \mathbf{q} = -\alpha_{\nabla\theta} \operatorname{grad}\theta\,, \quad \hat{\rho}^{\gamma} = -\delta_{\mu^{\gamma}}\, \mu^{\gamma}\,. \tag{5.68}$$

[5]The variables $\hat{\rho}^{\gamma}$ and $\operatorname{grad}\theta$ are not considered as process variables in the direct formulation of (5.48), but still are process variables considering (5.35), wherein the density ρ^{γ} is as function of $\hat{\rho}^{\gamma}$.

Therein, use has been made of the following definitions for the extra interaction forces $\hat{\mathbf{p}}_{\mathrm{E}}^{\gamma}$ and the chemical potential μ^{γ}, see also (2.25) and (2.26)[6], with

$$\hat{\mathbf{p}}_{\mathrm{E}}^{\gamma} = \hat{\mathbf{p}}^{\gamma} - \operatorname{grad} \mathrm{n}^{\mathbf{G}} \mathrm{p}^{\mathrm{G}\gamma} \,, \quad \mu^{\gamma} = \psi^{\gamma} + \frac{\mathrm{p}^{\mathrm{G}\gamma}}{\rho^{\mathrm{G}\gamma}} \,. \tag{5.69}$$

Moreover, the material parameters are restricted to

$$\delta_{\mathbf{w}_{\gamma\mathbf{S}}} \geq 0 \,, \quad \alpha_{\nabla\theta} \geq 0 \,, \quad \delta_{\mu^{\gamma}} \geq 0 \,. \tag{5.70}$$

Taking a closer look on relation $(5.68)_1$ for the extra momentum supply $\hat{\mathbf{p}}_{\mathrm{E}}^{\gamma}$, a more detailed demand can be formulated. For that, the individual momentum balance for component φ^{γ} (5.25) will be utilized. The ansatz $(5.68)_1$ as well as stress relation (5.65) are implemented to the momentum balance resulting in

$$\operatorname{div}(-\mathrm{n}^{\mathbf{G}} \mathrm{p}^{\mathrm{G}\gamma} \mathbf{I}) - \rho^{\gamma} \mathbf{b} + \mathrm{p}^{\mathrm{G}\gamma} \operatorname{grad} \mathrm{n}^{\mathbf{G}} - \delta_{\mathbf{w}_{\gamma\mathbf{S}}} \mathbf{w}_{\gamma\mathbf{S}} = \mathbf{o} \,. \tag{5.71}$$

Moreover, evaluating the stress divergence term with calculation rule (A.2) and considering $\operatorname{div} \mathbf{I} = 0$ leads to

$$-\mathrm{n}^{\mathbf{G}} \operatorname{grad} \mathrm{p}^{\mathrm{G}\gamma} - \rho^{\gamma} \mathbf{b} - \delta_{\mathbf{w}_{\gamma\mathbf{S}}} \mathbf{w}_{\gamma\mathbf{S}} = \mathbf{o} \,, \tag{5.72}$$

so that a general constitutive approach for the difference velocity is given with

$$\delta_{\mathbf{w}_{\gamma\mathbf{S}}} \mathbf{w}_{\gamma\mathbf{S}} = -\mathrm{n}^{\mathbf{G}} \operatorname{grad} \mathrm{p}^{\mathrm{G}\gamma} - \rho^{\gamma} \mathbf{b} \,. \tag{5.73}$$

Equation (5.73) can be used to find Darcy's or Fick's law, respectively, as well as an combined advective-diffusive approach. Considering the problem at hand where the gas mixture constitutes the fluid, the gravity acceleration term $\rho^{\gamma} \mathbf{b}$ in (5.73) can be neglected and finally

$$\delta_{\mathbf{w}_{\gamma\mathbf{S}}} \mathbf{w}_{\gamma\mathbf{S}} = -\mathrm{n}^{\mathbf{G}} \operatorname{grad} \mathrm{p}^{\mathrm{G}\gamma} \tag{5.74}$$

is valid.

Finally, also the chemical dissipative part can be viewed more closely. For a three-component reactive mixture with φ^{γ} with $\gamma = \{1, ..., 4\}$, considering that the fourth

[6] More on the chemical potential in Sect. 5.4.5.

component is inert[7], the chemical dissipative part $\mathcal{D}_{chem}$ reads

$$\mathcal{D}_{chem} := -\hat{\rho}^1 \mu^1 - \hat{\rho}^2 \mu^2 - \hat{\rho}^3 \mu^3 \geq 0 \,. \tag{5.75}$$

Considering the constraint for mass exchange between the gas components (5.13), (5.75) can be rewritten as

$$\hat{\rho}^2 \left(\mu^1 - \mu^2\right) + \hat{\rho}^3 \left(\mu^1 - \mu^3\right) \geq 0 \tag{5.76}$$

In order to fulfill $\mathcal{D}_{chem}$, the following approach is finally postulated with

$$\hat{\rho}^2 = -\delta_{\mu^2}(\mu^1 - \mu^2) \quad \text{and} \quad \hat{\rho}^3 = -\delta_{\mu^3}(\mu^1 - \mu^3) \,. \tag{5.77}$$

5.4.3. Identification of material parameters

Mass flux ($\mathcal{D}_{mom}$)
The material parameter $\delta_{\mathbf{w}_{\gamma\mathbf{S}}}$ of (5.74) is identified in the context of the approach for velocity and mass transport. For that, restriction (5.73) is invoked and modified by multiplying the expression with the gas volume fraction $\mathrm{n}^{\mathbf{G}}$. Thus, a general formulation for the modified filter velocity referring to DARCY's law[8], cf. (4.6), is initially obtained with

$$\mathrm{n}^{\mathbf{G}} \, \mathbf{w}_{\gamma\mathbf{S}} = -\frac{(\mathrm{n}^{\mathbf{G}})^2}{\delta_{\mathbf{w}_{\gamma\mathbf{S}}}} \left\{ \operatorname{grad} \mathrm{p}^{\mathrm{G}\gamma} \right\} . \tag{5.78}$$

Additionally, the definition for the diffusive mass fluxes (3.73) is invoked which yields a reformulation for the total mass flux by a split into a diffusive and an advective part with

$$\rho^{\gamma} \, \mathbf{w}_{\gamma\mathbf{S}} = \mathbf{j}^{\gamma}_{diff} + \rho^{\gamma} \, \mathbf{w}_{\mathbf{GS}} \,. \tag{5.79}$$

Recalling the definition for the partial mass density ρ^{γ}, see Tab. (5.1), and introducing as well the partial diffusive flux with

$$\mathbf{j}^{\gamma}_{diff} = \mathrm{n}^{\mathbf{G}} \, \mathbf{j}^{\mathrm{G}\gamma}_{diff} \,, \tag{5.80}$$

[7] e.g. nitrogen as given in the application following later
[8] DARCY's law originally contains the gravitational term $\rho \, \mathbf{b}$.

(5.79) is reformulated and equated with (5.78) to

$$\mathrm{n}^{\mathbf{G}}\,\mathbf{w}_{\gamma\mathbf{S}} \;=\; \frac{1}{\rho^{\mathrm{G}\gamma}}\,\mathrm{n}^{\mathbf{G}}\mathbf{j}_{diff}^{\mathrm{G}\gamma} + \mathrm{n}^{\mathbf{G}}\,\mathbf{w}_{\mathbf{GS}} \;\overset{!}{=}\; -\frac{(\mathrm{n}^{\mathbf{G}})^2}{\delta_{\mathbf{w}_{\gamma\mathbf{S}}}}\,\{\mathrm{grad}\,\mathrm{p}^{\mathrm{G}\gamma}\}\,. \tag{5.81}$$

Thus, an additive relation needs to be chosen for the prefactor to consider the split of the total flow into diffusion and advection:

$$\frac{(\mathrm{n}^{\mathbf{G}})^2}{\delta_{\mathbf{w}_{\gamma\mathbf{S}}}} \overset{!}{=} \{\mathrm{d}_0^{\gamma} + \mathrm{k}_0^{\gamma}\}\,. \tag{5.82}$$

Therein, d_0^{γ} and k_0^{γ} are introduced as general diffusion and advective variables, and (5.78) is replaced after inserting (5.82) by

$$\mathrm{n}^{\mathbf{G}}\,\mathbf{w}_{\gamma\mathbf{S}} = -\mathrm{d}_0^{\gamma}\,\mathrm{grad}\,\mathrm{p}^{\mathrm{G}\gamma} - \mathrm{k}_0^{\gamma}\,\mathrm{grad}\,\mathrm{p}^{\mathrm{G}\gamma}\,. \tag{5.83}$$

With the following chosen approaches

$$\mathrm{d}_0^{\gamma} = (\frac{\mathrm{n}^{\mathbf{G}}}{\rho^{\mathrm{G}\gamma}})\frac{D_{\mathrm{G}\gamma}}{\mathrm{R}^{\gamma}\theta} \quad \text{and} \quad \mathrm{k}_0^{\gamma} = \frac{1}{x_m^{\mathrm{G}\gamma}}\,\frac{\mathrm{K}^{\mathbf{S}}}{\eta^{\mathbf{G}\mathrm{R}}} = \frac{1}{x_m^{\mathrm{G}\gamma}}\,\mathrm{k}_0^{\boldsymbol{\beta}}\,. \tag{5.84}$$

the total filter velocity for component φ^{γ} can be split into the diffusive part according to Fick's law, cf. (4.5), as well as the advective part according to Darcy's law, cf. (4.6). Therein, $D_{\mathrm{G}\gamma}$ is the diffusion coefficient of component φ^{γ} in mixture $\varphi^{\mathbf{G}}$ according to (4.3), and R^{γ} denotes the specific gas constant for component φ^{γ}. Implementing (5.84) into (5.83) leads to

$$\mathrm{n}^{\mathbf{G}}\,\mathbf{w}_{\gamma\mathbf{S}} = -\frac{\mathrm{n}^{\mathbf{G}}}{\rho^{\mathrm{G}\gamma}}\,D_{\mathrm{G}\gamma}\,\mathrm{grad}\,\rho^{\mathrm{G}\gamma} - \frac{\mathrm{K}^{\mathbf{S}}}{\eta^{\mathbf{G}\mathrm{R}}}\,\mathrm{grad}\,\mathrm{p}^{\mathbf{G}\mathrm{R}}\,. \tag{5.85}$$

where Dalton's law of partial pressure, cf. (2.42) and (2.46), applied to the problem at hand with

$$\mathrm{p}^{\mathrm{G}\gamma} = \rho^{\mathrm{G}\gamma}\mathrm{R}^{\gamma}\theta \quad \text{and} \quad \mathrm{p}^{\mathrm{G}\gamma} = x_m^{\mathrm{G}\gamma}\,\mathrm{p}^{\mathbf{G}\mathrm{R}}\,, \tag{5.86}$$

is considered. To derive a mass flux formulation, (5.85) needs to be multiplied with the density $\rho^{\mathrm{G}\gamma}$, so that the total mass flux formulation reads

$$\begin{aligned} \mathbf{j}_{tot}^{\gamma} \;&=\; \mathrm{n}^{\mathbf{G}}\,\mathbf{j}_{tot}^{\mathrm{G}\gamma} \;&=\;& \mathrm{n}^{\mathbf{G}}\,\mathbf{j}_{diff}^{\mathrm{G}\gamma} &+\; \rho^{\mathrm{G}\gamma}\,\mathrm{n}^{\mathbf{G}}\,\mathbf{w}_{\mathbf{GS}} \\ &=\; \mathrm{n}^{\mathbf{G}}\rho^{\mathrm{G}\gamma}\mathbf{w}_{\gamma\mathbf{S}} \;&=\; -\;& \mathrm{n}^{\mathbf{G}}D_{\mathrm{G}\gamma}\,\mathrm{grad}\,\rho^{\mathrm{G}\gamma} &-\; \rho^{\mathrm{G}\gamma}\,\frac{\mathrm{K}^{\mathbf{S}}}{\eta^{\mathbf{G}\mathrm{R}}}\,\mathrm{grad}\,\mathrm{p}^{\mathbf{G}\mathrm{R}}\,. \end{aligned} \tag{5.87}$$

Moreover, by summing up (5.87), the total mass flux of the overall gas phase $\varphi^{\mathbf{G}}$ is obtained with

$$\begin{aligned}\sum_{\gamma} \mathrm{n}^{\mathbf{G}} \rho^{\mathrm{G}\gamma} \mathbf{w}_{\gamma\mathbf{S}} &= \mathrm{n}^{\mathbf{G}} \sum_{\gamma} \rho^{\mathrm{G}\gamma} \left(\mathbf{x}'_{\gamma} - \mathbf{x}'_{\mathbf{S}}\right) \\ &= \rho^{\mathbf{G}\mathrm{R}} \, \mathrm{n}^{\mathbf{G}} \sum_{\gamma} \omega^{\mathrm{G}\gamma} (\mathbf{x}'_{\gamma} - \mathbf{x}'_{\mathbf{S}}) \\ &= \rho^{\mathbf{G}\mathrm{R}} \, \mathrm{n}^{\mathbf{G}} \mathbf{w}_{\mathbf{GS}} \,,\end{aligned} \tag{5.88}$$

where the definition for the mass average velocity $(5.8)_1$ has been invoked. Taking a closer look on $(5.88)_3$ illustrates, that the prevailing transport process for the main phase is driven by Darcy flow, whereas the diffusive fluxes balance each other.

Likewise, formulations in molar units can be derived by choosing ${}_m\mathrm{d}_0^{\gamma}$ with

$${}_m\mathrm{d}_0^{\gamma} = \frac{\mathrm{n}^{\mathbf{G}} \, {}_mD_{\mathrm{G}\gamma}}{\mathrm{c}_m^{\mathrm{G}\gamma} \, \mathrm{R}_m \, \theta} \,, \tag{5.89}$$

so that the equivalent molar flux for component φ^{γ} reads

$$\begin{aligned}{}_m\mathbf{j}_{tot}^{\gamma} &= \mathrm{n}^{\mathbf{G}} \, {}_m\mathbf{j}_{tot}^{\mathrm{G}\gamma} &&= && \mathrm{n}^{\mathbf{G}} \, {}_m\mathbf{j}_{diff}^{\mathrm{G}\gamma} && + \; \mathrm{c}_m^{\mathrm{G}\gamma} \, \mathrm{n}^{\mathbf{G}} \, {}_m\mathbf{w}_{\mathbf{GS}} \\ &= \mathrm{n}^{\mathbf{G}} \mathrm{c}_m^{\mathrm{G}\gamma} \mathbf{w}_{\gamma\mathbf{S}} &&= - && \mathrm{n}_m^{\mathbf{G}} D_{\mathrm{G}\gamma} \, \mathrm{grad} \, \mathrm{c}_m^{\mathrm{G}\gamma} && - \; \mathrm{c}_m^{\mathrm{G}\gamma} \frac{\mathrm{K}^{\mathbf{S}}}{\eta^{\mathbf{G}\mathrm{R}}} \, \mathrm{grad} \, \mathrm{p}^{\mathbf{G}\mathrm{R}} \,.\end{aligned} \tag{5.90}$$

and the overall molar flux of the mixture $\varphi^{\mathbf{G}}$ is obtained with

$$\begin{aligned}\sum_{\gamma} \mathrm{c}_m^{\mathrm{G}\gamma} \, \mathrm{n}^{\mathbf{G}} \, \mathbf{w}_{\gamma\mathbf{S}} &= \mathrm{n}^{\mathbf{G}} \sum_{\gamma} \mathrm{c}_m^{\mathrm{G}\gamma} \left(\mathbf{x}'_{\gamma} - \mathbf{x}'_{\mathbf{S}}\right) \\ &= \mathrm{c}_m^{\mathbf{G}} \, \mathrm{n}^{\mathbf{G}} \sum_{\gamma} x_m^{\mathrm{G}\gamma} \left(\mathbf{x}'_{\gamma} - \mathbf{x}'_{\mathbf{S}}\right) \\ &= \mathrm{c}_m^{\mathbf{G}} \, \mathrm{n}^{\mathbf{G}} \, {}_m\mathbf{w}_{\mathbf{GS}} \,.\end{aligned} \tag{5.91}$$

Which formulation is used depends on the choice whether the concentration balance is invoked in mass or molar units.

Heat conduction ($\mathcal{D}_{heat}$)
The restriction for the heat flux vector $\mathbf{q}$ gained from the dissipation mechanism (5.66) and (5.68), respectively, can directly be identified as Fourier's law [53], which describes the heat conduction negative proportional to the temperature gradient with

$$\mathbf{q} = -\alpha_{\nabla\theta} \, \mathrm{grad} \, \theta \tag{5.92}$$

Thus, the material parameter $\alpha_{\nabla\theta}$ is determined as the heat conduction coefficient for the mixture.

Conversion ($\mathcal{D}_{chem}$)
As introduced in Sect. 2.5, the chemical potential characterizes, amongst others, the potential to react with other substances. Revealing relation (2.30) concerning chemical equilibrium for reactions, the material parameters δ_{μ^2} and δ_{μ^3} can be identified as the stoichiometric coefficients of the reactants. With that, (5.77) is transferred to

$$\hat{\rho}^2 = -v^2(\mu^1 - \mu^2) \quad \text{and} \quad \hat{\rho}^3 = -v^3(\mu^1 - \mu^3)\,. \tag{5.93}$$

5.4.4. Approach for Helmholtz free energy of solid matrix

The solid matrix is modeled assuming finite hyperelasticity. The elasticity for a homogeneous material is expressed with $\mathbf{P}^{\mathbf{S}} = \mathbf{P}^{\mathbf{S}}(\mathbf{F}_{\mathbf{S}})$, cf. e.g. Bonet and R. D. [16], indicating that the stress measure is only a function of the current deformation state. More specific, a conservative hyperelastic material formulation is chosen, so that the work done by the stresses during the deformation process is independent of its path.

The hyperelastic potential $\Psi^{\mathbf{S}}$, also denoted as strain energy is postulated with the mass-specific Helmholtz free energy $\psi^{\mathbf{S}}$ multiplied by the solid partial density in the reference configuration with

$$\Psi^{\mathbf{S}}(\mathbf{F}_{\mathbf{S}}) = \rho^{\mathbf{S}}_{0\mathbf{S}}\, \psi^{\mathbf{S}}(\mathbf{F}_{\mathbf{S}})\,. \tag{5.94}$$

Recalling the principles for material modeling, see Sect. 5.4, the strain energy density must remain invariant for a rigid body rotation of the current configuration and observer independent, so that

$$\Psi^{\mathbf{S}}(\mathbf{F}_{\mathbf{S}}) = \Psi^{\mathbf{S}}(\mathbf{B}_{\mathbf{S}}) = \Psi^{\mathbf{S}}(\mathbf{C}_{\mathbf{S}}) \tag{5.95}$$

is valid, cf. (5.48). An extensive description of finite hyperelasticity can e.g. be found in Holzapfel [65]. The strain energy function of isotropic materials can also be represented as a function of the invariants of the right and left Cauchy-Green

deformation tensor, respectively, since both tensors have the same principle invariants given as

$$\begin{aligned} I &= \mathbf{B_S} \cdot \mathbf{I} &&= \mathbf{C_S} \cdot \mathbf{I} \\ II &= \tfrac{1}{2}\,(I^2 - \mathbf{B_S}\,\mathbf{B_S} \cdot \mathbf{I}) &&= \tfrac{1}{2}\,(I^2 - \mathbf{C_S}\,\mathbf{C_S} \cdot \mathbf{I}) \\ III &= \det \mathbf{B_S} &&= \det \mathbf{C_S} \end{aligned} \tag{5.96}$$

For this work, the general approach of a Neo-Hookean energy function in terms of the invariants is chosen, based on Simo and Pister [94], which covers the elastic response for finite deformations of the solid matrix. The function is enhanced by a thermal part, cf. Bluhm [13] and references therein, and reads

$$\begin{aligned} \Psi^{\mathbf{S}} = &\frac{1}{2}\,\lambda^{\mathbf{S}}\,(\ln \mathrm{J_S})^2 - \mu^{\mathbf{S}} \ln \mathrm{J_S} + \frac{1}{2}\,\mu^{\mathbf{S}}\,(I-3) \\ &- 3\,\alpha^{\mathbf{S}}\,\mathrm{k}^{\mathbf{S}}\,(\ln \mathrm{J_S})\,(\theta - \theta_0) - \rho^{\mathbf{S}}_{0\mathbf{S}}\,\mathrm{c}^{\mathbf{S}}_{\mathrm{V}}\,(\theta \ln(\frac{\theta}{\theta_0}) - \theta + \theta_0)\,. \end{aligned} \tag{5.97}$$

Therein, $\lambda^{\mathbf{S}}$ and $\mu^{\mathbf{S}}$ denote the macroscopic Lamé constants of the solid, $\mathrm{k}^{\mathbf{S}} = \lambda^{\mathbf{S}} + \frac{2}{3}\,\mu^{\mathbf{S}}$ the bulk modulus, $\alpha^{\mathbf{S}}$ the thermal expansion coefficient, and $\mathrm{c}^{\mathbf{S}}_{\mathrm{V}}$ the specific heat capacity of the solid matrix, cf. (2.50).

5.4.5. Approach for Helmholtz free energy for gas components

The gas phase $\varphi^{\mathbf{G}}$ as well as its components φ^{γ} will be modeled as an ideal mixture of perfect gases, which fits the assumption according to Bowen [22]. Thus, Dalton's law (2.45) and the approach for the chemical potential are considered, cf. also Sect. 2.6.3.

For that, the potential of the main gas phase $\Psi^{\mathbf{G}}$ is introduced by summing up the Helmholtz free energies of its components (5.38) with

$$\Psi^{\mathbf{G}} = \rho^{\mathbf{G}\mathrm{R}}\,\psi^{\mathbf{G}} = \sum_{\gamma} \rho^{\mathrm{G}\gamma}\psi^{\gamma} = \sum_{\gamma} \psi^{\mathrm{G}\gamma} \tag{5.98}$$

Recalling restriction (5.53) as well as (5.62) and (5.63), the partial pressure $\mathrm{p}^{\mathrm{G}\gamma}$ is given with

$$\mathrm{p}^{\mathrm{G}\gamma} = \rho^{\mathrm{G}\gamma}\frac{\partial \psi^{\mathrm{G}\gamma}}{\partial \rho^{\mathrm{G}\gamma}} - \psi^{\mathrm{G}\gamma}\,, \tag{5.99}$$

which coincides with the derivations according to Bowen [22]. Therein, the components' mass-specific chemical potential μ^γ is identified as the partial derivative of its volume-specific HELMHOLTZ free energy with respect to its true density:

$$\mu^\gamma = \frac{\partial \psi^{\mathrm{G}\gamma}}{\partial \rho^{\mathrm{G}\gamma}} \,. \tag{5.100}$$

With (5.100) and (5.38), the relation for the partial pressure reads

$$\mathrm{p}^{\mathrm{G}\gamma} = \rho^{\mathrm{G}\gamma} \mu^\gamma - \psi^{\mathrm{G}\gamma} = \mu^{\mathrm{G}\gamma} - \psi^{\mathrm{G}\gamma} \,, \tag{5.101}$$

see also (5.69). Considering the postulated dependencies (5.48) with $\psi^\gamma = \psi^\gamma\,(\rho^\gamma,\, \theta)$, and taking into account the approach of the chemical potential for ideal gases, see Sect. 2.6.3, the mass-specific HELMHOLTZ free energy for the mixture components is finally postulated with

$$\psi^\gamma = \mu_0^\gamma + \mathrm{R}^\gamma\, \theta \left\{ \ln \left(\frac{\rho^{\mathrm{G}\gamma}}{\rho_0^{\mathrm{G}\gamma}} \right) - 1 \right\} - \mathrm{c}_{\mathrm{V}}^\gamma \left\{ \theta \ln \left(\frac{\theta}{\theta_0} \right) - \theta + \theta_0 \right\} . \tag{5.102}$$

A more detailed derivation of the free energy for the gas components is given in App. B.5.

5.4.6. Evaluation of thermodynamic potentials

The introduced HELMHOLTZ free energies provide the basis to evaluate the thermodynamic potentials gained from the evaluation of the entropy inequality given in Sect. 5.4.2.

The solid strain energy (5.97) combined with (5.94) is implemented into (5.60), and thus the non-linear thermo-elastic solid extra stresses read

$$\mathbf{T}_{\mathrm{E}}^{\mathbf{S}} = \frac{1}{\mathrm{J}_{\mathbf{S}}} \left\{ 2\, \mu^{\mathbf{S}}\, \mathbf{K}_{\mathbf{S}} + \lambda^{\mathbf{S}}\, (\ln \mathrm{J}_{\mathbf{S}})\, \mathbf{I} - 3\, \alpha^{\mathbf{S}}\, \mathrm{k}^{\mathbf{S}}\, (\theta - \theta_0)\, \mathbf{I} \right\} . \tag{5.103}$$

Therein, $\mathbf{K}_{\mathbf{S}}$ denotes the KARNI-REINER strain tensor referred to the actual placement of $\varphi^{\mathbf{S}}$, cf. $(3.52)_2$. Moreover, use has been made of the relation $\mathrm{J}_{\mathbf{S}} = \rho_{0\mathbf{S}}^{\mathbf{S}} / \rho^{\mathbf{S}}$, see also App. B.1.

The stresses of the overall gas phase are obtained by evaluating the gas pressure (5.65) together with (5.63). The partial pressure can be obtained by implementing the approach (5.102) in combination with (5.38) into (5.53), which leads to

$$\mathrm{p}^{\mathrm{G}\gamma} = \rho^{\mathrm{G}\gamma}\,\mathrm{R}^{\gamma}\,\theta\,. \tag{5.104}$$

where R^{γ} denotes the specific gas constant for gas component φ^{γ}. Implementing (3.28) yields the equivalent molar formulation with

$$\mathrm{p}^{\mathrm{G}\gamma} = \mathrm{c}_m^{\mathrm{G}\gamma}\,\mathrm{R}_m\,\theta\,. \tag{5.105}$$

By summing up the partial pressures according to $(5.63)_2$, the ideal gas law is obtained with

$$\sum_{\gamma}\rho^{\mathrm{G}\gamma}\,\mathrm{R}^{\gamma}\,\theta = \sum_{\gamma}\rho^{\mathrm{G}\gamma}\frac{\mathrm{R}}{\mathrm{M}_m^{\gamma}}\theta = \sum_{\gamma}\frac{\rho^{\mathrm{G}\gamma}}{\mathrm{M}_m^{\gamma}}\mathrm{R}\theta = \mathrm{R}\theta\underbrace{\sum_{\gamma}\mathrm{c}_m^{\mathrm{G}\gamma}}_{\mathrm{c}_m^{\mathbf{G}\mathrm{R}}}\,, \tag{5.106}$$

where R denotes the universal gas constant.

Finally, the specific entropy functions of the solid phase and the gas components are evaluated by invoking (5.54) and (5.55) as well as (5.97) and (5.102), leading to

$$\eta^{\mathbf{S}} = \frac{1}{\rho_{0\mathbf{S}}^{\mathbf{S}}}\,3\,\alpha^{\mathbf{S}}\,\mathrm{k}^{\mathbf{S}}\,(\ln\mathrm{J}_{\mathbf{S}}) + \mathrm{c}_{\mathrm{V}}^{\mathbf{S}}\,\{\ln(\frac{\theta}{\theta_0}) + 1\} - 1 \tag{5.107}$$

and

$$\eta^{\gamma} = -\mathrm{R}^{\gamma}\,\{\,\ln(\frac{\rho^{\mathrm{G}\gamma}}{\rho_0^{\mathrm{G}\gamma}}) - 1\,\} + \mathrm{c}_{\mathrm{V}}^{\gamma}\,\{\ln\,(\frac{\theta}{\theta_0}) + 1\} - 1\,. \tag{5.108}$$

5.4.7. Evaluation of mixture balance of energy

With the knowledge of the constitutive derivations, the mixture energy balance (5.30) can be rearranged in a simplified form. At first, the stress-strain rates are reformulated with (5.51), (5.60) and (5.52) to

$$-\mathbf{T}^{\mathbf{S}}\cdot\mathbf{D}_{\mathbf{S}} - \sum_{\gamma}\mathbf{T}^{\gamma}\cdot\mathbf{D}_{\gamma} = -\mathbf{T}_{\mathrm{E}}^{\mathbf{S}}\cdot\mathbf{D}_{\mathbf{S}} + \lambda\,\mathrm{n}^{\mathbf{S}}\,\mathbf{D}_{\mathbf{S}}\cdot\mathbf{I} + \lambda\sum_{\gamma}x_m^{\mathrm{G}\gamma}\,\mathrm{n}^{\mathbf{G}}\,\mathbf{D}_{\gamma}\cdot\mathbf{I}\,, \tag{5.109}$$

the mass balances (5.43) and (5.42) are implemented with

$$\mathrm{n}^{\mathbf{S}}\,\mathbf{D}_{\mathbf{S}}\cdot\mathbf{I}=-(\mathrm{n}^{\mathbf{S}})'_{\mathbf{S}}$$

$$\sum_{\gamma}x_m^{\mathrm{G}\gamma}\,\mathrm{n}^{\mathbf{G}}\,\mathbf{D}_{\gamma}\cdot\mathbf{I}=-(\mathrm{n}^{\mathbf{G}})'_{\mathbf{S}}-\frac{\mathrm{n}^{\mathbf{G}}}{\mathrm{c}_m^{\mathbf{G}}}\sum_{\gamma}(\mathrm{c}_m^{\mathrm{G}\gamma})'_{\gamma}-\operatorname{grad}\mathrm{n}^{\mathbf{G}}\sum_{\gamma}x_m^{\mathrm{G}\gamma}\cdot\mathbf{w}_{\gamma\mathbf{S}}+\frac{\mathrm{n}^{\mathbf{G}}}{\mathrm{c}_m^{\mathbf{G}}}\sum_{\gamma}\hat{\mathrm{c}}_m^{\mathrm{G}\gamma}\,, \tag{5.110}$$

so that (5.109) finally can be obtained with

$$-\mathbf{T}^{\mathbf{S}}\cdot\mathbf{D}_{\mathbf{S}}-\sum_{\gamma}\mathbf{T}^{\gamma}\cdot\mathbf{D}_{\gamma}=$$

$$-\mathbf{T}^{\mathbf{S}}_{\mathrm{E}}\cdot\mathbf{D}_{\mathbf{S}}+\lambda\,(-\frac{\mathrm{n}^{\mathbf{G}}}{\mathrm{c}_m^{\mathbf{G}}}\sum_{\gamma}(\mathrm{c}_m^{\mathrm{G}\gamma})'_{\gamma}-\operatorname{grad}\mathrm{n}^{\mathbf{G}}\sum_{\gamma}x_m^{\mathrm{G}\gamma}\cdot\mathbf{w}_{\gamma\mathbf{S}}+\frac{\mathrm{n}^{\mathbf{G}}}{\mathrm{c}_m^{\mathbf{G}}}\sum_{\gamma}\hat{\mathrm{c}}_m^{\mathrm{G}\gamma}\,)\,, \tag{5.111}$$

where additionally (5.40) has been considered.

Recalling the partial pressure formulation with (5.62) and $(5.63)_1$, as well as the definition for the direct momentum production $(5.69)_1$, the mixture balance of energy (5.30) reads after inserting (5.111)

$$\rho^{\mathbf{S}}\{(\psi^{\mathbf{S}})'_{\mathbf{S}}+(\theta)'_{\mathbf{S}}\,\eta^{\mathbf{S}}+\theta\,(\eta^{\mathbf{S}})'_{\mathbf{S}}\}+\sum_{\gamma}\rho^{\gamma}\{(\psi^{\gamma})'_{\gamma}+(\theta)'_{\gamma}\,\eta^{\gamma}+\theta\,(\eta^{\gamma})'_{\gamma}\}-\mathbf{T}^{\mathbf{S}}_{\mathrm{E}}\cdot\mathbf{D}_{\mathbf{S}}-$$

$$\mathrm{p}^{\mathbf{G}\mathrm{R}}\frac{\mathrm{n}^{\mathbf{G}}}{\mathrm{c}_m^{\mathbf{G}}}\sum_{\gamma}(\mathrm{c}_m^{\mathrm{G}\gamma})'_{\gamma}+\mathrm{p}^{\mathbf{G}\mathrm{R}}\frac{\mathrm{n}^{\mathbf{G}}}{\mathrm{c}_m^{\mathbf{G}}}\sum_{\gamma}\hat{\mathrm{c}}_m^{\mathrm{G}\gamma}+\operatorname{div}\mathbf{q}+\sum_{\gamma}\hat{\mathbf{p}}^{\gamma}_{\mathrm{E}}\cdot\mathbf{w}_{\gamma\mathbf{S}}+\sum_{\gamma}\hat{\rho}^{\gamma}\,(\psi^{\gamma}+\theta\eta^{\gamma})=0 \tag{5.112}$$

Moreover, the terms related to the gas pressure $\mathrm{p}^{\mathbf{G}\mathrm{R}}$ can be replaced by (5.45), hence, (5.112) reads

$$\rho^{\mathbf{S}}\{(\psi^{\mathbf{S}})'_{\mathbf{S}}+(\theta)'_{\mathbf{S}}\,\eta^{\mathbf{S}}+\theta\,(\eta^{\mathbf{S}})'_{\mathbf{S}}\}+\sum_{\gamma}\rho^{\gamma}\{(\psi^{\gamma})'_{\mathrm{G}\gamma}+(\theta)'_{\mathrm{G}\gamma}\,\eta^{\gamma}+\theta(\eta^{\gamma})'_{\mathrm{G}\gamma}\}-\mathbf{T}^{\mathbf{S}}_{\mathrm{E}}\cdot\mathbf{D}_{\mathbf{S}}-$$

$$\sum_{\gamma}\mathrm{p}^{\mathrm{G}\gamma}\frac{\rho^{\gamma}}{(\rho^{\mathrm{G}\gamma})^2}(\rho^{\mathrm{G}\gamma})'_{\gamma}+\operatorname{div}\mathbf{q}+\sum_{\gamma}\hat{\mathbf{p}}^{\gamma}_{\mathrm{E}}\cdot\mathbf{w}_{\gamma\mathbf{S}}+\sum_{\gamma}\hat{\rho}^{\gamma}\,(\psi^{\gamma}+\theta\eta^{\gamma}+\frac{\mathrm{p}^{\mathrm{G}\gamma}}{\rho^{\mathrm{G}\gamma}})=0\,. \tag{5.113}$$

Taking a closer look on the material time derivative of the solid Helmholtz energy

with $(5.49)_1$ and (5.60), the derivative can be written as follows:

$$\rho^{\mathbf{S}}\,(\psi^{\mathbf{S}})'_{\mathbf{S}} = \mathbf{T}^{\mathbf{S}}_{\mathrm{E}} \cdot \mathbf{D}_{\mathbf{S}} + \rho^{\mathbf{S}}\,\frac{\partial \psi^{\mathbf{S}}}{\partial \theta}\,(\theta)'_{\mathbf{S}}\,. \tag{5.114}$$

Considering furthermore the entropy restriction (5.54), the following relation can be found

$$\rho^{\mathbf{S}}\{(\psi^{\mathbf{S}})'_{\mathbf{S}} + (\theta)'_{\mathbf{S}}\,\eta^{\mathbf{S}}\} = \mathbf{T}^{\mathbf{S}}_{\mathrm{E}} \cdot \mathbf{D}_{\mathbf{S}}\,, \tag{5.115}$$

which cancels with the power of the extra solid stresses in (5.112). Likewise, the terms regarding the gas components can be simplified. According to (5.53) the partial pressure related to the components' density change can be replaced by

$$\sum_{\gamma} \mathrm{p}^{\mathrm{G}\gamma}\frac{\rho^{\gamma}}{(\rho^{\mathrm{G}\gamma})^2}(\rho^{\mathrm{G}\gamma})'_{\gamma} = \sum_{\gamma}(\frac{\rho^{\gamma}}{\rho^{\mathrm{G}\gamma}}\frac{\partial \psi^{\mathrm{G}\gamma}}{\partial \rho^{\mathrm{G}\gamma}} - \frac{\rho^{\gamma}}{(\rho^{\mathrm{G}\gamma})^2}\psi^{\mathrm{G}\gamma})(\rho^{\mathrm{G}\gamma})'_{\gamma}\,. \tag{5.116}$$

With the material time derivative of the gas components' HELMHOLTZ energy $(5.49)_2$ as well as the entropy relation (5.55), the equality

$$\sum_{\gamma} \rho^{\gamma}\{(\psi^{\gamma})'_{\gamma} + (\theta)'_{\gamma}\,\eta^{\gamma}\} = \sum_{\gamma} \mathrm{p}^{\mathrm{G}\gamma}\frac{\rho^{\gamma}}{(\rho^{\mathrm{G}\gamma})^2}(\rho^{\mathrm{G}\gamma})'_{\gamma} \tag{5.117}$$

in (5.112) can be found, which can also be shortened.

Taking a closer look to the mass production term, the specific GIBBS energy, defined as chemical potential μ^{γ}, cf. (2.26) or (5.100), can be identified with

$$\mu^{\gamma} = \psi^{\gamma} + \frac{\mathrm{p}^{\mathrm{G}\gamma}}{\rho^{\mathrm{G}\gamma}}\,. \tag{5.118}$$

Additionally, the specific enthalpy is defined with $h^{\gamma} = \mu^{\gamma} + \theta\,\eta^{\gamma}$, cf. (2.8), so that the mass production term reads

$$\sum_{\gamma} \hat{\rho}^{\gamma}(\mu^{\gamma} + \theta\eta^{\gamma}) = \sum_{\gamma} \hat{\rho}^{\gamma}(h^{\gamma})\,, \tag{5.119}$$

which illustrates the correlation to the heat of reaction (2.34) via (5.77) and (5.93). Finally, the energy balance of the mixture can be obtained in the general form

$$\theta\,\{\rho^{\mathbf{S}}(\eta^{\mathbf{S}})'_{\mathbf{S}} + \sum_{\gamma} \rho^{\gamma}(\eta^{\gamma})'_{\gamma}\} + \operatorname{div}\mathbf{q} = -\sum_{\gamma} \hat{\mathbf{p}}^{\gamma}_{\mathrm{E}} \cdot \mathbf{w}_{\gamma\mathbf{S}} - \sum_{\gamma} \hat{\rho}^{\gamma} h^{\gamma}\,, \tag{5.120}$$

The material time derivatives of the specific entropies $(\eta^{\mathbf{S}})'_{\mathbf{S}}$ and $(\eta^{\gamma})'_{\gamma}$ can then be evaluated by implementing the postulations for the HELMHOLTZ energies. For that, the material time derivatives with respect to the dependencies (5.48) are invoked with

$$\begin{aligned}(\eta^{\mathbf{S}})'_{\mathbf{S}} &= -\frac{\partial^2\psi^{\mathbf{S}}}{\partial\theta\,\partial\theta}(\theta)'_{\mathbf{S}} - \frac{\partial^2\psi^{\mathbf{S}}}{\partial\theta\,\partial\mathbf{C}_{\mathbf{S}}}(\mathbf{C}_{\mathbf{S}})'_{\mathbf{S}}\\ (\eta^{\gamma})'_{\gamma} &= -\frac{\partial^2\psi^{\gamma}}{\partial\theta\,\partial\theta}(\theta)'_{\gamma} - \frac{\partial^2\psi^{\gamma}}{\partial\theta\,\partial\rho^{\mathrm{G}\gamma}}(\rho^{\mathrm{G}\gamma})'_{\gamma}\,.\end{aligned} \tag{5.121}$$

Considering the energy function for the solid given in (5.97) related to (5.94), the second partial derivatives of $(\eta^{\mathbf{S}})'_{\mathbf{S}}$ are obtained with

$$\frac{\partial^2\psi^{\mathbf{S}}}{\partial\theta\,\partial\theta} = \frac{\mathrm{c}^{\mathbf{S}}_{\mathrm{V}}}{\theta} \quad \text{and} \quad \frac{\partial^2\psi^{\mathbf{S}}}{\partial\theta\,\partial\mathbf{C}_{\mathbf{S}}} = \frac{3}{2\,\rho^{\mathbf{S}}_{0\mathbf{S}}}\,\alpha^{\mathbf{S}}\,\mathrm{k}^{\mathbf{S}}(\mathbf{C}_{\mathbf{S}})^{-1}\,, \tag{5.122}$$

and $(\eta^{\gamma})'_{\gamma}$ is set up invoking (5.102) with

$$\frac{\partial^2\psi^{\gamma}}{\partial\theta\,\partial\theta} = \frac{\mathrm{c}^{\gamma}_{\mathrm{V}}}{\theta} \quad \text{and} \quad \frac{\partial^2\,\psi^{\gamma}}{\partial\theta\,\partial\rho^{\mathrm{G}\gamma}} = -\frac{\mathrm{R}^{\gamma}}{\rho^{\mathrm{G}\gamma}}\,. \tag{5.123}$$

By implementing the partial derivatives (5.122) and (5.123) into the general form (5.120), the constitutive mixture energy balance is obtained with

$$\begin{aligned}&\rho^{\mathbf{S}}\,\mathrm{c}^{\mathbf{S}}_{\mathrm{V}}\,(\theta)'_{\mathbf{S}} + \mathrm{J}^{-1}_{\mathbf{S}}\frac{3}{2}\,\theta\,\alpha^{\mathbf{S}}\,\mathrm{k}^{\mathbf{S}}(\mathbf{C}_{\mathbf{S}})^{-1}(\mathbf{C}_{\mathbf{S}})'_{\mathbf{S}} + \sum_{\gamma}\rho^{\gamma}\,\mathrm{c}^{\gamma}_{\mathrm{V}}\,(\theta)'_{\gamma} -\\ &\qquad \mathrm{n}^{\mathbf{G}}\sum_{\gamma}\frac{\mathrm{p}^{\mathrm{G}\gamma}}{\rho^{\mathrm{G}\gamma}}(\rho^{\mathrm{G}\gamma})'_{\gamma} + \operatorname{div}\mathbf{q} + \sum_{\gamma}\hat{\mathbf{p}}^{\gamma}_{\mathrm{E}}\cdot\mathbf{w}_{\gamma\mathbf{S}} + \sum_{\gamma}\hat{\rho}^{\gamma}\,h^{\gamma} = 0\,,\end{aligned} \tag{5.124}$$

where additionally the definition for the partial pressure (5.104) has been implemented with

$$\frac{\rho^{\gamma}}{\rho^{\mathrm{G}\gamma}}\,\theta\,\mathrm{R}^{\gamma} = \mathrm{n}^{\mathbf{G}}\,\frac{\mathrm{p}^{\mathrm{G}\gamma}}{\rho^{\mathrm{G}\gamma}}\,. \tag{5.125}$$

5.5. Summary and closure problem

In the following the summarized constitutive model setup is presented, and the closure problem for the coupled differential equations is compiled.

Governing model equations
The set of primary unknowns $\mathcal{R}$ is chosen with

$$\mathcal{R} = \mathcal{R}(\mathbf{x}, t) = \{\mathbf{u_S}, \mathrm{p}^{\mathbf{GR}}, \{\mathrm{c}_m^{\mathrm{G}\iota}\}, \theta\}\,, \tag{5.126}$$

including the displacement $\mathbf{u_S}$, the overall pressure $\mathrm{p}^{\mathbf{GR}}$, the amount of $(\nu - 1)$ molar concentrations $\{\mathrm{c}_m^{\mathrm{G}\iota}\}$ with $\mathrm{c}_m^{\mathrm{G}\iota} = (\mathrm{c}_m^{\mathrm{G1}}, \mathrm{c}_m^{\mathrm{G2}}, ..., \mathrm{c}_m^{\mathrm{G}(\nu-1)})$, and the temperature θ of the mixture. For the solution of these the following local forms of the balance equations are invoked:

- mixture balance equation of momentum for $\mathbf{u_S}$
- mixture balance equation of mass for $\mathrm{p}^{\mathbf{GR}}$
- single concentration balances for $\{\mathrm{c}_m^{\mathrm{G}\iota}\}$
- mixture balance equation of energy for θ

The mixture balance equation of momentum is derived by summing up the momentum balance of the solid $\varphi^{\mathbf{S}}$ and gas $\varphi^{\mathbf{G}}$, cf. (5.24), and moreover by considering the constraint for the interaction forces (5.15) with

$$\mathrm{div}\mathbf{T} + \rho\,\mathbf{b} = \mathbf{0}\,. \tag{5.127}$$

The required mixture balance equation of energy (5.120) is given with

$$\theta\{\rho^{\mathbf{S}}(\eta^{\mathbf{S}})'_{\mathbf{S}} + \sum_{\gamma} \rho^{\gamma}(\eta^{\gamma})'_{\gamma}\} + \mathrm{div}\,\mathbf{q} = -\sum_{\gamma} \hat{\mathbf{p}}^{\gamma}_{\mathrm{E}} \cdot \mathbf{w}_{\gamma\mathbf{S}} - \sum_{\gamma} \hat{\rho}^{\gamma} h^{\gamma}\,. \tag{5.128}$$

The overall pressure is calculated using the mixture balance of mass, which again is derived by summing up the macroscopic mass balance equations for the solid (5.16) and gas phase (5.17). After rearranging and implementing the known relations,

cf. Sect. B.6, the mixture mass balance reads

$$\operatorname{div}\left(\mathrm{n}^{\mathbf{G}}\mathbf{w}_{\mathbf{GS}} + \mathbf{x}'_{\mathbf{S}}\right) + \frac{\mathrm{n}^{\mathbf{G}}}{\rho^{\mathbf{G}\mathrm{R}}}(\rho^{\mathbf{G}\mathrm{R}})'_{\mathbf{G}} = 0\,. \tag{5.129}$$

The molar concentration balance for component φ^γ is given according to (5.22) with

$$\mathrm{n}^{\mathbf{G}}\,(\mathrm{c}_m^{\mathrm{G}\gamma})'_{\mathbf{S}} + \operatorname{div}\left(\mathrm{n}^{\mathbf{G}}\,\mathrm{c}_m^{\mathrm{G}\gamma}\,\mathbf{w}_{\gamma\mathbf{S}}\right) + \mathrm{c}_m^{\mathrm{G}\gamma}\operatorname{div}\mathbf{x}'_{\mathbf{S}} = \mathrm{n}^{\mathbf{G}}\,\hat{\mathrm{c}}_m^{\mathrm{G}\gamma}\,. \tag{5.130}$$

Explicit relations

The equations for the secondary variables are explicitly implemented into the governing equations. They are composed of volume fraction relations as well as flow and diffusion formulations. The volume fraction solid and its material time derivative can be calculated by

$$\mathrm{n}^{\mathbf{S}} = \mathrm{n}^{\mathbf{S}}_{0\mathbf{S}}\det\mathbf{F}_{\mathbf{S}}^{-1} \quad \text{and} \quad (\mathrm{n}^{\mathbf{S}})'_{\mathbf{S}} = -\mathrm{n}^{\mathrm{S}}\operatorname{div}\mathbf{x}'_{\mathbf{S}}\,. \tag{5.131}$$

see (5.16). The volume fraction of the gas and its material time derivative are solved utilizing the saturation condition (5.2) and derivative and (5.40) with

$$\mathrm{n}^{\mathbf{G}} = 1 - \mathrm{n}^{\mathbf{S}} \quad \text{and} \quad (\mathrm{n}^{\mathbf{G}})'_{\mathbf{S}} = -(\mathrm{n}^{\mathbf{S}})'_{\mathbf{S}} \tag{5.132}$$

The advective flow is directly computed with

$$\mathrm{n}^{\mathbf{G}}\,\mathbf{w}_{\mathbf{GS}} = \frac{\mathrm{K}^{\mathbf{S}}}{\eta^{\mathbf{G}\mathrm{R}}}\{\operatorname{grad}\mathrm{p}^{\mathbf{G}\mathrm{R}}\}\,, \tag{5.133}$$

and the total molar flux with (5.90)

$$\mathrm{n}^{\mathbf{G}}\,\mathrm{c}_m^{\mathrm{G}\gamma}\mathbf{w}_{\gamma\mathbf{S}} = -\mathrm{n}^{\mathbf{G}}{}_m D_{\mathrm{G}\gamma}\operatorname{grad}\mathrm{c}_m^{\mathrm{G}\gamma} - \mathrm{c}_m^{\mathrm{G}\gamma}\,\mathrm{n}^{\mathbf{G}}\,\mathbf{w}_{\mathbf{GS}}\,. \tag{5.134}$$

The heat flux is explicitly given by relation (5.92)

$$\mathbf{q} = -\alpha_{\nabla\theta}\operatorname{grad}\theta\,. \tag{5.135}$$

Moreover, since the overall pressure $\mathrm{p}^{\mathbf{G}\mathrm{R}}$ can be computed via the partial pressures,

cf. $(5.63)_2$ and (5.105), the ν-th component of $\{\mathrm{c}_m^{\mathrm{G}\gamma}\}$ is calculated with

$$\mathrm{c}_m^{\mathrm{G}\nu} = \frac{\mathrm{p}^{\mathbf{G}\mathrm{R}}}{\mathrm{R}_m\theta} - \sum_{\gamma=1}^{\nu-1} \mathrm{c}_m^{\mathrm{G}\gamma}\,. \tag{5.136}$$

Remark. *The term connected with the extra momentum supply* $\hat{\mathbf{p}}_{\mathrm{E}}^{\gamma}\cdot\mathbf{w}_{\gamma\mathbf{S}}$ *of the mixture energy balance* (5.128) *will be neglected, since the extra momentum supply vector is a function of seepage velocity itself, cf.* $(5.68)_1$*, and the square of the velocity is negligibly small for the problems to investigate and thus disregarded.*

Constitutive modeling

Finally, the following assumptions and constitutive relations are used, starting with the true and partial densities:

$$\begin{aligned} &\rho^{\mathbf{S}\mathrm{R}} = \text{const.} = \rho_{0\mathbf{S}}^{\mathbf{S}\mathrm{R}} \quad \Rightarrow (\rho^{\mathbf{S}\mathrm{R}})'_{\mathbf{S}} = 0 \quad \rho^{\mathbf{S}} = \mathrm{n}^{\mathbf{S}}\,\rho^{\mathbf{S}\mathrm{R}} \\ &\rho^{\mathbf{G}\mathrm{R}} = \sum_{\gamma} \rho^{\mathrm{G}\gamma} = \sum_{\gamma} \mathrm{c}_m^{\mathrm{G}\gamma}\,\mathrm{M}_m^{\gamma} \qquad\qquad \rho^{\mathbf{G}} = \mathrm{n}^{\mathbf{G}}\,\rho^{\mathbf{G}\mathrm{R}}\,. \end{aligned} \tag{5.137}$$

The solid stress and gas pressure as well as the specific entropies are calculated from the approaches of the Helmholtz energies, cf. (5.97) combined with (5.94) and (5.102) with (5.38), with

$$\begin{aligned} \mathbf{T}^{\mathbf{S}} &= -\mathrm{n}^{\mathbf{S}}\,\mathrm{p}^{\mathbf{G}\mathrm{R}}\,\mathbf{I} + \mathbf{T}_{\mathrm{E}}^{\mathbf{S}} \\ \mathbf{T}^{\mathbf{G}} &= -\mathrm{n}^{\mathbf{G}}\,\mathrm{p}^{\mathbf{G}\mathrm{R}}\,\mathbf{I} \\ \mathbf{T}_{\mathrm{E}}^{\mathbf{S}} &= 2\rho^{\mathbf{S}}\mathbf{F}_{\mathbf{S}}\frac{\partial\psi^{\mathbf{S}}}{\partial\mathbf{C}_{\mathbf{S}}}\,\mathbf{F}_{\mathbf{S}}^{\mathrm{T}} = \frac{1}{\mathrm{J}_{\mathbf{S}}}\,\{2\,\mu^{\mathbf{S}}\,\mathbf{K}_{\mathbf{S}} + \lambda^{\mathbf{S}}\,(\ln\mathrm{J}_{\mathbf{S}})\,\mathbf{I} - 3\,\alpha^{\mathbf{S}}\,\mathrm{k}^{\mathbf{S}}\,(\theta-\theta_0)\,\mathbf{I}\}, \\ \mathbf{T} &= \mathbf{T}^{\mathbf{S}} + \mathbf{T}^{\mathbf{G}} = -\mathrm{p}^{\mathbf{G}\mathrm{R}}\,\mathbf{I} + \mathbf{T}_{\mathrm{E}}^{\mathbf{S}}\,, \end{aligned} \tag{5.138}$$

where for the mixture stress $\mathbf{T}$ use has been made of the saturation condition (5.2). The partial pressure $\mathrm{p}^{\mathrm{G}\gamma}$ is derived with

$$\begin{aligned} \mathrm{p}^{\mathrm{G}\gamma} = \rho^{\mathrm{G}\gamma}\frac{\partial\psi^{\mathrm{G}\gamma}}{\partial\rho^{\mathrm{G}\gamma}} - \psi^{\mathrm{G}\gamma} &= \rho^{\mathrm{G}\gamma}\,\mathrm{R}^{\gamma}\,\theta \\ &= \mathrm{c}_m^{\mathrm{G}\gamma}\,\mathrm{R}_m\,\theta \end{aligned} \tag{5.139}$$

and the specific entropies with

$$\begin{aligned}\eta^{\mathbf{S}} &= -\frac{\partial\psi^{\mathbf{S}}}{\partial\theta} = \frac{1}{\rho_{0\mathbf{S}}^{\mathbf{S}}}\,3\,\alpha^{\mathbf{S}}\,\mathrm{k}^{\mathbf{S}}\,(\mathrm{lnJ}_{\mathbf{S}}) + \mathrm{c}_{\mathrm{V}}^{\mathbf{S}}\,\{\ln(\frac{\theta}{\theta_0}) + 1\} - 1 \\ \eta^{\gamma} &= -\frac{\partial\,\psi^{\gamma}}{\partial\,\theta} = -\mathrm{R}^{\gamma}\,\{\,\ln(\frac{\rho^{\mathrm{G}\gamma}}{\rho_0^{\mathrm{G}\gamma}}) - 1\,\} + \mathrm{c}_{\mathrm{V}}^{\gamma}\,\{\ln\,(\frac{\theta}{\theta_0}) + 1\} - 1\,.\end{aligned} \tag{5.140}$$

6. Numerical treatment

The coupled equation system of PDEs is solved with the FEM[1], provided by the FEAP by Taylor [98], which offers a platform to implement customized PDEs. Variational formulations of the governing PDEs for the set of unknowns $\mathcal{R}$ of the model (5.126) are needed for implementation. For that, the standard GALERKIN[2] procedure is invoked to gain weak formulations of the local PDEs, which are introduced for the problem at hand in Sect. 5.5.

The required weak formulations are obtained by a scalar multiplication of the governing PDE with a test function and subsequent integration over the considered domain Ω. For a solution, the derived functional is minimized to obtain equilibrium[3] or rather is varied until a steady solution is found. Moreover, the solution of the PDE is approximated by a suitable trial (ansatz) function replacing the unknown, which has to satisfies the boundary condition on $\partial\Omega$ (Sect. 6.1.5). For the BUBNOV-GALERKIN procedure, commonly used within the FE framework, test and trial function are selected equal. The procedure is also known as METHOD OF THE WEIGHTED RESIDUALS, where the test function can also be seen as a function, that weights the residuum (PDE with ansatz function) in an integral manner. The requirement, that the functional should vanish, is then fulfilled weakly for the integral and no longer strong in each local material point. A detailed derivation of this topic e.g. is given in Parisch [85].

Moreover, problems in solid mechanics are generally solved in the LAGRANGEAN description, cf. 3.3.1, whereas fluid mechanics are described in the EULER configuration.

[1] A detailed derivation of the FEM e.g. is given in Bathe [10] and Zienkiewitz and Taylor [112].

[2] The GALERKIN procedure represents a general solution method of differential equations of arbitrary type and thus is not restricted to problems requiring a potential (conservative systems).

[3] For conservative systems the functional equals the potential energy Π, for which the equilibrium state is described by the minimum of the potential energy. The equilibrium is determined by the demand for the first variation to be equal to zero with $\delta\Pi = 0$.

Since multi-phase materials are characterized by a fluid flowing through a solid matrix, a mixed LAGRANGE-EULER formulation is utilized. For that, the solid is covered by the LAGRANGEAN domain $\mathrm{B}_{\mathbf{S}}$ moving through time and space starting from a reference configuration to which everything is related. The fluid instead is covered by the EULER description, for which the LAGRANGE solid matrix serves as control space.

In the following the derivation of the required weak formulations of the governing PDEs is presented followed by an introduction to the element-wise spatial and temporal discretization and solution procedure.

6.1. Weak formulations

6.1.1. Mixture balance of momentum

As test function for the mechanical part of the coupled equation system the variation of the actual configuration $\delta\mathbf{u}_{\mathbf{S}} = \delta\left(\mathbf{x} = \mathbf{X}_{\mathbf{S}} + \mathbf{u}_{\mathbf{S}}\right)$, cf. (3.62), is chosen and multiplied with the local form of the mixture balance equation of momentum (5.127). Moreover, integration over the domain $\mathrm{B}_{\mathbf{S}}$ leads to the weak form in the actual configuration with

$$\mathrm{G}_u := \int_{\mathrm{B}_{\mathbf{S}}} (\mathrm{div}\mathbf{T} + \rho\mathbf{b}) \cdot \delta\mathbf{u}_{\mathbf{S}} \,\mathrm{dv} = 0\,. \tag{6.1}$$

The divergence of $\mathbf{T}$ can be rewritten via the identity (A.3)

$$\int_{\mathrm{B}_{\mathbf{S}}} (\mathrm{div}\mathbf{T}) \cdot \delta\mathbf{u}_{\mathbf{S}} \,\mathrm{dv} = \int_{\mathrm{B}_{\mathbf{S}}} \mathrm{div}(\mathbf{T}\,\delta\mathbf{u}_{\mathbf{S}}) \,\mathrm{dv} - \int_{\mathrm{B}_{\mathbf{S}}} \mathbf{T} \cdot \mathrm{grad}\,\delta\mathbf{u}_{\mathbf{S}} \,\mathrm{dv}\,, \tag{6.2}$$

so that the GAUSS integral theorem can be applied to the first term on the right hand side of (6.2) and the integral over the surface $\partial\mathrm{B}_{\mathbf{S}}$

$$\int_{\mathrm{B}_{\mathbf{S}}} \mathrm{div}(\mathbf{T}\,\delta\mathbf{u}_{\mathbf{S}}) \,\mathrm{dv} = \int_{\partial\mathrm{B}_{\mathbf{S}}} \mathbf{T}\,\mathbf{n} \cdot \delta\mathbf{u}_{\mathbf{S}} \,\mathrm{da} = \int_{\partial\mathrm{B}_{\mathbf{S}}} \mathbf{t} \cdot \delta\mathbf{u}_{\mathbf{S}} \,\mathrm{da}\,, \tag{6.3}$$

is obtained. This surface integral introduces the surface forces $\mathbf{t} = \mathbf{T}\,\mathbf{n}$ as stress boundary condition, cf. (3.76). Bringing together (6.3) and (6.2) with (6.1) yields the weak formulation of the mixture balance of momentum in the actual configuration

with

$$\int_{\mathrm{B}_\mathbf{S}} \mathbf{T} \cdot \operatorname{grad} \delta\mathbf{u}_\mathbf{S} \,\mathrm{dv} - \int_{\mathrm{B}_\mathbf{S}} \rho\mathbf{b} \cdot \delta\mathbf{u}_\mathbf{S} \,\mathrm{dv} = \int_{\partial\mathrm{B}_\mathbf{S}} \mathbf{t} \cdot \delta\mathbf{u}_\mathbf{S} \,\mathrm{da}\,. \tag{6.4}$$

To comply with the LAGRANGEAN description, a pull-back to the reference configuration is performed. Therefor, the volume element dv, the gradient grad and the surface element d$\mathbf{a}$ are referred to the reference configuration by invoking the transport theorems given in Section 3.3.3. Using (3.43) and (3.45) yields for the left hand side of (6.4)

$$\begin{aligned}
&\int_{\mathrm{B}_\mathbf{S}} \mathbf{T} \cdot \operatorname{grad} \delta\mathbf{u}_\mathbf{S} \,\mathrm{dv} - \int_{\mathrm{B}_\mathbf{S}} \rho\mathbf{b} \cdot \delta\mathbf{u}_\mathbf{S} \,\mathrm{dv} \\
&\qquad = \int_{\mathrm{B}_{0\mathbf{S}}} \mathbf{T} \cdot (\operatorname{Grad} \delta\mathbf{u}_\mathbf{S})\, \mathbf{F}_\mathbf{S}^{-1}\, \mathrm{J}_\mathbf{S} \,\mathrm{dV}_{0\mathbf{S}} \quad - \int_{\mathrm{B}_{0\mathbf{S}}} \rho\mathbf{b} \cdot \delta\mathbf{u}_\mathbf{S}\, \mathrm{J}_\mathbf{S} \mathrm{dV}_{0\mathbf{S}} \\
&\qquad = \int_{\mathrm{B}_{0\mathbf{S}}} \mathrm{J}_\mathbf{S} \mathbf{T}\, \mathbf{F}_\mathbf{S}^{\mathrm{T}-1} \cdot \operatorname{Grad} \delta\mathbf{u}_\mathbf{S} \,\mathrm{dV}_{0\mathbf{S}} \quad - \int_{\mathrm{B}_{0\mathbf{S}}} \rho\mathbf{b} \cdot \delta\mathbf{u}_\mathbf{S}\, \mathrm{J}_\mathbf{S} \mathrm{dV}_{0\mathbf{S}} \\
&\qquad = \int_{\mathrm{B}_{0\mathbf{S}}} \mathbf{P} \cdot \operatorname{Grad} \delta\mathbf{u}_\mathbf{S} \,\mathrm{dV}_{0\mathbf{S}} \quad - \int_{\mathrm{B}_{0\mathbf{S}}} \rho\mathbf{b} \cdot \delta\mathbf{u}_\mathbf{S}\, \mathrm{J}_\mathbf{S} \mathrm{dV}_{0\mathbf{S}}\,,
\end{aligned} \tag{6.5}$$

where additionally the definition the first PIOLA-KIRCHHOFF (1. PK) stress tensor (3.78) is implemented. The right hand side surface integral of (6.4) is referred to the reference configuration utilizing (3.44), which leads to

$$\begin{aligned}
\int_{\partial\mathrm{B}_\mathbf{S}} \mathbf{t} \cdot \delta\mathbf{u}_\mathbf{S} \,\mathrm{da} = \int_{\partial\mathrm{B}_\mathbf{S}} (\mathbf{T}^{\mathrm{T}} \delta\mathbf{u}_\mathbf{S}) \cdot \,\mathrm{d}\mathbf{a} &= \int_{\partial\mathrm{B}_{0\mathbf{S}}} (\mathbf{T}^{\mathrm{T}}\, \delta\mathbf{u}_\mathbf{S}) \cdot \mathrm{J}_\mathbf{S} \mathbf{F}^{\mathrm{T}-1} \,\mathrm{d}\mathbf{A}_{0\mathbf{S}} \\
&= \int_{\partial\mathrm{B}_{0\mathbf{S}}} \mathrm{J}_\mathbf{S}\, (\mathbf{F}^{-1}\mathbf{T}^{\mathrm{T}})\, \delta\mathbf{u}_\mathbf{S} \cdot \mathrm{d}\mathbf{A}_{0\mathbf{S}} \\
&= \int_{\partial\mathrm{B}_{0\mathbf{S}}} \delta\mathbf{u}_\mathbf{S} \cdot \mathrm{J}_\mathbf{S} \underbrace{(\mathbf{F}^{-1}\, \mathbf{T}^{\mathrm{T}})^{\mathrm{T}}}_{\mathbf{T}\mathbf{F}^{\mathrm{T}-1}} \mathrm{d}\mathbf{A}_{0\mathbf{S}} \\
&= \int_{\partial\mathrm{B}_{0\mathbf{S}}} \delta\mathbf{u}_\mathbf{S} \cdot \underbrace{\mathrm{J}_\mathbf{S}\, \mathbf{T}\, \mathbf{F}^{\mathrm{T}-1}}_{\mathbf{P}} \mathrm{d}\mathbf{A}_{0\mathbf{S}} \\
&= \int_{\partial\mathrm{B}_{0\mathbf{S}}} \delta\mathbf{u}_\mathbf{S} \cdot \mathbf{p}_0 \,\mathrm{dA}_{0\mathbf{S}}
\end{aligned} \tag{6.6}$$

with invoking the CAUCHY theorem (3.76)

$$\mathbf{p}_0 = \mathbf{P}\mathbf{n}_0 \,. \tag{6.7}$$

Therein, $\mathbf{n}_0$ denotes the outward normal vector in the reference configuration, see Fig. 3.3. Finally, the mixture momentum balance in the reference configuration is obtained with (6.5) and (6.6) as

$$\int_{\mathrm{B}_{0\mathbf{S}}} \mathbf{P} \cdot \operatorname{Grad} \delta\mathbf{u}_{\mathbf{S}} \, \mathrm{dV}_{0\mathbf{S}} - \int_{\mathrm{B}_{0\mathbf{S}}} \mathrm{J}_{\mathbf{S}} \, (\rho\mathbf{b}) \cdot \delta\mathbf{u}_{\mathbf{S}} \, \mathrm{dV}_{0\mathbf{S}} = \int_{\partial\mathrm{B}_{0\mathbf{S}}} \mathbf{p}_0 \cdot \delta\mathbf{u}_{\mathbf{S}} \, \mathrm{dA}_{0\mathbf{S}} \,. \tag{6.8}$$

6.1.2. Mixture balance of mass

Applying the GALERKIN procedure with the test function $\delta\mathrm{p}^{\mathbf{G}\mathrm{R}}$ for the pressure to the mixture balance equation of mass (5.129) yields

$$\mathrm{G}_p := \int_{\mathrm{B}_{\mathbf{S}}} \{\operatorname{div}(\mathrm{n}^{\mathbf{G}} \, \mathbf{w}_{\mathbf{GS}} + \mathbf{x}'_{\mathbf{S}}) + \frac{\mathrm{n}^{\mathbf{G}}}{\rho^{\mathbf{G}\mathrm{R}}} \, (\rho^{\mathbf{G}\mathrm{R}})'_{\mathbf{G}}\} \, \delta\mathrm{p}^{\mathbf{G}\mathrm{R}} \, \mathrm{dv} = 0 \,. \tag{6.9}$$

Therein, the divergence of the filter velocity can on the one hand be reduced to a first order differential equation by applying the identity (A.1), and on the other hand, a surface integral can be obtained by utilizing the GAUSS theorem:

$$\begin{aligned} \int_{\mathrm{B}_{\mathbf{S}}} \operatorname{div}(\mathrm{n}^{\mathbf{G}}\mathbf{w}_{\mathbf{GS}}) \, \delta\mathrm{p}^{\mathbf{G}\mathrm{R}} \, \mathrm{dv} &= \int_{\mathrm{B}_{\mathbf{S}}} \operatorname{div}(\mathrm{n}^{\mathbf{G}}\mathbf{w}_{\mathbf{GS}} \, \delta\mathrm{p}^{\mathbf{G}\mathrm{R}}) \, \mathrm{dv} \quad - \int_{\mathrm{B}_{\mathbf{S}}} \mathrm{n}^{\mathbf{G}}\mathbf{w}_{\mathbf{GS}} \cdot \operatorname{grad} \delta\mathrm{p}^{\mathbf{G}\mathrm{R}} \, \mathrm{dv} \\ &= \int_{\partial\mathrm{B}_{\mathbf{S}}} \mathrm{n}^{\mathbf{G}}\mathbf{w}_{\mathbf{GS}} \cdot \mathbf{n} \, \delta\mathrm{p}^{\mathbf{G}\mathrm{R}} \mathrm{da} \quad - \int_{\mathrm{B}_{\mathbf{S}}} \mathrm{n}^{\mathbf{G}}\mathbf{w}_{\mathbf{GS}} \cdot \operatorname{grad} \delta\mathrm{p}^{\mathbf{G}\mathrm{R}} \, \mathrm{dv} \,. \end{aligned} \tag{6.10}$$

The divergence of $\mathbf{x}'_{\mathbf{S}}$ is equal to $\operatorname{grad} \mathbf{x}'_{\mathbf{S}} \cdot \mathbf{I}$, see (3.57). With that, the weak formulation of the mixture mass balance (6.9) in the current placement reads

$$\begin{aligned} - \int_{\mathrm{B}_{\mathbf{S}}} \mathrm{n}^{\mathbf{G}}\mathbf{w}_{\mathbf{GS}} \cdot \operatorname{grad} \delta\mathrm{p}^{\mathbf{G}\mathrm{R}} \, \mathrm{dv} + \int_{\mathrm{B}_{\mathbf{S}}} \{\operatorname{grad} \mathbf{x}'_{\mathbf{S}} \cdot \mathbf{I} + \frac{\mathrm{n}^{\mathbf{G}}}{\rho^{\mathbf{G}\mathrm{R}}} (\rho^{\mathbf{G}\mathrm{R}})'_{\mathbf{G}}\} \, \delta\mathrm{p}^{\mathbf{G}\mathrm{R}} \, \mathrm{dv} = \\ - \int_{\partial\mathrm{B}_{\mathbf{S}}} \mathrm{n}^{\mathbf{G}}\mathbf{w}_{\mathbf{GS}} \cdot \mathbf{n} \, \delta\mathrm{p}^{\mathbf{G}\mathrm{R}} \, \mathrm{da} \,. \end{aligned} \tag{6.11}$$

Likewise, the mixture balance of mass is pulled back to the reference configuration by

utilizing the volume, first order gradient and surface transport, so that

$$\begin{aligned} &- \int_{\mathrm{B}_{0\mathbf{S}}} \mathrm{n}^{\mathbf{G}} \mathbf{w}_{\mathbf{GS},0} \cdot \operatorname{Grad} \delta \mathrm{p}^{\mathbf{G}\mathrm{R}} \, \mathrm{dV}_{0\mathbf{S}} + \int_{\mathrm{B}_{\mathbf{S}}} \mathrm{J}_{\mathbf{S}} \{ \operatorname{Grad} \mathbf{x}'_{\mathbf{S}} \cdot \mathbf{F}_{\mathbf{S}}^{\mathrm{T}-1} \\ &+ \frac{\mathrm{n}^{\mathbf{G}}}{\rho^{\mathbf{G}\mathrm{R}}} (\rho^{\mathbf{G}\mathrm{R}})'_{\mathbf{G}} \} \, \delta \mathrm{p}^{\mathbf{G}\mathrm{R}} \, \mathrm{dV}_{0\mathbf{S}} = - \int_{\partial \mathrm{B}_{0\mathbf{S}}} \mathrm{n}^{\mathbf{G}} \mathbf{w}_{\mathbf{GS},0} \cdot \mathbf{n}_0 \, \delta \mathrm{p}^{\mathbf{G}\mathrm{R}} \mathrm{dA}_{0\mathbf{S}} \end{aligned} \tag{6.12}$$

is obtained, where the reference filter velocity $\mathrm{n}^{\mathbf{G}} \mathbf{w}_{\mathbf{GS},0}$ is introduced with

$$\mathrm{n}^{\mathbf{G}} \mathbf{w}_{\mathbf{GS},0} = \mathrm{J}_{\mathbf{S}} \, \mathrm{n}^{\mathbf{G}} \mathbf{F}_{\mathbf{S}}^{-1} \mathbf{w}_{\mathbf{GS}} \, . \tag{6.13}$$

Moreover, the pressure gradient of the spatial filter velocity given in (5.133) needs a pull-back so that finally the expression containing the inverse of the right CAUCHY-GREEN tensor $(3.46)_1$ is obtained with

$$\mathrm{n}^{\mathbf{G}} \mathbf{w}_{\mathbf{GS},0} = \mathrm{J}_{\mathbf{S}} \, \frac{\mathrm{K}^{\mathbf{S}}}{\eta^{\mathbf{G}\mathrm{R}}} \{ \operatorname{Grad} \mathrm{p}^{\mathbf{G}\mathrm{R}} \, \mathbf{F}_{\mathbf{S}}^{-1} \} \mathbf{F}_{\mathbf{S}}^{\mathrm{T}-1} = \mathrm{J}_{\mathbf{S}} \, \frac{\mathrm{K}^{\mathbf{S}}}{\eta^{\mathbf{G}\mathrm{R}}} \{ \operatorname{Grad} \mathrm{p}^{\mathbf{G}\mathrm{R}} \} \, \mathbf{C}_{\mathbf{S}}^{-1} \, . \tag{6.14}$$

6.1.3. Concentration balance

The concentration balances are solved with the corresponding virtual molar concentration $\delta \mathrm{c}_m^{\mathrm{G}\gamma}$. With that, the weak formulation is derived from (5.130) after multiplying with the test function and integration over the domain $\mathrm{B}_{\mathbf{S}}$ as

$$\mathrm{G}c := \int_{\mathrm{B}_{\mathbf{S}}} \{ \mathrm{n}^{\mathbf{G}} (\mathrm{c}_m^{\mathrm{G}\gamma})'_{\mathbf{S}} + \operatorname{div} (\mathrm{n}^{\mathbf{G}} \, \mathrm{c}_m^{\mathrm{G}\gamma} \, \mathbf{w}_{\gamma\mathbf{S}}) + \mathrm{c}_m^{\mathrm{G}\gamma} \operatorname{div} \mathbf{x}'_{\mathbf{S}} - \mathrm{n}^{\mathbf{G}} \, \hat{\mathrm{c}}_m^{\mathrm{G}\gamma} \} \, \delta \mathrm{c}_m^{\mathrm{G}\gamma} \, \mathrm{dv} = 0 \tag{6.15}$$

Analogously to (6.10), the included divergence terms of the total molar flux ${}_m\mathbf{j}_{tot}^{\mathrm{G}\gamma} = \mathrm{c}_m^{\mathrm{G}\gamma} \mathbf{w}_{\gamma\mathbf{S}}$, see (5.90), is reformulated to

$$\begin{aligned} \int_{\mathrm{B}_{\mathbf{S}}} \operatorname{div} (\mathrm{n}^{\mathbf{G}} \, {}_m\mathbf{j}_{tot}^{\mathrm{G}\gamma}) \, \delta \mathrm{c}_m^{\mathrm{G}\gamma} \, \mathrm{dv} = & \int_{\mathrm{B}_{\mathbf{S}}} \operatorname{div} (\mathrm{n}^{\mathbf{G}} \, {}_m\mathbf{j}_{tot}^{\mathrm{G}\gamma} \, \delta \mathrm{c}_m^{\mathrm{G}\gamma}) \, \mathrm{dv} - \int_{\mathrm{B}_{\mathbf{S}}} \mathrm{n}^{\mathbf{G}} \, {}_m\mathbf{j}_{tot}^{\mathrm{G}\gamma} \cdot \operatorname{grad} \delta \mathrm{c}_m^{\mathrm{G}\gamma} \, \mathrm{dv} \\ = & \int_{\partial \mathrm{B}_{\mathbf{S}}} \mathrm{n}^{\mathbf{G}} \, {}_m\mathbf{j}_{tot}^{\mathrm{G}\gamma} \cdot \mathbf{n} \, \delta \mathrm{c}_m^{\mathrm{G}\gamma} \, \mathrm{da} - \int_{\mathrm{B}_{\mathbf{S}}} \mathrm{n}^{\mathbf{G}} \, {}_m\mathbf{j}_{tot}^{\mathrm{G}\gamma} \cdot \operatorname{grad} \delta \mathrm{c}_m^{\mathrm{G}\gamma} \, \mathrm{dv} \, , \end{aligned} \tag{6.16}$$

so that the concentration balance in the current configuration is obtained with

$$-\int_{\mathrm{B}_\mathbf{S}} \mathrm{n}^\mathbf{G}\, {}_m\mathbf{j}_{tot}^{\mathrm{G}\gamma} \cdot \operatorname{grad} \delta\mathrm{c}_m^{\mathrm{G}\gamma}\,\mathrm{dv} + \int_{\mathrm{B}_\mathbf{S}} \{\mathrm{n}^\mathbf{G}(\mathrm{c}_m^{\mathrm{G}\gamma})'_\mathbf{S} + \mathrm{c}_m^{\mathrm{G}\gamma} \operatorname{grad} \mathbf{x}'_\mathbf{S} \cdot \mathbf{I} - \mathrm{n}^\mathbf{G}\, \hat{\mathrm{c}}_m^{\mathrm{G}\gamma}\}\, \delta\mathrm{c}_m^{\mathrm{G}\gamma}\,\mathrm{dv} = -\int_{\partial\mathrm{B}_\mathbf{S}} \mathrm{n}^\mathbf{G}\, {}_m\mathbf{j}_{tot}^{\mathrm{G}\gamma} \cdot \mathbf{n}\, \delta\mathrm{c}_m^{\mathrm{G}\gamma}\,\mathrm{da}\,. \tag{6.17}$$

Applying again the transport theorems for volume, first order gradient and surface yields the concentration balance in Lagrangean description with

$$-\int_{\mathrm{B}_{0\mathbf{S}}} \mathrm{n}^\mathbf{G}\, {}_m\mathbf{j}_{tot,0}^{\mathrm{G}\gamma} \cdot \operatorname{Grad} \delta\mathrm{c}_m^{\mathrm{G}\gamma}\,\mathrm{dV}_{0\mathbf{S}} + \int_{\mathrm{B}_{0\mathbf{S}}} \mathrm{J}_\mathbf{S}\, \{\mathrm{c}_m^{\mathrm{G}\gamma} \operatorname{Grad} \mathbf{x}'_\mathbf{S} \cdot \mathbf{F}_\mathbf{S}^{\mathrm{T}-1}\}\, \delta\mathrm{c}_m^{\mathrm{G}\gamma}\,\mathrm{dV}_{0\mathbf{S}}$$
$$+\int_{\mathrm{B}_{0\mathbf{S}}} \mathrm{J}_\mathbf{S}\, \{\mathrm{n}^\mathbf{G}(\mathrm{c}_m^{\mathrm{G}\gamma})'_\mathbf{S} - \mathrm{n}^\mathbf{G}\, \hat{\mathrm{c}}_m^{\mathrm{G}\gamma}\}\, \delta\mathrm{c}_m^{\mathrm{G}\gamma}\,\mathrm{dV}_{0\mathbf{S}} = -\int_{\partial\mathrm{B}_{0\mathbf{S}}} \mathrm{n}^\mathbf{G}\, {}_m\mathbf{j}_{tot,0}^{\mathrm{G}\gamma} \cdot \mathbf{n}_0\, \delta\mathrm{c}_m^{\mathrm{G}\gamma}\,\mathrm{dA}_{0\mathbf{S}}\,. \tag{6.18}$$

with the reference total molar flux

$${}_m\mathbf{j}_{tot,0}^{\mathrm{G}\gamma} = \mathrm{J}_\mathbf{S}\, \mathbf{F}_\mathbf{S}^{-1}\, {}_m\mathbf{j}_{tot}^{\mathrm{G}\gamma}\,. \tag{6.19}$$

Moreover, the explicit relation of in the reference configuration reads with (6.14)

$$\begin{aligned} \mathrm{n}^\mathbf{G}\, {}_m\mathbf{j}_{tot,0}^{\mathrm{G}\gamma} &= -\mathrm{J}_\mathbf{S}\, (\mathrm{n}^\mathbf{G}\, {}_mD_{\mathrm{G}\gamma} \operatorname{grad} \mathrm{c}_m^{\mathrm{G}\gamma} + \mathrm{c}_m^{\mathrm{G}\gamma}\, \mathrm{n}^\mathbf{G}\, \mathbf{w}_\mathbf{GS})\, \mathbf{F}_\mathbf{S}^{\mathrm{T}-1} \\ &= -\mathrm{J}_\mathbf{S}\, (\mathrm{n}^\mathbf{G}\, {}_mD_{\mathrm{G}\gamma} \operatorname{Grad} \mathrm{c}_m^{\mathrm{G}\gamma} + \mathrm{c}_m^{\mathrm{G}\gamma}\, \frac{\mathrm{K}^\mathbf{S}}{\eta^{\mathbf{G}\mathrm{R}}} \operatorname{Grad} \mathrm{p}^{\mathbf{G}\mathrm{R}})\, \mathbf{C}_\mathbf{S}^{-1} \end{aligned} \tag{6.20}$$

6.1.4. Mixture balance of energy

Finally, the weak formulation of the balance of energy of the mixture is derived by multiplying the local form (5.128) with the test function $\delta\theta$ and integrating the weighted residual over the solid domain as

$$\mathrm{G}_\theta := \int_{\mathrm{B}_\mathbf{S}} \{\theta\rho^\mathbf{S}(\eta^\mathbf{S})'_\mathbf{S} + \theta \sum_\gamma \rho^\gamma(\eta^\gamma)'_\gamma + \operatorname{div} \mathbf{q} + \sum_\gamma \hat{\mathbf{p}}_\mathrm{E}^\gamma \cdot \mathbf{w}_{\gamma\mathbf{S}} + \sum_\gamma \hat{\rho}^\gamma h^\gamma\}\, \delta\theta\,\mathrm{dv} = 0\,, \tag{6.21}$$

wherein the energy transport via $\hat{\mathbf{p}}_\mathrm{E}^\gamma \cdot \mathbf{w}_{\gamma\mathbf{S}}$ is neglected, cf. 5.5. Moreover, the divergence of the heat flux is reduced to a first order differential equation again via the identity

and GAUSS theorem

$$\begin{aligned}\int_{\mathrm{B_S}} \operatorname{div}\mathbf{q}\,\delta\theta \mathrm{dv} &= \int_{\mathrm{B_S}} \operatorname{div}(\mathbf{q}\,\delta\theta)\,\mathrm{dv} \quad - \int_{\mathrm{B_S}} \mathbf{q}\cdot\operatorname{grad}\delta\theta\,\mathrm{dv} \\ &= \int_{\partial\mathrm{B_S}} \mathbf{q}\cdot\mathbf{n}\,\delta\theta\,\mathrm{da} \quad - \int_{\mathrm{B_S}} \mathbf{q}\cdot\operatorname{grad}\delta\theta\,\mathrm{dv}\,,\end{aligned} \tag{6.22}$$

which provides the boundary condition on the surface. With that, the weak formulation in the actual placement reads

$$\begin{aligned}\int_{\mathrm{B_S}} \{\theta\rho^{\mathbf{S}}(\eta^{\mathbf{S}})'_{\mathbf{S}} + \theta\sum_\gamma \rho^\gamma(\eta^\gamma)'_\gamma + \sum_\gamma \hat{\rho}^\gamma h^\gamma\}\,\delta\theta\,\mathrm{dv} \\ - \int_{\mathrm{B_S}} \mathbf{q}\cdot\operatorname{grad}\delta\theta\,\mathrm{dv} = -\int_{\partial\mathrm{B_S}} \mathbf{q}\cdot\mathbf{n}\,\delta\theta\,\mathrm{da}\,.\end{aligned} \tag{6.23}$$

Invoking the transport theorems, the weak formulation in the reference is obtained with

$$\begin{aligned}\int_{\mathrm{B_{0S}}} \mathrm{J_S}\{\theta\rho^{\mathbf{S}}(\eta^{\mathbf{S}})'_{\mathbf{S}} + \theta\sum_\gamma \rho^\gamma(\eta^\gamma)'_\gamma + \sum_\gamma \hat{\rho}^\gamma h^\gamma\}\,\delta\theta\,\mathrm{dV_{0S}} \\ - \int_{\mathrm{B_{0S}}} \mathbf{q}_{,0}\cdot\operatorname{Grad}\delta\theta\,\mathrm{dV_{0S}} = -\int_{\partial\mathrm{B_{0S}}} \mathbf{q}_{,0}\cdot\mathbf{N}\,\delta\theta\,\mathrm{dA_{0S}}\,.\end{aligned} \tag{6.24}$$

Therein, $\mathbf{q}_{,0}$ denotes the overall reference heat flux vector with

$$\mathbf{q}_{,0} = \mathrm{J_S}\,\mathbf{q}\,\mathbf{F}_{\mathbf{S}}^{\mathrm{T}-1}\,, \tag{6.25}$$

which is explicitly given with (5.135) as

$$\mathbf{q}_{,0} = -\mathrm{J_S}\,(\alpha_{\nabla\theta}\operatorname{Grad}\theta\,\mathbf{F}_{\mathbf{S}}^{-1})\,\mathbf{F}_{\mathbf{S}}^{\mathrm{T}-1} = -\mathrm{J_S}\,(\alpha_{\nabla\theta}\operatorname{Grad}\theta)\,\mathbf{C}_{\mathbf{S}}^{-1}\,. \tag{6.26}$$

6.1.5. Boundary conditions

For each unknown quantity of $\mathcal{R}$ to solve, either DIRICHLET (geometrical) or NEUMANN (forces) boundary conditions need to be applied on $\partial\mathrm{B_S}$, see Fig. 6.1. In the sequence of above-mentioned balance equations they read

- displacement $\mathbf{u_S}$ or mechanical force $\mathbf{t}$
- pore pressure p^{GR} or gas flux $\mathrm{n}^{\mathbf{G}}\mathbf{w_{GS}}$

- molar concentration via $c_m^{G\gamma}$ or total molar flux ${}_m\mathbf{j}_{tot}^{G\gamma}$

- temperature θ or heat flux $\mathbf{q}$

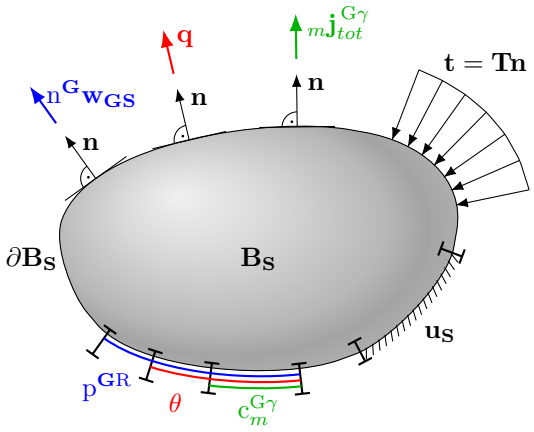

Figure 6.1.: Scheme of boundary conditions

6.2. Finite element formulation

For the FE analysis the physical continuum body under consideration is divided into and approximated through a finite number of elements. The geometric domain $B_{0\mathbf{S}}$ in the reference configuration is then given by $B_{0\mathbf{S}}^h$, which is composed of the union of n_{el} elements Ω_e :

$$B_{0\mathbf{S}} \approx B_{0\mathbf{S}}^h = \bigcup_{e=1}^{n_{el}} \Omega_e \,, \tag{6.27}$$

The surface $\partial B_{0\mathbf{S}}^h$ is comprised by the edges and planes, respectivley, of those elements situated on the edge, so that the real surface is approximated by

$$\partial B_{0\mathbf{S}} \approx \partial B_{0\mathbf{S}}^h = \bigcup_{e=1}^{n_{el}} \partial\Omega_e \,. \tag{6.28}$$

In the following, a short introduction to the spatial and temporal discretization of the unknown field variables and the element geometry are given on element level Ω_e.

6.2.1. Isoparametric concept and spatial discretization

The governing equations are discretized in the framework of the standard isoparametric procedure. That concept comprises, that the geometry is approximated with the same number of nodes $I = 1, ..., n_{node}$ per element as the field unknowns and moreover, that same ansatz functions N_I are used to interpolate geometry and solid displacement of the element Ω_e between the discrete grid points. For interpolating the geometry the approximation

$$\mathbf{X_S} \approx \mathbf{X_S^h} = \sum_I N_I(\boldsymbol{\xi})\, \mathbf{X_S^I}\,, \tag{6.29}$$

applies, where $\mathbf{X_S^I}$ denotes the discrete values of the nodal coordinates of the element configuration Ω_e. The shape functions are defined in the parameter space Ω_p with the natural coordinates $\boldsymbol{\xi} = (\xi, \eta, \zeta)^{\mathrm{T}}$, cf. Fig. 6.2.

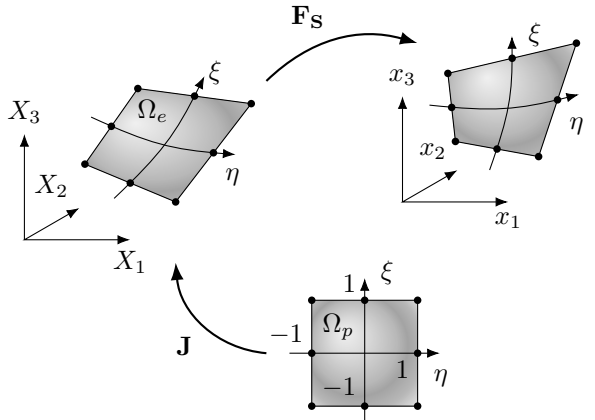

Figure 6.2.: Isoparametric bilinear 4-node LAGRANGE element

In the context of the isoparametric description, the solid displacement $\mathbf{u_S}$, the test function $\delta\mathbf{u_S}$ as well as the incremental value $\Delta\mathbf{u_S}$ (cf. Sect. 6.2.2) are approximated equally with

$$\begin{aligned} \mathbf{u_S} &\approx \mathbf{u_S^h} = \sum_I N^I(\boldsymbol{\xi})\, \mathbf{d}^I_{\mathbf{u_S}} \\ \delta\mathbf{u_S} &\approx \delta\mathbf{u_S^h} = \sum_I N^I(\boldsymbol{\xi})\, \delta\mathbf{d}^I_{\mathbf{u_S}} \\ \Delta\mathbf{u_S} &\approx \Delta\mathbf{u_S^h} = \sum_I N^I(\boldsymbol{\xi})\, \Delta\mathbf{d}^I_{\mathbf{u_S}}\,, \end{aligned} \tag{6.30}$$

where $\mathbf{d}^I_{\mathbf{us}}$, $\delta\mathbf{d}^I_{\mathbf{us}}$ and $\Delta\mathbf{d}^I_{\mathbf{us}}$ are the vectors collecting the corresponding nodal values. Moreover, the gradient of the solid displacement as well as of the test function and increment are determined by using the gradient of the shape functions $N_{I,\mathbf{X_S}}$.

$$\begin{aligned}
\operatorname{Grad}\mathbf{u_S} \approx \operatorname{Grad}\mathbf{u}^h_{\mathbf{S}} &= \sum_I N^I_{,\mathbf{X_S}}(\boldsymbol{\xi}) \otimes \mathbf{d}^I_{\mathbf{us}} \\
\operatorname{Grad}\delta\mathbf{u_S} \approx \operatorname{Grad}\delta\mathbf{u}^h_{\mathbf{S}} &= \sum_I N^I_{,\mathbf{X_S}}(\boldsymbol{\xi}) \otimes \delta\mathbf{d}^I_{\mathbf{us}} \\
\operatorname{Grad}\Delta\mathbf{u_S} \approx \operatorname{Grad}\Delta\mathbf{u}^h_{\mathbf{S}} &= \sum_I N^I_{,\mathbf{X_S}}(\boldsymbol{\xi}) \otimes \Delta\mathbf{d}^I_{\mathbf{us}}\,.
\end{aligned} \tag{6.31}$$

The remaining scalar field unknowns ($\mathrm{p}^{\mathbf{GR}}$, $\mathrm{c}^{\mathrm{G}\gamma}_m$, θ), the corresponding test functions and increments, and their spatial derivatives are likewise approximated with

$$\begin{aligned}
\Theta \approx \Theta^h &= \sum_I N^I(\boldsymbol{\xi})\,\mathrm{d}^I_\Theta \\
\delta\Theta \approx \delta\Theta^h &= \sum_I N^I(\boldsymbol{\xi})\,\delta\mathrm{d}^I_\Theta \\
\Delta\Theta \approx \Delta\Theta^h &= \sum_I N^I(\boldsymbol{\xi})\,\Delta\mathrm{d}^I_\Theta\,,
\end{aligned} \tag{6.32}$$

and

$$\begin{aligned}
\operatorname{Grad}\Theta \approx \operatorname{Grad}\Theta^h &= \sum_I N^I_{,\mathbf{X_S}}(\boldsymbol{\xi})\,\mathrm{d}^I_\Theta \\
\operatorname{Grad}\delta\Theta \approx \operatorname{Grad}\delta\Theta^h &= \sum_I N^I_{,\mathbf{X_S}}(\boldsymbol{\xi})\,\delta\mathrm{d}^I_\Theta \\
\operatorname{Grad}\Delta\Theta \approx \operatorname{Grad}\Delta\Theta^h &= \sum_I N^I_{,\mathbf{X_S}}(\boldsymbol{\xi})\,\Delta\mathrm{d}^I_\Theta\,.
\end{aligned} \tag{6.33}$$

where Θ is representative for the respective scalar degree of freedom.

The derivatives of the shape functions with respect to the physical coordinates and vice versa are given by invoking the chain rule with

$$N^I_{,\boldsymbol{\xi}} = \mathbf{J}(\boldsymbol{\xi})\,N^I_{,\mathbf{X_S}} \qquad \text{and} \qquad N^I_{,\mathbf{X_S}} = \mathbf{J}^{-1}(\boldsymbol{\xi})N^I_{,\boldsymbol{\xi}} \tag{6.34}$$

where use is made of the JACOBI matrix $\mathbf{J}(\boldsymbol{\xi}) = \partial\mathbf{X_S}/\partial\boldsymbol{\xi}$ and its inverse, see also Fig. 6.2.

Mixed finite elements: For the coupled equation system at hand, a monolithic

solution strategy is to be pursued, meaning that the resulting linear algebraic equation system[4] is solved simultaneously. For stability reasons, the displacement $\mathbf{u_S}$ is interpolated with quadratic shape functions, whereas the remaining degrees of freedom are interpolated linear. The stability is mathematically based on the so-called LBB condition (*Ladyzhenskaya–Babuska–Brezzi*), see e.g. [40], which states, that the discretization spaces of displacement $\mathbf{u}_\mathbf{S}^h$ and pressure p^h cannot be chosen arbitrarily and a linkage between them is necessary to solve the saddle-point problem. The condition, also known as *inf-sup* condition, is generally satisfied if the approximation of the displacement is higher by one order than that of the pressure. That is implemented by choosing so-called Taylor-Hood elements (Q2Q1) for spatial discretization. For the problem at hand extended Taylor-Hood elements are chosen, where the additional degrees of freedom besides the displacement and pressure are also interpolated linear, cf. Fig. 6.3. Furthermore, the choice of mixed finite elements is motivated by the

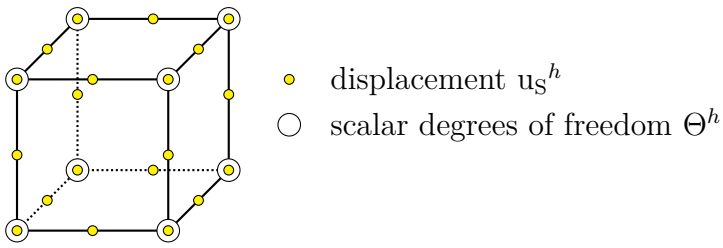

Figure 6.3.: 3D Taylor-Hood element

requirement to obtain an equivalent approximation of pressure and displacement during solving the mixture momentum balance. The mixture momentum balance contains the overall stress tensor $\mathbf{T}$ (6.4), which is composed of the pressure and temperature variable itself, and additionally the displacement in form of the KARNI-REINER strain tensor $\mathbf{K_S}$, cf. (5.138), which implies the derivative of the displacements. Thus, the displacement should be approximated with one order higher-valued shape functions than those of pressure and temperature to end up with equivalent approximations.

The discretized weak formulations of the governing equations can be found in App. C.1.

[4] after applying the NEWTON linearization scheme, cf. (6.2.2)

6.2.2. Newton-Raphson method

The coupled, non-linear problem is solved with a sequence of linear approximations utilizing NEWTON's method.

For that, the weak formulations have to be linearized defining the vectors of field unknowns and their time derivatives with

$$\mathbf{u} = [\mathbf{u_S}\,, \mathrm{p}^{\mathbf{GR}}\,, \{\mathrm{c}^{\mathrm{G}\iota}_{\mathrm{mol}}\}\,, \theta]^{\mathrm{T}} \quad \text{and} \quad \dot{\mathbf{u}} = [\dot{\mathbf{u}}_{\mathbf{S}}\,, \dot{\mathrm{p}}^{\mathbf{GR}}\,, \{\dot{\mathrm{c}}^{\mathrm{G}\iota}_{\mathrm{mol}}\}\,, \dot{\theta}]^{\mathrm{T}}\,, \tag{6.35}$$

the vector $\mathbf{g}(\mathbf{u}\,, \dot{\mathbf{u}})$ collecting the weak formulations from (6.8), (6.12), (6.18), and (6.24), as well as the vector $\mathbf{v}$ collecting the dependencies (6.35)

$$\mathbf{g}(\mathbf{u}\,, \dot{\mathbf{u}}) = \begin{bmatrix} \mathrm{G}_u(\mathbf{u}, \dot{\mathbf{u}}) \\ \mathrm{G}_p(\mathbf{u}, \dot{\mathbf{u}}) \\ \{\mathrm{G}_{c^\iota}(\mathbf{u}, \dot{\mathbf{u}})\} \\ \mathrm{G}_\theta(\mathbf{u}, \dot{\mathbf{u}}) \end{bmatrix}\,, \quad \mathbf{v} = [\mathbf{u}\,, \dot{\mathbf{u}}]^T \tag{6.36}$$

With these definitions the NEWTON iteration is given with

$$\mathbf{g}(\mathbf{v}^{i+1}) \approx \mathbf{g}(\mathbf{v}^i) + D\mathbf{g}(\mathbf{v}^i)[\mathbf{v}] = \mathbf{o}\,, \tag{6.37}$$

where $D\mathbf{g}(\mathbf{v}^i)[\mathbf{v}]$ denotes the directional derivative of $\mathbf{g}(\mathbf{v})$ in the direction of $\mathbf{v}$, in the following denoted with $\Delta\mathbf{g}(\mathbf{v})$. Thus, for each NEWTON iteration the linearized set of equations

$$\Delta\mathbf{g}(\mathbf{v}^i) = -\mathbf{g}(\mathbf{v}^i) \tag{6.38}$$

has to be solved for $\mathbf{v}$. Moreover, linearizing $\mathbf{g}(\mathbf{v})$ with respect to the vectors of unknowns as well as their time derivatives leads to the form

$$\Delta\mathbf{g}(\mathbf{v}^i) = \frac{\partial\mathbf{g}}{\partial\mathbf{u}^i}\Delta\mathbf{u}^i + \frac{\partial\mathbf{g}}{\partial\dot{\mathbf{u}}^i}\Delta\dot{\mathbf{u}}^i = \mathbf{K}\Delta\mathbf{u}^i + \mathbf{D}\Delta\dot{\mathbf{u}}^i\,, \tag{6.39}$$

where $\mathbf{K}$ denotes the tangential stiffness matrix (dependent on the actual deformation) and $\mathbf{D}$ the damping matrix (constant), respectively. The time-dependent unknowns $\dot{\mathbf{u}}$ are solved using the implicit time integration via the NEWMARK-β-method[5]. The

[5]For the quasi-static problem at hand an implicit EULER time-integration scheme would be sufficient, but to ensure in general the possibility for a dynamic calculation, the NEWMARK procedure is implemented.

procedure yields a condensation of the damping term $\mathbf{D}\Delta\dot{\mathbf{u}}^i$ to a so-called effective stiffness matrix $\mathbf{K}^*$.

The original form of the NEWMARK method assumes a constant acceleration between two time steps, see Fig. 6.4, where the overall time integral $[0,T]$ to be integrated is divided into NT time steps Δt with

$$[0,T] = \bigcup_{n=1}^{NT} t_{n+1} - t_n\,, \qquad \Delta t = t_{n+1} - t_n\,. \tag{6.40}$$

Starting from a constant or linear approach for the course of the acceleration vector

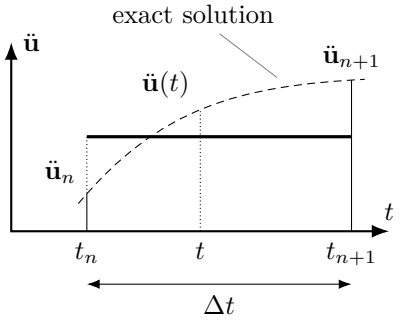

Figure 6.4.: NEWMARK approach for constant acceleration

$\ddot{\mathbf{u}}$ within one time step Δt, the NEWMARK-equations for velocity $\dot{\mathbf{u}}$ and the unknown variable $\mathbf{u}$ itself at t_{n+1} yield after integration

$$\begin{aligned} \mathbf{u}_{n+1} &= \mathbf{u}_n + \dot{\mathbf{u}}_n\,\Delta t + [(\frac{1}{2} - \beta)\ddot{\mathbf{u}}_n + \beta\ddot{\mathbf{u}}_{n+1}]\,\Delta t^2 \\ \dot{\mathbf{u}}_{n+1} &= \dot{\mathbf{u}}_n + [(1-\gamma)\,\ddot{\mathbf{u}}_n + \gamma\,\ddot{\mathbf{u}}_{n+1}]\,\Delta t\,, \end{aligned} \tag{6.41}$$

where $(\beta = 1/4\,, \gamma = 1/2)$ traces back to a constant acceleration and $(\beta = 1/6\,, \gamma = 1/2)$ to a linear approach. The approaches (6.41) are reformulated yielding two equations for $\ddot{\mathbf{u}}_{n+1}$ and $\dot{\mathbf{u}}_{n+1}$ (acceleration/velocity at time t_n+1), which are afterwards only functions of the known variables at time t_n and the unknown NEWTON variable $\mathbf{u}_{n+1}$:

$$\begin{aligned} \dot{\mathbf{u}}_{n+1}(\mathbf{u}_{n+1}) &= \frac{\gamma}{\beta\Delta t}(\mathbf{u}_{n+1} - \mathbf{u}_n) \;-(\frac{\gamma}{\beta} - 1)\,\dot{\mathbf{u}}_n \quad -(\frac{\gamma}{2\beta} - 1)\,\Delta t\,\ddot{\mathbf{u}}_n \\ \ddot{\mathbf{u}}_{n+1}(\mathbf{u}_{n+1}) &= \frac{1}{\beta\Delta t^2}(\mathbf{u}_{n+1} - \mathbf{u}_n) - (\frac{1}{\beta\Delta t} - 1)\,\dot{\mathbf{u}}_n - (\frac{1}{2\beta} - 1)\,\ddot{\mathbf{u}}_n\,. \end{aligned} \tag{6.42}$$

These are implemented to the discretized equation of motion, see e.g. [109], so that a nonlinear algebraic equation for the unknowns $\mathbf{u}_{n+1}^{i}$ follows with

$$\mathbf{g}(\mathbf{u}_{n+1}^{i}) = \mathbf{M}\ddot{\mathbf{u}}_{n+1}(\mathbf{u}_{n+1}^{i}) + \mathbf{D}\dot{\mathbf{u}}_{n+1}(\mathbf{u}_{n+1}^{i}) + \mathbf{K}(\mathbf{u}_{n+1}^{i})\mathbf{u}_{n+1} - \mathbf{f}_{n+1} = \mathbf{o} \tag{6.43}$$

Therein, $\mathbf{M}$ denotes the mass matrix and $\mathbf{f}$ the vector of the external forces. Utilizing (6.43), temporary auxiliary variables for the velocity $\bar{\dot{\mathbf{u}}}$ and unknown $\bar{\mathbf{u}}$ are gained with

$$\begin{aligned} \bar{\dot{\mathbf{u}}}_{n+1} &= \dot{\mathbf{u}}_n + (1-\beta)\,\ddot{\mathbf{u}}_n\,\Delta t \\ \bar{\mathbf{u}}_{n+1} &= \mathbf{u}_n + \dot{\mathbf{u}}_n\,\Delta t + (\beta-\gamma)\,\ddot{\mathbf{u}}_n\,\Delta t^2 \end{aligned} \tag{6.44}$$

so that acceleration and velocity at time t_{n+1} are calculated via

$$\begin{aligned} \ddot{\mathbf{u}}_{n+1} &= \frac{1}{\beta\Delta t^2}\left[\mathbf{u}_{n+1} - \bar{\mathbf{u}}_{n+1}\right] \\ \dot{\mathbf{u}}_{n+1} &= \bar{\dot{\mathbf{u}}}_{n+1} + \gamma\,\ddot{\mathbf{u}}_{n+1}\,\Delta t\,. \end{aligned} \tag{6.45}$$

The incremental values $\Delta\ddot{\mathbf{u}}_{n+1}$ and $\Delta\dot{\mathbf{u}}_{n+1}$ required for the NEWTON procedure are derived by linearizing (6.41) with respect to $\mathbf{u}_{n+1}$ with

$$\begin{aligned} \Delta\ddot{\mathbf{u}}_{n+1} &= \frac{1}{\beta\Delta t^2}\Delta\mathbf{u}_{n+1} \\ \Delta\dot{\mathbf{u}}_{n+1} &= \frac{\gamma}{\beta\Delta t}\,\Delta\mathbf{u}_{n+1}\,. \end{aligned} \tag{6.46}$$

For the problem at hand, accelerations are neglected, so that the resulting NEWTON-RAPHSON procedure for the solution of the vector of unknown field variables $\mathbf{u}$ at time t_{n+1} reads

$$\begin{aligned} \left[\frac{\gamma}{\beta\Delta t}\,\mathbf{D} + \mathbf{K}(\mathbf{u}_{n+1}^{i})\right]\Delta\mathbf{u}_{n+1}^{i+1} &= -\mathbf{g}(\mathbf{u}_{n+1}^{i}) \\ \left[\mathbf{K}^{*}(\mathbf{u}_{n+1}^{i})\right]\Delta\mathbf{u}_{n+1}^{i+1} &= -\mathbf{g}(\mathbf{u}_{n+1}^{i})\,, \end{aligned} \tag{6.47}$$

where the constant damping term is added up to the tangential stiffness matrix yielding the effective tangential stiffness $\mathbf{K}^{*}$. The unknown field variables are updated via

$$\mathbf{u}_{n+1}^{i+1} = \mathbf{u}_{n+1}^{i} + \Delta\mathbf{u}_{n+1}^{i+1}\,. \tag{6.48}$$

The structure of the effective tangential stiffness matrix, where in this work the single entries are derived by a numerical tangent procedure, is shown in App. C.2.

7. Methane oxidation in landfill cover layers

7.1. Motivation

Global warming nowadays is more than ever an important concern to our everyday life, and politics and economy need to rethink their decisions based on scientific findings. The Intergovernmental Panel on Climate Change (IPCC) periodically releases assessment reports, which scientifically evaluate the physical aspects of the climate system and its change. The focus is on the vulnerability of socio-economic and natural systems to the climate change, as well as on options to mitigate the progress of global warming through preventing greenhouse gas emissions, see `http://www.ipcc.ch`.

Climate indicators, like temperature, greenhouse gas concentrations, sea ice, etc. show the long-term evolution of these key variables that can be used to assess the global and regional trends of a changing climate. The Fifth Assessment Report (AR5) documents the unequivocal warming of the climate system, and illustrates the increasing surface temperatures during the last century, see also Fig. 7.1. The climate change and increasing surface temperature on earth is increasingly influenced by humans through an unreasonable use of natural resources. For example the use of fossil fuels for society, economy, industry and agriculture increases the natural greenhouse gases, mainly carbon dioxide (CO_2), methane (CH_4), nitrous oxide (N_2O) and fluorinated gases (F-gases). The atmospheric concentrations of these have increased to levels unprecedented in at least the last 800.000 years, cf. [99]. Figure 7.2 gives an overview about the atmospheric greenhouse gas emissions of the last decades, which reached the highest values in human history since the 2000s. CO_2 still remains the major global

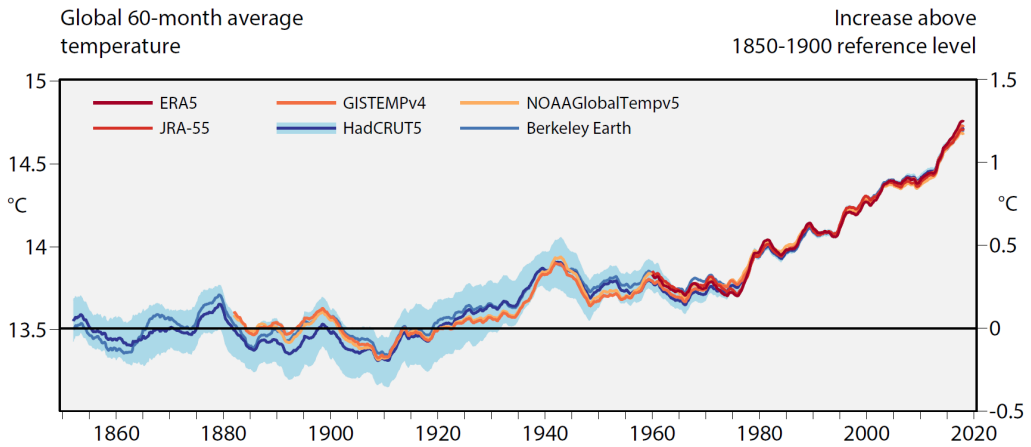

Figure 7.1.: Global average near-surface temperature for centred running 60-month periods (left-hand axis) and increase above the 1850–1900 level (right-hand axis) according to different datasets, see [86].

greenhouse gases (GHG) with concentrations reaching 400 parts per million (ppm) followed by methane CH_4 with about 1800 parts per billion (ppb),[1] see Fig. 7.2.

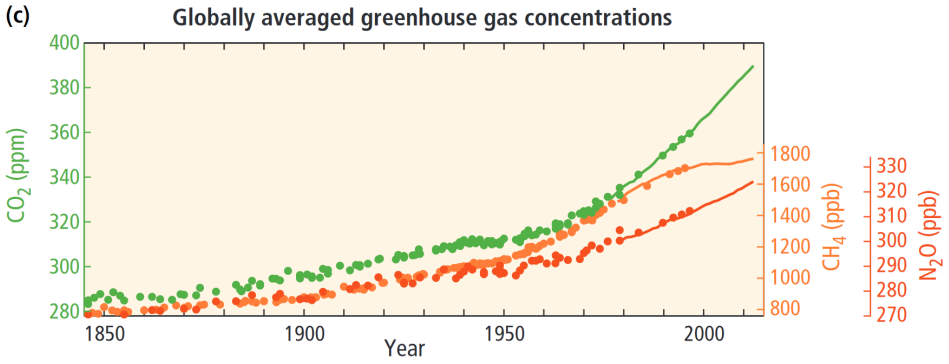

Figure 7.2.: Atmospheric concentrations of the greenhouse gases carbon dioxide (green), methane (orange) and nitrous oxide (red) determined from ice core data (dots) and from direct atmospheric measurements (lines), source: Fig. SPM.1 [99]

In this context the global warming potential (GWP) is introduced as an index, measuring the radiative forcing of a certain greenhouse gas relative to that of carbon dioxide for a chosen time horizon, see Annex I of [41]. It enables the quantification of the contribution of different substances to global warming. Figure 7.3 shows an excerpt from a table listing the global warming potentials of the major greenhouse

[1] Here: billion $\hat{=}10^9$

gases. Even though methane contributes less to the GHG emissions, its reduction is of great interest, since its impact on global warming is up to 30 times higher on a 100-year-horizon compared to carbon dioxide, and even 85 times higher in a 20-year-horizon.

Acronym, Common Name or Chemical Name	Chemical Formula	Lifetime (Years)	Radiative Efficiency (W m^{-2} ppb^{-1})	AGWP 20-year (W m^{-2} yr kg^{-1})	GWP 20-year	AGWP 100-year (W m^{-2} yr kg^{-1})	GWP 100-year
Carbon dioxide	CO_2	see*	1.37e-5	2.49e-14	1	9.17e-14	1
Methane	CH_4	12.4†	3.63e-4	2.09e-12	84	2.61e-12	28
Fossil methane‡	CH_4	12.4†	3.63e-4	2.11e-12	85	2.73e-12	30
Nitrous Oxide	N_2O	121†	3.00e-3	6.58e-12	264	2.43e-11	265

Figure 7.3.: Excerpt from Table 8.A.1 [96] showing GWP of major greenhouse gases

A man-made contributor to methane emissions is the sector of waste management, wherein landfills are the most preferred method for municipal solid waste (MSW) disposal [82]. During the operational and aftercare phase of MSW landfills, methane and carbon dioxide are produced nearly in equal shares through the biochemical degradation of organic waste. Worldwide, landfills rank on the 6th place in the list of CH_4 producers, in Europe they are the 2nd largest source of anthropogenic caused methane. Technologies for the recovery and treatment of landfill gas are applied to capture and destroy the emitting methane, usually by extracting energy from the gas with e.g. waste incineration plants, biogas biofilters or lean gas flares.

Active gas extraction systems are installed to capture emissions, but several old landfills in Germany and Europe are not equipped with these systems leading to uncontrolled emissions of methane to the atmosphere. Even with a gas extraction system, the gas recovery may be inconsistent and was found to be highly variable - usually not more than 50 % of the formed landfill gas could be captured [93]. A surface covering can increase this amount. Additionally, lean gas emissions in the aftercare phase, which are no longer applicable for the utilization as energy source, have to be treated passively *in-situ*. Figure 7.4 schematically shows the amount of gas produced over the years in a landfill, caused by the biological driven degradation and conversion of organic waste. The first decades of operation and an active aftercare phase of a landfill are characterized by the degradation of organic waste, which produces high methane emissions; these are technically captured, flared or used for biogas power

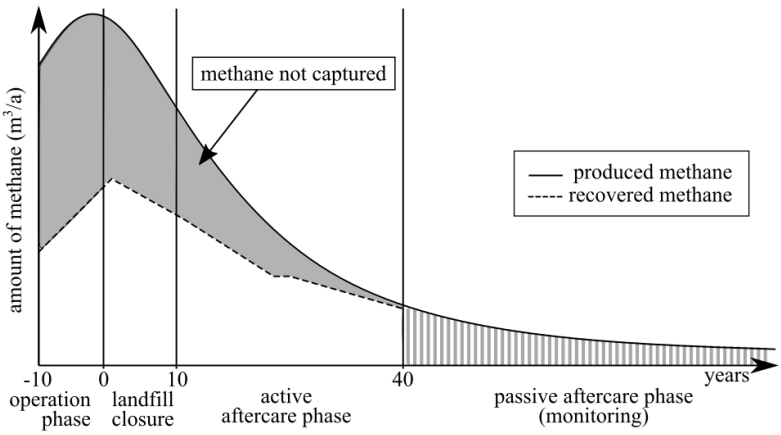

Figure 7.4.: Qualitative course of gas production in a landfills' lifetime according to [66]

plants. At the point where the active treatment of the gas is no longer economically efficient due to lean gas emissions, the biological oxidation of methane in a landfill cover layer can be taken as a passive treatment of the harmful emissions.

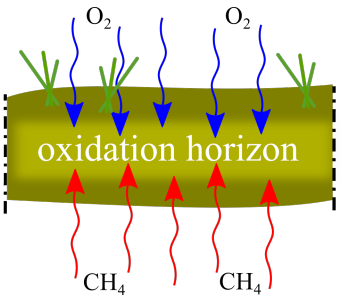

Figure 7.5.: Principle of methane oxidation horizon

The natural and thus cost-effective treatment of bacterial methane oxidation follows the reaction equation

$$CH_4 + 2\,O_2 = CO_2 + 2\,H_2O + 883\,\mathrm{kJ/mol}\,. \tag{7.1}$$

Bacterial microorganisms can oxidize methane utilizing atmospheric oxygen, see Fig. 7.6. They are ubiquitous in natural soils, so that a passive aftercare of the lean gas emissions is automatically given with the installation of a landfill cover soil. Oxidation rates at landfills can vary over several orders of magnitude, and range from zero to 100% of the methane flux entering the cover soil. The oxidation capacity underlies several environmental and physical influences such as temperature, moisture content and physical and chemical properties of the soil. Further, long-term exposure of soils

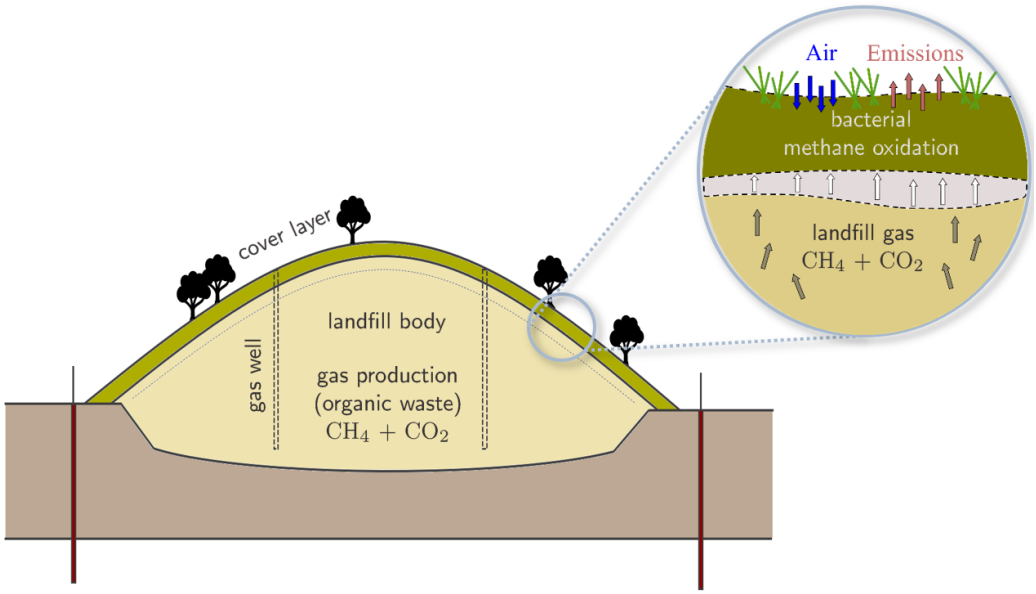

Figure 7.6.: Schematic landfill cover

to high levels of methane can encourage the growth of methanotrophic populations with high capacities for methane oxidation. Figure 7.5 schematically shows the spatial area inside the cover layer, where the highest oxidation rates are achieved, called the methane horizon. It is characterized by a sufficient amount of oxygen and methane concentrations so that in relation these rates are produced, indicated also by a temperature increase.

This horizon generally occurs at the shallow depth up to 0.4 m, while the maximum oxidation locates at the depth between 0.15 and 0.2m, see [92]. A reliable predictive capability, which considers all influencing environmental, physical and biochemical factors on methane oxidation rates in landfill cover soils, is desirable and required.

7.2. State of the art

To understand the processes involved in biological methane oxidation, execution of laboratory batch and column experiments were the most common approach used by researchers in the late 1990's and at the beginning of the new millennium. Whalen, Reeburgh, and Sandbeck [108] reported results from a study of CH_4 oxidation by microbial community in topsoil and investigated the influence of environmental

conditions such as temperature and substrate dependence on the oxidation rate. They pointed out, that methane oxidation in soils was a poorly understood term in the global CH_4 budget, which is getting more important under prospective warmer and dryer climate conditions, cf. [108]. In this context, they showed the importance of the moisture content of the soil to methane oxidation. Deviating moisture contents from an optimum one ($\sim 11\%$) led to significantly decreasing CH_4 oxidation rates, until the state of visibly saturated soils, with water contents of $\sim 40 - 75\%$, where only minor variances in oxidation rates occured. They attributed these observations of decreasing oxidation rates with increasing moisture content to the change of molecular diffusion from gaseous to aqueous, which is 10^4 times slower and thus, the transport of CH_4 to its oxidizers proceeds slower. Otherwise, the soil has to be prevented from desiccation, which was indicated by the decreasing oxidation rates with a moisture content below $\sim 11\%$.

These observations were also made by Boeckx, van Cleemput, and Villaralvo [14] and Czepiel et al. [29], who investigated the methane emissions from a covered landfill site under seasonally varying CH_4 fluxes. Kightley, Nedwell, and Cooper [69] and De Visscher et al. [39] examined the oxidation potential of different soils taking a closer look on methane oxidation kinetics in CH_4-rich and CH_4-low environments and the effects of nutrient amendments to the soil [69]. De Visscher et al. [39] additionally included the limiting aspect of O_2-availability in order get ideas for the optimization of cover soils. Methane oxidation rates and kinetics were also examined by Bogner, Spokas, and Burton [15], who performed a whole-landfill oxidation experiment including temporal variations. They suggest, that two major groups of methanotrophs coexist in landfill cover soils; one group favouring low CH_4/high O_2 settings, the other one higher CH_4/lower O_2 concentrations. Both group's activities can be approximated by Michaelis-Menten kinetics. Czepiel et al. [30] determined a linear correlation between measured CH_4 emissions from a landfill and atmospheric pressure showing decreasing emissions with increasing pressure. On the other hand that observed relationship should not be directly applicable to other landfills due to the high variability of landfill characteristics. Hilger, Liehr, and Barlaz [64] and Hilger, Cranford, and Barlaz [63] (and references therein) found, that in long-term laboratory simulations, the CH_4 oxidation rate has consistently exhibited a peak followed by a decrease to a lower steady-state value. They attribute this effect to an accumulation of extrapolymeric substance (EPS) produced by the bacteria and coating the soil, which reduces the O_2

availability to microbial activity sites due to a limiting gas diffusion.

Computational models for the simulation of gas transport in saturated and/or unsaturated soils and especially also methane oxidation models have been developed and extended during the last decades, and thus, a variety of models exist. Focusing on the modeling of multi-component gas mixtures and the transport of gas components, one can divide the models into one group using an additive approach for advection and diffusion, modeled with DARCY's and FICK's law, respectively, the advection-diffusion model (ADM), and one group using STEFAN-MAXWELL equations and the dusty-gas model (DGM).

The ADM and the implemented FICK's first law of diffusion is originally applicable to binary gases in clear fluids. The gradients of two gases are directly related to each other, so only a single gradient needs to be specified, cf. [107]. By introducing a factor depending on the porosity and gas saturation, e g. see Millington and Quirk [76], FICK's law is also applicable to porous media. The basic equations for the ADM are introduced in Chapter 4.

The DGM-approach, developed by Evans, Watson, and Mason [48, 49], extends the STEFAN-MAXWELL equations, valid for multi-component gases, by including the porous medium as a "dusty gas" component with large molecules fixed in space, treated as a component of the gas mixture [107]. Furthermore, the DGM-approach includes Knudsen diffusion, a process that occurs when the pores are so narrow that molecule-wall collisions are the main transport mechanism, cf. [38], and thus, important for low permeability areas. The DGM is able to reproduce the coupling effects of advection and diffusion, but its computational cost is higher. Comparisons of both models have shown, that the DGM is more accurate, but for higher permeabilities, the additive approach of the ADM is sufficient, cf. [107] and references therein. Veldsink et al. [106] reported, that the additive approach is satisfactorily accurate to estimate mass transport with chemical reactions in porous media and the results deviate only slightly from the DGM, which required substantially more computational time. Thorstenson and Pollock [102] observed, that FICK's law applied to stationary coordinates is totally inadequate for "stagnant" gases (non-reactive, no sources or sinks) like nitrogen in subsoil environments, but for any gases, it is an accurate estimate of the diffusive flux component relative to the mean molar velocity and an approximate estimate of the total diffusive flux of a gas component [102].

However, using the generalized FICK's law for a multi-component mixture, cf. (4.2), provides equivalent results to the DGM, see also Sect. 4.1. Moreover, the multi-component diffusion coefficient can be estimated based on the Maxwell-Stefan equations, see Lu and Feng [72] and authors therein.

In the abundance of existing models dealing with multi-component gas transport in saturated or unsaturated soils and the vadose zone, the special focus is in what follows on biological methane oxidation models in landfill covers.

Within the group of previously categorized ADM approach, Stein, Hettiratchi, and Achari [95] developed a simple 1D reactive-transport model for the gaseous phase with a four component gas mixture (CH_4, O_2, CO_2 and N_2), wherein the composition of the gas phase is determined by a combination of the physical transport of the gases and the microbial consumption and production of these [95]. The biological CH_4 oxidation rate modeled by dual-substrate kinetics depends on the soil bulk density and moisture content. To account for the multi-component gas mixture, concentration-dependent diffusion coefficients have been taken for FICK's diffusion. De Visscher and van-Cleemput [38] set up a comparable model, but taking Stefan-Maxwell equations for the molar flux and incorporating a dynamic methanotropic activity profile by introducing specific growth rates for the biomass. They also introduced a temperature correction factor for the kinetic parameters. Looking at the steady state, both models give nearly same predictions, but the dynamic methanotrophic activity may become important when e.g. desiccation effects should be considered. Molins and Mayer [77] point out the importance of the two-way coupling between gas transport and biogeochemical reactions that affects the composition of the gas phase. A decrease in gas volume caused by aerobic CH_4 oxidation contributes to a decrease in gas phase pressure and hence causes viscous gas transport into the reaction zone, cf. [77]. To consider all of these effects, they incorporate the DGM equations to a reactive transport model based on the model described in Mayer, Frind, and Blowes [75], which also includes the mass conservation equation for the aqueous phase. The underlying model of Mayer, Frind, and Blowes [75] assumes in a first step that the transport of pore gas can be adequately described by FICKian diffusion for reactive gases as also pointed out by Thorstenson and Pollock [102] and mentioned before. Comparison of the DGM by Molins and Mayer [77] with the results of De Visscher and van-Cleemput [38] showed only slight differences in concentration profiles. The study of Molins et al. [78] investigates the capacity of landfill cover soils to attenuate methane and also

trace compounds within the landfill gas with the aid of aforementioned model by Molins and Mayer [77] extended with terms to consider EPS and water production. A sensitivity analysis of landfill gas composition, moisture content, porosity and permeability is documented. They state, that in general the production of EPS seems to have a more important effect than water production since the EPS accumulation is concentrated in the reaction zone, cf. [78]. Hettiarachchi, Hettiaratchi, and Mehrotra [61] and Hettiarachchi et al. [62] developed a coupled numerical model using the ADM formulation for the gas transport including a balance equation for water and heat as well as dual-substrate kinetics for the biological reactions with two correction factors for temperature and moisture content dependencies. The model serves as a tool to design field-scale methane biofiltration (MBF) systems. They also agree with other authors who point out the importance of considering EPS formation within a model, but their results indicate that on field-scale it is of no particular concern. Ng, Feng, and Liu [83] also present a coupled water-gas-heat transport ADM for methane oxidation implemented in commercial FE software and performed parametric studies focussing on the influences of oxidation-generated water and heat on methane oxidation. Adopting this model, Feng et al. [51] present 2D numerical studies of methane oxidation efficiency of sloping landfill covers. Abichou et al. [5, 4] performed numerical studies based on a model given in [2, 110] to scale methane oxidation model parameters from laboratory to field conditions and the impact of vegetation in landfill covers. The model also considers the coupling of water and heat with gas transport and oxidation using the additive split of Fick's diffusion and Darcy flow.

The stable carbon isotope method has also been employed to determine the oxidation in landfill cover soils, cf. [3, 1, 25, 26, 70]. The isotopic methods rely on the preference of methanotrophic bacteria for the stable carbon isotope of smaller mass, so that they oxidize $^{12}CH_4$ at a slightly more rapid rate than $^{13}CH_4$, cf. [92]. This leads to an increase of the $^{13}CH_4/^{12}CH_4$ ratio of the remaining CH_4, which can be used to estimate methane oxidation, cf. [73]. Based on the model developed by De Visscher and van-Cleemput [38], Mahieu et al. [73] implemented different diffusion coefficients for the isotopes to account for the fractionation by diffusion and a fractionation factor to calculate the different isotope reaction rates from the overall reaction rate. However, the technique of stable isotope probing, see also [93], is quite expensive and the calculated methane oxidation efficiencies are sensitive to infinitesimal changes in the magnitudes of the fractionation due to diffusive gas transport [50].

Scheutz et al. [92] give an comprehensive overview of the state of the art regarding process understanding, case studies and modeling of microbial CH_4 oxidation. However, existing models are currently not able to holistically describe the multi-component bio-chemo-thermo-hydro coupled conversion processes including finite solid deformation in a continuum mechanical and thermodynamically consistent framework.

7.3. Model validation on laboratory scale

Methane oxidation in cover layers has been recognized and investigated for a long time and documented in the wealth of literature, but further investigations towards a predictive numerical model simulating the performance of a cover layer is required. The numerical model should cover the coupled thermo-biochemical mechanical processes in order to give predictions on methane emissions under critical environmental conditions such as desiccation, cold or rainy periods, or changing gas fluxes due to changes in atmospheric pressure, etc.

To that aim, the research project funded by the German Research Foundation (DFG) *'Description of limit and failure states for biological methane oxidation in landfills: experimental investigation, chemical analysis, mechanical modeling and computational simulation'* was interdisciplinary conducted together by three groups - Department of Urban Water and Waste Management under supervision of Prof. Widmann, Department of Instrumental Analytical Chemistry under supervision of Prof. Schmidt, both at the University of Duisburg-Essen (UDE), and the Institute of Mechanics, Structural Analysis and Dynamics under supervision of Prof. Ricken, University of Stuttgart, where the last one constitutes the affiliation of the author of this thesis.

The joint research project aimed to experimentally investigate and record the functioning and performance of the methane oxidation layer in landfills and to model it within the framework of a coupled multi-field simulation based on the Theory of Porous Media. The model should also be applicable for limit states, e.g. unfavorable temperature conditions or low methane loads, and be able to predict possible failure states, i.e. incomplete biological oxidation of the methane emitted from the landfill.

The basic understanding of the methane oxidation layer in landfills also opens the possibility of transferability to other boundary layers where methane oxidation occurs,

such as permafrost soils or the root zone of flooded plants.

For this purpose, in a first step the determining influencing variables were examined experimentally and mathematically transferred to the numerical model. The investigations are based on the hypothesis that the number and activity of methanotrophic bacteria are determined by the following major process variables: Temperature, moisture content, substrate (methane and oxygen) concentration, and bacterial number and type.

Accordingly, broad experimental studies were conducted at the Waste Management Department with the aim of determining the gas concentration rates under various initial and boundary conditions during the methane oxidation process. The experimental results, see Gehrke [54], served as calibration, verification and validation for the computational simulations based on mechanical model, developed for this purpose by the author of this thesis. The comparisons of experimental and computational simulation results are presented in Section 7.3.1 and 7.3.2. Additionally, the Department of Instrumental Analytical Chemistry performed investigations regarding the stable isotope analysis and CO_2/CH_4-ratios. For details see Schulte et al. [93]. The experimental setups were jointly developed by the project partners and served as base of the chemical analysis as well as the verification of the mechanical model.

The verification results of the numerical model through batch reactor tests are published in Ricken, Sindern[2] et al. [90], which is resumed in Section 7.3.1. Proceeding from this, Ricken, Thom et al. [89] documents the subsequent soil reactor experiments, which yield further validation techniques for a more comprehensive model verification. The application is described in Section 7.3.2.

All applied numerical simulations are developed and performed by this thesis' author in order to reproduce the experimental results and are documented in the following sections. For these, some further model assumptions additional to those described in Section 5.2, are taken in advance: the gas mixture contains the four gas components

$$\varphi^{\mathbf{G}} \bigcup_{\gamma} \varphi^{\gamma} \quad \text{with} \quad \gamma \in \{\mathrm{M,O,C,N}\}\,, \tag{7.2}$$

describing methane with M:=CH_4, oxygen with O:=O_2, carbon dioxide with C:=CO_2 and nitrogen N:=N_2. The soil moisture is considered sufficient that optimal conditions

[2]Published under the author's birth name.

for the bacteria are prevailing, represented by the assumption of the trapped liquid $\varphi^{\mathbf{L}}$ in the solid matrix $\varphi^{\mathbf{S}}$. Furthermore, according to Feng et al. [50], gas dissolution is ignored, since at steady state the amount of the gas in gaseous phase and dissolved gas in water are at equilibrium state, that is, no more gas dissolution can occur. Likewise, as applied for this thesis, the convective gas flow is often described by the momentum conservation law in the form of DARCY's law, as the flow in landfills is usually slow, and its REYNOLDS number is typically smaller than one, see Lu and Feng [72]. Regarding dispersion, cf. Section 4, they state "that dispersion may play a significant role in heterogeneous media characterized by widely spread vaues of permeability. If this is the case, a dependence of the effective diffusivity on the flow velocity must be accounted for. However, only few studies have considered the dispersion process in landfill gas transport. The molecular diffusion of gas components caused by Brownian motion results in an equalization of the concentration gradients of the species." Following that, including a dispersion coefficient is not considered for this work.

The major mechanisms for gas transport through a landfill cover soil are diffusion and advection, see Morris et al. [80] and authors therein. Diffusive transport is caused by a concentration gradient through the soil, whereas advective transport results from pressure gradients induced by wind, changing barometric pressure, or internal pressure build-up from landfill gas generation. Both advection- and diffusion-controlled fluxes need to be accounted for when modeling gas transport through soil covers. These principle transport mechanisms are further investigated in Section 7.4, to show the functionality of the model setup, where all other influencing factors like reaction or mechanical deformation are excluded.

As described above, the fundamental processes and material parameter were investigated by experiments and verified with related simulations based on reduced laboratory setups with focus on specific issues. Starting with an experimental setup of closed batch reactor systems, see Section 7.3.1, the laboratory measured data were used to examine the substrate kinetics for methane and oxygen and their related half-saturation constants for the bacterial methane conversion. Different experiments were conducted in dependency of the type of prevailing methanotrophic bacteria preferring either low (type I) or higher (type II) CH_4 concentrations with $> 4\%$, cf. Hanson and Hanson [58], as well as a number of samplings with different temperatures adjusted in order to determine the optimum temperature for bacterial conversion.

The results of the batch reactor experiments were recalculated by the author with the developed coupled FE model, with the result that the elementary reaction kinetics and their parameters could be verified and calibrated.

The subsequent experimental setup was designed in order to gain a continuous laboratory system in form of a soil reactor, such that thermal imaging can be applied, cf. Section 7.3.2. With the thermal imaging technique the heat of reaction produced during the process of methane oxidation, see (7.1), can be made visible and thus, the model can additionally be validated in terms of energy production. Moreover, soil samples were taken at different sampling ports over the height of the soil reactor, and measured and documented by the groups of UDE. The measurements provided information about the vertical gas concentration profiles and their isotopic distribution. The gas profiles in combination with the thermal image data were utilized by the author of this thesis to validate the developed model with focus on the vertical concentration distribution in combination with the heat generation during methane oxidation in a two-dimensional (2D) numerical FE simulation, where the main flow direction is basically one-dimensional. Additionally, the numerical study regarding the modeling of mixture diffusion coefficients according to Section 4.1 is performed by reference to this experimental setup.

Based on the validation of the simulation model, numerical calculations were subsequently carried out by the author determining the gaseous mass transport, especially the advective and diffusive fluxes, with the aim to verify, that the model is capable to represent these processes correctly, presented in Section 7.4. For that, the process of oxidation was disabled during the simulations, so that only the pure mass transport could be highlighted. A validation through laboratory experiments hence was not provided.

Unless otherwise noted, all calculations, simulations and related plots presented in the following sections are accomplished by the author of this thesis.

7.3.1. Batch reactor tests

The work of Ricken et al. [90] documents the basic isothermal multi-component, biphasic model approach validated by batch reactor tests. This investigation focuses

on the methane oxidation process coupled to the methanotrophic bacteria growth dependent on different initial conditions. For that, the set of unknowns contains $\mathcal{R}(\mathbf{x}, \mathrm{t}) = \{\mathbf{u_S}, \mathrm{p}^{\mathbf{GR}}, \mu^{\mathrm{G}\gamma}, \bar{\mathrm{c}}^{\mathrm{SB}}\}$, compare (5.126), where the concentration balances are varied with the corresponding chemical potential $\mu^{\mathrm{G}\gamma}$ instead of the molar concentration $\mathrm{c}_m^{\mathrm{G}\gamma}$. The investigation is conducted for different, but constant temperatures, so that the balance of energy (6.24) and temperature θ as degree of freedom is not invoked. Moreover, the amount of methanotrophic cells $\bar{\mathrm{c}}^{\mathrm{SB}}$ is introduced and solved together with an evolution equation for the bacteria given with

$$\int_{\mathrm{B_S}} \{(\bar{\mathrm{c}}^{\mathrm{SB}})'_{\mathbf{S}} - \hat{\rho}^{\mathrm{SB}}\}\, \delta\bar{\mathrm{c}}^{\mathrm{SB}}\, \mathrm{dv} = 0\,, \tag{7.3}$$

wherein $\hat{\rho}^{\mathrm{SB}}$ denotes the growth rate of the bacteria. A detailed description of the bacteria growth rate is given in Ricken et al. [90].

For the investigation of the reaction kinetics, a discontinuous experimental system in form of batch reactors was installed, see Fig. 7.7. Batch tests offer a well-established small-scale laboratory tool with a limited probe volume. Such a setup allows the precise adjustment of initial boundary conditions. The batch reactors contained initial

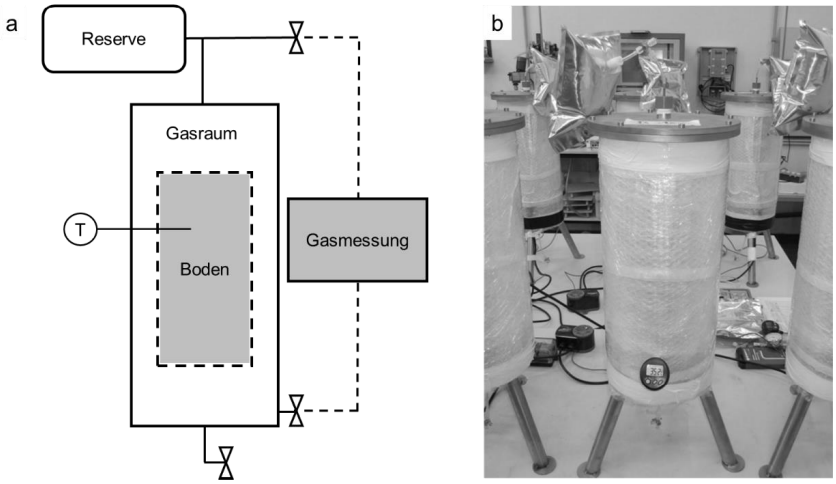

Figure 7.7.: Schematic diagram of the internal structure (a) and picture of a batch reactor (b), see Gehrke [54].

methane concentrations of 20% on the one hand and 8% on the other hand, and were conducted for constant temperatures from 5°C to 40°C in steps of 5 degrees. A constant liquid content of the contained soil probe was measured daily over a period

of about 14 days, see [90], which verifies the assumption of the liquid phase to be included in the solid phase and not to be considered as degree of freedom for the related computational simulations. Additionally, the concentrations of CH_4, CO_2 and O_2 were measured daily for the duration of the experiment, which provided information on the maximum methane degradation rate $\hat{\rho}^{\mathrm{GM}}_{\mathrm{max}}$ for each temperature, as well as the optimum temperature for the methanotrophic bacteria θ_{opt}, see (7.6).

The methane oxidation rate $\hat{\rho}^{\mathrm{GM}}$, dependent on limiting factors substrate, temperature and cell number, is established in the model with

$$\hat{\rho}^{\mathrm{GM}} = -\hat{\rho}^{\mathrm{GM}}_{\mathrm{max}}\,\hat{\rho}^{\mathrm{GM}}_{\mathrm{GM}}\,\hat{\rho}^{\mathrm{GM}}_{\mathrm{GO}}\,\hat{\rho}^{\mathrm{GM}}_{\theta}\,\bar{\mathrm{c}}^{\mathrm{SB}}\,, \tag{7.4}$$

as e.g. proposed by Haarstrick et al. [57]. The conversion rate $\hat{\rho}^{\mathrm{GM}}$ is calculated by the maximum rate per cell $\hat{\rho}^{\mathrm{GM}}_{\mathrm{max}}$, multiplied by the rate limiting functions $\hat{\rho}^{\mathrm{GM}}_{\mathrm{GM}}$, $\hat{\rho}^{\mathrm{GM}}_{\mathrm{GO}}$ and $\hat{\rho}^{\mathrm{GM}}_{\theta}$ and the actual cell number. The first two functions reflect the dual-substrate Michaelis-Menten kinetics for biochemical processes, which is the general-purpose model for methane oxidation, see e.g. Scheutz et al. [92]. Moreover, $\hat{\rho}^{\mathrm{GM}}_{\theta}$ describes the temperature dependency of bacterial oxidation. All rate limiting functions vary dimensionless between 0 and 1, see Figure 7.8. Figure 7.8a plots the relation for the substrate dependencies of methane and oxygen. These are based on the standard kinetics referring to Monod [79] with

$$\hat{\rho}^{\mathrm{GM}}_{\mathrm{GM}} = \frac{(\mathrm{c}^{\mathrm{GM}}_{m})^2}{\mathrm{K}_{\mathrm{GM}} + (\mathrm{c}^{\mathrm{GM}}_{m})^2} \qquad \text{and} \qquad \hat{\rho}^{\mathrm{GM}}_{\mathrm{GO}} = \frac{(\mathrm{c}^{\mathrm{GO}}_{m})^2}{\mathrm{K}_{\mathrm{GO}} + (\mathrm{c}^{\mathrm{GO}}_{m})^2}\,, \tag{7.5}$$

where for the batch test simulations a quadratic approach for the molar concentrations suited better in the simulation than the linear MONOD relation[3]. The parameters K_{GM} and K_{GO} denote the half saturation constants for methane and oxygen. Additionally, Fig. 7.8b shows the temperature dependency based on the proposed exponential function

$$\hat{\rho}^{\mathrm{GM}}_{\theta} = \exp\left[-\kappa_{\theta 2}(\theta - \theta_{opt})^2\right], \tag{7.6}$$

with the material parameter $\kappa_{\theta 2}$. The stoichiometry for the methane oxidation equation (7.1) is implemented into the model with rates for the oxygen and carbon

[3] A plot of the comparison of measured methane oxidation rate to the calculated rates through the simulation is documented in [90].

dioxide mass exchange $\hat{\rho}^{\mathrm{GO}}$ and $\hat{\rho}^{\mathrm{GC}}$, which are functions of the methane conversion rate in accordance to (5.93) with

$$\hat{\rho}^{\mathrm{GO}} = +2\,\hat{\rho}^{\mathrm{GM}} \qquad \text{and} \qquad \hat{\rho}^{\mathrm{GC}} = -1\,\hat{\rho}^{\mathrm{GM}}\,. \tag{7.7}$$

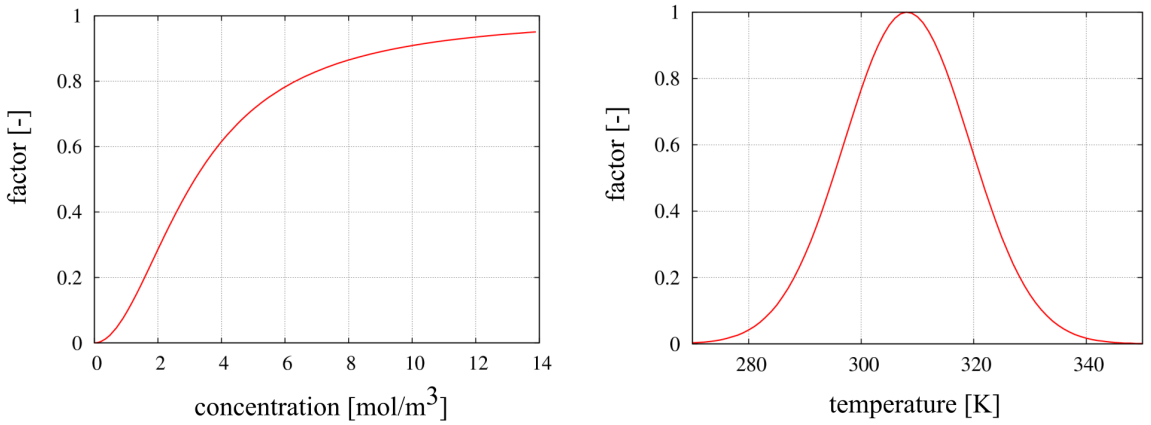

(a) $\hat{\rho}^{\mathrm{GM}}_{\mathrm{GM}}/\hat{\rho}^{\mathrm{GM}}_{\mathrm{GO}}$ for $\mathrm{K_{GM}/K_{GO}} = 10$ **(b)** $\hat{\rho}^{\mathrm{GM}}_{\theta}$ for $\kappa_{\theta 2}$=0.004

Figure 7.8.: Rate limiting functions applied in the model depending on substrate and temperature, cf. Ricken, Sindern et al. [90].

For verification of the chosen model equations regarding the reaction kinetics and included material parameters (7.4)-(7.7), simulations were performed corresponding to the given initial concentrations and temperature adjusted for the batch experiments. The comparative results of the calculated concentrations by the FE simulations to the measured concentrations of the batch experiments for a duration of ten days are given in Figure 7.9. A detailed description of the material parameters used for these simulations can be looked up in [90]. The picked examples started with high initial methane concentrations (∼20 vol.-%), so that mainly methanotrophs type II accounted for the methane degradation. The well matching curves of the measured batch concentrations and the calculated ones allow the conclusion that the chosen equations are reasonable and can represent the reaction processes during bacterial methane oxidation well.

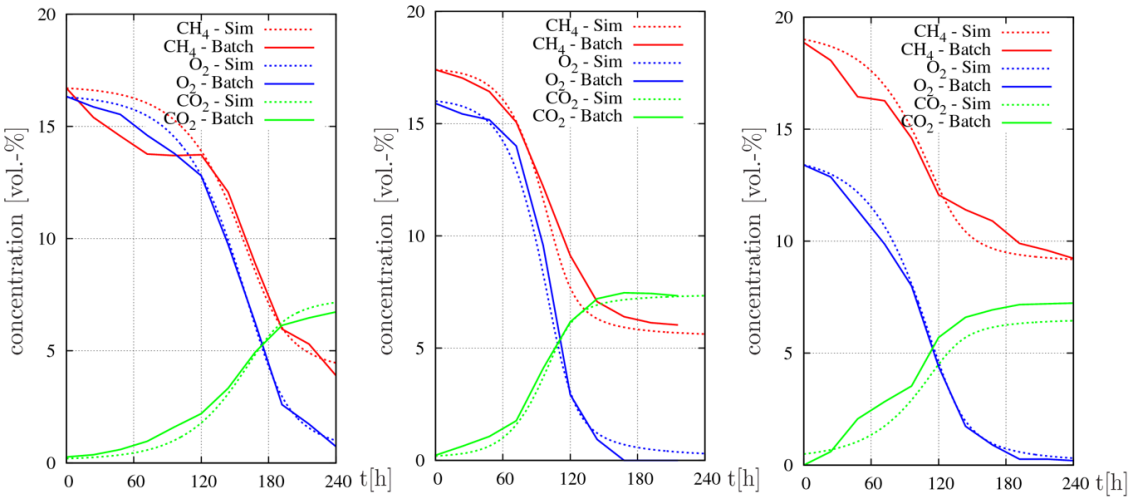

(a) $\theta = 30°C$ (b) $\theta = 35°C$ (c) $\theta = 40°C$

Figure 7.9.: Concentration profiles calculated by FE simulation (dotted lines) and measured concentrations during batch experiments (continuous lines), taken from Ricken, Sindern et al. [90]

.

7.3.2. Soil reactor system and thermal imaging technique

The theoretical model is further validated by an experimental setup developed for this purpose in cooperation with the project partners, published in Schulte et al. [93] and Ricken, Thom et al. [89]. The setup enables the visualization of the spatial distribution of the methane horizon via thermal imaging in addition to measurements of the gas concentrations. As methanotrophic bacteria emit energy in form of heat as a by-product of their metabolism, cf. (7.1), this effect can be related to bacterial activity and utilized to locate the position of the oxidation horizon in a reaction vessel.

The technical installation was designed to enable a reactor system for a soil sample, illustrated in Fig. 7.10. Two plexiglass plates fixed to two stainless steel frames were arranged in front of each other with a gap of 12 cm in between to serve as the framework for the soil reactor system.

The structure inside the slab consists of a gas distribution layer, followed by filled soil with a height of about 110cm (0.26m^3 top soil, water content 9.7% w/w, organic dry substance 2.2%). The residual volume above the soil section (head space $\sim$ 25cm) acts as atmosphere and is flushed by air from a mass flow controller (MFC). At the bottom

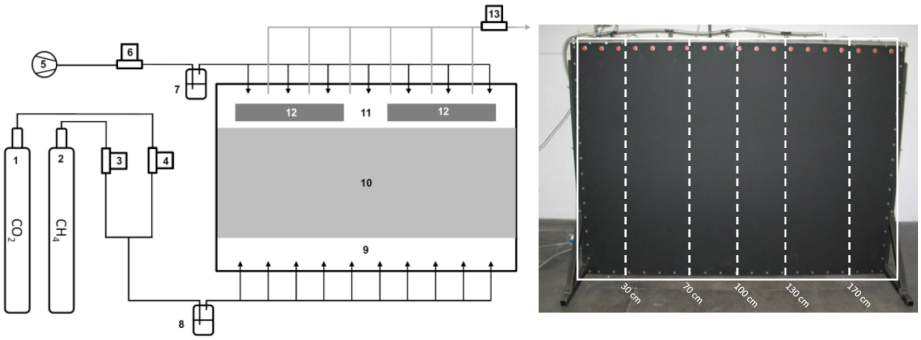

Figure 7.10.: Experimental setup, see [89]. Left: (1) carbon dioxide supply, (2) methane supply (3) MFC for CH_4 (4) MFC for CO_2 (5) compressor (6) MFC for air (7+8) humidifier (9) gas distribution layer (10) soil section (11) atmospheric gas phase (12) heat exchanger (13) MFM for air (14) off-gas. Right: Front of the blackened plexiglass plate with marked area for thermal imaging, broken lines indicate sampling profiles.

of the reactor system two further mass flow controllers were installed to feed the soil system via ten evenly distributed ports with humidified methane and carbon dioxide, to avoid desiccation of the soil body. Fig. 7.10 (right) indicates the five individual sampling profiles (dashed lines) for the documentation of the gas distributions.
Additionally, a thermographic camera was installed in front of the reaction system. In order to achieve a high resolution of the thermal images and to eliminate reflections, the front plexiglass plate was blackened. Except for the front side of the system facing the thermal imager, the reactor was insulated. The camera was calibrated for 'heated surfaces' in an air-conditioned room in which the laboratory experiment was conducted, cf. [93]. Steady state temperatures throughout the soil body for the initial state were assumed to be reached when the temperature of the inflowing and outflowing gases approached steady values [93].

For the numerical calculation of the corresponding initial boundary value problem (IBVP) only one sampling profile with a width of 10 cm is modeled exemplarily, see Fig. 7.11, although the experiment showed slightly varying concentration and temperature profiles across the different sampling ports, which is due to natural heterogeneities of the soil. The set of unknowns for the simulation is given with

$$\mathcal{R}(\mathbf{x}, \mathrm{t}) = \{\mathbf{u_S}, \mathrm{p}^{\mathbf{GR}}, \mathrm{c}_m^{\mathrm{GM}}, \mathrm{c}_m^{\mathrm{GO}}, \mathrm{c}_m^{\mathrm{GC}}, \theta\}, \tag{7.8}$$

cf. (5.126). In this simulation, additionally the temperature degree of freedom is

included, whereas the actual cell number $\bar{c}^{\mathrm{SB}}$ is skipped and replaced by the maximum oxidation rate per unit soil with

$$\hat{\rho}^{\mathrm{GM}}_{\mathrm{max}} = \mathrm{V}_{max}\, \rho^{\mathbf{S}\mathrm{R}}\,, \tag{7.9}$$

providing a suitable approach for continuous experiments leading to a steady state with constant fluxes. V_{max} can be chosen from literature, cf. Berger [11], depending on the given soil.

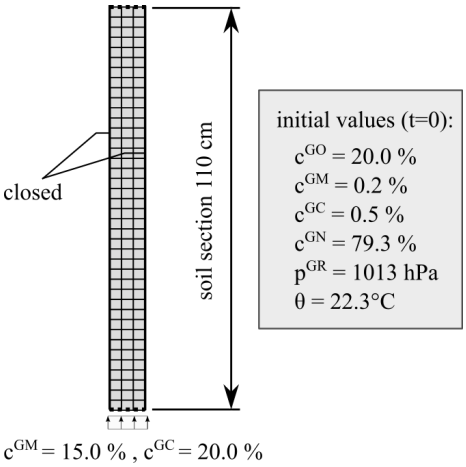

Figure 7.11.: IBVP of the soil reactor simulation

Figure 7.11 illustrated the modeled IBVP, where the initial values at t = 0 were chosen referring to atmospheric conditions with percentage values for O_2 = 20.0%, N_2 = 79.3%, CO_2 = 0.5% and CH_4 = 0.2%. Additionally a standard atmosphere of $\mathrm{p}_0^{\mathbf{G}\mathrm{R}}$ = 1013 hPa was applied. The experiment revealed a room temperature of 22.3°C, and the gas flows during the experiment were adjusted with 10mL/min each for CH_4 and CO_2, which led to entering concentrations of 15.0% for CH_4 and 20.0% for CO_2 to the soil serving as DIRICHLET boundary conditions for the numerical model. The head space of the reactor system is also considered as DIRICHLET boundary, i.e. the upper horizontal boundary of the model is fixed with the initial atmospheric values but held permeable, so that gas fluxes adjust over the surface. The vertical boundaries at each side are impermeable for all degrees of freedom, as well as the lower horizontal boundary, which is impermeable for O_2 and heat exchange.

The initial values and further material parameter of the model can be observed in Tab. 7.1, where $(...)_0$ indicates the initial values at time t = 0.

Table 7.1.: Initial values and material parameters

Parameter	Symbol	Value	Unit
volume fraction solid/gas	$n_0^{\mathbf{S}}/n_0^{\mathbf{G}}$	0.88/0.12	[-]
density solid	$\rho^{\mathbf{S}^{\mathrm{R}}}$	1200	[kg/m^3]
temperature	θ_0	22.3	[°C]
pressure	$p_0^{\mathbf{G}^{\mathrm{R}}}$	1013.25	[hPa]
diffusion coefficient CH_4/CO_2	D_{GM}/D_{GC}	6.0E-6/1.0E-4	[m^2/s]
diffusion coefficient O_2/N_2	D_{GO}/D_{GN}	1.9E-5/1.3E-5	[m^2/s]
intrinsic permeability	$K^{\mathbf{S}}$	10E-14	[m^2]
dynamic viscosity gas mixture	$\eta^{\mathbf{G}^{\mathrm{R}}}$	13E-6	[Ns/m^2]
heat dilatation coefficient	$\alpha^{\mathbf{S}}$	20E-6	[1/K]
heat conductivity coefficient	$\alpha_{\nabla\theta}$	1.6	[W/(mK)]
specific heat capacity solid	$c_V^{\mathbf{S}}$	800	[J/(kgK)]
specific heat capacity CH_4/CO_2	c_V^M/c_V^C	2160/v	[J/(kgK)]
specific heat capacity O_2/N_2	c_V^O/c_V^N	1000/930	[J/(kgK)]
max oxidation rate	V_{max}	7.5E-7	[mol/(kgs)]
half saturation constant CH_4/O_2	K_{GM}/K_{GO}	0.005/0.001	[-]

The reactor system was monitored over several days by the project partners at UDE. At experiment start (denoted with t = 0) a tolerably homogeneous temperature distribution throughout the soil of about 23°C could be documented, see Fig. 7.12a. The soil temperature adjusted finally to the surrounding room temperature of ∼22.3°C, which was chosen as initial value for the numerical model, cf. Fig. 7.12b. Moreover, a clearly observable oxidation horizon could be observed after approximately four days of experiment (t = 4 days), with a slight temperature increase of 0.3°C.

The initial higher temperature throughout the soil at experiment start is presumable due to the fact, that at the beginning the bacterial activity is evenly distributed over the whole soil section, as the bacteria discover optimal substrate conditions where oxygen is available everywhere. This changes, once the initially available oxygen is consumed. A steady state is then achieved by the incoming flow of oxygen from the atmosphere and the methane flow from the bottom gas supply. The corresponding simulation to validate the model by the thermal image data is described hereafter, see also Figure 7.20.

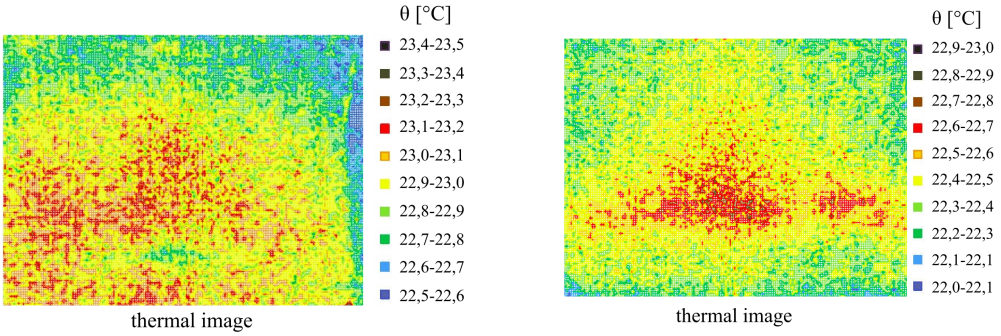

(a) t = 0 **(b)** t = 4 days

Figure 7.12.: Contour plot of thermal images of soil section indicated by temperature θ [°C] at experiment start and after 4 days, see [89]. Data provided by T. Gehrke, edited by A. Thom.

With the chosen IBVP described in Figure 7.11, the simulations were performed and verified by the author utilizing the measured concentrations profiles during the experiments and additionally with the help of the thermal image data, where the experimental part again was obtained by the UDE partners. Adopting the conditions that have emerged in the course of thermal image validation, the simulation was executed to cover in total a period of four days. For a validation of the calculated concentration profiles in the steady state, a simulation covering one hour with time increments of Δt = 10s was executed. In order to validate the energy production and temperature development, the simulations were restarted after reaching the steady state and covered an additional period of four days by invoking time increments of Δt = 60s.

Concentration profiles

Investigating the concentration profiles, Figure 7.13 and 7.14 show the spatial distribution of oxygen and methane, which has been set during the FE simulation at different time increments, indicated by their molar fractions. In the right, the FE simulation plots of the calculated concentrations for simulation time steps at 10s, 1min, 5min, 10min, 30min, and 1h are presented. For these selected time steps, the corresponding graphs of the concentration values are plotted over the height of the geometric soil model - diagrams in the left part. Initially, oxygen is evenly distributed over the height of the model domain with a concentration of about 12%. As soon as the applied

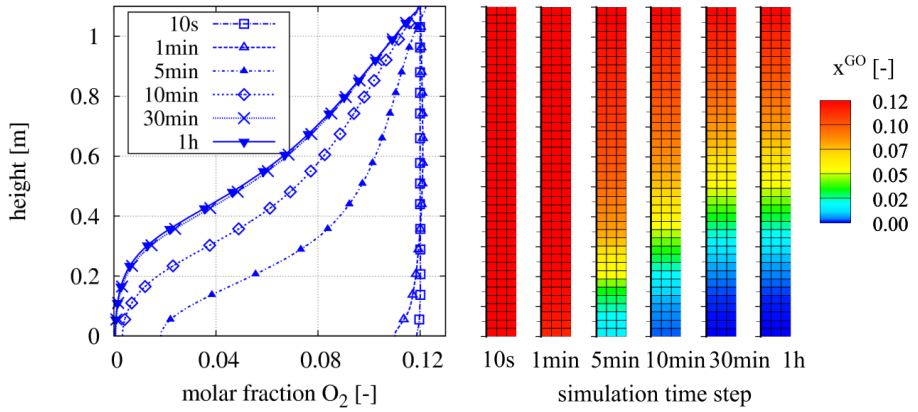

Figure 7.13.: Molar fraction of oxygen x_m^{GO} [-] over height of soil reactor for different time steps of the simulation

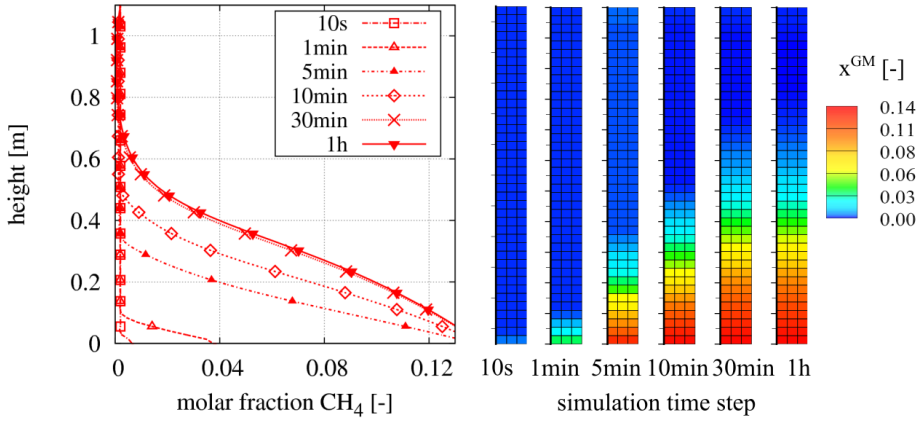

Figure 7.14.: Molar fraction of methane x_m^{GM} [-] over height of soil reactor for different time steps of the simulation

methane develops upwards from the bottom boundary, and both gases required for the reaction are sufficiently present, the available oxygen is consumed. For the reaction of methane and oxygen the steady state is approximately established after 30min, which can also be followed in Fig. 7.15. Therein, the methane oxidation rate is plotted over the height of the model at the chosen time increments of the simulation. Initially, there are much higher oxidation rates than in the steady state from 30min on due to the higher molar concentrations of O_2 and CH_4. Lower substrate concentrations reduce the oxidation rate by the rate limiting functions (7.4).

The equivalent plots of the mole fractions of the remaining gases of the mixture nitrogen and carbon dioxide can be found in App. D.1. Since these gases are inert, the steady states are reached immediately after approximately 5 minutes.

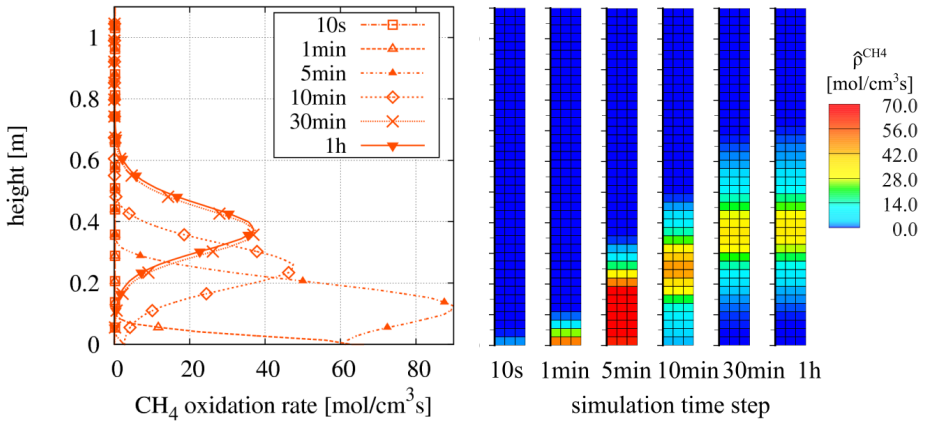

Figure 7.15.: Methane oxidation rate $\hat{\rho}^{\mathrm{GM}}$ [mol/m^{3}s] over height of soil reactor for different time steps of the simulation

For model validation the gas concentration distributions over the height of the soil reactor are invoked for the steady state at 30min, and the calculated values through the simulation (continuous lines) are plotted against the measured concentration values of the experiment (symbols), see Fig. 7.16. One can observe nearly exact matching curves of oxygen and methane, where also the area of the methane horizon at about 0.4 m height was exactly hit. Only the simulated distribution of carbon dioxide deviates from this point on, where the simulation overestimates the CO_2 production. The curve indicates, that also CO_2 is consumed and/or can be attributed to the changing soil permeability, which can conclude from biomass production, as methanotrophic bacteria use carbon also for catabolism, which is not implemented in the model equations. Moreover, CO_2 is preferentially partitioned to soil moisture because it is more soluble than CH_4, see Scheutz et al. [92]. The numerical simulations

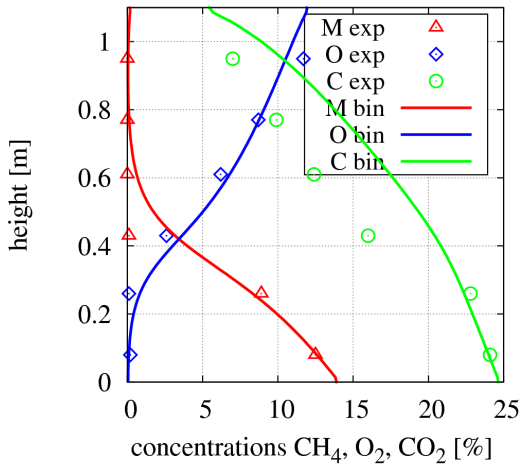

Figure 7.16.: Concentration distribution with binary diffusion coefficients for CH_4 (M bin), O_2 (O bin), CO_2 (C bin) over the height of the soil reactor calculated by simulation (lines) in comparison to measured experimental values (symbols) at steady state.

ran with fixed binary diffusion coefficients, see Table 7.1, which are based on the values of the diffusion coefficients of the respective gas in air, without considering the changing composition of the gas mixture during methane oxidation. The comparison to the implementation of calculated diffusion coefficients for mixtures according to (4.3) is given in Section 7.3.2.

Figure 7.17 displays the pressure change of the gas mixture during the simulation. The simulation starts with an initial pressure of $p_0^{GR} = 1013$ hPa of the gas mixture. In the further course of the simulation a depression and thus density reduction develops in the region of the oxidation horizon at 0.4m ± 0.2m, due to the given molar reaction equation, cf. (7.1).

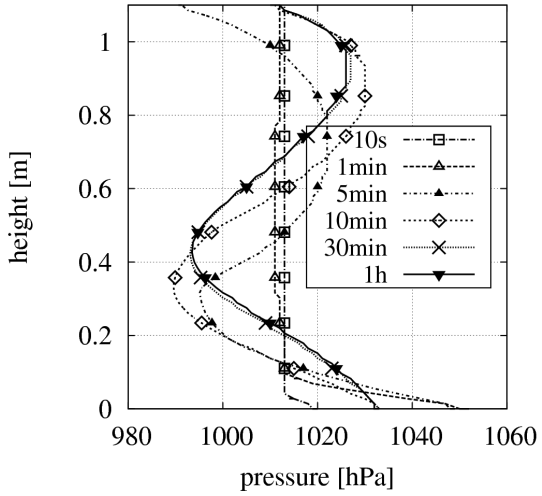

Figure 7.17.: Calculated pressure p^{GR} distribution by simulation over height of soil model for different time steps of simulation

The reaction equation states, that three gaseous molecules are reacting to one leading to a pressure and thus density decrease. Since the upper boundary is fixed with the atmospheric gas pressure of 1013 hPa as DIRICHLET boundary condition, a gaseous flux over the surface develops to keep the given pressure, which in turn leads to an overpressure and increasing density in the upper model area at 0.8 m ± 0.2 m. The upper boundary holds as well fixed values for the atmospheric concentrations of O_2, CO_2 and CH_4 adapted to the experimental conditions, so that the pressure compensation takes place with the flux of N_2, see also Fig. 7.19b.

Having a closer look on the magnitudes of the molar fluxes of the four gas components during the simulation, Figures 7.18 and 7.19, reveals that the methane oxidation in this experimental setup is mainly diffusion-driven. In these figures, the total molar

fluxes (grey lines) are compared to the diffusive ones (blue, red, green and pink lines for O_2, CH_4, CO_2, and N_2) for selected time steps (at 5, 10 and 60 minutes) of the simulation and plotted again over the height of the soil model domain.

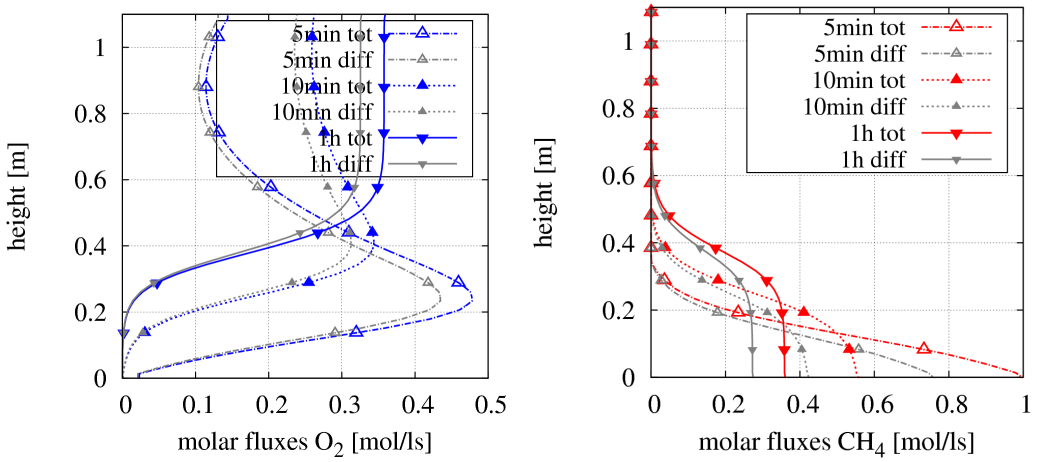

(a) O_2 **(b)** CH_4

Figure 7.18.: Magnitudes of total molar fluxes ${}_m\mathbf{j}^{G\gamma}_{tot}$ in comparison to diffusive part ${}_m\mathbf{j}^{G\gamma}_{diff}$ for $\gamma \in \{O_2, CH_4\}$ at different time steps of simulation

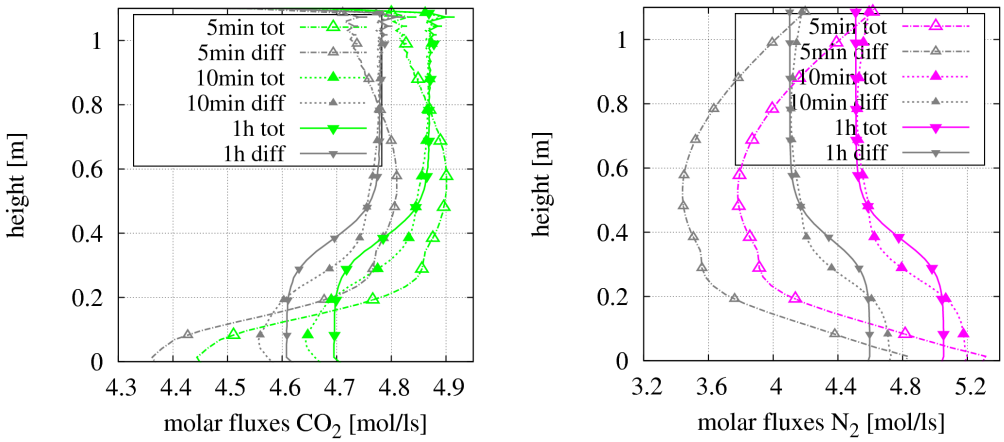

(a) CO_2 **(b)** N_2

Figure 7.19.: Magnitudes of total molar fluxes ${}_m\mathbf{j}^{G\gamma}_{tot}$ in comparison to diffusive part ${}_m\mathbf{j}^{G\gamma}_{diff}$ for $\gamma \in \{CO_2, N_2\}$ at different time steps of simulation

It becomes clear, that for all gas components the magnitudes of the diffusive parts are nearly the same as the magnitudes of the total fluxes despite their different courses. This is even more evident for the fluxes of oxygen and methane, where the

corresponding curves are almost on top of each other, cf. Fig. 7.18. For the inert gases carbon dioxide and nitrogen a more pronounced difference can be made out, where the diffusive fraction is at around 97% of the total amount for CO_2 and around 90% for CH_4 on average, see Figure 7.19. Here, the advective amount is higher as a consequence of the density and thus pressure change during methane oxidation, compare Figure 7.17, so that the pressure difference is compensated by suction of the inert gases to the area of reaction (mainly in the range of ∼0.3 - 0.8m soil height).

Additional pressure build-ups occuring *in-situ* in landfills leading to advective gas flow like surface winds, changing barometric pressure, landfill gas generation, are not relevant for these laboratory soil reactor conditions. The general interaction of diffusive and advective gas flows for different conditions are investigated in Section 7.4.

Thermal imaging

A further validation technique offers the method of thermal imaging, which was applied by the participants of the project to visualize the heat of reaction of methane oxidation. With this procedure, temperature profiles could be determined over the width and height of the soil reactor, which were compared to the calculated temperature distribution through the simulation. Figure 7.20 shows the spatial temperature development for selected time steps of the simulation, that covered in total a period of 96 hours, in comparison to measured temperature data at the fourth day of experiment. The representative simulation time steps to demonstrate the temperature development were chosen with 1h, 12h, 48h, 72h, and 96h. The laboratory temperature data in graph 7.20 (left) were taken from the thermal image resolutions provided by the project partners of UDE, in which a temperature is assigned to each pixel of the images. Figure 7.20 (right) shows the FE plots of the temperature distribution of the corresponding simulation for the selected time steps. From these FE calculations the vertical temperature profiles over the height of the soil model domain were derived (dashed-dotted lines of Fig. 7.20 (left)) and compared to the experimentally derived temperature profile. The error bars are indicating minimum and maximum temperature values over the width of the laboratory soil reactor.

As documented in Fig. 7.12b, a clear methane horizon was observed after four days

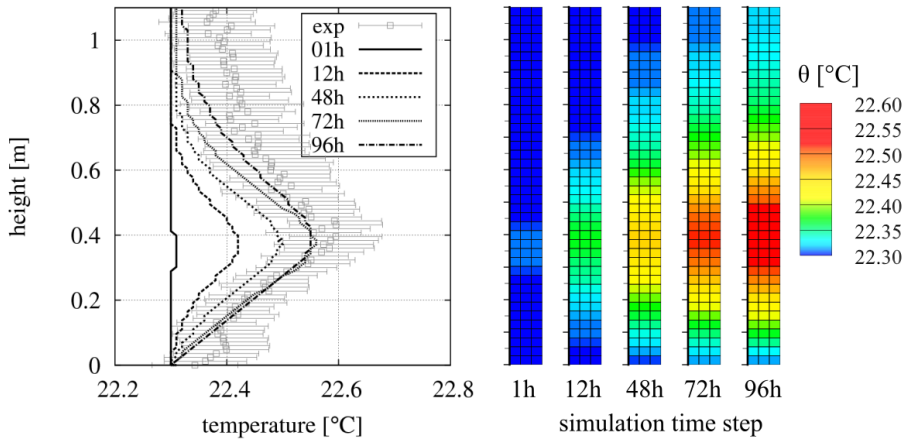

Figure 7.20.: Comparison of temperature distribution at different time steps of simulation (dashed-dotted lines) and averages of measured temperature over height of soil reactor (symbols) after 4 days (96h); error bars indicating min/max values

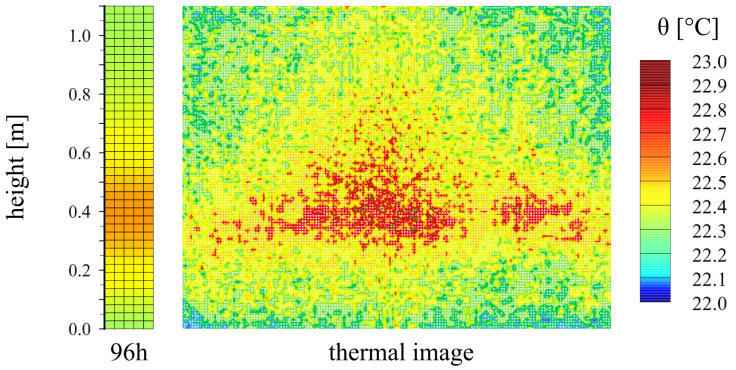

Figure 7.21.: Simulated temperature distribution (left) after 4 days (96h) in comparison to thermal image of reactor system (right).

of experiment, which led to a simulation time covering a period of 96 hours. Figure 7.21 shows the matching values of the simulation[4] (left) and the experiment (right) at t = 4 days, where the simulated temperature distribution lies totally within the scope of the averaged measured values. The temperature peak at a height of 0.4 m illustrates the region of the oxidation horizon, which is also in accordance with the location of the calculated maximum methane oxidation rate at steady state in the simulation, compare Fig. 7.15.

[4]The temperature range was rescaled for this comparison from 22.3-22.6 to 22.0-23.0 °C to fit the range of the thermal image.

Investigation of diffusion coefficients

The previous numerical calculation used fixed binary diffusion coefficients according to Table 7.1. These were chosen referring to values of the respective gas diffusing in air without considering the changing gas mixture. But, as derived in Sect. 4.1, for a multi-component mixture the calculation of mixture diffusion coefficient (4.3) is more suitable. Preliminary studies on the calculation of the diffusion coefficients applied to the topic of methane oxidation are published in Thom et al. [101]. The soil reactor experiment as well as the corresponding simulation presented in the previous section are invoked as references.

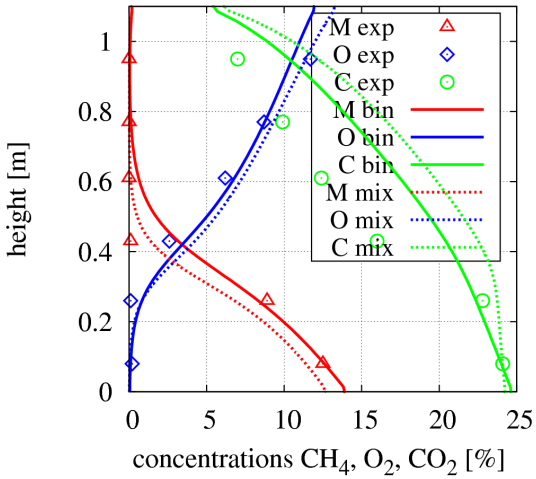

Figure 7.22.: Comparison of experimental data (symbols), reference simulation from Fig. 7.16 with binary diffusion coefficients (continuous lines), and simulation with mixture diffusion coefficient according to (4.3) (dotted lines).

For that, still binary diffusion coefficients need to be implemented, which were taken from Molins and Mayer [77]. With these, the mixture coefficient according to (4.3) is calculated throughout the simulation.

Figure 7.22 shows the comparison of the three concentration distributions for the experimental values plotted with symbols, the reference simulation of Section 7.3.2 plotted by continuous curves and the calculation with (4.3) plotted with dotted curves. The simulation with a calculation of the mixture coefficients fits well and slightly better to the experimental data, especially for the flow of methane and oxygen. The course of the CO_2 concentration, on the other hand, worsens, and the production is overestimated even more. The possible explanations for that issue as given in Section 7.3.2 remain, and a triphasic simulation might promise improvement. However, for future simulations, the implementation of the mixture diffusion coefficient

should be followed. This calculation only needs the given initial values for the binary diffusion coefficients $D_{\beta\iota}$, which can be taken from literature, and the following calculations of the mixture coefficient, depending on the actual concentrations via $x_m^{\alpha\beta}$ and $\omega^{\alpha\beta}$, respectively, provides automatically the right values. With this procedure, a fit of a constant diffusion coefficient as done in Section 7.3.2 is obsolete.

The application of the tortuosity coefficient τ, see (4.4) was not expedient for this calculation. Implementing the formula according to Millington and Quirk [76] produced very small diffusion coefficients with approximated values for the saturation and fluid content, which was not suitable. Simply the basic generalized FICK's law (4.2) in combination with the mixture diffusion coefficient (4.3) and the implementation in the multi-phase description with ${}_m\mathbf{j}^{\gamma}_{diff} = \mathrm{n}^{\mathbf{G}}\,{}_m\mathbf{j}^{\mathrm{G}\gamma}_{diff}$, cf. Table 3.2, was sufficient to reproduce the concentration developments.

7.4. Numerical investigation of gaseous mass transport

In order to investigate basic properties and capabilities of the model regarding the diffusive and advective mass fluxes and their interaction, additional comparative simulations were performed by the author on the following IBVP, see Figure 7.23. The spatial area for examination is defined as a 0.10m wide strip with a thickness of 0.02m. Therein, the spatial positions of three nodes are marked for later identification, node 1 in red (n1), node 2 in green (n2) and node 3 in blue (n3). The vertical boundaries at x=0.0m and x=0.10m are basically permeable for gas flow, which can be adjusted with either DIRICHLET or NEUMANN boundary conditions for the overall pressure and each considered concentration, cf. also Figure 6.1.

For the following examples the left vertical boundary at x=0.0m can be chosen as DIRICHLET boundary for the overall pressure $\mathrm{p}^{\mathbf{G}\mathrm{R}}$, indicated by black arrows, as well as for the concentrations $\mathrm{c}^{\mathrm{G}\gamma}_m$ indicated by the blue arrows, here oxygen. The right vertical boundary at x=0.10m can be chosen as NEUMANN boundary and thus offers outflow conditions for $\mathrm{p}^{\mathbf{G}\mathrm{R}}$ and $\mathrm{c}^{\mathrm{G}\gamma}_m$. The horizontal boundaries at y=0.0m and y=0.02m are impermeable for gas flow, but tangential gas flow is enabled at the interface, yielding slip wall conditions. Moreover, for the simulations solid deformation is prevented by applying a rigid solid matrix and moreover, the temperature is held

constant yielding isothermal conditions. As in the former sections, the gas mixture contains the four gas components $\varphi^{\mathbf{G}} \bigcup_{\gamma} \varphi^{\gamma}$ with $\gamma \in \{\mathrm{M,O,C,N}\}$, describing methane with M:=CH_4, oxygen with O:=O_2, carbon dioxide with C:=CO_2 and nitrogen N:=N_2. For all upcoming presented simulations, the bacterial reaction of methane and oxygen is disabled so that the focus is on the purely diffusive and advective mass transport and its interaction.

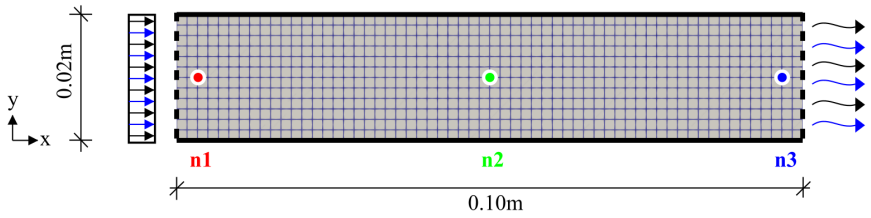

Figure 7.23.: IBVP for principle advective-diffusive investigations. Points n1, n2, n3 characterize nodes 1,2, and 3

For a good assessment of the simulation results, characteristic atmospheric values for air as well as soil are chosen and parameters are given as follows: the soil porosity has an intrinsic permeability $\mathrm{K}^{\mathbf{S}} = 10^{-12}$ m^2 and an initial volume fraction of $\mathrm{n}^{\mathbf{S}}$= 0.8. The dynamic viscosity of air is $\eta^{\mathbf{GR}} = 1.8 * 10^{-5}(\mathrm{Ns/m^2})$, yielding the coefficient of $\mathrm{k}_0^{\mathbf{G}} = 5.5 * 10^{-7}(\mathrm{m^4/Ns})$, cf. (4.7). The initial pressure is set to $\mathrm{p}_0^{\mathbf{GR}} = 1013\mathrm{hPa}$, and the molar fractions to $x_m^{\mathrm{GM}} = 0.0016$, $x_m^{\mathrm{GO}} = 0.02$, and $x_m^{\mathrm{GC}} = 0.04$. The remaining molar fraction for the main component of air, nitrogen, x_m^{GN} is calculated by the model according to (3.20). The boundary conditions are chosen in such a way that a constant atmospheric concentration of oxygen with $x_m^{\mathrm{GO}} = 0.20$ as DIRICHLET boundary condition is applied on the left vertical boundary at x=0.0m, whereas the right vertical boundary at x=0.1m is permeable for fluxes in x-direction, representing an oxygen depleted soil, so that an oxygen inflow is created. The remaining variables of the model are chosen equally to Table 7.1, whereas the temperature is set to $\theta_0 = 20°\mathrm{C}$.

7.4.1. Diffusion and low advection

In the first comparison of IBVP‘s, a purely diffusive problem is simulated (in the following left columns of Figures 7.24 - 7.28) and compared to a problem with a low

pressure gradient of Δp^{GR}=1hPa (right columns of following figures), inducing a slow filter velocity and thus slight advection. For that, a concentration of oxygen is applied for a time of 10s to the left vertical boundary, and thereafter stopped, see Fig. 7.24. The graphs show the increasing molar fraction for node 1 (n1) until a simulation time of 10s. The right vertical boundary at x=0.1m is closed for oxygen flux but fixed with the initial atmospheric pressure of 1013hPa, so that an overall gas flux adjusts to hold this value. Figure 7.24a shows the approaching values for

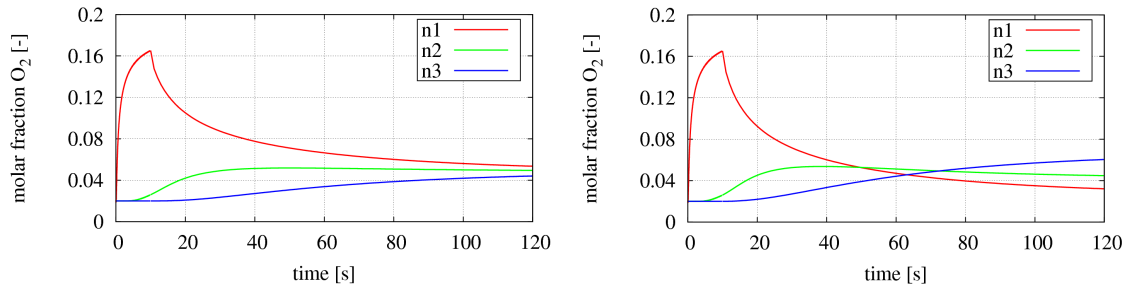

(a) diffusion **(b)** low advection

Figure 7.24.: Molar fraction of oxygen x_m^{GO} for node 1 (n1), node 2 (n2) and node 3 (n3) over simulation time

node 1, node 2 and node 3 over time, indicating the temporal concentration balancing process of diffusion, whereas Fig. 7.24b shows decreasing values for node 1 and further increasing values for node 3, what is attributed to the slow advection process which slightly transports and accumulates the concentration build up from the left to the right vertical boundary. The diffusive and slow advection processes can be followed

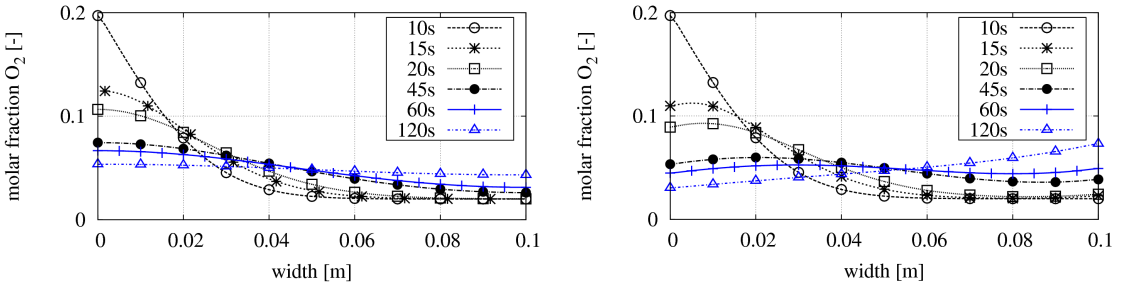

(a) diffusion **(b)** low advection

Figure 7.25.: Comparison of molar fraction x_m^{GO} over model width for different simulation time steps

by Fig. 7.25, where the spatial distributions of the molar fraction of oxygen over the width of the geometric model for different simulation time steps are plotted. Looking

at Fig. 7.25a one can see, that at t=120s the graph is nearly horizontal from left to right boundary, indicating the almost constant concentration distribution at steady state. In contrast to that, the graph for the same simulation time step shows the concentration accumulation at the right boundary.

Figure 7.26 plots the corresponding results of the finite element simulation. Moreover, comparing the spatial concentration profiles to the trend curves of Fig. 4.2 indicates, that the example with a low induced filter velocity, (Fig. 7.25b) still seems to be driven by diffusion and thus can be categorized as a process with a small PECLÉT number.

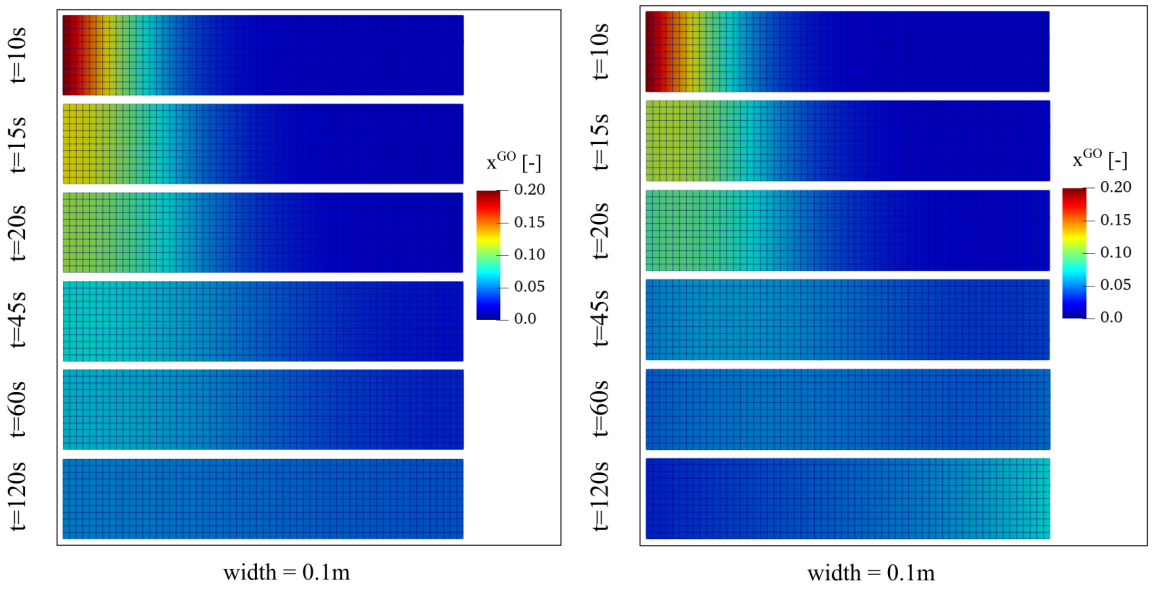

(a) diffusion **(b)** low advection

Figure 7.26.: FE contour plots of molar fraction of oxygen x_m^{GO} at increasing simulation time steps from top down

A further look is taken on the corresponding molar fluxes, exemplarily shown at three simulation time steps at t=15s, t=45s and t=120s. Fig. 7.27 illustrates the total partial molar fluxes of oxygen for the announced time steps of the FE simulation.

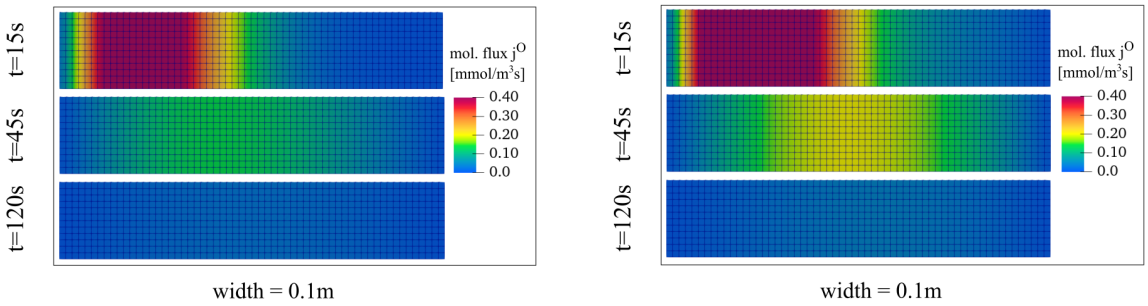

(a) diffusion **(b)** low advection

Figure 7.27.: FE contour plots for the total partial molar flux $\mathbf{j}_m^{\mathrm{O}}$ at simulation time steps t=15s (up), t=45s (middle), t=120s (bottom)

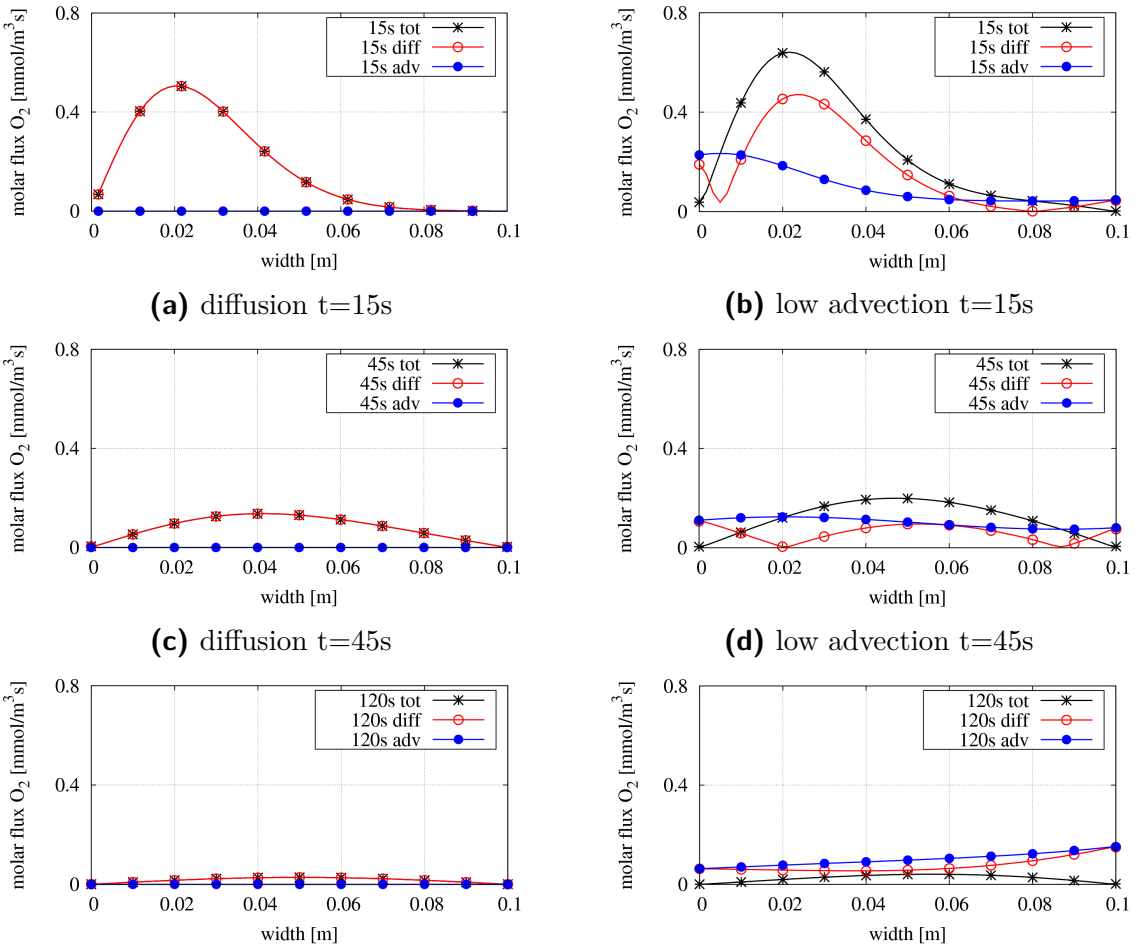

(a) diffusion t=15s **(b)** low advection t=15s

(c) diffusion t=45s **(d)** low advection t=45s

(e) diffusion t=120s **(f)** low advection t=120s

Figure 7.28.: Total, diffusive and advective proportions of partial molar fluxes of oxygen $\mathbf{j}_m^{\mathrm{O}}$ [mmol/m^3] at different simulation time steps over width of model domain

A difference can be made out comparing e.g. time step t=45s, where the absolute values are higher by approximately 10% for the calculation with additional advection induced mass transport. Moreover, the spatial spread of the molar fluxes over geometry width is more pronounced for the low advection process.

At the same time, Fig. 7.28 subdivides these absolute total values (black curves) into their advective (blue curves) and diffusive parts (red curves). The left column collects the graphs for the solely diffusive concentration balancing, which prove, that no advective process is induced (blue curves at zero). On the other hand, the total flow during the additional advective process is composed of both parts. At simulation start the diffusive parts nearly have equal values, Fig. 7.28a and 7.28b, whereas for the low advection calculation the total flow adds up to a higher value due to the additional advective part. Furthermore, the all fluxes go down to zero during the purely diffusive process as the steady state is reached over the time, see Fig. 7.28e, while the simulation with slow advective mass transport reveals, that also a diffusive amount is induced to hold the boundary conditions, see Fig. 7.28d and 7.28f.

7.4.2. Strong advection

The same initial boundary value problem as described in the former section is investigated with a strong advective mass transport induced by a pressure gradient of Δp^{GR}=10hPa, shown in the diagrams and plots in the left columns of Fig. 7.29 - 7.33. That simulation is compared to a similar IBVP, where the only difference is an open boundary for oxygen flux at x=0.1m. The corresponding diagrams and plots are documented in the right columns of Fig. 7.29 - 7.33.

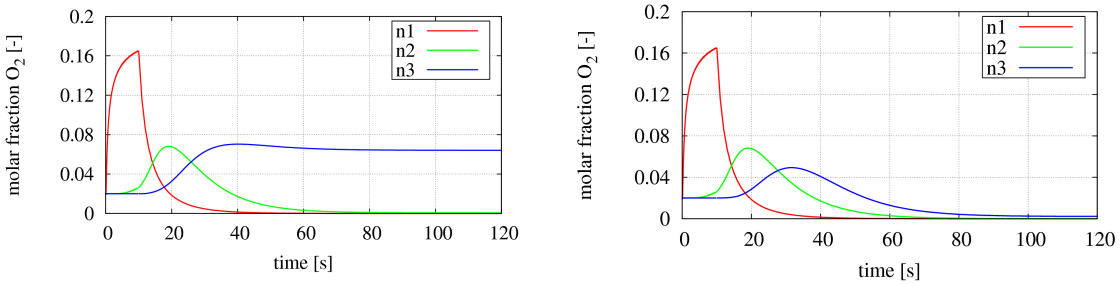

(a) disabled oxygen outflux

(b) enabled oxygen outflux

Figure 7.29.: Molar fraction of oxygen x_m^{GO} for node 1 (n1), node 2 (n2) and node 3 (n3) over time of simulation

These calculations identify a clearly dominating advective transport. Fig. 7.30 illustrates the FE simulation plots for the molar fraction of oxygen at different simulation time steps, where clearly a transported concentration peak can be followed. The

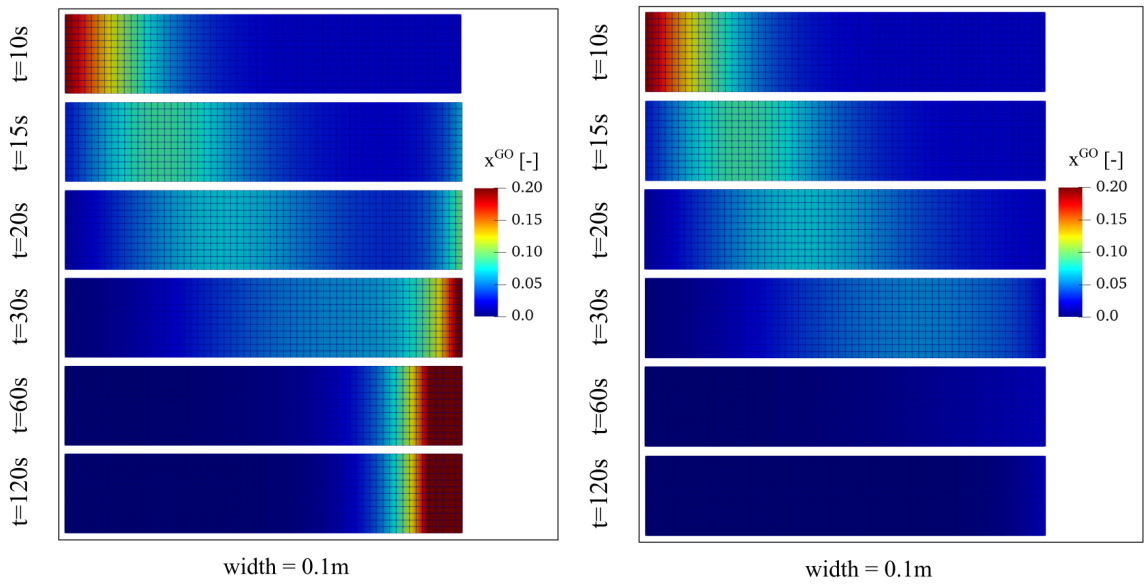

(a) disabled oxygen outflux **(b)** enabled oxygen outflux

Figure 7.30.: FE simulation contour plots of molar fraction of oxygen x_m^{GO} at increasing simulation time steps from top down.

difference between the two IBVP's is obviously the accumulating oxygen concentration in the vicinity of the right end of the geometric domain due to a disabled oxygen outflux (Fig. 7.30a), whereas the right column FE plots (Fig. 7.30b) show, that the oxygen is pressed out of the model domain over time by the applied overpressure.

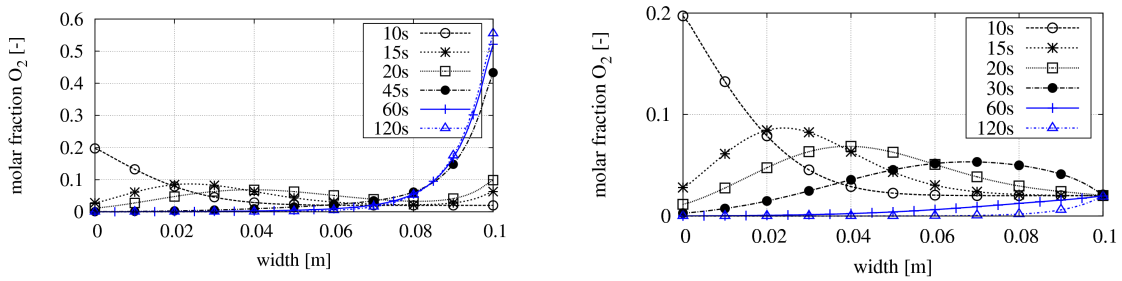

(a) disabled oxygen outlux **(b)** enabled oxygen outflux

Figure 7.31.: Comparison of molar fraction x_m^{GO} over width of model domain for different simulation time steps

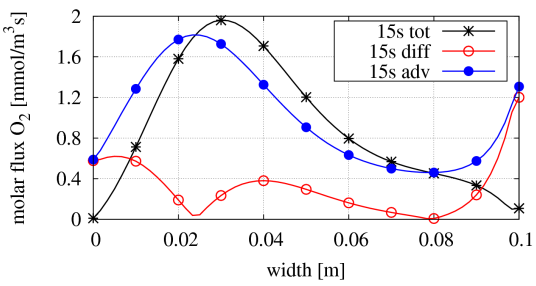

(a) disabled oxygen outflux t=15s

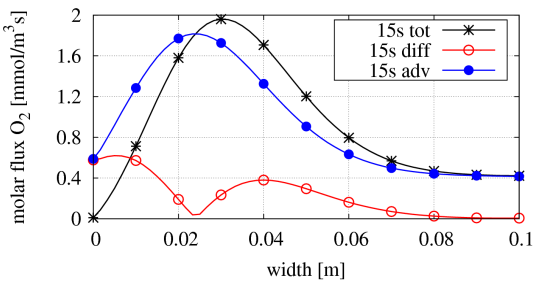

(b) enabled oxygen outflux t=15s

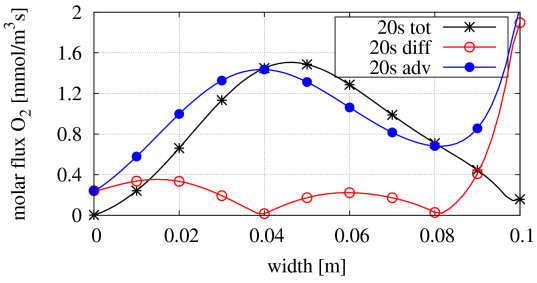

(c) disabled oxygen outflux t=20s

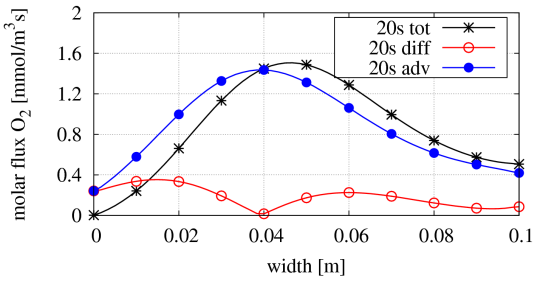

(d) enabled oxygen outflux t=20s

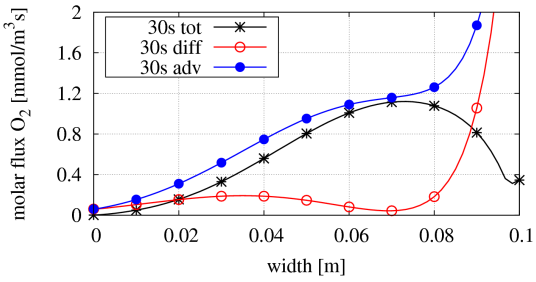

(e) disabled oxygen outflux t=30s

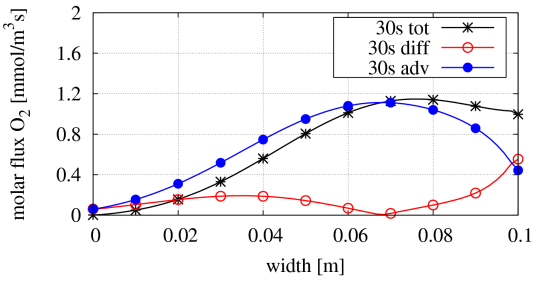

(f) enabled oxygen outflux t=30s

Figure 7.32.: Total, diffusive and advective proportions of partial molar fluxes of oxygen $\mathbf{j}_m^{\mathrm{O}}$ [mmol/m^3] at different simulation time steps over width of model domain

For this purpose, compare the curves for the spatial distribution of the oxygen concentration for different simulation time steps.

Looking more into detail on the total partial fluxes and their advective and diffusive proportions shows identical values and pathways until about 30s of simulation time, cf. Fig. 7.32, which is roughly the time when the transported concentration approaches the right model boundary. Until that instant of time, one can clearly follow, that the concentration transport in this example is predominantly driven by advection (blue curves), but with a slight compensating transport by diffusion (red curves).

When approaching the right vertical model boundary, the boundary conditions for the oxygen has to be fulfilled, which obviously leads to differing fluxes, cf. Fig. 7.33. For a better comparability of the results, the same scale of the y-axis was chosen in the diagrams, which results in the curves being cut off at the right edge of the left columns diagrams. Due to the oxygen accumulation at that position induced by the disabled outflux, the values of the advective and diffusive fluxes increase very strongly. The diagrams of the right column (Fig. 7.33) show the development for an enabled outflux for oxygen, which causes the oxygen concentration to 'leave' the model and the fluxes to disappear over time.

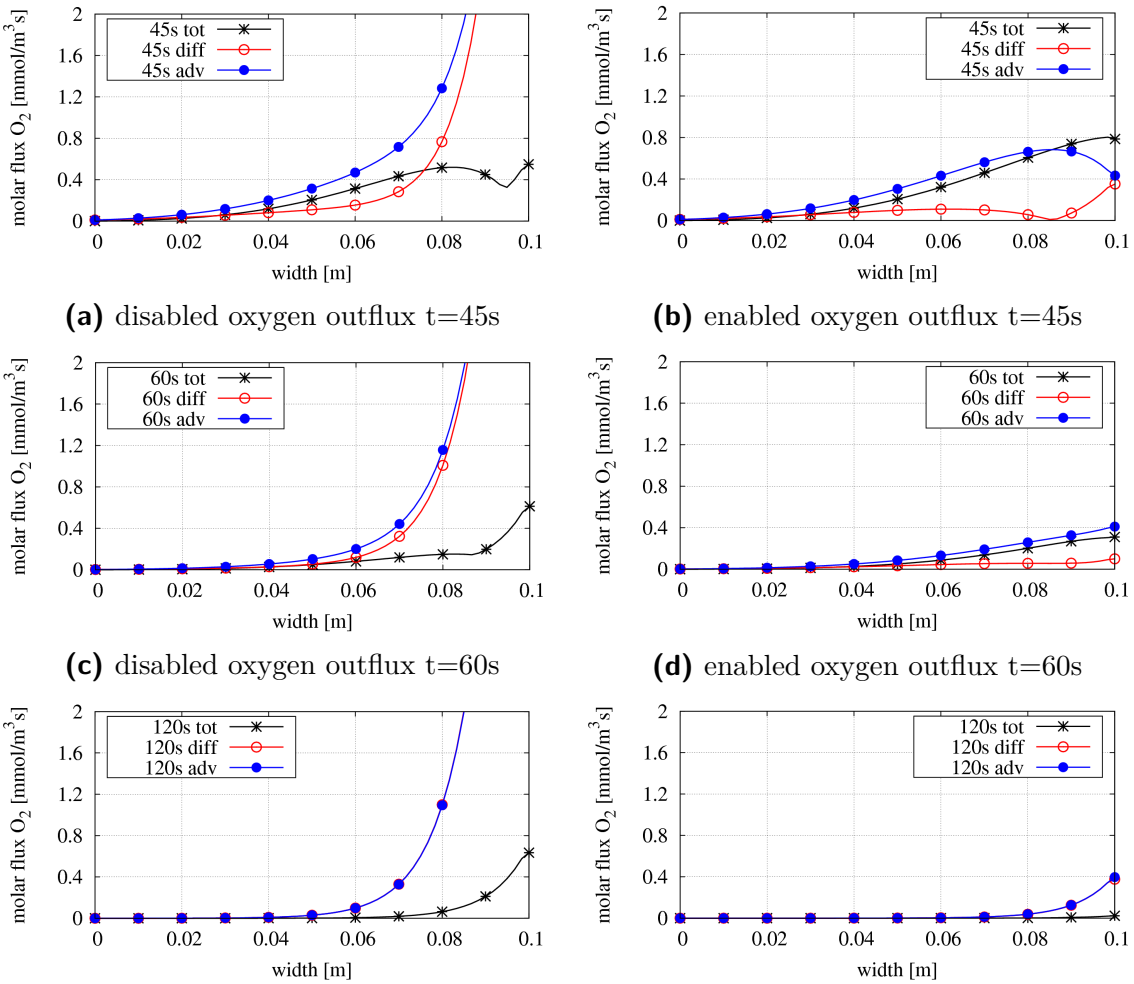

(a) disabled oxygen outflux t=45s

(b) enabled oxygen outflux t=45s

(c) disabled oxygen outflux t=60s

(d) enabled oxygen outflux t=60s

(e) disabled oxygen outflux t=120s

(f) enabled oxygen outflux t=120s

Figure 7.33.: Total, diffusive and advective proportions of partial molar fluxes of oxygen $\mathbf{j}_m^{\mathrm{O}}$ [mmol/m^3] at different simulation time steps over width of model domain

7.4.3. Constant diffusion with slow and strong advection

The subsequent comparison is done by two calculations with again a simulation time of t=120s with increments of Δt=0.01s, and (a) a first calculation with an excess pressure of Δp^{GR} = 1hPa applied on the left vertical boundary at x=0.0m, and (b) a second calculation with Δp^{GR} = 10hPa. Additionally, for this investigation oxygen is constantly applied as DIRICHLET boundary on the left margin, thus inducing a constant oxygen diffusion through the model domain. The right vertical boundary is open for oxygen flux.

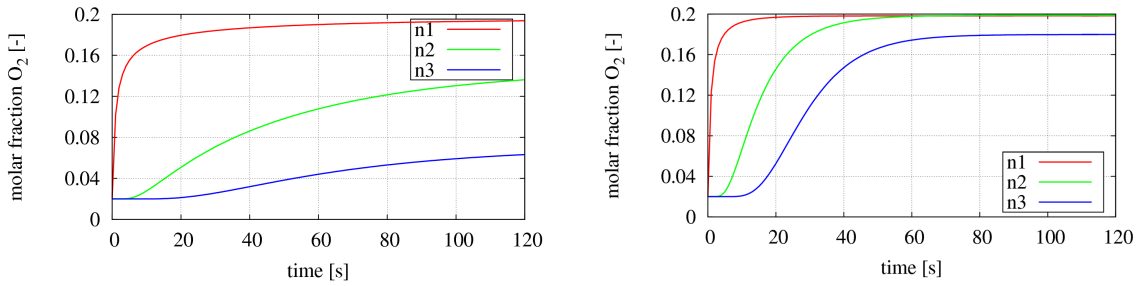

(a) overpressure 1hPa **(b)** overpressure 10hPa

Figure 7.34.: Comparison of molar fractions of oxygen x_m^{GO} for node 1 (n1), node 2 (n2) and node 3 (n3) over simulation time

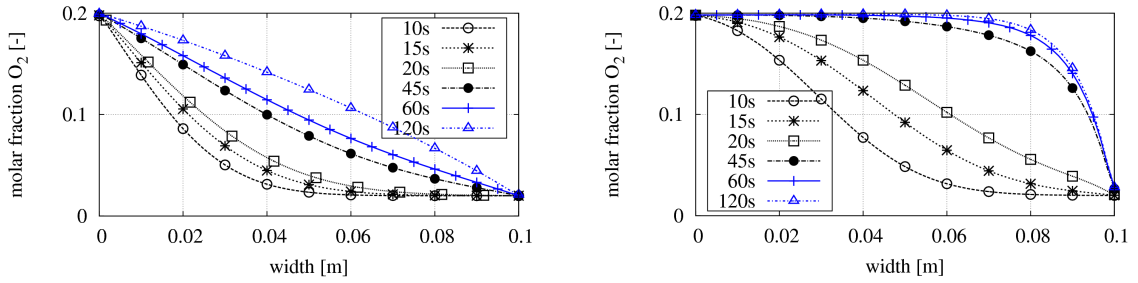

(a) overpressure 1hPa **(b)** overpressure 10hPa

Figure 7.35.: Comparison of molar fractions of oxygen x_m^{GO} for different simulation time steps over model width

Figure 7.34 plots the temporal development of the oxygen concentration by following the molar fraction x_m^{GO} for the three different nodes marked in Fig. 7.23. The higher overpressure of 10hPa leads to equal values over the time for n1 and n2, see Fig. 7.34b. Node 3, however, near the right vertical boundary is influenced by the open

boundary which enables a constant outflux, so that the value adjusts at a lower value,. The lower overpressure of calculation (a) leads to a later attainment of the steady state; Fig. 7.34a indicates, that at nodes n2 and n3 the final values have not been reached after 120s and values are still increasing. Continuing that, Fig. 7.35 plots the spatial distribution of x_m^{GO} for different simulation time steps, where the steady state is reached for a high overpressure (b) at around 60s. The steady state is not reached for a lower overpressure after twice the time.

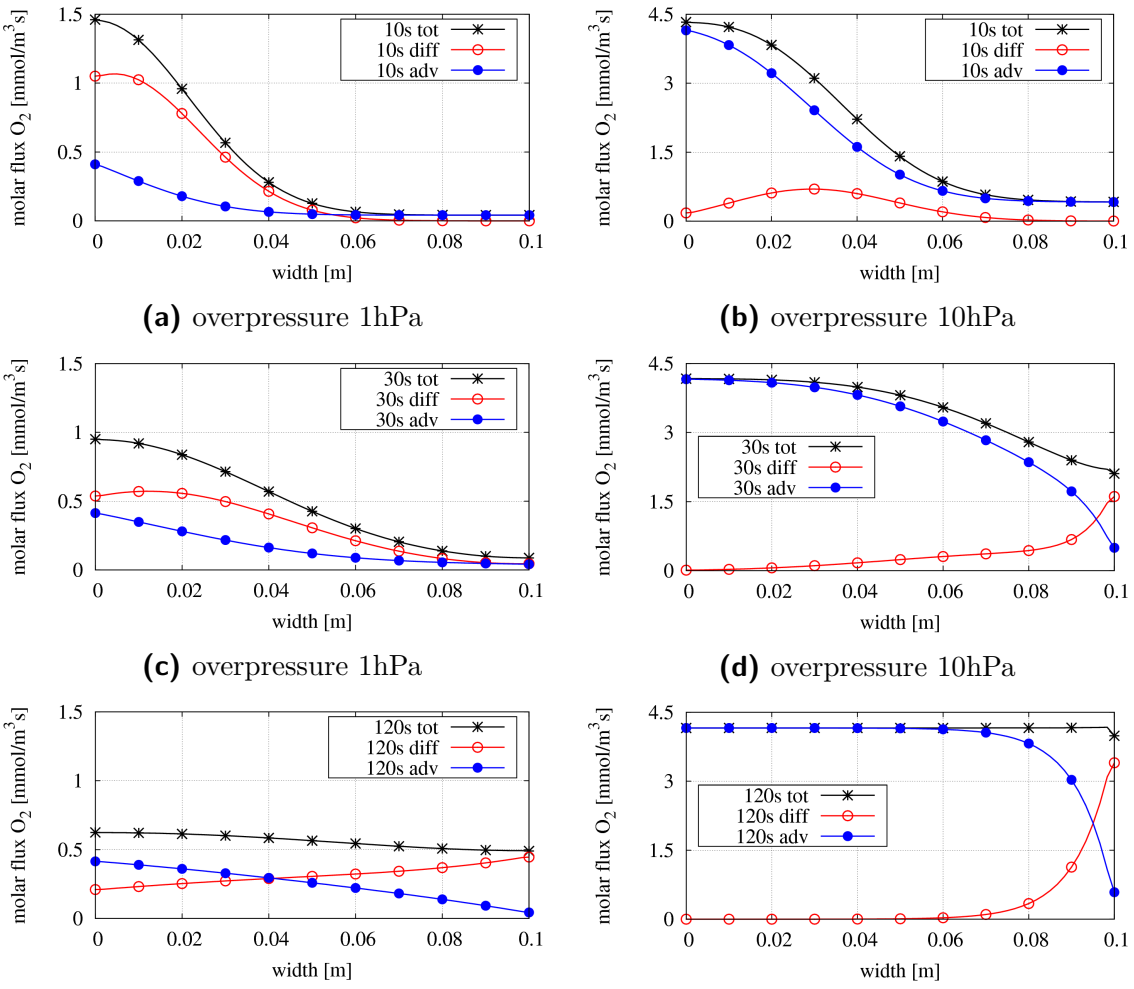

(a) overpressure 1hPa

(b) overpressure 10hPa

(c) overpressure 1hPa

(d) overpressure 10hPa

(e) overpressure 1hPa

(f) overpressure 10hPa

Figure 7.36.: Total, diffusive and advective proportions of partial molar fluxes of oxygen $\mathbf{j}_m^{\mathrm{O}}$ [mmol/m^3] at different simulation time steps over width of model

Figure 7.36 differentiates the total molar flux (black curves) of oxygen into its

advective (blue curves) and diffusive part (red curves) for both investigated cases. The small pressure gradient in simulation (a) leads to both advective and diffusive fluxes, whereas the higher pressure gradient leads to a prevailing advective flux. Not only the qualitative progressions differ, but also their magnitudes. The slow advection in combination with diffusion leads to smaller amounts of mass transport, where at the stage of concentration balancing the partitions of the fluxes have nearly same values, cf. Fig. 7.36e. The high pressure gradient of simulation (b) also enables a diffusive flux in the beginning, see Fig. 7.36b, whereas it depresses the diffusion in the steady state, cf. Fig. 7.36f, although a constant concentration influx is applied. More interim stages of molar fluxes can be followed in App. D.2.

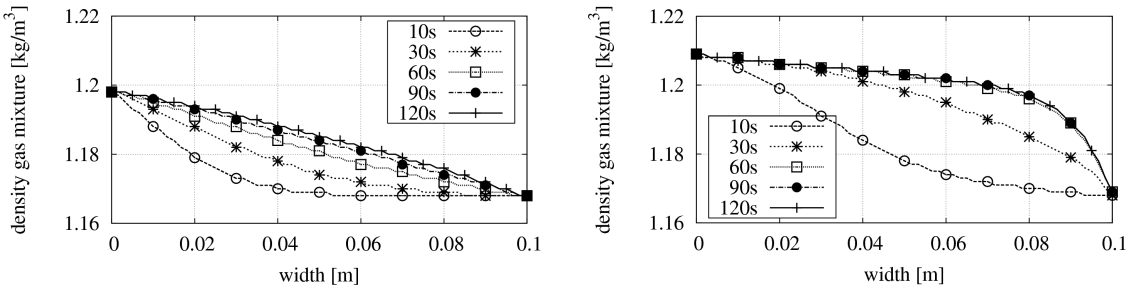

(a) overpressure 1hPa **(b)** overpressure 10hPa

Figure 7.37.: Comparison of mixture density ρ^{GR} at different simulation time steps over width of model domain

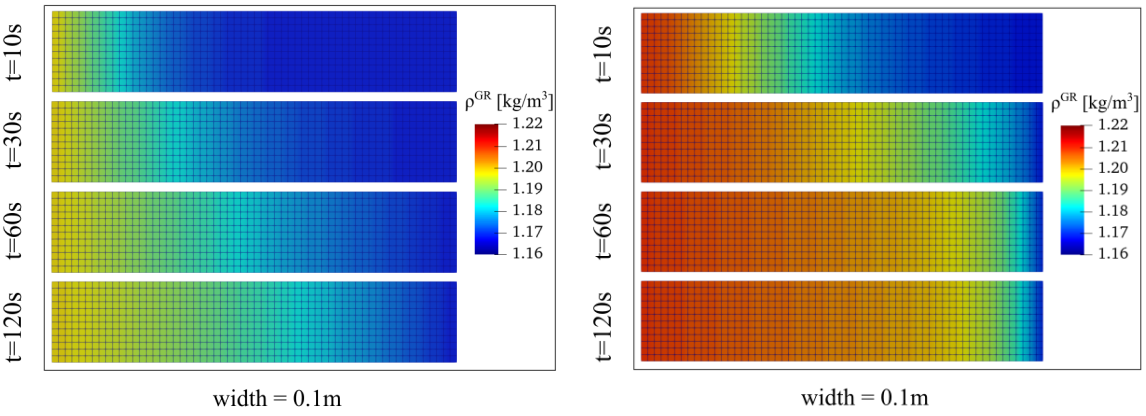

(a) overpressure 1hPa **(b)** overpressure 10hPa

Figure 7.38.: FE simulation plots of density of gas mixture ρ^{GR} at increasing time steps from top down.

Looking finally at the mixture density, which arises by summing up the partial pore

densities of the components φ^γ according to (5.7), one can follow suitable results. At the spatial points where the realistic composition of air is obtained by the incoming oxygen, the density adjusts to the value of $\rho^{\mathbf{GR}} \approx 1.2$ [kg/m^3], which is the value for air at standard conditions at $\theta = 20°$C and $\mathrm{p}^{\mathbf{GR}} = 1013$ hPa. The higher pressure leads to an increasing density as expected, see also the plot from the FE simulation in Fig. 7.38.

8. Summary and outlook

For this work, a numerical model for the simulation of multiphasic and multicomponent porous media based on the continuum-mechanical description of the extended Theory of Porous Media (eTPM) is set up and the required foundations are provided. The focus lies on a thermodynamically consistent model and material description for biphasic mixture body containing an incompressible solid phase and a compressible gas mixture consisting of different mixture components. Thus, the basic principles of thermodynamics are included in this thesis and set in relation to continuum mechanics. With the derived general theoretical model base simulations can be applied to study environmentally relevant problems including reactive mass transport processes. Subsequently, the calculation and constitutive modeling concept is applied to bacterial methane oxidation in landfill cover layers, which was part of the interdisciplinary project *'Description of limit and failure states for biological methane oxidation in landfills: experimental investigation, chemical analysis, mechanical modeling and computational simulation'* funded by the German Research Foundation (DFG).

As global warming nowadays is a concern, and methane and carbon dioxide are the biggest contributors among the climate-relevant gases, a reduction of these is more important than ever. Although methane is present in smaller amounts in the atmosphere, its impact on global warming is significantly higher in direct comparison to carbon dioxide. Through the bacterial methane oxidation in landfill cover layers, the long-term methane emissions of landfills are converted to the less harmful carbon dioxide. Once a landfill is closed, the landfill operator is obligated to give proof, that the still emitting methane fluxes do not exceed certain limit values. A numerical simulation model can serve as support and evidence through forecasts regarding methane emissions under varying environmental conditions.

For that, the numerical model setup was verified and validated by the author of this thesis through tailored experiments performed by the project partners of the interdisciplinary DFG project. During the project, the basic processes regarding mass transfer and the degradation kinetics of methane oxidation in soils were experimentally investigated depending on different influencing parameters, as well as varying initial and boundary conditions. The results served as validation of the numerical model and were also used for calibration. With the holistic concept of experimental analysis and verified associated numerical simulations, the model can be used to predict remaining methane fluxes through landfill cover layers in a supportive manner.

The large spatial problem with regard to the dimensions of a landfill with hundreds of meters stretch of land was examined on small-scale laboratory setups first. In order to select the basic descriptive processes from the overall complex multi-physical issue, this approach was initially necessary and sufficient, as they represent the describing processes well enough and neglect disturbing influences out of focus. Proceeding from that, the corresponding numerical simulations were performed on reduced two-dimensional geometric model domains, but could now be transferred to higher dimensional problems.

For model validation both closed and thus discontinuous systems as well as an open system leading to a continuous experimental setup were conducted. The closed batch reactors were utilized to investigate the degradation kinetics implemented in the model equations for low and high methane concentrations under different constant ambient temperatures. Furthermore, an innovative experimental assembly using additionally thermography techniques was installed as continuous setup. Using this experimental composition, both concentration and temperature profiles could be measured and visualized over the height of a soil layer and reproduced by the numerical simulations. The eminent matches of experiments and simulations using this continuous setup and the good forecast ability regarding temperature and concentration development provided the reasonable assumption, that the developed model is capable to be applied to a three-dimensional FE landfill cover model. However, due to laboratory conditions, the process of methane oxidation was mainly diffusion driven in the continuous setup. In order to also investigate advective influences on the gas fluxes, which can become quite relevant in *in-situ* conditions on landfills, further numerical simulations were performed to verify the model focussing on the mass transport mechanisms without reactive influences.

The derived numerical model is able to give stable predictions about the bacterial degradation of methane under varying environmental conditions like soil parameters, gas freights, atmospheric pressure, soil moisture and cold or warm periods. In the authors opinion, the implementation of the water content as an additional parameter, as done here in the model, is sufficient to predict the remaining methane emissions and concentrations after passing through the soil layer. However, to give more precise predictions regarding e.g. the carbon dioxide production throughout the bacterial conversion and its uptake in the aqueous phase, it would be advisable to include the water as an additional macroscopic mobile liquid phase to the model. Nevertheless, this will lead to a higher computational effort as further degrees of freedom need to be implemented, increasing the complexity of the model. Moreover, additional physical phenomena such as capillarity effects between the macroscopic phases would have to be considered for a triphasic model.

For further application and validation of the model, *in-situ* inspections of a landfill would be appropriate. Measurements of soil parameters like permeabilities, volume fractions and also chemical compositions could be supplied to the model as initial and boundary values and thus provide information about the remaining methane emissions under varying climatic conditions.

A. Derivations - Chapter 3

A.1. Calculation rules

The selected computation rules for the divergence operator are taken from Ehlers [46]:

$$\operatorname{div}(\phi\mathbf{v}) = \mathbf{v}\cdot\operatorname{grad}\phi + \phi\operatorname{div}\mathbf{v} \tag{A.1}$$

$$\operatorname{div}(\phi\,\mathbf{T}) = \mathbf{T}\operatorname{grad}\phi + \phi\operatorname{div}\mathbf{T} \tag{A.2}$$

$$\operatorname{div}(\mathbf{T}\,\mathbf{v}) = (\operatorname{div}\mathbf{T}^{\mathrm{T}})\cdot\mathbf{v} + \mathbf{T}^{\mathrm{T}}\cdot\operatorname{grad}\mathbf{v} \tag{A.3}$$

$$\operatorname{div}(\mathbf{x}\times\mathbf{T}) = \mathbf{x}\times\operatorname{div}\mathbf{T} + \operatorname{grad}\mathbf{x}\times\mathbf{T}\,. \tag{A.4}$$

A.2. Derivation local master formulation

Evaluating the left-hand side total time derivatives of (3.81), (3.82), and (3.83) for the scalar-valued balances[1] according to (3.36), (3.37) and (3.38), yields

$$\begin{aligned}
\frac{\mathrm{d}}{\mathrm{dt}}\int_{\mathrm{B}}\Upsilon\,\mathrm{dv} &= \int_{\mathrm{B}}[\dot{\Upsilon}\,\mathrm{dv} + \Upsilon(\mathrm{dv})^{\cdot}] &&= \int_{\mathrm{B}}(\dot{\Upsilon} + \Upsilon\operatorname{div}\dot{\mathbf{x}})\,\mathrm{dv}\,,\\
\frac{\mathrm{d}_{\boldsymbol{\alpha}}}{\mathrm{dt}}\int_{\mathrm{B}}\Upsilon^{\boldsymbol{\alpha}}\,\mathrm{dv} &= \int_{\mathrm{B}}[\Upsilon^{\boldsymbol{\alpha}})'_{\boldsymbol{\alpha}}\,\mathrm{dv} + \Upsilon^{\boldsymbol{\alpha}}(\mathrm{dv})^{\cdot}] &&= \int_{\mathrm{B}}(\Upsilon^{\boldsymbol{\alpha}})'_{\boldsymbol{\alpha}} + \Upsilon^{\boldsymbol{\alpha}}\operatorname{div}\mathbf{x}'_{\boldsymbol{\alpha}})\,\mathrm{dv}\,,\\
\frac{\mathrm{d}_{\beta}}{\mathrm{dt}}\int_{\mathrm{B}}\Upsilon^{\beta}\,\mathrm{dv} &= \int_{\mathrm{B}}[\Upsilon^{\beta})'_{\beta}\,\mathrm{dv} + \Upsilon^{\beta}(\mathrm{dv})^{\cdot}] &&= \int_{\mathrm{B}}(\Upsilon^{\beta})'_{\beta} + \Upsilon^{\beta}\operatorname{div}\mathbf{x}'_{\beta})\,\mathrm{dv}\,,
\end{aligned} \tag{A.5}$$

[1] Analogously for vector-valued balance equations

where use has been made of (3.45) and the relation $(\det \mathbf{F})^{\cdot} = \mathrm{J} \operatorname{div} \dot{\mathbf{x}}$. Furthermore, applying the GAUSS integral theorem, cf. e.g. Ehlers [46],

$$\int_{\partial \mathrm{B}} (\boldsymbol{\phi} \cdot \mathbf{n}) \, \mathrm{da} = \int_{\mathrm{B}} \operatorname{div} \boldsymbol{\phi} \, \mathrm{dv} \tag{A.6}$$

to the right-hand side surface integral of (3.81), (3.82), and (3.83), the local balance equations in general form can be derived for mixture body φ, constituent $\varphi^{\boldsymbol{\alpha}}$ and component φ^{β} as

$$\begin{aligned} \dot{\Upsilon} + \Upsilon \operatorname{div} \dot{\mathbf{x}} &= \operatorname{div} \boldsymbol{\phi} + \xi + \hat{\Upsilon} \,, \\ (\Upsilon^{\boldsymbol{\alpha}})'_{\boldsymbol{\alpha}} + \Upsilon^{\boldsymbol{\alpha}} \operatorname{div} \mathbf{x}'_{\boldsymbol{\alpha}} &= \operatorname{div} \boldsymbol{\phi}^{\boldsymbol{\alpha}} + \xi^{\boldsymbol{\alpha}} + \hat{\Upsilon}^{\boldsymbol{\alpha}} \,, \\ (\Upsilon^{\beta})'_{\beta} + \Upsilon^{\beta} \operatorname{div} \mathbf{x}'_{\boldsymbol{\alpha}} &= \operatorname{div} \boldsymbol{\phi}^{\beta} + \xi^{\beta} + \hat{\Upsilon}^{\beta} \,. \end{aligned} \tag{A.7}$$

A.3. Material time derivatives in terms of relative velocties

For some applications it is necessary to formulate the material time derivatives in terms of the relative velocities arising from the multi-phase and -component description. For that, the formulations of the material time derivatives introduced in Sect. 3.3.2 are rearranged with respect to the explicit part with

$$\frac{\partial \Gamma}{\partial \mathrm{t}} = \dot{\Gamma} - \operatorname{grad} \Gamma \cdot \dot{\mathbf{x}} \,, \qquad \frac{\partial \boldsymbol{\Gamma}}{\partial \mathrm{t}} = \dot{\boldsymbol{\Gamma}} - (\operatorname{grad} \boldsymbol{\Gamma}) \, \dot{\mathbf{x}} \,, \tag{A.8}$$

$$\frac{\partial \Gamma}{\partial \mathrm{t}} = (\Gamma)'_{\boldsymbol{\alpha}} - \operatorname{grad} \Gamma \cdot \mathbf{x}'_{\boldsymbol{\alpha}} \qquad \frac{\partial \boldsymbol{\Gamma}}{\partial \mathrm{t}} = (\boldsymbol{\Gamma})'_{\boldsymbol{\alpha}} - (\operatorname{grad} \boldsymbol{\Gamma}) \, \mathbf{x}'_{\boldsymbol{\alpha}} \,, \tag{A.9}$$

$$\frac{\partial \Gamma}{\partial \mathrm{t}} = (\Gamma)'_{\beta} - \operatorname{grad} \Gamma \cdot \mathbf{x}'_{\beta} \qquad \frac{\partial \boldsymbol{\Gamma}}{\partial \mathrm{t}} = (\boldsymbol{\Gamma})'_{\beta} - (\operatorname{grad} \boldsymbol{\Gamma}) \, \mathbf{x}'_{\beta} \,. \tag{A.10}$$

Inserting as a next step (A.8) into (3.37) and utilizing definition (3.66), the material time derivative for an arbitrary scalar- or vector-valued field quantity with respect to the motion of the main phase $\varphi^{\boldsymbol{\alpha}}$ can be formulated as

$$(\Gamma)'_{\boldsymbol{\alpha}} = \dot{\Gamma} + \operatorname{grad} \Gamma \cdot \mathbf{d}_{\boldsymbol{\alpha}} \quad \text{and} \quad (\boldsymbol{\Gamma})'_{\boldsymbol{\alpha}} = \dot{\boldsymbol{\Gamma}} + \operatorname{grad} \boldsymbol{\Gamma} \, \mathbf{d}_{\boldsymbol{\alpha}} \,, \tag{A.11}$$

The same procedure can be applied to derive the material time derivative with respect to the motion of φ^β by inserting (A.9) into (3.38) and utilizing the diffusion velocity (3.65):

$$(\Gamma)'_\beta = (\Gamma)'_{\boldsymbol{\alpha}} + \operatorname{grad}\Gamma \cdot \mathbf{d}_{\beta\boldsymbol{\alpha}} \quad \text{and} \quad (\boldsymbol{\Gamma})'_\beta = (\boldsymbol{\Gamma})'_{\boldsymbol{\alpha}} + (\operatorname{grad}\boldsymbol{\Gamma})\,\mathbf{d}_{\beta\boldsymbol{\alpha}}\,. \tag{A.12}$$

Likewise, the material time derivatives with respect to the deforming solid are given with

$$\begin{aligned} (\Gamma)'_{\boldsymbol{\alpha}} &= (\Gamma)'_{\mathbf{S}} + \operatorname{grad}\Gamma \cdot \mathbf{w}_{\boldsymbol{\alpha}\mathbf{S}} \quad \text{and} \quad (\boldsymbol{\Gamma})'_{\boldsymbol{\alpha}} = (\boldsymbol{\Gamma})'_{\mathbf{S}} + (\operatorname{grad}\boldsymbol{\Gamma})\,\mathbf{w}_{\boldsymbol{\alpha}\mathbf{S}}\,. \\ (\Gamma)'_{\beta} &= (\Gamma)'_{\mathbf{S}} + \operatorname{grad}\Gamma \cdot \mathbf{w}_{\beta\mathbf{S}} \quad \text{and} \quad (\boldsymbol{\Gamma})'_{\beta} = (\boldsymbol{\Gamma})'_{\mathbf{S}} + (\operatorname{grad}\boldsymbol{\Gamma})\,\mathbf{w}_{\beta\mathbf{S}}\,, \end{aligned} \tag{A.13}$$

A.4. Summation of local master balance equations

The summation of a local master balance equation (either scalar- or vector-/tensor-valued) for $\varphi^{\boldsymbol{\alpha}}$ or φ^β (3.85) yields the higher level balance equation. This is shown exemplarily for the scalar-valued partial field quantity $\Upsilon^{\boldsymbol{\alpha}}$ and Υ^β.
Starting with $\Upsilon^{\boldsymbol{\alpha}}$, the reformulation of the material time derivative with reference to motion $\varphi^{\boldsymbol{\alpha}}$ in terms of the overall diffusion velocity (A.11) is utilized, and moreover the expansion $\mathbf{x}'_{\boldsymbol{\alpha}} = (\dot{\mathbf{x}} + \mathbf{d}_{\boldsymbol{\alpha}})$, so that

$$(\Upsilon^{\boldsymbol{\alpha}})'_{\boldsymbol{\alpha}} = \dot{\Upsilon}^{\boldsymbol{\alpha}} + \operatorname{grad}\Upsilon^{\boldsymbol{\alpha}} \cdot \mathbf{d}_{\boldsymbol{\alpha}} \quad \text{and} \quad \Upsilon^{\boldsymbol{\alpha}} \operatorname{div}\mathbf{x}'_{\boldsymbol{\alpha}} = \Upsilon^{\boldsymbol{\alpha}} \operatorname{div}(\dot{\mathbf{x}} + \mathbf{d}_{\boldsymbol{\alpha}})\,. \tag{A.14}$$

is given. Connecting the equations (A.14) yields for the left-hand side of $(3.85)_1$

$$(\Upsilon^{\boldsymbol{\alpha}})'_{\boldsymbol{\alpha}} + \Upsilon^{\boldsymbol{\alpha}} \operatorname{div}\mathbf{x}'_{\boldsymbol{\alpha}} = \dot{\Upsilon}^{\boldsymbol{\alpha}} + \Upsilon^{\boldsymbol{\alpha}} \operatorname{div}\dot{\mathbf{x}} + \operatorname{grad}\Upsilon^{\boldsymbol{\alpha}} \cdot \mathbf{d}_{\boldsymbol{\alpha}} + \Upsilon^{\boldsymbol{\alpha}} \operatorname{div}\mathbf{d}_{\boldsymbol{\alpha}}\,, \tag{A.15}$$

and utilizing the divergence calculation rule

$$\operatorname{div}(\Upsilon^{\boldsymbol{\alpha}}\mathbf{d}_{\boldsymbol{\alpha}}) = \mathbf{d}_{\boldsymbol{\alpha}} \cdot \operatorname{grad}\Upsilon^{\boldsymbol{\alpha}} \quad + \Upsilon^{\boldsymbol{\alpha}} \operatorname{div}\mathbf{d}_{\boldsymbol{\alpha}}\,, \tag{A.16}$$

the local balance equation $(3.85)_1$ is reformulated to

$$\dot{\Upsilon}^{\boldsymbol{\alpha}} + \Upsilon^{\boldsymbol{\alpha}} \operatorname{div}\dot{\mathbf{x}} = \operatorname{div}(\phi^{\boldsymbol{\alpha}} - \Upsilon^{\boldsymbol{\alpha}}\,\mathbf{d}_{\boldsymbol{\alpha}}) + \xi^{\boldsymbol{\alpha}} + \hat{\Upsilon}^{\boldsymbol{\alpha}}\,, \tag{A.17}$$

where summation over $\boldsymbol{\alpha}$ yields

$$\sum_{\boldsymbol{\alpha}}(\dot{\Upsilon}^{\boldsymbol{\alpha}} + \Upsilon^{\boldsymbol{\alpha}}\mathrm{div}\,\dot{\mathbf{x}}) = \sum_{\boldsymbol{\alpha}}[\mathrm{div}\,(\phi^{\boldsymbol{\alpha}} - \Upsilon^{\boldsymbol{\alpha}}\,\mathbf{d}_{\boldsymbol{\alpha}}) + \xi^{\boldsymbol{\alpha}} + \hat{\Upsilon}^{\boldsymbol{\alpha}}]\,. \tag{A.18}$$

The same procedure is invoked for the reformulation of the local master balance of component φ^{β}. Proceeding from

$$(\Upsilon^{\beta})'_{\beta} = (\Upsilon^{\beta})'_{\boldsymbol{\alpha}} + \mathrm{grad}\,\Upsilon^{\beta}\cdot\mathbf{d}_{\beta\boldsymbol{\alpha}} \quad \text{and} \quad \Upsilon^{\beta}\,\mathrm{div}\,\mathbf{x}'_{\beta} = \Upsilon^{\beta}\mathrm{div}\,(\mathbf{x}'_{\boldsymbol{\alpha}} + \mathbf{d}_{\beta\boldsymbol{\alpha}})\,. \tag{A.19}$$

where use has been made of (A.12), the local master formulation $(3.85)_2$ yields after inserting again the divergence calculation rule

$$(\Upsilon^{\beta})'_{\boldsymbol{\alpha}} + \Upsilon^{\beta}\mathrm{div}\,\mathbf{x}'_{\boldsymbol{\alpha}} = \mathrm{div}\,(\phi^{\beta} - \Upsilon^{\beta}\,\mathbf{d}_{\beta\boldsymbol{\alpha}}) + \xi^{\beta} + \hat{\Upsilon}^{\beta}\,, \tag{A.20}$$

and summation over β yields

$$\sum_{\beta}[(\Upsilon^{\beta})'_{\boldsymbol{\alpha}} + \Upsilon^{\beta}\mathrm{div}\,\mathbf{x}'_{\boldsymbol{\alpha}}] = \sum_{\beta}[\mathrm{div}\,(\phi^{\beta} - \Upsilon^{\beta}\,\mathbf{d}_{\beta\boldsymbol{\alpha}}) + \xi^{\beta} + \hat{\Upsilon}^{\beta}]\,. \tag{A.21}$$

A.5. Derivation of local balance of linear momentum for $\varphi^{\boldsymbol{\alpha}}$

The derivation of the local balance is shown exemplarily for $\varphi^{\boldsymbol{\alpha}}$. Implementing the associated quantities from $(3.99)_2$ to $(3.85)_2$ yields

$$(\rho^{\boldsymbol{\alpha}}\,\mathbf{x}'_{\boldsymbol{\alpha}})'_{\boldsymbol{\alpha}} + (\rho^{\boldsymbol{\alpha}}\,\mathbf{x}'_{\boldsymbol{\alpha}})\,\mathrm{div}\,\mathbf{x}'_{\boldsymbol{\alpha}} = \mathrm{div}\,\mathbf{T}^{\boldsymbol{\alpha}} + \rho^{\boldsymbol{\alpha}}\,\mathbf{b} + \hat{\mathbf{s}}^{\boldsymbol{\alpha}}\,. \tag{A.22}$$

With $(3.91)_2$ the left-hand side can be rewritten as

$$(\rho^{\boldsymbol{\alpha}}\,\mathbf{x}'_{\boldsymbol{\alpha}})'_{\boldsymbol{\alpha}} + (\rho^{\boldsymbol{\alpha}}\,\mathbf{x}'_{\boldsymbol{\alpha}})\,\mathrm{div}\,\mathbf{x}'_{\boldsymbol{\alpha}} = \mathbf{x}'_{\boldsymbol{\alpha}}\,\underbrace{[(\rho^{\boldsymbol{\alpha}})'_{\boldsymbol{\alpha}} + \rho^{\boldsymbol{\alpha}}\,\mathrm{div}\,\mathbf{x}'_{\boldsymbol{\alpha}}]}_{\hat{\rho}^{\boldsymbol{\alpha}}} + \rho^{\boldsymbol{\alpha}}\,\mathbf{x}''_{\boldsymbol{\alpha}}\,, \tag{A.23}$$

so that the local balance of momentum finally reads

$$\rho^{\boldsymbol{\alpha}}\,\mathbf{x}''_{\boldsymbol{\alpha}} = \mathrm{div}\,\mathbf{T}^{\boldsymbol{\alpha}} + \rho^{\boldsymbol{\alpha}}\,\mathbf{b} + \hat{\mathbf{s}}^{\boldsymbol{\alpha}} - \hat{\rho}^{\boldsymbol{\alpha}}\,\mathbf{x}'_{\boldsymbol{\alpha}}\,. \tag{A.24}$$

Analogously, the local balance of momentum can be derived for component φ^{β}.

A.6. Derivation of local balance of angular momentum for $\varphi^{\boldsymbol{\alpha}}$

The derivation of the local balance is shown exemplarily for $\varphi^{\boldsymbol{\alpha}}$. Implementing (3.105) into $(3.85)_2$ yields

$$[\mathbf{x} \times (\rho^{\boldsymbol{\alpha}} \mathbf{x}'_{\boldsymbol{\alpha}})]'_{\boldsymbol{\alpha}} + [\mathbf{x} \times (\rho^{\boldsymbol{\alpha}} \mathbf{x}'_{\boldsymbol{\alpha}})] \operatorname{div} \mathbf{x}'_{\boldsymbol{\alpha}} = \operatorname{div} (\mathbf{x} \times \mathbf{T}^{\boldsymbol{\alpha}}) + \mathbf{x} \times \rho^{\boldsymbol{\alpha}} \mathbf{b} + \hat{\mathbf{h}}^{\boldsymbol{\alpha}} \,. \tag{A.25}$$

Evaluating the left-hand side and implementing $(3.91)_2$ results in

$$[\mathbf{x} \times (\rho^{\boldsymbol{\alpha}} \mathbf{x}'_{\boldsymbol{\alpha}})]'_{\boldsymbol{\alpha}} + [\mathbf{x} \times (\rho^{\boldsymbol{\alpha}} \mathbf{x}'_{\boldsymbol{\alpha}})] \operatorname{div} \mathbf{x}'_{\boldsymbol{\alpha}} = \mathbf{x} \times (\mathbf{x}'_{\boldsymbol{\alpha}} \underbrace{[(\rho^{\boldsymbol{\alpha}})'_{\boldsymbol{\alpha}} + \rho^{\boldsymbol{\alpha}} \operatorname{div} \mathbf{x}'_{\boldsymbol{\alpha}}]}_{\hat{\rho}^{\boldsymbol{\alpha}}}) + \mathbf{x} \times \rho^{\boldsymbol{\alpha}} \mathbf{x}''_{\boldsymbol{\alpha}} \,, \tag{A.26}$$

where $\mathbf{x}'_{\boldsymbol{\alpha}} \times \rho^{\boldsymbol{\alpha}} \mathbf{x}'_{\boldsymbol{\alpha}} = 0$ is inserted. Furthermore, the calculation rule for the outer product (A.4) is utilized, where in this case $\operatorname{grad} \mathbf{x} = \mathbf{I}$. Inserting (A.4) together with (A.26) into (A.25) yields after rearranging

$$\mathbf{0} = \mathbf{I} \times \mathbf{T}^{\boldsymbol{\alpha}} + \mathbf{x} \times \underbrace{[\operatorname{div} \mathbf{T}^{\boldsymbol{\alpha}} + \rho^{\boldsymbol{\alpha}} (\mathbf{b} - \mathbf{x}''_{\boldsymbol{\alpha}})]}_{-\hat{\mathbf{p}}^{\boldsymbol{\alpha}}} + \hat{\mathbf{h}}^{\boldsymbol{\alpha}} - \mathbf{x} \times \hat{\rho}^{\boldsymbol{\alpha}} \mathbf{x}'_{\boldsymbol{\alpha}} \,. \tag{A.27}$$

Therein, the local balance of linear momentum $(3.100)_2$ is used, so that finally, the local balance of angular momentum reads considering (3.101)

$$\mathbf{0} = \mathbf{I} \times \mathbf{T}^{\boldsymbol{\alpha}} + \hat{\mathbf{h}}^{\boldsymbol{\alpha}} - \mathbf{x} \times \hat{\mathbf{s}}^{\boldsymbol{\alpha}} \,. \tag{A.28}$$

Analogously, the local balance of angular momentum can be derived for component φ^{β}.

A.7. Derivation of local balance of energy for φ^{α}

Implementing (3.114) into $(3.85)_1$ yields

$$\begin{aligned}[\rho^{\boldsymbol{\alpha}}(\varepsilon^{\boldsymbol{\alpha}}+\frac{1}{2}\,\mathbf{x}'_{\boldsymbol{\alpha}}\cdot\mathbf{x}'_{\boldsymbol{\alpha}})]'_{\boldsymbol{\alpha}}+[\rho^{\boldsymbol{\alpha}}(\varepsilon+\frac{1}{2}\,\mathbf{x}'_{\boldsymbol{\alpha}}\cdot\mathbf{x}'_{\boldsymbol{\alpha}})]\,\mathrm{div}\,\mathbf{x}'_{\boldsymbol{\alpha}}=\\ \mathrm{div}[(\mathbf{T}^{\boldsymbol{\alpha}})^{\mathrm{T}}\,\mathbf{x}'_{\boldsymbol{\alpha}}-\mathbf{q}^{\boldsymbol{\alpha}}]+\rho^{\boldsymbol{\alpha}}(\mathbf{b}\cdot\mathbf{x}'_{\boldsymbol{\alpha}}+\mathrm{r}^{\boldsymbol{\alpha}})+\hat{\mathrm{e}}^{\boldsymbol{\alpha}}\end{aligned} \tag{A.29}$$

Evaluating the left-hand side and implementing $(3.91)_2$ results in

$$\begin{aligned}[\rho^{\boldsymbol{\alpha}}(\varepsilon^{\boldsymbol{\alpha}}+\frac{1}{2}\,\mathbf{x}'_{\boldsymbol{\alpha}}\cdot\mathbf{x}'_{\boldsymbol{\alpha}})]'_{\boldsymbol{\alpha}}+[\rho^{\boldsymbol{\alpha}}(\varepsilon^{\boldsymbol{\alpha}}+\frac{1}{2}\,\mathbf{x}'_{\boldsymbol{\alpha}}\cdot\mathbf{x}'_{\boldsymbol{\alpha}})]\,\mathrm{div}\,\mathbf{x}'_{\boldsymbol{\alpha}}=\\ \varepsilon^{\boldsymbol{\alpha}}\underbrace{[(\rho^{\boldsymbol{\alpha}})'_{\boldsymbol{\alpha}}+\rho^{\boldsymbol{\alpha}}\,\mathrm{div}\,\mathbf{x}'_{\boldsymbol{\alpha}}]}_{\hat{\rho}^{\boldsymbol{\alpha}}}+\rho^{\boldsymbol{\alpha}}(\varepsilon^{\boldsymbol{\alpha}})'_{\boldsymbol{\alpha}}+\rho^{\boldsymbol{\alpha}}\,\mathbf{x}'_{\boldsymbol{\alpha}}\cdot\mathbf{x}''_{\boldsymbol{\alpha}}+\frac{1}{2}\,\mathbf{x}'_{\boldsymbol{\alpha}}\cdot\mathbf{x}'_{\boldsymbol{\alpha}}\underbrace{[(\rho^{\boldsymbol{\alpha}})'_{\boldsymbol{\alpha}}+\rho^{\boldsymbol{\alpha}}\,\mathrm{div}\,\mathbf{x}'_{\boldsymbol{\alpha}}]}_{\hat{\rho}^{\boldsymbol{\alpha}}},\end{aligned} \tag{A.30}$$

so that

$$\begin{aligned}[\rho^{\boldsymbol{\alpha}}(\varepsilon^{\boldsymbol{\alpha}}+\frac{1}{2}\,\mathbf{x}'_{\boldsymbol{\alpha}}\cdot\mathbf{x}'_{\boldsymbol{\alpha}})]'_{\boldsymbol{\alpha}}+[\rho^{\boldsymbol{\alpha}}(\varepsilon^{\boldsymbol{\alpha}}+\frac{1}{2}\,\mathbf{x}'_{\boldsymbol{\alpha}}\cdot\mathbf{x}'_{\boldsymbol{\alpha}})]\,\mathrm{div}\,\mathbf{x}'_{\boldsymbol{\alpha}}=\\ \varepsilon^{\boldsymbol{\alpha}}\hat{\rho}^{\boldsymbol{\alpha}}+\rho^{\boldsymbol{\alpha}}(\varepsilon^{\boldsymbol{\alpha}})'_{\boldsymbol{\alpha}}+\mathbf{x}'_{\boldsymbol{\alpha}}\cdot[\rho^{\boldsymbol{\alpha}}\,\mathbf{x}''_{\boldsymbol{\alpha}}+\frac{1}{2}\,\hat{\rho}^{\boldsymbol{\alpha}}\,\mathbf{x}'_{\boldsymbol{\alpha}}].\end{aligned} \tag{A.31}$$

With calculation rule (A.3), the divergence term in (A.29) can be reformulated with (3.56) to

$$\mathrm{div}[(\mathbf{T}^{\boldsymbol{\alpha}})^{\mathrm{T}}\,\mathbf{x}'_{\boldsymbol{\alpha}}-\mathbf{q}^{\boldsymbol{\alpha}}]=\mathbf{x}'_{\boldsymbol{\alpha}}\cdot\mathrm{div}\,\mathbf{T}^{\boldsymbol{\alpha}}+\mathbf{T}^{\boldsymbol{\alpha}}\cdot\mathbf{L}_{\alpha}-\mathrm{div}\,\mathbf{q}^{\boldsymbol{\alpha}}. \tag{A.32}$$

Implementing (A.31) and (A.32) into (A.29) and considering $(3.100)_2$ yields after rearranging

$$\begin{aligned}\hat{\rho}^{\boldsymbol{\alpha}}\,\varepsilon^{\boldsymbol{\alpha}}+\rho^{\boldsymbol{\alpha}}(\varepsilon^{\boldsymbol{\alpha}})'_{\boldsymbol{\alpha}}+\mathbf{x}'_{\boldsymbol{\alpha}}\cdot[\underbrace{\rho^{\boldsymbol{\alpha}}\mathbf{x}''_{\boldsymbol{\alpha}}-\mathrm{div}\,\mathbf{T}^{\boldsymbol{\alpha}}-\rho^{\boldsymbol{\alpha}}\mathbf{b}}_{\hat{\mathbf{p}}^{\boldsymbol{\alpha}}}+\frac{1}{2}\,\hat{\rho}^{\boldsymbol{\alpha}}\,\mathbf{x}'_{\boldsymbol{\alpha}}]=\\ \mathbf{T}^{\boldsymbol{\alpha}}\cdot\mathbf{L}_{\boldsymbol{\alpha}}-\mathrm{div}\,\mathbf{q}^{\boldsymbol{\alpha}}+\rho^{\boldsymbol{\alpha}}\mathrm{r}^{\boldsymbol{\alpha}}+\hat{\mathrm{e}}^{\boldsymbol{\alpha}}\end{aligned} \tag{A.33}$$

and finally

$$\rho^{\boldsymbol{\alpha}}(\varepsilon^{\boldsymbol{\alpha}})'_{\boldsymbol{\alpha}}=\mathbf{T}^{\boldsymbol{\alpha}}\cdot\mathbf{L}_{\boldsymbol{\alpha}}-\mathrm{div}\mathbf{q}^{\boldsymbol{\alpha}}+\rho^{\boldsymbol{\alpha}}\mathrm{r}^{\boldsymbol{\alpha}}+\hat{\mathrm{e}}^{\boldsymbol{\alpha}}-\hat{\mathbf{p}}^{\boldsymbol{\alpha}}\cdot\mathbf{x}'_{\boldsymbol{\alpha}}-\hat{\rho}^{\boldsymbol{\alpha}}(\varepsilon^{\boldsymbol{\alpha}}+\frac{1}{2}\,\mathbf{x}'_{\boldsymbol{\alpha}}\cdot\mathbf{x}'_{\boldsymbol{\alpha}}). \tag{A.34}$$

Analogously, the local balance of energy can be derived for component φ^{β}.

A.8. Derivation of local balance of entropy for $\varphi^{\boldsymbol{\alpha}}$

By implementing (3.123) into $(3.85)_1$ one obtains

$$(\rho^{\boldsymbol{\alpha}}\,\eta^{\boldsymbol{\alpha}})'_{\boldsymbol{\alpha}} + \rho^{\boldsymbol{\alpha}}\,\eta^{\boldsymbol{\alpha}}\,\mathrm{div}\,\mathbf{x}'_{\boldsymbol{\alpha}} = -\mathrm{div}\,(\frac{\mathbf{q}^{\boldsymbol{\alpha}}}{\theta^{\boldsymbol{\alpha}}}) + \frac{\rho^{\boldsymbol{\alpha}}\,\mathrm{r}^{\boldsymbol{\alpha}}}{\theta^{\boldsymbol{\alpha}}} + \hat{\eta}^{\boldsymbol{\alpha}}\,, \tag{A.35}$$

which can be reformulated by using the local mass balance $(3.91)_2$ for the left-hand side to

$$\rho^{\boldsymbol{\alpha}}\,(\eta^{\boldsymbol{\alpha}})'_{\boldsymbol{\alpha}} + \eta^{\boldsymbol{\alpha}}\,[(\rho^{\boldsymbol{\alpha}})'_{\boldsymbol{\alpha}} + \rho^{\boldsymbol{\alpha}}\,\mathrm{div}\,\mathbf{x}'_{\boldsymbol{\alpha}}] = \rho^{\boldsymbol{\alpha}}\,(\eta^{\boldsymbol{\alpha}})'_{\boldsymbol{\alpha}} + \hat{\rho}^{\boldsymbol{\alpha}}\,\eta^{\boldsymbol{\alpha}} = -\,\mathrm{div}(\frac{\mathbf{q}^{\boldsymbol{\alpha}}}{\theta^{\boldsymbol{\alpha}}}) + \frac{\rho^{\boldsymbol{\alpha}}\,\mathrm{r}^{\boldsymbol{\alpha}}}{\theta^{\boldsymbol{\alpha}}} + \hat{\eta}^{\boldsymbol{\alpha}}\,. \tag{A.36}$$

As before, the local entropy balance of the components φ^{β} can be derived analogously.

B. Derivations - Chapter 5

B.1. Volume balance solid main phase

Starting from

$$(\mathrm{J}_{\mathbf{S}})'_{\mathbf{S}} = \frac{\partial \mathrm{J}_{\mathbf{S}}}{\partial \mathbf{F}_{\mathbf{S}}} \frac{\partial \mathbf{F}_{\mathbf{S}}}{\partial \mathrm{t}} = \underbrace{\frac{\partial \det \mathbf{F}_{\mathbf{S}}}{\partial \mathbf{F}_{\mathbf{S}}}}_{= \mathrm{J}_{\mathbf{S}} \mathbf{F}_{\mathbf{S}}^{\mathrm{T}-1}} \cdot (\mathbf{F}_{\mathbf{S}})'_{\mathbf{S}} \tag{B.1}$$

and utilizing the expression for the material velocity gradient $(\mathbf{F}_{\mathbf{S}})'_{\mathbf{S}}$, cf. (3.55), relation

$$(\mathrm{J}_{\mathbf{S}})'_{\mathbf{S}} = \mathrm{J}_{\mathbf{S}} \mathbf{F}_{\mathbf{S}}^{\mathrm{T}-1} \mathbf{F}_{\mathbf{S}}^{\mathrm{T}} \cdot \mathbf{L}_{\mathbf{S}} = \mathrm{J}_{\mathbf{S}}\, \mathbf{I} \cdot \mathbf{L}_{\mathbf{S}} = \mathrm{J}_{\mathbf{S}}\, \mathrm{div} \mathbf{x}'_{\mathbf{S}} \tag{B.2}$$

is gained by utilizing (3.57). Implementing this relation into (5.16) yields

$$(\mathrm{n}^{\mathbf{S}})'_{\mathbf{S}} + \mathrm{n}^{\mathbf{S}} \frac{1}{\mathrm{J}_{\mathbf{S}}} (\mathrm{J}_{\mathbf{S}})'_{\mathbf{S}} = 0 \quad \Leftrightarrow \quad \frac{(\mathrm{n}^{\mathbf{S}})'_{\mathbf{S}}}{\mathrm{n}^{\mathbf{S}}} = -\frac{(\mathrm{J}_{\mathbf{S}})'_{\mathbf{S}}}{\mathrm{J}_{\mathbf{S}}}\,. \tag{B.3}$$

Integrating $(\mathrm{B}.3)_2$ leads to

$$\begin{aligned} \int_{\mathrm{t}_0}^{\mathrm{t}} \frac{(\mathrm{n}^{\mathbf{S}})'_{\mathbf{S}}}{\mathrm{n}^{\mathbf{S}}}\, \mathrm{dt} = -\int_{\mathrm{t}_0}^{\mathrm{t}} \frac{(\mathrm{J}_{\mathbf{S}})'_{\mathbf{S}}}{\mathrm{J}_{\mathbf{S}}}\, \mathrm{dt} \quad &\Leftrightarrow \quad \ln|\mathrm{n}^{\mathbf{S}}| - \ln|\mathrm{n}^{\mathbf{S}}_{0\mathbf{S}}| = -\ln|\mathrm{J}_{\mathbf{S}}| + \underbrace{\ln|1|}_{=0} \\ &\Leftrightarrow \quad \boxed{\mathrm{n}^{\mathbf{S}} = \frac{1}{\mathrm{J}_{\mathbf{S}}}\, \mathrm{n}^{\mathbf{S}}_{0\mathbf{S}}}\,. \end{aligned} \tag{B.4}$$

B.2. Volume balance equation of main gas phase

Starting from

$$\sum_{\gamma}[(\rho^{\gamma})'_{\gamma} + \rho^{\gamma}\,\mathrm{div}\,\mathbf{x}'_{\gamma}] = \underbrace{\sum_{\gamma}\hat{\rho}^{\gamma}}_{=\,0} \quad \Leftrightarrow \quad \sum_{\gamma}[(\rho^{\gamma})'_{\mathbf{G}} + \mathrm{grad}\,\rho^{\gamma}\cdot\mathbf{d}_{\gamma\mathbf{G}} + \rho^{\gamma}\,\mathrm{div}\,\mathbf{x}'_{\gamma}] = 0 \tag{B.5}$$

where use has been made of $(A.12)_1$. Furthermore, calculation rule (A.1) is applied to '$\rho^{\gamma}\,\mathrm{div}\,\mathbf{x}'_{\gamma}$', so that rearrangement of (B.5) leads to

$$\sum_{\gamma}[(\rho^{\gamma})'_{\mathbf{G}} - \mathrm{grad}\,\rho^{\gamma}\cdot\mathbf{x}'_{\mathbf{G}} + \mathrm{div}\,(\rho^{\gamma}\,\mathbf{x}'_{\gamma})] = 0\,. \tag{B.6}$$

Implementing the averaged velocity $(3.61)_1$ and additionally applying again (A.1), (B.6) reads

$$\sum_{\gamma}[(\rho^{\gamma})'_{\mathbf{G}} + \rho^{\gamma}\,\mathrm{div}\,\mathbf{x}'_{\mathbf{G}}] = 0 \quad \Rightarrow \quad (\rho^{\mathbf{G}})'_{\mathbf{G}} + \rho^{\mathbf{G}}\,\mathrm{div}\,\mathbf{x}'_{\mathbf{G}} = 0 \tag{B.7}$$

by additionally using (3.24) and (3.26). The final version of the gas volume balance equation (5.17) can be derived by inserting (5.12) into (B.7).

B.3. Overall gas balance in terms of molar concentration

Proceeding from (5.41), summation of the concentration balances and additionally expansion by $[1/\mathrm{c}_m^{\mathbf{G}}]$ yields

$$\begin{aligned} &\sum_{\gamma}\mathrm{c}_m^{\mathrm{G}\gamma}\,(\mathrm{n}^{\mathbf{G}})'_{\gamma} + \mathrm{n}^{\mathbf{G}}\sum_{\gamma}(\mathrm{c}_m^{\mathrm{G}\gamma})'_{\gamma} + \mathrm{n}^{\mathbf{G}}\sum_{\gamma}\mathrm{c}_m^{\mathrm{G}\gamma}\,\mathrm{div}\,\mathbf{x}'_{\gamma} = \mathrm{n}^{\mathbf{G}}\sum_{\gamma}\hat{\mathrm{c}}_m^{\mathrm{G}\gamma} \\ \Rightarrow\ &\sum_{\gamma}\frac{\mathrm{c}_m^{\mathrm{G}\gamma}}{\mathrm{c}_m^{\mathbf{G}}}(\mathrm{n}^{\mathbf{G}})'_{\gamma} + \frac{\mathrm{n}^{\mathbf{G}}}{\mathrm{c}_m^{\mathbf{G}}}\sum_{\gamma}(\mathrm{c}_m^{\mathrm{G}\gamma})'_{\gamma} + \mathrm{n}^{\mathbf{G}}\sum_{\gamma}\frac{\mathrm{c}_m^{\mathrm{G}\gamma}}{\mathrm{c}_m^{\mathbf{G}}}\,\mathrm{div}\,\mathbf{x}'_{\gamma} = \frac{\mathrm{n}^{\mathbf{G}}}{\mathrm{c}_m^{\mathbf{G}}}\sum_{\gamma}\hat{\mathrm{c}}_m^{\mathrm{G}\gamma}\,. \end{aligned} \tag{B.8}$$

Considering the definition for the molar fraction (3.18), (B.8) then reads

$$\sum_{\gamma} x_m^{\mathrm{G}\gamma} \left(\mathrm{n}^{\mathbf{G}}\right)'_{\gamma} + \frac{\mathrm{n}^{\mathbf{G}}}{\mathrm{c}_m^{\mathbf{G}}} \sum_{\gamma} (\mathrm{c}_m^{\mathrm{G}\gamma})'_{\gamma} + \mathrm{n}^{\mathbf{G}} \sum_{\gamma} x_m^{\mathrm{G}\gamma} \operatorname{div} \mathbf{x}'_{\mathrm{G}\gamma} = \frac{\mathrm{n}^{\mathbf{G}}}{\mathrm{c}_m^{\mathbf{G}}} \sum_{\gamma} \hat{\mathrm{c}}_m^{\mathrm{G}\gamma} \,. \tag{B.9}$$

The first material time derivative of (B.9) rewritten with respect to the deforming solid (A.13) and moreover (3.20) reads

$$\sum_{\gamma} x_m^{\mathrm{G}\gamma} \left(\mathrm{n}^{\mathbf{G}}\right)'_{\gamma} = \underbrace{\sum_{\gamma} x_m^{\mathrm{G}\gamma}}_{=1} \left(\mathrm{n}^{\mathbf{G}}\right)'_{\mathbf{S}} + \operatorname{grad} \mathrm{n}^{\mathbf{G}} \sum_{\gamma} x_m^{\mathrm{G}\gamma} \cdot \mathbf{w}_{\gamma\mathbf{S}} \,, \tag{B.10}$$

and after implementing the overall concentration balance reads

$$\left(\mathrm{n}^{\mathbf{G}}\right)'_{\mathbf{S}} = -\frac{\mathrm{n}^{\mathbf{G}}}{\mathrm{c}_m^{\mathbf{G}}} \sum_{\gamma} (\mathrm{c}_m^{\mathrm{G}\gamma})'_{\gamma} - \mathrm{n}^{\mathbf{G}} \sum_{\gamma} x_m^{\mathrm{G}\gamma} \operatorname{div} \mathbf{x}'_{\gamma} - \operatorname{grad} \mathrm{n}^{\mathbf{G}} \sum_{\gamma} x_m^{\mathrm{G}\gamma} \cdot \mathbf{w}_{\gamma\mathbf{S}} + \frac{\mathrm{n}^{\mathbf{G}}}{\mathrm{c}_m^{\mathbf{G}}} \sum_{\gamma} \hat{\mathrm{c}}_m^{\mathrm{G}\gamma} \,. \tag{B.11}$$

B.4. Closure of equation system

The number of constitutive equations required can be determined by the number of describing field equations ($\#\mathcal{FE}$) and the number of field quantities ($\#\mathcal{FQ}$) contained. The difference between these numbers, cf. (B.12), provides the number of required constitutive equations ($\#\mathcal{CE}$) to solve the equation system, which at the same time should not violate the physical laws. To derive

$$\#\mathcal{FQ} - \#\mathcal{FE} = \#\mathcal{CE} \tag{B.12}$$

the equations established so far will be analyzed and thus the number of constitutive quantities identified. The describing field equations for the solid - gas mixture are collected in Tab. B.1. As shown, the number of relevant field equations sums up to

$$\#\mathcal{FE} = 26 + 4\gamma \,, \tag{B.13}$$

Table B.1.: Describing field equations

field equation		scalar amount
volume balance solid	(5.16)	1
volume balance gas	(5.17)	1
concentration balance	(5.22)	1γ
momentum balance solid	$(5.24)_1$	3
momentum balance gas	$(5.24)_2$	3
momentum balance concentration	$(5.25)_1$	3γ
energy balance mixture	(5.30)	1
constraint mass exchange	(5.13)	1
constraint stresses	$(5.25)_2$	6
constraint interaction forces	(5.15)	3
constraint free energy	$(5.32)_1$	1
constraint entropy	$(5.32)_2$	1
partial density solid	$(5.4)_1$	1
partial density gas	$(5.4)_2$	1
constraint partial pore density	(5.7)	1
constraint mass fractions	(5.6)	1
saturation condition	(5.2)	1
total		$26 + 4\gamma$

for γ components of the mixture. The system of field equations given in Tab. B.1 contains the total number of

$$\#\mathcal{FQ} = 41 + 16\gamma\,, \tag{B.14}$$

field variables, namely the following:

$$\begin{aligned}\mathcal{FQ} = \{\, &\boldsymbol{\chi}^{\mathbf{S}},\, \boldsymbol{\chi}^{\mathbf{G}},\, \boldsymbol{\chi}^{\gamma},\, \mathbf{T}^{\mathbf{S}},\, \mathbf{T}^{\mathbf{G}},\, \mathbf{T}^{\gamma},\, \hat{\mathbf{p}}^{\mathbf{S}},\, \hat{\mathbf{p}}^{\mathbf{G}},\, \hat{\mathbf{p}}^{\gamma},\, \mathbf{q},\, \mathbf{b},\\ &\psi^{\mathbf{S}},\, \psi^{\mathbf{G}},\, \psi^{\gamma},\, \eta^{\mathbf{S}},\, \eta^{\mathbf{G}},\, \eta^{\gamma},\, \theta,\, \rho^{\mathbf{S}},\, \rho^{\mathbf{G}},\, \rho^{\gamma},\, \rho^{\mathbf{SR}},\, \rho^{\mathbf{GR}},\, \mathrm{n}^{\mathbf{S}},\, \mathrm{n}^{\mathbf{G}},\, \hat{\rho}^{\gamma}\,\}\,. \end{aligned} \tag{B.15}$$

Therein, the tensor-valued stresses are counted with 6 entries considering the symmetry with $\mathbf{T}^{\boldsymbol{\alpha}} = (\mathbf{T}^{\boldsymbol{\alpha}})^{\mathrm{T}}$. From (B.15), the number of known quantities ($\#\mathcal{KQ}$)

$$\#\mathcal{KQ} = 4 \tag{B.16}$$

can be identified, namely the gravitational acceleration $\mathbf{b}$ and the constant density of the solid phase with

$$\mathcal{KQ} = \{\, \mathbf{b},\, \rho^{\mathbf{SR}} = \rho_{0\mathbf{S}}^{\mathbf{SR}} \,\}\,. \tag{B.17}$$

Considering (B.15), (B.17) and the total number of field equations (B.13), the following amount of constitutive relations is required:

$$\begin{array}{lll} & 41 + 16\gamma & \#\mathcal{FQ} \\ - & 4 & \#\mathcal{KQ} \\ - & (26 + 4\gamma) & \#\mathcal{FE} \\ \hline & 11 + 12\gamma & \#\mathcal{CE} \end{array} \tag{B.18}$$

Finally, $(11 + 12\gamma)$ field quantities remain for which constitutive relations have to be found. The constitutive quantities ($\#\mathcal{CQ}$) are chosen with

$$\mathcal{CQ} = \{\, \mathbf{T}^{\mathbf{S}},\, \mathbf{T}^{\gamma},\, \hat{\mathbf{p}}^{\gamma},\, \hat{\rho}^{\gamma}, \psi^{\mathbf{S}},\, \psi^{\gamma},\, \eta^{\mathbf{S}}, \eta^{\gamma}, \mathbf{q} \,\}\,. \tag{B.19}$$

B.5. Derivation of Helmholtz energy gas

Considering restriction (5.100) as well as a mass approach based on the equation for the molar chemical potential for ideal gases, cf. (2.56), the following request is postulated:

$$\mu^{\gamma} = \frac{\partial \psi^{\mathrm{G}\gamma}}{\partial \rho^{\mathrm{G}\gamma}} \stackrel{!}{=} \mu_0^{\gamma} + \mathrm{R}^{\gamma}\, \theta\, \ln(\frac{\rho^{\mathrm{G}\gamma}}{\rho_0^{\mathrm{G}\gamma}}). \tag{B.20}$$

By integration the approach for the volume-specific Helmholtz potential of the gas components is derived with

$$\psi^{\mathrm{G}\gamma} = \rho^{\mathrm{G}\gamma}\mu_0^{\gamma} + \rho^{\mathrm{G}\gamma}\, \mathrm{R}^{\gamma}\, \theta\, [\ln(\frac{\rho^{\mathrm{G}\gamma}}{\rho_0^{\mathrm{G}\gamma}}) - 1] + f^{\mathrm{G}\gamma}(\theta) \tag{B.21}$$

and hence, for the mass-specific energy

$$\psi^{\gamma} = \frac{\psi^{\mathrm{G}\gamma}}{\rho^{\mathrm{G}\gamma}} = \mu_0^{\gamma} + \mathrm{R}^{\gamma}\, \theta\, [\ln(\frac{\rho^{\mathrm{G}\gamma}}{\rho_0^{\mathrm{G}\gamma}}) - 1] + f^{\gamma}(\theta)\,, \tag{B.22}$$

where $f^{\mathrm{G}\gamma}(\theta)$ and $f^{\gamma}(\theta)$, respectively, denote the temperature dependent integration constants.

With (B.21) and (3.28), the ansatz for the molar-specific chemical potential $\mu_m^\gamma = \mathrm{M}_m^\gamma\,\mu^\gamma$ can additionally be derived via

$$\begin{aligned}\mu^\gamma = \frac{\partial \psi^{\mathrm{G}\gamma}}{\partial \rho^{\mathrm{G}\gamma}} = \frac{\partial \psi^{\mathrm{G}\gamma}}{\partial(\mathrm{c}_m^{\mathrm{G}\gamma}\,\mathrm{M}_m^\gamma)} &= \frac{1}{\mathrm{M}_m^\gamma}[\frac{\partial \psi^{\mathrm{G}\gamma}}{\partial \mathrm{c}_m^{\mathrm{G}\gamma}}] \\ &= \frac{1}{\mathrm{M}_m^\gamma}[\mathrm{M}_m^\gamma\,\mu_0^{\mathrm{G}\gamma} + \mathrm{M}_m^\gamma \mathrm{R}^\gamma\,\theta\ln(\frac{\mathrm{c}_m^{\mathrm{G}\gamma}}{\mathrm{c}_{m,0}^{\mathrm{G}\gamma}})]\end{aligned} \tag{B.23}$$

which finally leads to

$$\mu_m^\gamma = \mu_{m,0}^\gamma + \mathrm{R}_m\,\theta\ln(\frac{\mathrm{c}_m^{\mathrm{G}\gamma}}{\mathrm{c}_{m,0}^{\mathrm{G}\gamma}})\,. \tag{B.24}$$

Therein, $\mathrm{R}_m = \mathrm{M}_m^\gamma\,\mathrm{R}^\gamma$ denotes the universal gas constant.

Additionally, the free energy is postulated to be a function of the temperature θ, see also (5.48). Referring to that, the approach for $f^{\mathrm{G}\gamma}(\theta)$ and $f^{\gamma}(\theta)$, cf. (B.21) and (B.22), has to be found.

According to the general fundamental principles of thermodynamics the heat capacity measured at constant volume is defined with

$$\mathrm{c}_\mathrm{V}^\gamma = \frac{\partial \varepsilon^\gamma}{\partial \theta} = \frac{\partial(\psi^\gamma + \theta\,\eta^\gamma)}{\partial \theta}, \tag{B.25}$$

see (2.50), where the specific internal energy ε can be replaced by the specific Helmholtz energy (2.7) with

$$\psi^\alpha = \varepsilon^\gamma - \theta\,\eta^\gamma. \tag{B.26}$$

The specific entropy η^γ is defined with $(2.13)_4$ as

$$\eta^\gamma = -\frac{\partial \psi^\gamma}{\partial \theta}, \tag{B.27}$$

so that (B.27) implemented into (B.25) reads, additionally with (5.55) and (5.57),

$$\mathrm{c}_\mathrm{V}^\gamma = -\theta\,\frac{\partial^2 \psi^\gamma}{\partial^2 \theta} = -\frac{\theta}{\rho^{\mathrm{G}\gamma}}\frac{\partial^2 \psi^{\mathrm{G}\gamma}}{\partial^2 \theta}\,. \tag{B.28}$$

Considering (B.21) and the second derivative with respect to the temperature, the following constraint together with (B.28) is postulated:

$$\frac{\partial^2 \psi^{\mathrm{G}\gamma}}{\partial^2 \theta} = \frac{\partial^2 f^{\mathrm{G}\gamma}}{\partial^2 \theta} \stackrel{!}{=} -\frac{\mathrm{c}_{\mathrm{V}}^{\gamma}\, \rho^{\mathrm{G}\gamma}}{\theta}\,. \tag{B.29}$$

By double integration the term $f^{\mathrm{G}\gamma}(\theta)$ is determined with

$$f^{\mathrm{G}\gamma} = -\rho^{\mathrm{G}\gamma} \mathrm{c}_{\mathrm{V}}^{\gamma}\,[\,\theta \ln(\frac{\theta}{\theta_0}) - \theta + \theta_0] = \mathrm{c}_{\mathrm{V}}^{\mathrm{G}\gamma}\,[\,\theta \ln(\frac{\theta}{\theta_0}) - \theta + \theta_0]\,. \tag{B.30}$$

and likewise the mass-specific term $f^{\gamma}(\theta)$

$$f^{\gamma} = -\mathrm{c}_{\mathrm{V}}^{\gamma}\,[\,\theta \ln(\frac{\theta}{\theta_0}) - \theta + \theta_0]\,. \tag{B.31}$$

Finally, combining the integration results with (B.21) and (B.22), the Helmholtz energies for the gas component φ^{γ} read

$$\begin{aligned} \psi^{\gamma} &= \mu_0^{\gamma} + \mathrm{R}^{\gamma}\,\theta\,[\ln(\frac{\rho^{\mathrm{G}\gamma}}{\rho_0^{\mathrm{G}\gamma}}) - 1] - \mathrm{c}_{\mathrm{V}}^{\gamma}\,[\,\theta \ln(\frac{\theta}{\theta_0}) - \theta + \theta_0] \\ \psi^{\mathrm{G}\gamma} &= \mu_0^{\mathrm{G}\gamma} + \mathrm{R}^{\gamma}\,\theta\,[\ln(\frac{\rho^{\mathrm{G}\gamma}}{\rho_0^{\mathrm{G}\gamma}}) - 1] - \mathrm{c}_{\mathrm{V}}^{\mathrm{G}\gamma}[\,\theta \ln(\frac{\theta}{\theta_0}) - \theta + \theta_0]\,. \end{aligned} \tag{B.32}$$

B.6. Mixture balance equation of mass for solid and gas

The sum of the volume balances of the main phases solid and gas, (5.16) and (5.17), reads

$$(\mathrm{n}^{\mathbf{S}})'_{\mathbf{S}} + (\mathrm{n}^{\mathbf{G}})'_{\mathbf{G}} + \mathrm{n}^{\mathbf{S}}\,\mathrm{div}\,\mathbf{x}'_{\mathbf{S}} + \mathrm{n}^{\mathbf{G}}\,\mathrm{div}\,\mathbf{x}'_{\mathbf{G}} + \frac{\mathrm{n}^{\mathbf{G}}}{(\rho^{\mathbf{G}\mathrm{R}})'_{\mathbf{G}}}(\rho^{\mathbf{G}\mathrm{R}})'_{\mathbf{G}}\,. \tag{B.33}$$

Implementing the material time derivative of the volume fraction of gas $\mathrm{n}^{\mathbf{G}}$ with respect to the solid motion $(\mathrm{A}.13)_3$ with

$$(\mathrm{n}^{\mathbf{G}})'_{\mathbf{G}} = (\mathrm{n}^{\mathbf{G}})'_{\mathbf{S}} + \mathrm{grad}\,\mathrm{n}^{\mathbf{G}}\,\mathbf{w}_{\mathbf{GS}}\,, \tag{B.34}$$

and furthermore considering the relation of the material time derivative of the saturation condition (5.40) yields the alternative formulation

$$\mathrm{n}^{\mathbf{S}} \operatorname{div} \mathbf{x}'_{\mathbf{S}} + \mathrm{n}^{\mathbf{G}} \operatorname{div} \mathbf{x}'_{\mathbf{G}} + \operatorname{grad} \mathrm{n}^{\mathbf{G}} \, \mathbf{w}_{\mathbf{GS}} + \frac{\mathrm{n}^{\mathbf{G}}}{(\rho^{\mathbf{G}\mathrm{R}})'_{\mathbf{G}}} (\rho^{\mathbf{G}\mathrm{R}})'_{\mathbf{G}} \,, \tag{B.35}$$

which is transferred to

$$\mathrm{n}^{\mathbf{S}} \operatorname{div} \mathbf{x}'_{\mathbf{S}} + \mathrm{n}^{\mathbf{G}} \operatorname{div} \mathbf{x}'_{\mathbf{G}} + \operatorname{div} (\mathrm{n}^{\mathbf{G}} \, \mathbf{w}_{\mathbf{GS}}) - \mathrm{n}^{\mathbf{G}} \operatorname{div} \mathbf{w}_{\mathbf{GS}} + \frac{\mathrm{n}^{\mathbf{G}}}{(\rho^{\mathbf{G}\mathrm{R}})'_{\mathbf{G}}} (\rho^{\mathbf{G}\mathrm{R}})'_{\mathbf{G}} \,, \tag{B.36}$$

by using the divergence calculation rule (A.1). Moreover, after implementing the saturation condition $\mathrm{n}^{\mathbf{G}} = 1 - \mathrm{n}^{\mathbf{G}}$ into the fourth term, (B.36) can be reduced to the final form

$$\operatorname{div} (\mathrm{n}^{\mathbf{G}} \mathbf{w}_{\mathbf{GS}} + \mathbf{x}'_{\mathbf{S}}) + \frac{\mathrm{n}^{\mathbf{G}}}{\rho^{\mathbf{G}\mathrm{R}}} (\rho^{\mathbf{G}\mathrm{R}})'_{\mathbf{G}} = 0 \,. \tag{B.37}$$

C. FEM

C.1. Discretized equation system

For the matrix formulation required for the FEM approximation, the *B-matrix* $\mathbf{B_{us}}$ is utilized, which arranges the partial derivatives of the ansatz functions as follows:

$$\mathbf{B}^I_{\mathbf{uS}} = \begin{bmatrix} N^I_{,X} & 0 & 0 & N^I_{,Y} & 0 & N^I_{,Z} & 0 & 0 & 0 \\ 0 & N^I_{,Y} & 0 & 0 & N^I_{,X} & 0 & 0 & N^I_{,Z} & 0 \\ 0 & 0 & N^I_{,Z} & 0 & 0 & 0 & N^I_{,X} & 0 & N^I_{,Y} \end{bmatrix}^T . \tag{C.1}$$

Moreover, the approximation of the gradients of the scalar values, the *B-matrix* $\mathbf{B}_\Theta$ is introduced, which gathers the derivatives of the ansatz functions in the respective vector

$$\mathbf{B}^I_\Theta = [N^I_{,X}\,, N^I_{,Y}\,, N^I_{,Z}]^T\,, \tag{C.2}$$

where Θ is representative for the scalar values $\Theta = \{\{\mathrm{c}^{\mathrm{G}\iota}_{\mathrm{mol}}\},\, \mathrm{p}^{\mathbf{G}\mathrm{R}},\, \theta\}$.

With that, the finite element approximation of the weak formulations given in Section 6.1 read after implementing the approaches for the virtual test functions for one element, starting with the mixture balance of momentum:

$$\mathrm{G}^{el}_u := \sum_I^n (\mathrm{d}\delta\mathbf{u}^I_{\mathbf{S}})^T \{ \int_{\Omega_e} (\mathbf{B}^I_{\mathbf{us}})^T\, \mathbf{P}^{(v)}\, \mathrm{d}\Omega - \int_{\Omega_e} N^I \rho_0\, \mathbf{b}\, \mathrm{d}\Omega - \int_{\partial\Omega_e} N^I \bar{\mathbf{p}}_{\mathbf{0}}\, \mathrm{d}\, \partial\Omega \} \tag{C.3}$$

where the stress tensor $\mathbf{P} = \dim\,[3\mathrm{x}3]$ has been rewritten to the vector $\mathbf{P}^{(v)} = \dim\,[9\mathrm{x}1]$ and use has been made of $\rho_0 = \mathrm{J}_{\mathbf{S}}\,\rho$, cf. also (B.4). The discretized form of the

mixture mass balance reads

$$\mathrm{G}_p^{el} := \sum_I^n (\mathrm{d}\delta \mathrm{p}^{\mathbf{G}\mathrm{R}})^I \Big\{ - \int_{\Omega_e} (\mathbf{B}_p^I)^T \, \mathrm{n}^{\mathbf{G}} \mathbf{w}_{\mathbf{GS},0} \, \mathrm{d}\Omega + \int_{\Omega_e} N^I \, \mathrm{J}_{\mathbf{S}} \, \{\mathrm{Grad}\, \mathbf{x}'_{\mathbf{S}} \cdot \mathbf{F}_{\mathbf{S}}^{\mathrm{T}-1}\} \, \mathrm{d}\Omega + \int_{\Omega_e} N^I \, \mathrm{J}_{\mathbf{S}} \, \{\frac{\mathrm{n}^{\mathbf{G}}}{\rho^{\mathbf{G}\mathrm{R}}} (\rho^{\mathbf{G}\mathrm{R}})'_{\mathbf{G}}\} \, \mathrm{d}\Omega + \int_{\partial\Omega_e} N^I \, \bar{\mathbf{n}}^{\mathbf{G}} \mathbf{w}_{\mathbf{GS},0} \, \mathrm{d}\, \partial\Omega \Big\} \tag{C.4}$$

with $\bar{\mathbf{n}}^{\mathbf{G}} \mathbf{w}_{\mathbf{GS},0} = \mathrm{n}^{\mathbf{G}} \mathbf{w}_{\mathbf{GS},0} \cdot \mathbf{n}_0$ denoting the boundary term. The discretized form of the concentration balance reads

$$\mathrm{G}_c^{el} := \sum_I^n (\mathrm{d}\delta \mathrm{c}_m^{\mathrm{G}\gamma})^I \Big\{ - \int_{\Omega_e} \mathrm{n}^{\mathbf{G}} \, (\mathbf{B}_c^I)^T \, {}_m\mathbf{j}_{tot,0}^{\mathrm{G}\gamma} \, \mathrm{d}\Omega + \int_{\Omega_e} N^I \, \mathrm{J}_{\mathbf{S}} \, \{\mathrm{c}_m^{\mathrm{G}\gamma} \, \mathrm{Grad}\, \mathbf{x}'_{\mathbf{S}} \cdot \mathbf{F}_{\mathbf{S}}^{\mathrm{T}-1}\} \, \mathrm{d}\Omega + \int_{\Omega_e} N^I \, \mathrm{J}_{\mathbf{S}} \, \{\mathrm{n}^{\mathbf{G}} (\mathrm{c}_m^{\mathrm{G}\gamma})'_{\mathbf{S}} - \mathrm{n}^{\mathbf{G}} \, \hat{\mathrm{c}}_m^{\mathrm{G}\gamma}\} \, \mathrm{d}\Omega + \int_{\partial\Omega_e} N^I \, {}_m\bar{\mathbf{j}}_{tot,0}^{\mathrm{G}\gamma} \, \mathrm{d}\, \partial\Omega \Big\} \tag{C.5}$$

with ${}_m\bar{\mathbf{j}}_{tot,0}^{\mathrm{G}\gamma} = \mathrm{n}_m^{\mathbf{G}} \mathbf{j}_{tot,0}^{\mathrm{G}\gamma} \cdot \mathbf{n}_0$ denoting the boundary term. Finally the discretized mixture energy balance is given with

$$\mathrm{G}_\theta^{el} := \sum_I^n (\mathrm{d}\delta\theta)^I \Big\{ - \int_{\Omega_e} (\mathbf{B}_\theta^I)^T \, \mathbf{q}_{,0} \, \mathrm{d}\Omega + \int_{\Omega_e} N^I \, \mathrm{J}_{\mathbf{S}} \, \{\theta \, (\rho^{\mathbf{S}} (\eta^{\mathbf{S}})'_{\mathbf{S}} + \sum_\gamma \rho^\gamma (\eta^\gamma)'_{\mathrm{G}\gamma})\} \, \mathrm{d}\Omega + \int_{\Omega_e} N^I \, \sum_\gamma \hat{\rho}^\gamma h^\gamma \, \mathrm{d}\Omega + \int_{\partial\Omega_e} N^I \, \bar{\mathbf{q}}_{,0} \, \mathrm{d}\, \partial\Omega \Big\} \tag{C.6}$$

with $\bar{\mathbf{q}}_{,0} = \mathbf{q}_{,0} \cdot \mathbf{n}_0$ denoting the boundary term.

The integral over the element domain Ω_e is referred to the isoparametric reference with the following relation

$$\int_{\Omega_e} (...) \, \mathrm{d}\Omega = \int_{\Omega_\square} (...) \, \mathrm{det}\mathbf{J}_e \, \mathrm{d}_\square \,, \tag{C.7}$$

and furthermore, the integration over $\Omega_\square$ is solved numerically utilizing the Gauss integration scheme, cf. [109].

C.2. Linearization for Newton's method

Each discretized weak formulation has to be linearized for the NEWTON procedure according to Section 6.2.2. For that, the incremental parts $\Delta \mathrm{G}_u^{el}$, $\Delta \mathrm{G}_p^{el}$, $\Delta \mathrm{G}_c^{el}$, and $\Delta \mathrm{G}_\theta^{el}$ can be developed analytically by deriving each term of the weak form towards the degrees of freedom and their time derivatives with the general procedure given in (6.39). This yields the tangent term for one node with

$$\Delta \mathbf{g}^* = \begin{bmatrix} \mathbf{k}_{uu} & \mathbf{k}_{up} & \mathbf{k}_{uc} & \mathbf{k}_{u\theta} \\ \mathrm{k}_{pu} & \mathrm{k}_{pp} & \mathrm{k}_{pc} & \mathrm{k}_{p\theta} \\ \mathbf{k}_{cu} & \mathbf{k}_{cp} & \mathbf{k}_{cc} & \mathbf{k}_{c\theta} \\ \mathrm{k}_{\theta u} & \mathrm{k}_{\theta p} & \mathrm{k}_{\theta c} & \mathrm{k}_{\theta\theta} \end{bmatrix} \begin{bmatrix} \Delta \mathrm{d}\mathbf{u}_{\mathbf{S}} \\ \Delta \mathrm{dp}^{\mathbf{G}\mathrm{R}} \\ \Delta \mathrm{d}\mathbf{c}_{\mathrm{mol}}^{\mathrm{G}\iota} \\ \Delta \mathrm{d}\theta \end{bmatrix} = \mathbf{K}^* \Delta \mathbf{u} \tag{C.8}$$

where $\Delta \mathbf{g}^*$ is denotes the effective tangent stiffness vector, see (6.47). The bold-typed entries show the multidimensionality of the displacements as well as the set of molar concentrations to solve. Moreover, the indices of each entry of $\mathbf{K}^*$ indicate the arrangement of the weak formulations and the respective derivations, wherein the first index stands for the balance equation, the second for the directional derivative.

In this work the effective tangent matrix is derived through a numerical tangent by utilizing the forward difference quotient with

$$\mathbf{k}_m \approx \frac{\mathbf{g}(\mathbf{v}^i + h_m \mathbf{e}_m) - \mathbf{g}(\mathbf{v}^\mathbf{i})}{h_m}\,, \tag{C.9}$$

where h_m denotes the increment size and $\mathbf{e}_m$ a vector, which is zero for all entries except entry m, where it is equal to one, cf. [109]. Moreover, the index m denotes the respective degree of freedom $m \in \{\{u\}, p, \{c\}, \theta\}$. With that, the tangent stiffness matrix is composed of the columns $\mathbf{k}_{mm}$ as

$$\mathbf{K}^* = \begin{bmatrix} \mathbf{k}_{mu} & \mathbf{k}_{mp} & \mathbf{k}_{mc} & \mathbf{k}_{m\theta} \end{bmatrix}\,. \tag{C.10}$$

D. Applications

D.1. Thermal Imaging

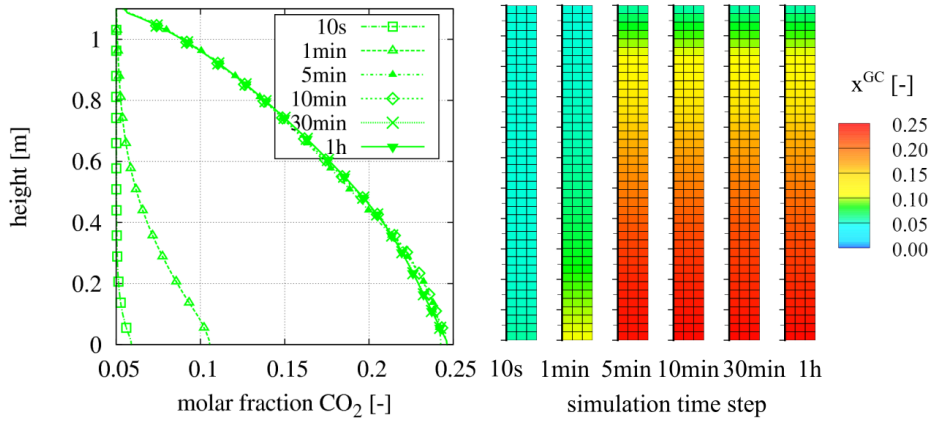

Figure D.1.: Molar fraction of carbon dioxide x_m^{GC} [-] over height for different time steps of the simulation

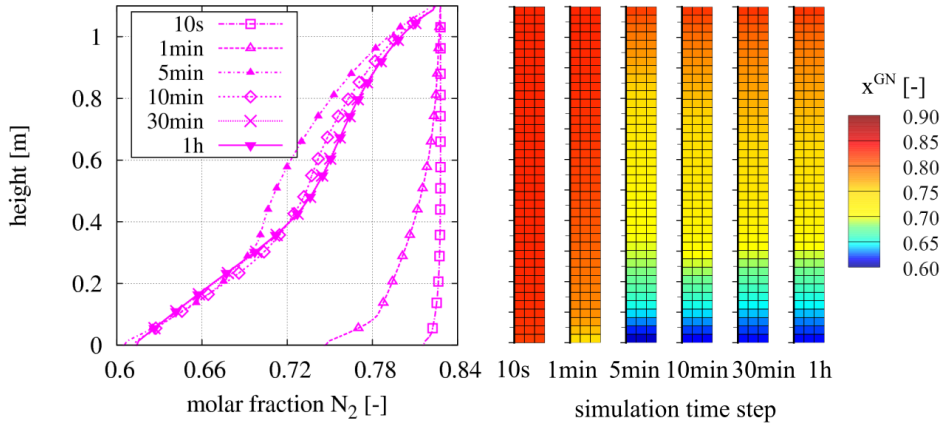

Figure D.2.: Molar fraction of nitrogen x_m^{GN} [-] over height for different time steps of the simulation

Fig. D.1 and D.2 depict the distribution of nitrogen and carbon dioxide, respectively, at different simulation time steps. Since both gases are not directly involved in methane oxidation, the steady states are reached immediately after approximately 5 minutes.

D.2. Constant diffusion with slow and strong advection

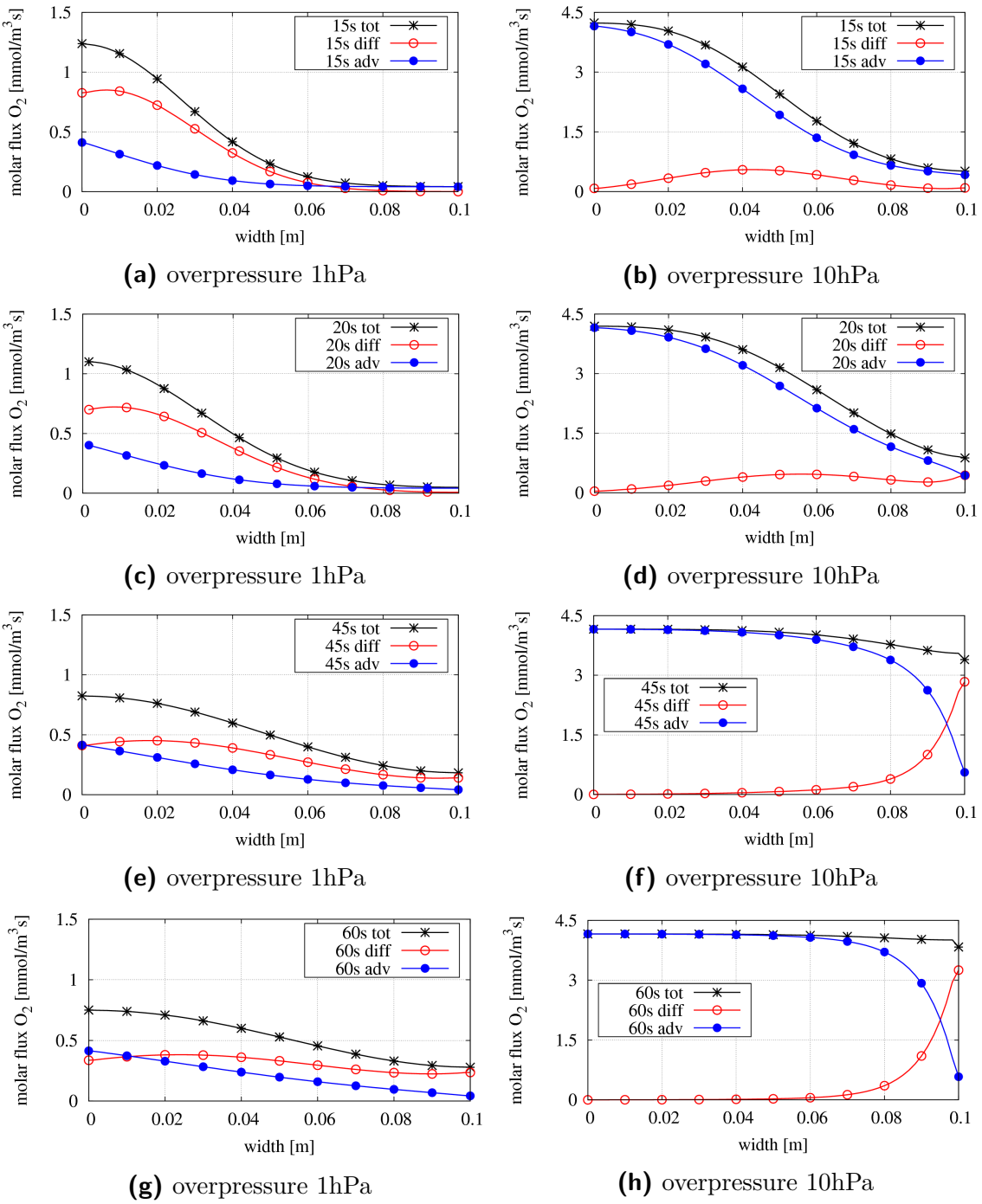

(a) overpressure 1hPa

(b) overpressure 10hPa

(c) overpressure 1hPa

(d) overpressure 10hPa

(e) overpressure 1hPa

(f) overpressure 10hPa

(g) overpressure 1hPa

(h) overpressure 10hPa

Figure D.3.: Total, diffusive and advective proportions of partial molar fluxes of oxygen $\mathbf{j}_m^{\mathrm{O}}$ [mmol/m^3] at different simulation time steps over width of model

Bibliography

[1] T. Abichou, D. Powelson, J. Chanton, S. Escoriaza, and J. Stern. "Characterization of methane flux and oxidation at a solid waste Landfill". In: *Journal of Environmental Engineering* 132 (2006), pp. 220–228.

[2] T. Abichou, K. Mahieu, L. Yuan, J. Chanton, and G. Hater. "Effects of compost biocovers on gas flow and methane oxidation in a landfill cover". In: *Waste Management* 29 (2009), pp. 1595–1601.

[3] T. Abichou, J. Chanton, D. Powelson, J. Fleiger, S. Escoriaza, L. Yuan, and J. Stern. "Methane flux and oxidation at two types of intermediate landfill covers". In: *Waste Management* 26 (2006), pp. 1305–1312.

[4] T. Abichou, T. Kormi, L. Yuan, T. Johnson, and E. Francisco. "Modeling the effects of vegetation on methane oxidation and emissions through soil landfill final covers across different climates". In: *Waste Management* 36 (2015), pp. 230–240.

[5] T. Abichou, K. Mahieu, J. Chanton, M. Romdhane, and I. Mansouri. "Scaling methane oxidation: From laboratory incubation experiments to landfill cover field conditions". In: *Waste Management* 31 (2011), pp. 978–986.

[6] A. Acartürk. "Simulation of Charged Hydrated Porous Media". PhD thesis. Institute of Applied Mechanics, Universität Stuttgart, 2009.

[7] R. A. Alberty. "Use of Legendre transforms in chemical thermodynamics (IUPAC Technical Report)". In: *Pure and Applied Chemistry* 73 (2001), pp. 1349–1380.

[8] H. Altenbach. *Kontinuumsmechanik - Einführung in die materialunabhängigen und materialabhängigen Gleichungen*. Springer Vieweg, 2018.

[9] P. Atkins and J. de Paula. *Atkins' Physical Chemistry*. Oxford University Press, 2014.

[10] K. J. Bathe. *Finite-Elemente-Methoden*. Springer, Berlin, 2002.

[11] J. Berger. “Biologische Methanoxidation in Deponieabdeckschichten”. PhD thesis. Institut WAR, Technische Universität Darmstadt, 2008.

[12] R. B. Bird, W. E. Stewart, and E. N. Lightfoot. *Transport Phenomena*. John Wiley & Sons, New York, 2007.

[13] J. Bluhm. “Modelling of saturated thermo-elastic porous solids with different phase temperatures”. In: *Porous Media: Theory, Experiments and Numerical Applications*. Ed. by W. Ehlers and J. Bluhm. Springer-Verlag, Berlin, 2002, pp. 87–118.

[14] P. Boeckx, O. van Cleemput, and I. Villaralvo. “Methane emission from a landfill and the methane oxidising capacity of its covering soil”. In: *Soil Biology and Biochemistry* 28 (1996), pp. 1397–1405.

[15] J. E. Bogner, K. A. Spokas, and E. A. Burton. “Kinetics of methane oxidation in a land fill cover soil: temporal variations, a whole land fill oxidation experiments, and modeling of net CH4 emissions”. In: *Journal of Environmental Science & Engineering* 31 (1997), pp. 2504–2514.

[16] J. Bonet and Wood. R. D. *Nonlinear Continuum Mechanics for Finite Element Analysis*. Cambridge University Press, 1997.

[17] D. Bothe. “On the Maxwell-Stefan approach to multicomponent diffusion”. In: *Parabolic problems*. Springer, Basel, 2011, pp. 81–93.

[18] R. M. Bowen. “Compressible porous media models by use of the theory of mixtures”. In: *International Journal of Engineering Science* 20 (1982), pp. 697–735.

[19] R. M. Bowen. “Incompressible porous media models by use of the theory of mixtures”. In: *International Journal of Engineering Science* 18 (1980), pp. 1129–1148.

[20] R. M. Bowen. “The thermochemistry of a reacting mixture of elastic materials with diffusion”. In: *Archive for Rational Mechanics and Analysis* 34 (1969), pp. 97–127.

[21] R. M. Bowen. “Theory of mixtures”. In: *Continuum Physics*. Ed. by A. C. Eringen. Vol. III. Academic Press, New York, 1976, pp. 1–127.

[22] R. M. Bowen. “Toward a thermodynamics and mechanics of mixtures”. In: *Archives for Rational Mechanics and Analysis* 24 (1967), pp. 370–403.

[23] H. C. Brinkman. “A calculation of the viscous force exerted by a flowing fluid on a dense swarm of particles”. In: *Applied Scientific Research* A1 (1949), pp. 27–34.

[24] H. B. Callen. *Introduction to Thermodynamics and Thermostatistics*. John Wiley & Sons, New York, 1985.

[25] J. Chanton and K. Liptay. "Seasonal variation in methane oxidation in a landfill cover soil as determined by an in situ stable isotope technique". In: *Global Biogeochemical Cycles* 14 (2000), pp. 51–60.

[26] J. Chanton, D. Powelson, T. Abichou, and G. Hate. "Improved field methods to quantify methane oxidation in landfill cover materials using stable carbon isotopes". In: *Environmental Science & Technology* 42 (2008), pp. 665–670.

[27] R. Clausius. *Abhandlungen über die mechanische Wärmetheorie, Vol. 1.* Friedrich Vieweg und Sohn, Braunschweig, 1864.

[28] B. D. Coleman and W. Noll. "The thermodynamics of elastic materials with heat conduction and viscosity". In: *Archives for Rational Mechanics and Analalyis* 13 (1963), pp. 167–178.

[29] P. M. Czepiel, B. Mosher, P. M. Crill, and R. C. Harriss. "Quantifying the effect of oxidation on landfill methane emissions". In: *Journal of geophysical research: Atmospheres* 101 (1996), pp. 16721–16729.

[30] P. M. Czepiel, J. H. Shorter, B. Mosher, E. Allwine, J. B. McManus, R. C. Harriss, C. E. Kolb, and B. K. Lamb. "The influence of atmospheric pressure on landfill methane emissions". In: *Waste Management* 23 (2003), pp. 593–598.

[31] J. Dalton. "Essay IV. On the expansion of elastic fluids by heat". In: *Memoirs of the Literary and Philosophical Society of Manchester* 5 (1802), pp. 595–602.

[32] H. Darcy. *Les fontaines publiques de la ville de Dijon: exposition et application.* Dalmont, 1856.

[33] R. de Boer. *Theory of Porous Media – highlights in the historical development and current state*. Springer, Berlin, 2000.

[34] R. de Boer. "Theory of porous media – past and present". In: *Journal of Applied Mathematics and Mechanics* 78 (1998), pp. 441–466.

[35] R. de Boer. *Vektor-und Tensorrechnung für Ingenieure*. Springer, Berlin, 1982.

[36] R. de Boer and W. Ehlers. "The development of the concept of effective stresses". In: *Acta Mechanica* 83 (1990), pp. 77–92.

[37] S. R. De Groot. *Thermodynamics of irreversible processes*. North Holland, Amsterdam, 1951.

[38] A. De Visscher and O. van-Cleemput. "Simulation model for gas diffusion and methane oxidation in landfill cover soils". In: *Waste Management* 23 (2003), pp. 581–591.

[39] A. De Visscher, D. Thomas, P. Boeckx, and O. van Cleemput. “Methane oxidation in simualted landfill cover soil environments”. In: *Environmental Science & Technology* 33 (1999), pp. 1854–1859.

[40] J. Donea and A. Huerta. *Finite Element Methods for Flow Problems*. John Wiley & Sons, Chichester, 2003.

[41] O. Edenhofer, R. Pichs-Madruga, Y. Sokona, E. Farahani, S. Kadner, K. Seyboth, A. Adler, I. Baum, S. Brunner, P. Eickemeier, B. Kriemann, J. Savolainen, S. Schlömer, C. von Stechow, T. Zwickel, and J. C. (eds.) Minx. *IPCC, 2014: Climate Change 2014: Mitigation of Climate Change. Contribution of Working Group III to the Fifth Assessment Report of the Intergovernmental Panel on Climate Change*. Tech. rep. IPCC Geneva, Switzerland, 2014.

[42] W. Ehlers. “Constitutive equations for granular materials in geomechanical context”. In: *Continuum Mechanics in Environmental Sciences and Geophysics*. Ed. by K. Hutter. Springer-Verlag, Vienna, 1993, pp. 313–402.

[43] W. Ehlers. “Darcy, Forchheimer, Brinkman and Richards: classical hydromechanical equations and their significance in the light of the TPM”. In: *Archive of Applied Mechanics* 92 (2022), pp. 619–639.

[44] W. Ehlers. *Elemente der nichtlinearen Kontinuumsthermodynamik*. Lecture notes, Institute of Applied Mechanics, Chair of Continuum Mechanics, University of Stuttgart, 1996.

[45] W. Ehlers. “Foundations of multiphasic and porous materials”. In: *Porous Media: Theory, Experiments and Numerical Applications*. Ed. by W. Ehlers and J. Bluhm. Springer-Verlag, Berlin, 2002, pp. 3–86.

[46] W. Ehlers. *Vector and Tensor Calculus: An Introduction*. Lecture notes, Institute of Applied Mechanics, Chair of Continuum Mechanics, University of Stuttgart, 2018.

[47] W. Ehlers and G. Eipper. “Finite Elastic Deformations in Liquid-Saturated and Empty Porous Solids”. In: *Transport in Porous Media* 34 (1999), pp. 179–191.

[48] R. B. Evans, G. M. Watson, and E. A. Mason. “Gaseous Diffusion in Porous Media at Uniform pressure”. In: *The Journal of Chemical Physics* 35 (1961), pp. 2076–2083.

[49] R. B. Evans, G. M. Watson, and E. A. Mason. “Gaseous Diffusion in Porous Media. II. Effect of Pressure Gradients”. In: *The Journal of Chemical Physics* 36 (1962), pp. 1894–1902.

[50] S. Feng, H. W. Liu, A. C. F. Chiu, and C. W. W. Ng. “A steady-state analytical profile method for determining methane oxidation in landfill cover”. In: *Science of the Total Environment* 646 (2019), pp. 1528–1535.

[51] S. Feng, C. W. W. Ng, A. K. Leung, and H. W. Liu. “Numerical modelling of methane oxidation efficiency and coupled water-gas-heat reactive transfer in a sloping landfill cover”. In: *Waste Management* 68 (2017), pp. 355–368.

[52] P. Forchheimer. “Wasserbewegung durch Boden”. In: *Zeitschrift des Vereins Deutscher Ingenieure* 45 (1901), pp. 1781–1788.

[53] J. B. J. Fourier. *Théorie analytique de la chaleur*. Didot, F., Paris, 1822.

[54] T. Gehrke. “Entwicklung von Methoden zur Untersuchung einer biologisch aktiven Methanoxidationsschicht”. PhD thesis. Urban Water and Waste Management, Universität Duisburg-Essen, 2021.

[55] S. Ghadiani. “A multiphasic continuum mechanical model for design investigations of an effusion-cooled rocket thrust chamber”. PhD thesis. Institute of Applied Mechanics, Universität Stuttgart, 2005.

[56] T. Graf. “Multiphasic flow processes in deformable porous media under consideration of fluid phase transitions”. PhD thesis. Institute of Applied Mechanics, Universität Stuttgart, 2008.

[57] A. Haarstrick, D. C. Hempel, L. Ostermann, H. Ahrens, and D. Dinkler. “Modelling of the biodegradation of organic matter in municipal landfills”. In: *Waste Management & Research* 19 (2001), pp. 320–331.

[58] R. S. Hanson and T. E. Hanson. “Methanotrophic bacteria”. In: *Microbiological reviews* 60 (1996), pp. 439–471.

[59] S. M. Hassanizadeh and W. G. Gray. “General conservation equations for multi-phase systems: 2. Mass, momenta, energy, and entropy equations.” In: *Advances in Water Resources* 2 (1979), pp. 191–208.

[60] P. Haupt. *Continuum Mechanics and Theory of Materials*. Springe, Berlin, 2002.

[61] V. C. Hettiarachchi, J. P. A. Hettiaratchi, and A. K. Mehrotra. “Comprehensive one-dimensional mathematical model for heat, gas, and moisture transport in methane biofilters”. In: *Practice Periodical of Hazardous, Toxic, and Radioactive Waste Management* 11 (2007), pp. 225–233.

[62] V. C. Hettiarachchi, P. J. Hettiaratchi, A. K. Mehrotra, and S. Kumar. “Field-scale operation of methane bio filtration systems to mitigate point source methane emissions”. In: *Environmental Pollution* 159 (2011), pp. 1715–1720.

[63] H. A. Hilger, D. F. Cranford, and M. Barlaz. “Methane oxidation and microbial expolymer production in landfill cover soil”. In: *Soil Biology & Biochemistry* 23 (2000), pp. 457–467.

[64] H. A. Hilger, S. K. Liehr, and M. Barlaz. “Exopolysaccharide control of methane oxidation in landfill cover soil”. In: *Journal of Environmental Engineering* 23 (1999), pp. 457–467.

[65] G. Holzapfel. *Nonlinear Solid Mechanics*. John Wiley & Sons, Chichester, 2000.

[66] M. Huber-Humer, J. Gebert, and H. Hilger. “Biotic systems to mitigate landfill methane emissions”. In: *Waste Management & Research* 26 (2008), pp. 33–46.

[67] J. M. Huyghe and P. H. M. Bovendeerd. “Biological mixtures”. In: *Modelling coupled phenomena in saturated porous materials : advanced course, Bydgoszcz*. Institute of Fundamental Technological Research, 2004, pp. 227–278.

[68] G. Juncu, A. Nicola, C. Popa, and E. Stroila. “Numerical solution of the parabolic multicomponent convection–diffusion mass transfer equations by a splitting method”. In: *Numerical Heat Transfer, Part A: Applications* 71 (2017), pp. 72–90.

[69] D. Kightley, D. B. Nedwell, and M. Cooper. “Capacity for methane oxidation in landfill cover soils measured in laboratory-scale soil microcosms”. In: *Applied and Environmental Microbiology* 61 (1995), pp. 592–601.

[70] K. Liptay, J. Chanton, P. Czepiel, and B. Mosher. “Use of stable isotopes to determine methane oxidation in landfill cover soils”. In: *Journal of Geophysical Research* 103 (1998), pp. 8243–8250.

[71] I.-S. Liu. “Method of Lagrange multipliers for exploitation of the entropy principle”. In: *Archive for Rational Mechanics and Analysis* 46 (1972), pp. 131–148.

[72] S. F. Lu and S. J. Feng. “Comprehensive overview of numerical modeling of coupled landfill processes”. In: *Waste Management* 118 (2020), pp. 161–179.

[73] K. Mahieu, A. De Visscher, P. A. Vanrolleghem, and O. van Cleemput. “Modelling of stable isotope fractionation by methane oxidation and diffusion in landfill cover soils”. In: *Waste Management* 28 (2008), pp. 1535–1542.

[74] T. R. Marrero and E. A. Mason. “Gaseous diffusion coefficients”. In: *Journal of Physical and Chemical Reference Data* 1 (1972), pp. 3–118.

[75] K. U. Mayer, E. O. Frind, and D. W. Blowes. “Multicomponent reactive transport modeling in variably saturated porous media using a genegeneral

formulation for kinetically concontrol reactions". In: *Water Resources Research* 38 (2002), pp. 1174–1185.

[76] R. J. Millington and J. P. Quirk. "Permeability of porous solids". In: *Transactions of the Faraday Society* 57 (1961), pp. 1200–1207.

[77] S. Molins and K. U. Mayer. "Coupling between geochemical reactions and Multicomponent gas and solute transport in unsaturated media: A reactive transport modeling study". In: *Water Resoures Research* 43 (2007).

[78] S. Molins, K. U. Mayer, C. Scheutz, and P. Kjeldsen. "Transport and reaction processes affecting the attenuation of landfill gas in cover soils". In: *Journal of Environmental Quality* 37 (2008), pp. 459–468.

[79] J. Monod. "The growth of bacterial cultures". In: *Annual Review of Microbiology* 3 (1949), pp. 371–394.

[80] J. W. F. Morris, M. D. Caldwell, J. M. Obereiner, S. T. O Donnell, T. R. Johnson, and T. Abichou. "Modeling methane oxidation in landfill cover soils as indicator of functional stability with respect to gas management". In: *Journal of the Air & Waste Management Association* 69 (2019), pp. 13–22.

[81] I. Müller. *Thermodynamik: die Grundlagen der Materialtheorie*. Bertelsmann-Universitätsverlag, 1973.

[82] S. Nanda and F. Berruti. "Municipal solid waste management and landfilling technologies: a review". In: *Environmental Chemistry Letters* (2020), pp. 1–24.

[83] C. W. W. Ng, S. Feng, and H. W. Liu. "A fully coupled model for water-gas-heat-reactive transport with methane oxidation in landfill covers". In: *Science of the Total Environment* 508 (2015), pp. 307–319.

[84] V. Novaresioa, M. Garcia-Camprubib, S. Izquierdoa, P. Asinaria, and N. Fueyob. "An open-source library for the numerical modeling of mass-transport in solid oxide fuel cells". In: *Computer Physics Communications* 183 (2012), pp. 125–146.

[85] H. Parisch. *Festkörper-Kontinuumsmechanik*. Vol. 144. B. G. Teubner, Stuttgart, 2003.

[86] The Copernicus Programme. *Climate indicator temperature*. 2021-09-14. 2021. URL: `https://climate.copernicus.eu/index.php/climate-indicators/temperature`.

[87] R. C. Reid, J. M. Prausnitz, and B. E. Poling. *The Properties of Gases and Liquids*. McGraw-Hill, New York, 1987.

[88] T. Ricken, N. Waschinsky, and D. Werner. “Simulation of steatosis zonation in liver lobule - a continuum-mechanical bi-scale, tri-phasic, multicomponent approach”. In: *Biomedical Technology*. Ed. by W. Ehlers and A. Wagner. Springer International Publishing, 2018, pp. 15–33.

[89] T. Ricken, A. Thom, T. Gehrke, M. Denecke, R. Widmann, M. Schulte, and T. C. Schmidt. “Biological driven phase transition in fully or partly saturated porous media - a multi-component FEM simulation based on the theory of porous media”. In: *Views on Multiscale Modelling of Granular Materials. Advances in Mechanics and Mathematics*. Ed. by Giovine P., Mariano P. M., and Mortara G. Vol. 44. Birkhäuser, Cham, 2020, pp. 157–183.

[90] T. Ricken, A. Sindern, J. Bluhm, DeneckeM., T. Gehrke, and T. C. Schmidt. “Concentration driven phase transitions in multiphase porous media with application to methane oxidation in landfill cover layers”. In: *Journal of Applied Mathematics and Mechanics* 94 (2014), pp. 609–622.

[91] T. Ricken, D. Werner, H. G. Holzhütter, M. König, and O. Dahmen U. und Dirsch. “Modeling function–perfusion behavior in liver lobules including tissue, blood, glucose, lactate and glycogen by use of a coupled two-scale PDE–ODE approach”. In: *Biomechanics and Modeling in Mechanobiology* 14 (2015), pp. 515–536.

[92] C. Scheutz, P. Kjeldsen, A. De Visscher, J. Gebert, H. A. Hilger, M. Huber-Humer, and K. Spokas. “Microbial methane oxidation processes and technologies for mitigation of landfill gas emissions”. In: *Waste Management & Research* 27 (2009), pp. 409–455.

[93] M. Schulte, M. A. Jochmann, T. Gehrke, A. Thom, T. Ricken, M. Denecke, and T. C. Schmidt. “Characterization of methane oxidation in a simulated landfill cover system by comparing molecular and stable isotope mass balances”. In: *International Journal of Environment and Waste Management* 69 (2017), pp. 281–288.

[94] J. C. Simo and K. S. Pister. “Remarks on rate constitutive equations for finite deformation problems: Computational implications”. In: *Computer Methods in Applied Mechanics and Engineering* 46 (1984), pp. 201–215.

[95] V. B. Stein, J. P. A. Hettiratchi, and G. Achari. “Numerical model for biological oxidation and migration of methane in soils”. In: *Practice Periodical of Hazardous, Toxic, and Radioactive Waste Management* 5 (2001), pp. 225–234.

[96] T. F. Stocker, D. Qin, G.-K. Plattner, M. Tignor, S. K. Allen, J. Boschung, A. Nauels, Y. Xia, V. Bex, and P. M. (eds.) Midgley. *IPCC, 2013: Climate Change 2013: The Physical Science Basis, Contribution of Working Group I to the Fifth Assessment Report of the Intergovernmental Panel on Climate Change*. Tech. rep. IPCC Geneva, Switzerland, 2013.

[97] R. Taylor and R. Krishna. *Multicomponent mass transfer*. Vol. 2. John Wiley & Sons, New York, 1993.

[98] R. L. Taylor. *FEAP-A Finite Element Analysis Program, Version 8.4 Programmer Manual*. Department of Civil and Environmental Engineering, University of California at Berkeley, 2014.

[99] Core Writing Team, R. K. Pachauri, and L. A. (eds.) Meyer. *IPCC, 2014: Climate Change 2014: Synthesis report. Contribution of Working Groups I, II and III to the Fifth Assessment Report of the Intergovernmental Panel on Climate Change*. Tech. rep. 151pp. IPCC Geneva, Switzerland, 2014.

[100] K. Terzaghi. *Theoretical Soil Mechanics*. John Wiley & Sons, New York, 1943.

[101] A. Thom, T. Ricken, M. Koßler, T. Gehrke, M. Denecke, R. Widmann, M. Schulte, and T. C. Schmidt. "Numerical investigations of diffusion coefficients in the context of multi-component gas transport within the Theory of Porous Media". In: *PAMM* 18 (2018), e201800446.

[102] D. C. Thorstenson and D. W. Pollock. "Gas transport in unsaturated porous media: the adequacy of Fick's law". In: *Reviews of Geophysics* 27 (1989), pp. 61–78.

[103] C. Truesdell. *Rational Thermodynamics*. 2nd ed. Springer, New York, 1984.

[104] C. Truesdell and W. Noll. "The non-linear field theories of mechanics". In: *Handbuch der Physik*. Ed. by S. Flügge. Vol. III/3. Springer-Verlag, Berlin Heidelberg, 1965.

[105] C. Truesdell and R. Toupin. "The classical field theories". In: *Handbuch der Physik*. Ed. by S. Flügge. Vol. III/1. Springer-Verlag, Berlin Heidelberg, 1960, pp. 226–858.

[106] J. W. Veldsink, R. M. J. Damme, G. F. Versteeg, and W. P. M. van Swaaij. "The use of the dusty-gas model for the description of mass transport with chemical reaction in porous media". In: *The Chemical Engineering Journal* 57 (1995), pp. 115–125.

[107] S. W. Webb. "Gas transport mechanisms". In: *Gas Transport in Porous Media*. Ed. by C. K. Ho and S. W. Webb. Vol. 20. Springer, 2006. Chap. 2, pp. 5–26.

[108] S. C. Whalen, W. S. Reeburgh, and K. A. Sandbeck. “Rapid methane oxidation in landfill cover soil”. In: *Applied and Environmental Microbiology* 56 (1990), pp. 3405–3411.

[109] P. Wriggers. *Nichtlineare Finite-Element-Methoden*. Springer, Berlin, 2001.

[110] L. Yuan, T. Abichou, J. Chanton, D. Powelson, and A. De Visscher. “Long-term numerical simulation of methane transport and oxidation in a compost biofilter”. In: *Practice Periodical of Hazardous, Toxic, and Radioactive Waste Management* 13 (2009), pp. 196–202.

[111] O. C. Zienkiewitz and R. L. Taylor. *The Finite Element Method for Solid and Structural Mechanics*. 6th ed. Butterworth-Heinemann, London, 2005.

[112] O. C. Zienkiewitz and R. L. Taylor. *The Finite Element Method - Its Basis and Fundamentals*. 6th ed. Butterworth-Heinemann, London, 2005.

This dissertation was written as part of the interdisciplinary research project on the modeling and simulation of a methane oxidation layer in municipal solid waste landfills, funded by the German Research Foundation (DFG). Over several decades, landfill sites produce methane (CH_4) and carbon dioxide (CO_2) in nearly equal shares by the bacterial degradation of the organic fraction of the deposited municipal solid waste. Thus, an aftercare treatment of the gas emissions still occurring after landfill closure is required by authorities.

Being one of the strongest drivers of the greenhouse effect, methane is much more damaging over a 20-year period than carbon dioxide. Passive conversion of methane to carbon dioxide by naturally occurring bacterial methane oxidation in aerated soils is both an environmental and economic option to address residual emissions in the post-closure phase of landfilling.

A mathematical model based on the continuum mechanical Theory of Porous Media (TPM) was developed by the author of this thesis for the numerical simulation of methane oxidation in soils. It was verified and validated using small-scale experiments from laboratory. The resulting numerical calculation concept enables the balancing of gas fluxes through existing cover layers under the given conditions and the design of landfill cover layers in such a way that the functionality of methane oxidation can be guaranteed even under unfavorable external environmental conditions.

Institut für Statik und Dynamik
der Luft- und Raumfahrtkonstruktionen
Univ.-Prof. Dr.-Ing. Tim Ricken

9 783942 807098